# Abstract

This thesis develops diffusion models for modern electrochemical experiments involving the transport of particles to electrodes and adsorbing surfaces. In particular, the models are related to the 'impact' method where particles stochastically arrive at an electrode and detected electrochemically. The studies are carried out using numerical simulations and also analytical methods.

Chapter 1 is introductory and outlines some fundamental concepts in mass transport and kinetics, and their relation to electrochemical measurements which are of importance for the reader. Chapter 2 describes the numerical methods which are used for electrochemical simulations. Chapter 3 focuses on a specific two dimensional simulation system and the development of a high performance voltammetry simulation.

Chapters 4 and 5 study the stochastic impacts of particles at an electrode surface. In Chapter 4, a 'diffusion only' model is developed using a probabilistic study and random walk simulations in order to provide expressions that can be used in so-called 'impact' experiments. In Chapter 5, the practical cases of microdisc and microwire electrodes are investigated. Expressions for the number of impacts are developed and the concept of the lower limit of detection in ultra-dilute solutions is introduced. Then, a comparison study between the microwire electrode and the microdisc electrode explores a geometrical effect and its implications for experimental setups.

In Chapter 6, a numerical and analytical study is developed to examine the effect of hindered diffusion as a particle moves close to an adsorbing surface. The study identifies the conditions under which this hindered diffusion is significant even in a non-confined space. The study shows that the domination of hindered diffusion is strongly dependant on the sizes of both the particle and the target. The study focuses on a variety of target shapes and allows the number of hits/impacts to be estimated in practical ‘impact’ experiments. Moreover, a drastic effect on the calculation of the mean first passage time is observed for a sub-micron sized target, showing the importance of this effect not only for electrochemistry but also in biological systems.

Chapters 7 and 8 investigate the properties of an adsorbing insulating surface adjacent to an electrode. In Chapter 7, a numerical study of the effect of ’shielding’ by the insulating sheath is carried out. The study examines the influence of this effect on the magnitude of the current in chronoamperometry experiments. Chapter 8 explores the case of reversible adsorption on the insulating surface for voltammetric enhancement by pre-concentration on the sheath surface. The results identify the conditions under which enhancement of the voltammetric signal can be observed.

Finally, Chapter 9 looks at geometrical effects on the current response of insulating particles modified with an electroactive surface layer. Numerical models are developed to model the diffusion of charge transfer between electro-active sites on a modified surface of insulating particles. The current-time responses are simulated for particles with the shape of a sphere, a cube/cuboid, and a cylinder on an electrode. The characteristic current-time responses are calculated for the various shapes. The observations show that the model can be utilised in experiments to determine the coverage or the diffusion coefficient of charge dissipation on modified insulating particles and, in some situations to identify the particle shape.

# Acknowledgments

I would like to express my sincere gratitude to my advisor Professor Richard Compton for his immeasurable help in every aspect, the encouragement, and the guidance throughout my DPhil.

I would also like to deeply thank Dr. Enno Kätelhön for his continuous help and advice in research and in general his friendship.

I also wish to thank:

Dr. Kristina Tschulik for her great help and large contribution to my research over the years. Dr. Chris Batchelor-McAuley, for his large contribution to my research through all my Dphil. Stan Sokolov, Kamonwad Ngamchuea, and Javor Novev for the great discussions and the enjoyable collaborations. The fellows in the Compton group past and present, for making the time very enjoyable. St Cross College and the College friends who made my time in Oxford unique and inspiring.

I acknowledge the ERC, E.P. Abraham Scholarship and St Cross College, and Oxford Chemistry Department for funding my DPhil.

Personal thanks to my close family, as well as Ron Kindler, Tzion Raz, Matan-yah Ben-Zion, and Yatir Sadia. Finally, thanks to Olivia Fiertag.

# Contents

**1 Introduction** **1**

1.1 Mass transport in electrochemistry . . . . . . . . . . . . . . . . . . . . . . 2

1.1.1 Migration and convection . . . . . . . . . . . . . . . . . . . . . . . . 3

1.2 Fundamentals of an electrochemical reaction . . . . . . . . . . . . . . . . . 5

1.3 Electrochemical reactions . . . . . . . . . . . . . . . . . . . . . . . . . . . . 8

1.3.1 Electrode kinetics . . . . . . . . . . . . . . . . . . . . . . . . . . . . 9

1.4 Electrochemical experiments . . . . . . . . . . . . . . . . . . . . . . . . . . 12

1.4.1 Cell configuration . . . . . . . . . . . . . . . . . . . . . . . . . . . . 12

1.4.2 The supporting electrolyte . . . . . . . . . . . . . . . . . . . . . . . 14

1.5 Main techniques . . . . . . . . . . . . . . . . . . . . . . . . . . . . . . . . . 15

1.5.1 Chrono-amperometry . . . . . . . . . . . . . . . . . . . . . . . . . . 15

1.5.2 Cyclic voltammetry . . . . . . . . . . . . . . . . . . . . . . . . . . . 18

1.6 Microelectrodes . . . . . . . . . . . . . . . . . . . . . . . . . . . . . . . . . 22

1.6.1 Microelectrode voltammetry . . . . . . . . . . . . . . . . . . . . . . 23

1.6.2 Microelectrode chronoamperometry . . . . . . . . . . . . . . . . . . 24

1.6.3 Micro-wire electrodes . . . . . . . . . . . . . . . . . . . . . . . . . . 26

**2 Electrochemical simulation** **31**

2.1 Random walk modelling . . . 32
2.2 Numerical method for solving of the diffusion equation . . . 33
2.3 Finite difference method . . . 33
  2.3.1 Motivation . . . 33
  2.3.2 The numerical basis of finite difference simulation . . . 35
  2.3.3 Explicit and implicit methods . . . 37
  2.3.4 Typical adaptations . . . 39
  2.3.5 Implementation . . . 42
  2.3.6 Conclusions . . . 42

**3 Implementing high performance voltammetry simulation using the implicit parallel algorithm 46**

3.1 Introduction . . . 47
3.2 Physical model . . . 48
  3.2.1 Boundary Conditions . . . 50
  3.2.2 Current Calculation . . . 52
3.3 Numerical Methods . . . 52
  3.3.1 Memory allocation in the GPU device . . . 55
  3.3.2 Implementation . . . 56
3.4 Calculations . . . 57
  3.4.1 Typical Voltammetry . . . 58
  3.4.2 The simulation of kinetics in voltammetry, and of amperometry . . . 60
  3.4.3 Performance tests . . . 62
3.5 Conclusions . . . 63

**4 Diffusion in the stochastic limit - application for the impact method 66**

4.1 Introduction . . . . . . . . . . . . . . . . . . . . . . . . . . . . . . . . . 67

4.2 Theory . . . . . . . . . . . . . . . . . . . . . . . . . . . . . . . . . 71

4.2.1 Linear diffusion - Macro-sized absorbing wall . . . . . . . . . . . . . 71

4.2.2 Validation using the ‘random-walk’ method . . . . . . . . . . . . . 77

4.2.3 Convergent (radial) diffusion - absorbing sphere . . . . . . . . . . . 78

4.3 Discussion . . . . . . . . . . . . . . . . . . . . . . . . . . . . . . . . . 81

4.3.1 Linear diffusion regime . . . . . . . . . . . . . . . . . . . . . . . . 81

4.3.2 ‘Random-walk’ study . . . . . . . . . . . . . . . . . . . . . . . . . 83

4.3.3 Convergent (radial) diffusion regime . . . . . . . . . . . . . . . . . 87

4.4 Conclusions . . . . . . . . . . . . . . . . . . . . . . . . . . . . . . . . 92

4.5 Appendix: Non-continuous media and the approximation of continuous media using Fick’s second law . . . . . . . . . . . . . . . . . . . . . . . . 93

**5 Diffusional impacts of nanoparticles on microdisc and microwire 107**

5.1 Introduction . . . . . . . . . . . . . . . . . . . . . . . . . . . . . . . . 108

5.2 Theory . . . . . . . . . . . . . . . . . . . . . . . . . . . . . . . . . . 109

5.2.1 Microdisc electrode . . . . . . . . . . . . . . . . . . . . . . . . . . 109

5.2.2 Microwire electrode . . . . . . . . . . . . . . . . . . . . . . . . . . 113

5.3 Discussion . . . . . . . . . . . . . . . . . . . . . . . . . . . . . . . . 117

5.3.1 Microdisc electrode . . . . . . . . . . . . . . . . . . . . . . . . . . 117

5.3.2 Microwire electrode . . . . . . . . . . . . . . . . . . . . . . . . . . 119

5.3.3 Comparison between microdisc and microwire geometries . . . . . . 123

5.4 Conclusions . . . . . . . . . . . . . . . . . . . . . . . . . . . . . . . . 124

**6 Hindered diffusion towards small targets 129**

6.1 Introduction . . . . . 130

6.2 Simplified model . . . . . 134

6.3 Numerical study . . . . . 136

6.3.1 1D cell and a macro-scale target . . . . . 137

6.3.2 1D cell - a finite sphere target . . . . . 141

6.4 Near-wall Hindered diffusion of particles towards a finite disc and a wire . 149

6.4.1 Hindered diffusion of particles towards a finite disc . . . . . 149

6.4.2 Hindered diffusion towards a wire . . . . . 154

6.5 Conclusions . . . . . 157

6.6 Appendix . . . . . 158

6.6.1 Computational methods . . . . . 158

6.6.2 Diffusion to a finite sphere . . . . . 160

6.6.3 Anisotropic hindered diffusion towards a disc: . . . . . 163

6.6.4 Residual maps of the flux towards a sphere and a disc . . . . . 164

**7 Shielding of a microdisc electrode surrounded by an adsorbing surface 172**

7.1 Introduction . . . . . 173

7.2 Theory . . . . . 174

7.2.1 Boundary Conditions . . . . . 175

7.2.2 Numerical Methods . . . . . 179

7.3 Results and discussion . . . . . 182

7.3.1 Model validation - simple microdisc electrode chronoamperometry . 183

7.3.2 The shielding effect - full sticking on the surrounding surface (sheath) 184

7.3.3 Shielding effect - kinetically controlled adsorption . . . . . 186

7.4 Conclusions . . . . . . . . . . . . . . . . . . . . . . . . . . . . . . . . 192

**8 Voltammetric sensitivity enhancement by using pre-concentration 197**

8.1 Introduction . . . . . . . . . . . . . . . . . . . . . . . . . . . . . . . . 198

8.2 Theory . . . . . . . . . . . . . . . . . . . . . . . . . . . . . . . . . . . 202

8.2.1 Dimensionless coordination representation . . . . . . . . . . . . . . 203

8.2.2 Boundary conditions . . . . . . . . . . . . . . . . . . . . . . . . . 206

8.2.3 Initial conditions . . . . . . . . . . . . . . . . . . . . . . . . . . . 210

8.2.4 Current calculation . . . . . . . . . . . . . . . . . . . . . . . . . . 210

8.2.5 Numerical methods . . . . . . . . . . . . . . . . . . . . . . . . . . 211

8.3 Results and discussion . . . . . . . . . . . . . . . . . . . . . . . . . . 213

8.3.1 Cyclic voltammetry with a reversible adsorbing sheath - a representative case . . . . . . . . . . . . . . . . . . . . . . . . . . . . . . . 213

8.3.2 Parametric study . . . . . . . . . . . . . . . . . . . . . . . . . . . 217

8.4 Conclusions . . . . . . . . . . . . . . . . . . . . . . . . . . . . . . . . 230

**9 Charge diffusion on the surface of particles with simple geometries 235**

9.1 Introduction . . . . . . . . . . . . . . . . . . . . . . . . . . . . . . . . 236

9.2 Model . . . . . . . . . . . . . . . . . . . . . . . . . . . . . . . . . . . 239

9.3 Numerical model . . . . . . . . . . . . . . . . . . . . . . . . . . . . . 241

9.3.1 ‘Cylinder on its base’ . . . . . . . . . . . . . . . . . . . . . . . . . 241

9.3.2 Dimensionless form . . . . . . . . . . . . . . . . . . . . . . . . . . 242

9.3.3 Boundary conditions and flux . . . . . . . . . . . . . . . . . . . . . 243

9.4 ‘Cylinder on its side’ . . . . . . . . . . . . . . . . . . . . . . . . . . . 244

9.4.1 Dimensionless form . . . . . . . . . . . . . . . . . . . . . . . . . . 245

9.4.2 Boundary conditions and flux . . . . . . . . . . . . . . . . . . . . . . 245

9.5 Numerical model: a sphere . . . . . . . . . . . . . . . . . . . . . . . . . . 245

9.5.1 Dimensionless form . . . . . . . . . . . . . . . . . . . . . . . . . . . . 246

9.5.2 Boundary conditions and flux . . . . . . . . . . . . . . . . . . . . . . 246

9.6 Numerical model: a cube and a cuboid . . . . . . . . . . . . . . . . . . . . 248

9.6.1 Dimensionless form . . . . . . . . . . . . . . . . . . . . . . . . . . . . 249

9.6.2 Boundary conditions and flux . . . . . . . . . . . . . . . . . . . . . . 250

9.6.3 Cuboid . . . . . . . . . . . . . . . . . . . . . . . . . . . . . . . . . . . 251

9.7 Results and Discussion . . . . . . . . . . . . . . . . . . . . . . . . . . . . 251

9.8 Conclusions . . . . . . . . . . . . . . . . . . . . . . . . . . . . . . . . . . 262

9.9 Appendix . . . . . . . . . . . . . . . . . . . . . . . . . . . . . . . . . . . 263

9.9.1 Discretization and grids: ‘cylinder on its base’ . . . . . . . . . . . . 263

9.9.2 Discretization: ‘cylinder on its side’ . . . . . . . . . . . . . . . . . . 267

9.9.3 Discretization: ‘sphere’ . . . . . . . . . . . . . . . . . . . . . . . . . . 269

9.9.4 Discretization and grids: cube/cuboid . . . . . . . . . . . . . . . . . 271

**10 Conclusions** **280**

# The following papers have contributed to the thesis:

- S. Eloul and R. G. Compton Journal of Electroanalytical Chemistry, vol. 771, pp. 50-55, 2016.
- S. Eloul, E. Kätelhön, C. Batchelor-McAuley, K. Tschulik, and R. G. Compton The Journal of Physical Chemistry C, vol. 119, no. 25, pp. 14400-14410, 2015.
- S. Eloul, E. Kätelhön, C. Batchelor-McAuley, K. Tschulik, and R. G. Compton Journal of Electroanalytical Chemistry, vol. 755, pp. 136-142, 2015.
- S. Eloul, E. Kätelhön, and R. G. Compton, Physical Chemistry Chemical Physics, Accepted for publication, 2016.
- S. Eloul and R. G. Compton, The Journal of Physical Chemistry Letters, vol. 7, pp. 4317-4321, 2016.
- S. Eloul and R. G. Compton ChemElectroChem, vol. 1, pp. 917-924, 2014.
- S. Eloul and R. G. Compton The Journal of Physical Chemistry C, vol. 118, pp. 24520-24532, 2014.
- S. Eloul and R. G. Compton The Journal of Physical Chemistry C, vol. 119, no. 49, pp. 27540-27549, 2015.
- S. Eloul, C. Batchelor-McAuley, and R. G. Compton The Journal of Solid State Electrochemistry, vol. 18, no. 12, pp. 3239-3243, 2014.

# Chapter 1

# Introduction

Transport of particles in solution is governed by diverse physical phenomena. In many systems across science, diffusion overwhelms other forms of transport and its role in chemical and biological systems is central. Electrochemistry besides becoming a field that provides central tools for research and many applications, allows the observation of diffusional processes under 'laboratory' conditions[1,2]. This advantage is highly relevant for understanding diffusion processes as they can be seen in well-defined and modellable experiments. Hence some of the theoretical conclusions in this thesis rely on experimental conclusions, and vice versa.

In a conventional experiment, the experimental cell contains a solution with electroactive species in well-controlled conditions so their transport is via pure Brownian motion. Therefore, the current response from the reaction of the species on an electrode can be modelled with high accuracy as a diffusion problem. The exceptional accuracy of such experiments, not only provides necessary tools for analytical chemistry, but it also allows the identification and quantification of reaction rates, as well as other processes such as adsorption, reaction mechanisms, and thermodynamic properties. This thesis discusses the transport of particles and their stochastic detection at electrode surfaces due to diffusion, usually in relation to electrochemical detection processes, and surface properties. It is therefore necessary to first outline some fundamental concepts in mass transport and their relation to electrochemical measurements. Later in this chapter, the fundamentals of electrochemical reactions and kinetics are discussed, and descriptions of important electrochemical methods are provided as a necessary background for this study.

## 1.1 Mass transport in electrochemistry

In electrochemistry, the transport of interest is the flow of electro-active species from the bulk towards the electrode surface. In many electrochemical cells this transport is dominated by diffusion[1].

In 1855, Fick applied the heat equation to the diffusion phenomena[3]. Fick's $1^{st}$ law shows that the diffusion flux is proportional to the local gradient of substance from high to low concentration:

$$j = -D\frac{\partial c}{\partial x} \tag{1.1}$$

where $D$ is the diffusivity of the chemical species ($m^2s^{-1}$), $c$ is the concentration ($mol \cdot m^{-3}$), and $j$ is the diffusive flux density ($mol \cdot s^{-1}m^{-2}$).

The diffusion equation can be derived from the continuity equation, which requires that effectively, density changes in the inflow and outflow are zero:

$$\frac{\partial c}{\partial t} + \nabla \cdot j = 0 \tag{1.2}$$

This leads (combining eq. 1.2 and eq. 1.1) to Fick's second law and the general form of the diffusion equation:

$$\frac{\partial c}{\partial t} = \nabla \cdot (D(c, x)\nabla c) \tag{1.3}$$

Usually in electrochemistry, a relatively dilute solution are used, where the diffusion coefficient does not depend on the concentration, and the partial differential equation becomes linear[4]. In 1905, Einstein considered the diffusion problem from the atomistic point of view, as the result of Brownian motion[5]. Einstein, described the evolution in time of the probability density of particles which reproduces the well-known diffusive behaviour[4]. For example in one dimension ($x$ coordinate) the root mean square displacement of a particle is:

$$\sqrt{|x^2|} = \sqrt{2Dt} \tag{1.4}$$

For the purpose of this thesis, the main realisation is that for Brownian motion, there is no difference between the probability distribution of the location of a single particle, or the concentration of a collection of particles[4]. This similarity allows the modelling of diffusion by solving Fick's second law to give the local change in concentration, or to model the movement of individual particles by using the random walk method[4]. This is important for studying the stochastic diffusion of particles towards electrodes. I further cover, in detail, the application of Fick's second law for very dilute solutions and its relation to Einstein's equation in chapter 4.

### 1.1.1 Migration and convection

The mass transport of ions in the cell can also be a result of migration and/or convection. The time dependant Nernst-Planck equation describes the motion by diffusion, migration, and convection of a charged chemical species ($i$) in a solution[6]:

$$\frac{\partial c_i}{\partial t} = \nabla \cdot D_i \nabla c_i + \nabla \cdot \frac{z_i F D_i}{RT} c_i \nabla \phi + \nu \cdot \nabla c_i \tag{1.5}$$

$D_i$ is the diffusivity of the chemical species ($m^2 s^{-1}$), $c_i$ is the concentration ($mol \cdot m^{-3}$) and $z_i$ is the charge of the species $i$, $\nu$ is the velocity field of the fluid medium, and $\phi$ is the potential ($V$). $F$ is the Faraday constant ($96485 Cmol^{-1}$), $R$ is the universal gas constant ($J(mol \cdot K)^{-1}$) and $T$ is the temperature ($K$).

Migration is the movement of ions resulting from a non-uniform electrical potential giving rise to an electrical field ($\nabla\phi$). This is described by the migrative term (second term) in the Nernst-Planck equation. When a potential is applied to an electrode, charged particles move up or down the electrical field depending on the sign of their charge, and can contribute to the mass transport. In many electrochemical systems, the migration can be eliminated by using an excess of supporting electrolyte to confine changes to only close distances to the electrode[2]. This is usually desirable in order to provide transport that is dominated by diffusion, as is discussed later.

Convection is described by the third term in the Nernst-Planck equation. It becomes important if an additional force such as density driven velocity, thermal convection, or magnetic forces dominate the flux in the cell[6,7]. In order to accurately capture the diffusion process in the context of particle's diffusing in an electrochemical cell, a constant temperature, the elimination of physical vibration, and the use of a Faraday cage are elementary experiential requirements[1].

The thesis focuses on modelling electrochemical systems which are dominanted by diffusional transport, whereas migration or convection are negligible.

The transport of particles and chemical species leads to their arrival near an electrode where an electrochemical reaction can be measured through the current response. Hence, the next sections of this chapter discuss the fundamentals of electrochemical reactions and electrochemical methods.

## 1.2 Fundamentals of an electrochemical reaction

An electrochemical reaction involves the process of charge transfer between a chemical species and an electrode. Consider the equilibrium between species $A$ and the reduced form of the species $B$:

$$A + e^- \leftrightarrows B \tag{1.6}$$

The chemical potential of each species is determined by the change of the net Gibbs energy ($G$) with the amount of moles ($N_j$) of the species $j$:

$$\mu_j = \frac{\partial G}{\partial N_j} \tag{1.7}$$

where, assuming ideality, the chemical potential in solution is given as:

$$\mu_j = \mu_j^0 + RT \ln(c_j/c_j^0) \tag{1.8}$$

and $\mu^0$ is the standard chemical potential of each species for a standard $c_j^0$ where this is usually 1M concentration. As an electrode is involved in the reaction, the electrical potential of the electrode and the solution need to be considered and should be taken into account in the change of Gibbs energy. Therefore the electrochemical potential $\bar{\mu}_j$ is introduced, which is the combination of the chemical potential of the species $\mu_A$ or $\mu_B$

and their energy per mole due to the electrical potential ($\phi$):

$$\bar{\mu_j} = \mu_j + z_j F\phi \qquad j = A\, or\, B \tag{1.9}$$

$F$ is the Faraday constant ($Q/mol$). $z_j$ is the charge of each species $j$. An electrochemical reaction is dominated by the exchange of electrons between the electrode and solution, and therefore two electrical potentials are taken into account; $\phi_m$ of an electrode (such as a metal wire), and $\phi_s$, for the species in the solution. At equilibrium, the net change in Gibbs energy is zero and therefore the balance can be rewritten as:

$$\bar{\mu_A} + \bar{\mu_{e^-}} = \bar{\mu_B} \tag{1.10}$$

Substituting equations 1.8 and 1.9 in the electrochemical potential balance (eq. 1.10) gives the Nernst equation[1,2]:

$$\phi_m - \phi_s = \frac{\Delta\mu^0}{F} + (RT/F)ln\frac{c_A}{c_B} \tag{1.11}$$

All the standards values are reflected in $\Delta\mu^0$.

Equation 1.11 relates to single electrode-solution interface. However it is impossible to measure the potential using only one electrode; a second reference electrode is needed to complete an electrical circuit. The measured potential difference ($E$) is therefore:

$$E = \phi_m - \phi_s - (\phi_m^{ref} - \phi_s^{ref}) \tag{1.12}$$

The reference electrode is based on a known electrochemical reaction with the reactants and products at well-defined/constant concentrations, so that the term $(\phi_m^{ref} - \phi_s^{ref})$ is constant and hence a standard potential for a specific reaction can be defined as:

$$E^{\Theta} = \frac{\Delta\mu^0}{F} + (\phi_m^{ref} - \phi_s^{ref}) \tag{1.13}$$

Usually, and by IUPAC advice[8], the standard hydrogen electrode is used as the primary reference electrode which is based on the following reaction:

$$2H^+(aq) + 2e^- \rightarrow H_2(g) \tag{1.14}$$

In this electrode the redox reaction occurs, to ensure equilibrium, a 'platinum-black' electrode is dipped in an acidic solution and pure hydrogen gas is bubbled through it. The concentration of both the reduced form and oxidised form is maintained constant (pressure of $H_2$ and concentration of $H^+$). Assuming ideality, the Nernst equation for a hydrogen electrode as a reference electrode is therefore:

$$\phi_m^{ref} - \phi_s^{ref} = \frac{\Delta\mu^0}{F} + \frac{RT}{F} ln \frac{c(H^+)}{\sqrt{P(H_2)}} \tag{1.15}$$

The potential of the hydrogen reaction $(\phi_m^{ref} - \phi_s^{ref})$ is chosen by IUPAC[8] to be 0.0V potential and is called the standard hydrogen electrode, if the concentration of the $H^+$ and the pressure of $H_2$ are close to unity (standard pressure of $H_2 \sim 1atm$ and concentration of $H^+ \sim 1M$), so the second term vanishes. The hydrogen reaction also defines the scale of the standard potential for all reactions.

In practice, the solution of the hydrogen reaction is not ideal, and the activity of the proton should be taken into account ($\gamma_{H^+} \sim 0.85$ for 0.1M HCl). The concentration of

$H^+$ is required to be 1.18M[1,8].

Finally the measured potential difference in two electrode system relative to the standard hydrogen electrode is:

$$E = E^{\Theta} + \frac{RT}{F} ln \frac{\gamma_A c_A}{\gamma_B c_B} \tag{1.16}$$

where $\gamma_A$ and $\gamma_B$ are the activity coefficients for species $A$ and $B$, respectively. It is also noted that when the solution is non-ideal the formal potential is invariably used ($E_f^{\Theta}$) to include the activities of concentrations[1]. Specifically:

$$E^{\Theta} + \frac{RT}{F} ln \frac{\gamma_A c_A}{\gamma_B c_B} = [E^{\Theta} + \frac{RT}{F} ln \frac{\gamma_A}{\gamma_B}] + \frac{RT}{F} ln \frac{c_A}{c_B} = E_f^{\Theta} + \frac{RT}{F} ln \frac{c_A}{c_B} \tag{1.17}$$

and the Nernst equation for two electrode system becomes:

$$E = E_f^{\Theta} + \frac{RT}{F} ln \frac{c_A}{c_B} \tag{1.18}$$

## 1.3 Electrochemical reactions

For an electrochemical system of two electrodes, in order to reduce $A$ to $B$, a sufficiently negative potential, $E$ is applied to the electrode relative to a reference electrode to achieve a thermodynamic favoured reduced state. In that case electrons transfer from the electrode to species $A$ which are converted to $B$ and (by convention) a positive current is produced. Conversely, at large positive potentials, $B$ species are oxidised and electrons transfer to the electrode, and a negative current is produced. At a certain potential, an equilibrium can be achieved, the reaction is balanced for both directions, and therefore no net flow can be measured. This equilibrium potential is derived from the above Nernst equation. As a result, any new material which arrives close to the electrode will generate a reaction to equilibrate the concentration ratio as calculated from the Nernst equation. The resulting current can be calculated directly from the mass transport towards the electrode. For instance, in the case of diffusion only transport, the current response from a one electron reaction is evaluated solely by first Fick's law:

$$I = F\mathrm{A}\left(D_A \frac{\partial c_A}{\partial x}\bigg|_{x=0} - D_B \frac{\partial c_B}{\partial x}\bigg|_{x=0}\right) \tag{1.19}$$

where the electrode is positioned arbitrary at $x = 0$ and A is the surface area of the electrode assumed uniform. $D_A$ and $D_B$ are the diffusion coefficients of species $A$ and $B$, respectively. This condition is easily achieved in some experiments and a pure diffusion transport can be observed for many processes. Yet as we see next, the reaction can be also controlled by kinetics.

### 1.3.1 Electrode kinetics

The Nernst equation presented above assumes a thermodynamic state, which means that reactions occur immediately when a potential is applied. This condition requires fast electron transfer kinetics. In other cases, the rate of electron transfer reaction must be considered. The basic model for electrode kinetics assumes a first order reaction happens at the interface of the electrode solution:

$$j = k_{red} c_A^0 - k_{ox} c_B^0 \tag{1.20}$$

where $c_A^0$ and $c_B^0$ are the surface concentrations. In this way, the flux depends on the reduction and oxidation rate constants ($k_{red}$ and $k_{ox}$). These coefficients are dependant on the potential applied to the electrode. The most fundamental relationship of how the electrical current on an electrode depends on the electrode potential is governed by the Butler-Volmer theory[9,10]. A typical reaction profile for a fixed $\phi_m$ and $\phi_s$ is shown in figure 1.1. Making the potential of the electrode $\phi_m$ more negative relative to $\phi_s$ would raise the energy of the reactant which includes the $e^-(m)$ relative to $B$. Conversely, making the solution more negatively charged the products energy would relatively decrease. Hence the reduction or the oxidation reaction depends on the thermodynamically favourable state, and the rates are dependant on the Gibbs activation energies via the Arrhenius equation[11]:

$$\begin{aligned} k_{red} &= A_c \exp\left[\frac{-\Delta G_c}{RT}\right] \\ k_{ox} &= A_a \exp\left[\frac{-\Delta G_a}{RT}\right] \end{aligned} \tag{1.21}$$

$\Delta G_c$, and $\Delta G_a$ are the activation energies for the reduction or oxidation reaction, which are the difference between $G^0(R)$ or $G^0(P)$ and the transition state, respectively (figure 1.1). The pre-exponential factors ($A_c$ and $A_a$) describe the frequency of collisions with the

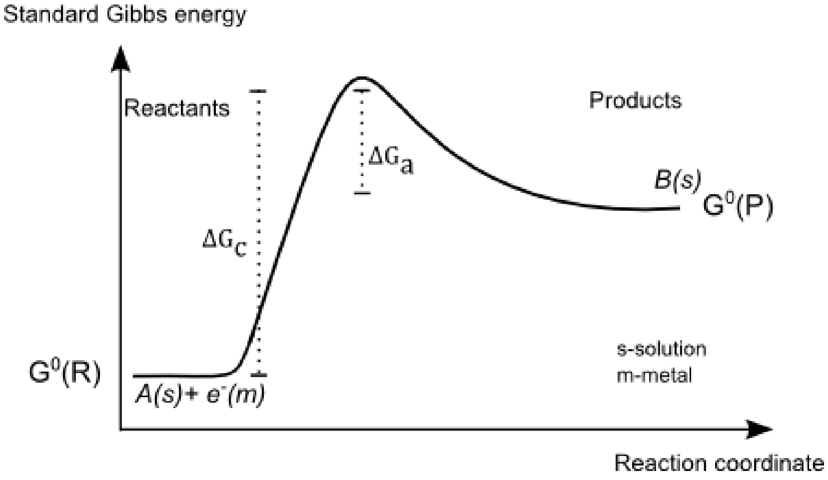

Figure 1.1: A reaction profile for the electrode process $A + e^- \rightarrow B$. The activation energies $\Delta G_c$ and $\Delta G_a$ are shown with the dotted lines.

electrode surface. The transition state energy is not known, but the difference of energy between $G^0(R)$ and $G^0(P)$ is the standard molar Gibbs energy equals $F(\phi_m - \phi_s) + const$, evaluated from their electrochemical potential. Therefore, recognising the transition state energy to be in between $G^0(R)$ and $G^0(P)$, the activation energies follow:

$$\Delta G_c = \alpha F(\phi_m - \phi_s)) + const, \quad \Delta G_a = (1-\alpha)F(\phi_m - \phi_s)) + const \tag{1.22}$$

The value $\alpha$ is called the transfer coefficient. This is a semi-empirical quantity which often found to be $\sim 0.5$. $\alpha$ shows whether the transition state is reactant or product-like[12].

From equation 1.22:

$$\begin{aligned} k_{red} &= k_c \exp\left[-\alpha \frac{F(E - E_f^{\Theta})}{RT}\right] \\ k_{ox} &= k_a \exp\left[(1-\alpha) \frac{F(E - E_f^{\Theta})}{RT}\right] \end{aligned} \tag{1.23}$$

The $k_c$ and $k_a$ reflect the constants in eq 1.22 and also the pre-exponential factors $A_c$ and $A_a$.

Substituting $k_{red}$ and $k_{ox}$ to the flux in equation 1.19:

$$j = k_c \exp\left[-\alpha \frac{F(E - E_f^{\Theta})}{RT}\right] c_A^0 - k_a \exp\left[(1-\alpha) \frac{F(E - E_f^{\Theta})}{RT}\right] c_B^0 \tag{1.24}$$

At equilibrium, the potential when no net flux flows ($j = 0$), the equation can be rewritten as:

$$E = E_f^{\Theta} + \frac{RT}{F} ln \frac{c_A^0}{c_B^0} + \frac{RT}{F} ln \frac{k_a}{k_b} \tag{1.25}$$

It is clear, that it requires $k_a = k_b$ to agree with Nernst equation. Therefore, the final form of the Butler-Volmer equation can be rewritten as:

$$\begin{aligned} k_{red} &= k_0 \exp\left[-\alpha \frac{F(E - E_f^{\Theta})}{RT}\right] \\ k_{ox} &= k_0 \exp\left[(1-\alpha) \frac{F(E - E_f^{\Theta})}{RT}\right] \end{aligned} \tag{1.26}$$

where $k_a = k_c = k_0$, the standard electrochemical rate constant, $k_0$, provides the electrochemical reaction rate ($ms^{-1}$). The term $E - E_f^{\Theta}$ corresponds to the over-potential which is the driving force for the cathodic (reduction) and anodic (oxidation) reaction.

The current towards an electrode with homogeneous current-density over a surface area A is:

$$I = -F\mathrm{A}j \tag{1.27}$$

As in the case of the Nernst equation, it is a concentration dependant reaction, and the current measured, is the result of transport of species to the surface, and their reaction close to the electrode surface. Electrochemical techniques in experiments use the Butler-Volmer model to study kinetics of reactions, and are discussed later in this chapter.

## 1.4 Electrochemical experiments

### 1.4.1 Cell configuration

An electrochemical cell usually consists of three electrodes; a working electrode, a reference electrode, and a counter electrode. The cell is illustrated in figure 1.2. The working electrode is used to measure the reaction of interest by applying a potential relative to the reference electrode.

The reference electrode is usually positioned close to the working electrode to minimise any ohmic drop. The reference electrode consists of a known electrochemical reaction maintained at equilibrium and therefore has a stable and well-known potential. The stable potential is usually achieved by employing a redox system with buffered or saturated concentrations of the redox reaction, as was discussed for the standard hydrogen electrode.

In order to complete the electrical circuit a third electrode is introduced - the counter electrode. The current induced in the working electrode flows through the counter electrode at the surface of which a reaction takes place by virtue of the counter electrode being 'driven' to a suitable potential.

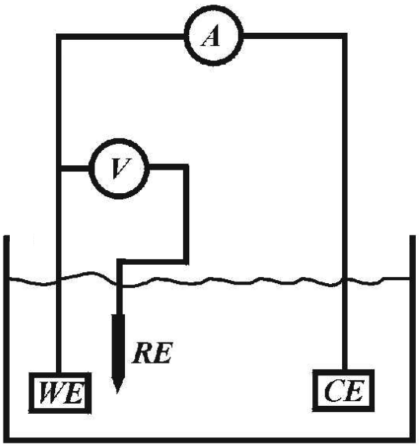

Figure 1.2: Schematic of the electrical circuit and the electrodes in a cell. WE - working electrode, RE - reference electrode, CE - counter electrode, V -where the voltage is applied and measured, and A- where the current is measured.

The voltage is measured between the reference electrode and the working electrode. Since the reference is in chemical equilibrium with the solution a voltmeter with a high resistance can measure the potential with a negligible current passage. The measuring of the current, is therefore made between the working electrode and the counter electrode.

### 1.4.2 The supporting electrolyte

A typical electrochemical experiment consists of the molecules of interest in solution with an added excess of electrolyte. At the working electrode, the reaction of interest generates a positive or a negative flow of electrons which in turn generates an opposite reaction on the counter electrode. In the solution, ions are the charge carriers and move away or towards the electrodes. During the experiment, charge starts to accumulate next to the electrode. Without an electrolyte, the accumulation of charge would generate a gradient of potential beyond the zone of the electron transfer reaction, as shown schematically in figure 1.3. Since reactants have to be within an electron tunnelling distance of the electrode, the interfacial potential drop ($\phi_e - \phi_s$) in the zone of interfacial electron transfer reaction is reduced in comparison to the real applied overpotential. In fully 'supported' solution (such as formed by adding salt to the solution), the excess of charge carriers causes the full potential drop to occurs at a much shorter distance, and within the zone of electron transfer (ZET), see figure 1.3.

Two other important reasons for using a fully supported solution are first to provide a high conductivity solution. In this way migration can be eliminated and the reaction can be studied using various electrochemical techniques based on diffusion only. Second, in a low conductivity medium, the current density would be strongly dependant on geometrical effects, and could result in large variations of the potential on the surface of the electrode. This would cause a non-homogeneity of the reaction[6,13]. Adding a supporting electrolyte, removes this problem, and therefore is essential for most electrochemical systems.

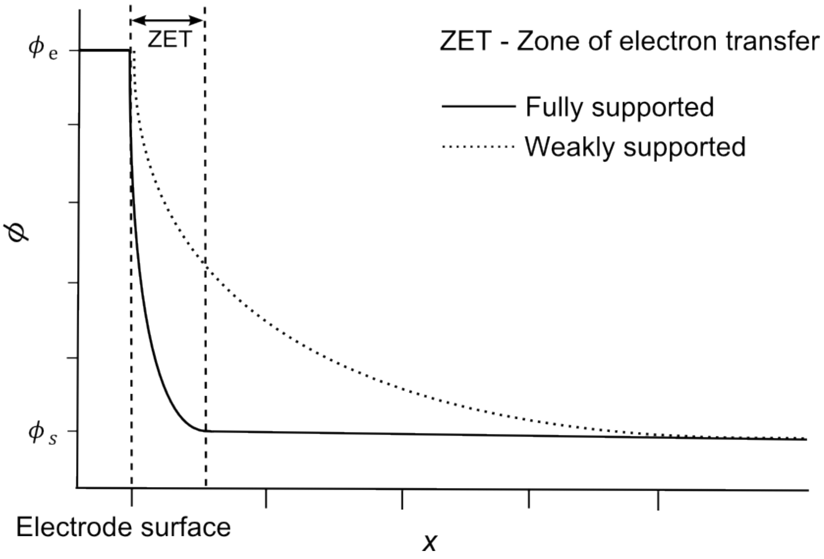

Figure 1.3: The importance of supporting electrolyte for keeping the interfacial potential drop within the zone of electron transfer (ZET). The solid line shows the potential drop in solution case of a solution with supporting electrolyte. The dotted line shows the potential drop in solution for the case of no electrolyte in solution. $\phi_e$ is the electrode potential, and $\phi_s$ is the solution potential.

## 1.5 Main techniques

Amperometry and voltammetry are the main tools in electrochemistry. In amperometry, the investigation of mass transport and especially diffusion can be achieved by holding the electrode at a fixed potential to measure the current over a period of time resulting from the oxidation or reduction of the Faradaically reacting entities. In voltammetry, the potential is scanned to measure the current over a potential range[1]. These methods are modelled and discussed in the thesis and the principles of the methods are described in this section.

### 1.5.1 Chrono-amperometry

Consider a reduction reaction: $A + ne^- \rightarrow B$. At the start of the experiment only species $A$ is present in the solution and the potential is held at a value which no reduction occurs. The potential is then stepped to a sufficiently negative overpotential to fully drive a diffusion-control reduction reaction without a kinetic limitation (in a case of oxidation reaction, the potential is stepped to a sufficient positive overpotential). With a large overpotential applied, any species that arrives in the zone of electron transfer is reduced immediately. The measurement outputs the current response over time, providing an insight to the diffusion process of species towards the electrode. A typical current response is shown in figure 1.4. The current starts with a high value due to reducing of available species on the electrode surface, and decreases sharply with time due to dilution of species. For large electrodes (macro-scale), the current ($I$) versus the time ($t$) follows the Cottrell equation[14]:

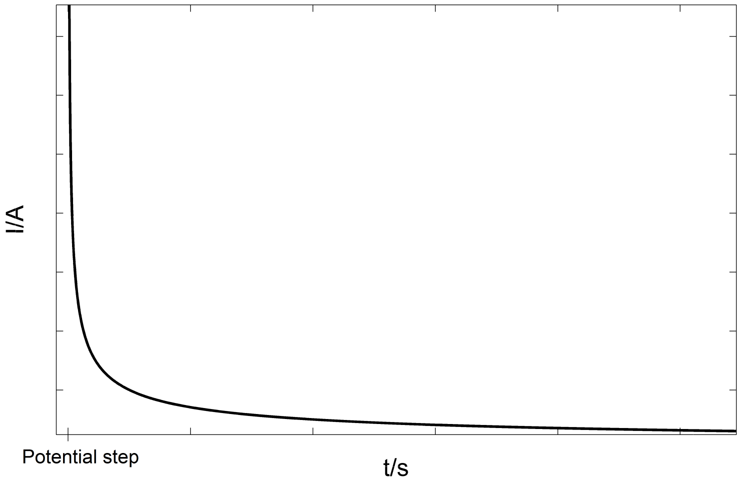

Figure 1.4: The typical current response versus time of electrochemical reaction due to a large potential step applied to the electrode.

$$I = nFc^{*}\mathrm{A}\sqrt{\frac{D}{\pi t}} \tag{1.28}$$

where $n$ is the number of electrons in a reaction, $D$ is the diffusion coefficient and $c^{*}$ is the bulk solution concentration of the reactant. Therefore, if the concentration is known the diffusion coefficient can be measured.

The Cottrell equation is the analytical solution of the diffusion problem in one dimension towards a fully adsorbing electrode, where the surface concentration is effectively zero. Since the current response is affected by the transport towards the electrode, the electrode geometry, diffusion coefficients, and other properties can affect the diffusion and therefore can be observed and studied in chronoamperometry.

### Diffusion layer

In chronoamperometry measurements, the current response is proportional to the gradient of the concentration adjacent to the electrode surface. The concentration profiles are given as:

$$c(x,t) = c^{*}\mathrm{erf}(\frac{\mathrm{x}}{2\sqrt{\mathrm{Dt}}}) \tag{1.29}$$

Figure 1.5 shows how the concentration profile evolves with the time of measurement. At the beginning of the experiment the gradient of the concentration on the surface of the electrode is large, and therefore a large current is observed. During the measurement the dilution expands to larger distances. The dilution zone is defined as the ‘diffusion layer’, where the concentration is below that of the bulk concentration. $\delta(t)$ is a measure of the diffusion layer thickness and is obtained by linearising the profile, as shown in figure 1.5. It is noted that according to Cottrell (eq. 1.28), at infinity, the current should decay to

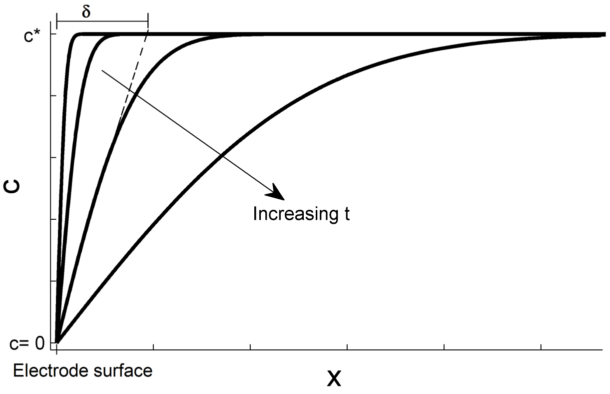

Figure 1.5: Concentration profiles for various times when a large potential step is applied to an electrode. An example of how to estimate the diffusion layer thickness ($\delta$) is shown for an arbitrary profile.

zero, and the diffusion layer thickness should be infinite. In practice, the current achieves a small, but still measurable limit value. Nernst proposed that $\delta$ becomes constrained to a finite, steady value, since the bulk is usually in a well mixed condition[1].

It is shown later how other conditions can change the current response and provide physical information about the system. This work specifically pays attention to understand influences on the current response in chronoamperometry measurements[15,16] under various conditions and for particle detection applications[17].

### 1.5.2 Cyclic voltammetry

Consider the oxidation reaction of a reduced species, $A \rightleftarrows B + ne^-$. In the beginning of the experiment only species $A$ is present in the solution. In cyclic voltammetry, in contrast to chronoamperometry, instead of setting the potential to a fixed value, the potential is scanned from a high-negative overpotential to a high-positive overpotential and then is swept back.

In the case of 'fast' electrode kinetics, the voltammogram has a typical response which is defined as a 'reversible' process. A typical voltammogram for the case of a reversible process is shown in figure 1.6 for an oxidation of $A$. At the starting point (stage 1), the potential is set to a large negative value with respect to the formal potential of the reaction, and no oxidation occurs. Then the potential increases at a specific rate and an oxidation reaction starts to take a place (stage 2) resulting in a positive current. When $E = E_f^0$, the surface concentrations of species $A$ and $B$ are equal ($c_A^0 = c_B^0$ for the case of $D_A = D_B$).

At stage 3, the reaction is almost fully driven and oxidation of the species next to the electrode maximises the current. As the overpotential increases the concentration of the reactant $A$ next to the electrode is further diluted and the reaction becomes limited by the mass transport of new species to the electrode. Thus an oxidation peak is observed, followed by a decay of the current. At a sufficient large potential the scan is reversed and the potential sweeps towards negative values. In this backward scan the oxidised species go through a reduction reaction and a reduction peak is observed near the formal potential (stage 4). At more negative overpotentials the diffusion dominates the mass transport, and the current decays back to zero (stage 5).

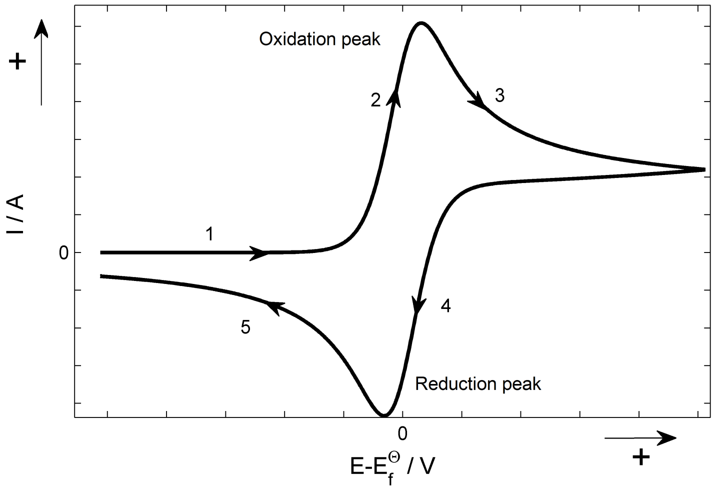

Figure 1.6: Typical cyclic voltammogram of a species oxidized in the forward scan and reduced in the backward scan.

The rate of the scanned potential is an important parameter that has an effect on the voltammetry. The current value of the forward peak ($I_p$) is proportional to the square root of the scan rate, and for a reversible process is given by the equation[1]:

$$I_p = 0.446nFAc^* \sqrt{\frac{nFD\nu}{RT}} \tag{1.30}$$

where $\nu(Vs^{-1})$ is the scan rate. This relation is derived from the diffusional transport. Einstein's theory for diffusion shows that the root mean square displacement of particles in one dimension is[5]:

$$\sqrt{|x^2|} = \sqrt{2Dt} \tag{1.31}$$

$\sqrt{|x^2|}$ is also the measure of the diffusion layer expansion in time. This leads to the result that the diffusion layer is proportional to the inverse square root of the scan rate:

$$|x| \propto \sqrt{\frac{1}{\nu}} \tag{1.32}$$

Since the flux is proportional to the inverse of the diffusion layer, the current increases with the square root of the scan rate.

### Electrochemical kinetics

The limit of a reversible process is achieved when the electrode kinetics are much faster than the mass transport. In an irreversible process, the electrode kinetics are much slower than the mass transport. It was also shown in the previous section that the current is proportional to square root of the scan rate and therefore also to the rate of the mass transport. Matsuda and Ayabe introduced the parameter $\Lambda$, to define the transition between a reversible and an irreversible process[18]:

$$\Lambda = \frac{k_0}{\sqrt{\frac{FD\nu}{Rt}}} \tag{1.33}$$

and estimated that a system is reversible for $\Lambda > 15$ at a macro-electrode.

In kinetic controlled reactions, the peak height as well as the as the separation between the forward and backward peaks, is influenced by $k_0$ for a specific scan rate. Figure 1.7 shows three voltammograms at different $k_0$. The first solid curve shows the case of a fully reversible reaction with an artificially high value of $k_0 = 100ms^{-1}$.

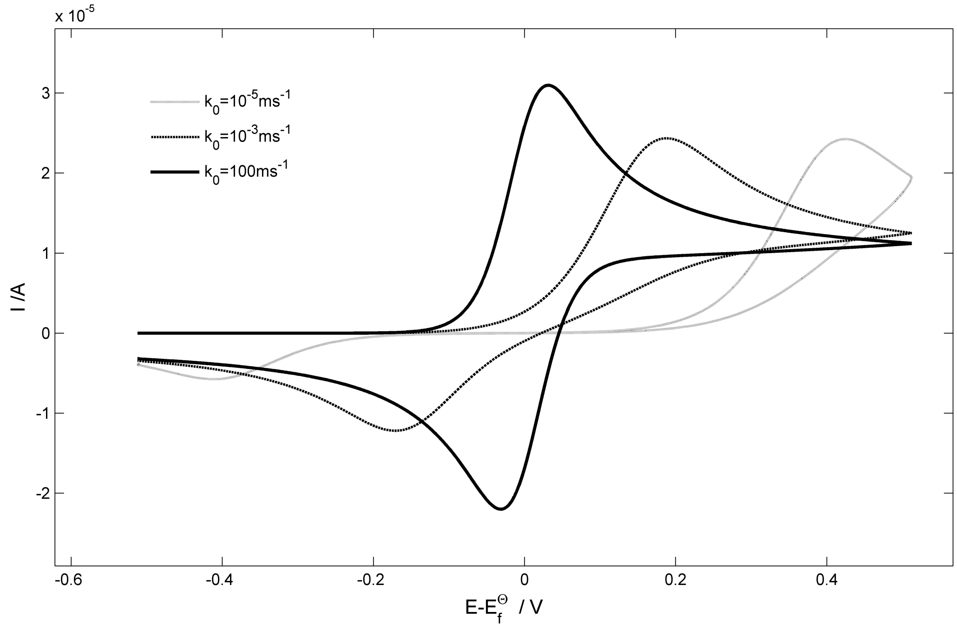

Figure 1.7: The effect of electron transfer kinetics on the voltammogram, using the following parameters for a one electron reaction: $c^0 = 10mM$, radius of a disk electrode of 1mm, $D_A = D_B = 10^{-9}m^2s^{-1}$, $\alpha = 0.5$, and for standard electrochemical rate constants: $k_0 = 10^{-5}ms^{-1}$, $10^{-3}ms^{-1}$, and $100ms^{-1}$.

The black-dashed line shows intermediate electrochemical kinetics, and the grey-dashed curve is for an irreversible case. It can be seen that the separation between the peaks gets larger for smaller $k_0$, due to the larger overpotential needed to drive the reaction. The forward and backward peak currents decrease with $k_0$ but reaching a limited value for the forward peak. The forward peak height equation in the irreversible case is given by:

$$I_p = 0.469nFA\sqrt{\alpha + n'}c^* \sqrt{\frac{FD\nu}{RT}} \tag{1.34}$$

$n'$ is the number of electrons transferred before the rate determining electron transfer in a case of a multiple step overall $n$ electron transfer reaction[1]. Simulations of the diffusion transport for electrochemical processes can be carried out to fit experimental results and extract kinetic parameters as well as the diffusion coefficient[19]. Moreover, cyclic voltammetry in conjugation with simulation provides a strong tool for the investigation of multi-step reaction mechanisms[20].

## 1.6 Microelectrodes

Microelectrodes have transformed the dynamic range of electrochemistry since their introduction and popularisation dating from the 1970s[21,22]. The diversity and range of their application continues to expand beyond that of fundamental voltammetry research. In particular, recent applications have included the addressing of biological problems[23], the examination of surfaces with SCEM[24], covalently modified and functionalised microelectrodes for various applications[25], and the study of nano particles[26].

Microelectrodes are defined to be an electrode which has at least one dimension of the order of a micron size. This can be a disc or a sphere with a micron scale radius, or a long wire of macro size length but a thickness of a few micrometres.

The popularity of microelectrodes is mainly due to the diffusion behaviour observed as the electrode gets smaller. In large electrodes, the diffusion layer expands in a linear direction as illustrated in figure 1.8 for a 'macroelectrode'. The result is a fast dilution of species which causes the decay of the flux in proportion to $1/\sqrt{t}$. When the electrode is small enough, diffusion becomes convergent due to a constant supply of species from all directions. This results in a steady state flux and a finite diffusion layer (figure 1.8).

We can consider the analytical solution of the diffusion problem towards a sphere electrode, held at a large potential[2]. The flux density of species towards the surface of a

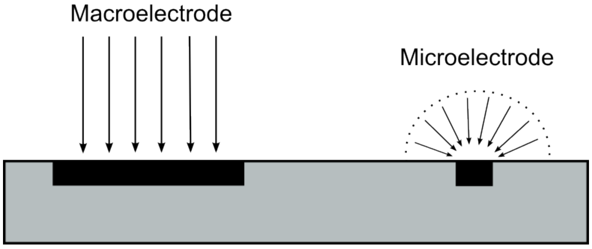

Figure 1.8: Illustration of the diffusion field of species towards a macro (left) and a micro (right) scale disc electrode. The dotted line around the micro shows the convergent of the diffusion field.

sphere is given as:

$$j = c^*(r_s, t_0) D \left[ \frac{1}{\sqrt{\pi D_0 t}} + \frac{1}{r_s} \right] \tag{1.35}$$

where $r_s$ is the sphere radius. We discuss this expression and its derivation in chapters 4 and 6. The expression consists of a steady state term $1/r_s$ and a transient term $1/\sqrt{\pi D_0 t}$. The steady state term becomes larger and more dominant as the sphere radius decreases. Hence as the electrode gets smaller, higher flux densities are observed. Additionally, for small radii the transient response becomes negligible at shorter times, which leads to a faster establishment of the steady-state. This is an important feature of microelectrodes and which makes them 'fast-response' electrodes[1].

### 1.6.1 Microelectrode voltammetry

A typical voltammetry response from an electrochemically reversible reaction (with a typical correspond solution diffusion coefficient) on a micro-disc electrode of a $5\mu m$ radius is shown in figure 1.9. It shows that at a scan rate of $100 mV s^{-1}$, a steady state behaviour is observed with no peak. This is due to the short time it takes to reach the steady state and establish a convergent diffusion layer. At very large scan rates ($10 V s^{-1}$), the peak shape of a cyclic voltammetry is seen; The high scan rate increases the mass transport, allowing the current to increase before the diffusion layer is fully established.

A fast-response electrode is desirable for monitoring fast kinetics in voltammetry measurements. Microelectrodes allow high scan rates to be employed in order to observe the typical voltammogram and hence to extract faster electron transfer kinetics. In fact, the smaller is the electrode, the faster is the response and hence, and the faster the electron transfer kinetics that can be detected. For micron-sized electrodes, a standard electrochemical rate constants of $k_0 \sim 1ms^{-1}$ can be measured[27]. Sub-micro electrodes and ultra-fast voltammetry ($\nu \sim MVs^{-1}$) are also employed to detect even faster $k_0$[28], but their relatively complex fabrication and the very small net current responses ($I \sim pA$) make them a less popular approach.

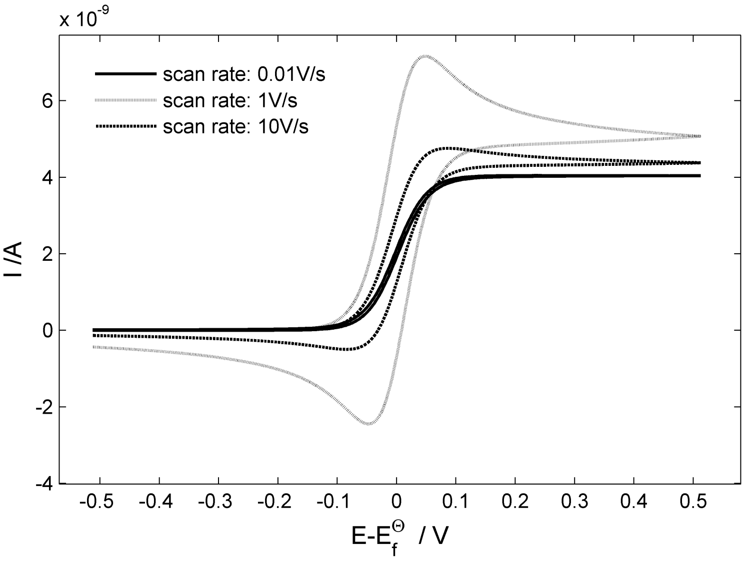

Figure 1.9: Typical voltammograms for a reversible reaction on a microdisc electrode with a radius $r_d = 5\mu m$ at various scan rates $(0.01Vs^{-1}, 1Vs^{-1}, 10Vs^{-1})$. $c^0 = 10mM$, $D_A = D_B = 10^{-9}m^2s^{-1}$.

### 1.6.2 Microelectrode chronoamperometry

As shown in equation 6.6 for the flux towards a spherical electrode, the flux density increases with a decrease in the radius of the sphere. In chronoamperometry measurements this rapidly leads to a steady state current response. The steady-state current from the whole electrode surface is therefore:

$$I = 4\pi F D c^* r_s \tag{1.36}$$

For a very common electrode - the microdisc, the steady state can also be calculated analytically to be[29]:

$$I = 4FDc^* r_d \tag{1.37}$$

where $r_d$ is the disc radius. In the case of a disc, an approximate expression for the time-dependant current response of a potential step from zero current to diffusion limited current is given by Shoup-Szabo[30]:

$$J = 4Dc^* r_d f(\tau) \tag{1.38}$$

where

$$f(\tau) = 0.7854 + 0.8862\tau^{-1/2} + 0.2146\exp(-0.7823\tau^{-1/2}) \tag{1.39}$$

and $\tau$ is a dimensionless time parameter, which is defined as:

$$\tau = 4Dt/r_d^2 \tag{1.40}$$

The Shoup-Szabo response from a disc is shown in figure 1.10 plotted from equation 5.5. The figure also contrasts the behaviour with the response from the Cottrell equation 1.28 representing the case of an infinite planar electrode. It can be seen that the decay of the current follows Cottrell behaviour at short time. However, at long time the current

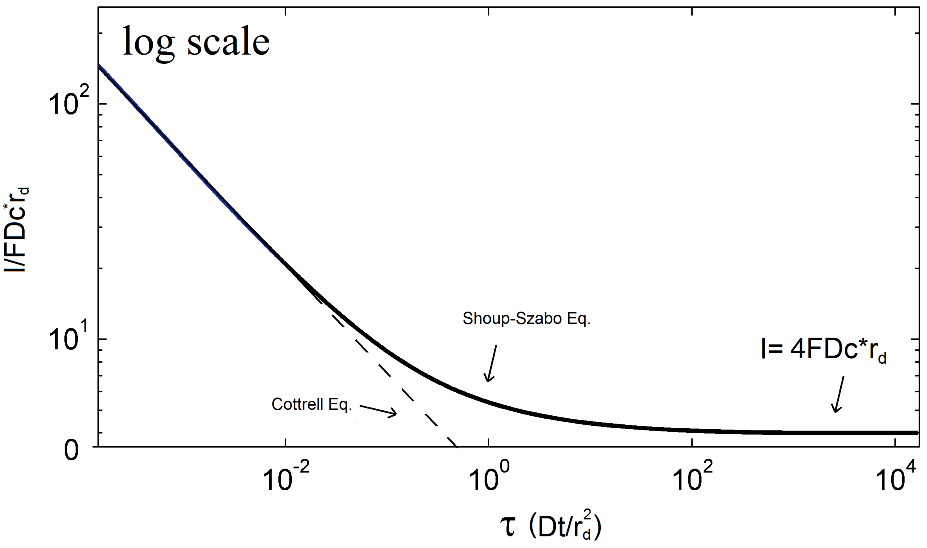

Figure 1.10: The chronoamperometry response for microdisc electrode. The solid line follows shoup szabo equation, and the dashed line follows the Cottrell equation for an infinite planar electrode.

deviates from Cottrell towards the steady state value ($4FDc^{*}r_d$). For a typical microdisc, and a diffusion coefficient $10^{-9}m^2s^{-1}$, the steady-state would be reached in less than a second.

### 1.6.3 Micro-wire electrodes

The micro-wire electrode is also used in electrochemistry applications. A microwire (microcylinder) electrode features a macro dimension in terms of its length $l$ and a micro dimension in terms of its radius $r_c$. The diffusion layer in this spacial case is characterised with a mixed behaviour. Szabo[31] found an expression for the transient net flux towards a semi-infinite hemicylinder, which is accurate to within 1.3% for short and long times:

$$J(t) = \pi Dc^{*}lf(\tau) \tag{1.41}$$

where $l$ is the length of the cylinder and $f(\tau)$ is:

$$f(\tau) = \frac{e^{-\sqrt{\pi\tau}/10}}{\sqrt{\pi\tau}} + \frac{1}{ln[(4e^{-\gamma}\tau)^{1/2} + e^{5/3}]} \tag{1.42}$$

$\tau$ is defined as $Dt/r_c^2$, where $r_c$ is the radius of the cylinder, and $\gamma = 0.5772$ is the Euler-Mascheroni constant. In the case of a wire the flux decays slowly at large time but never reaches a steady-state. Later in the thesis, I discuss further the diffusional behaviour of microelectrodes and consider especially the cases of a disc and wire electrodes in relation to the electrochemical detection methods of particles.

## Conclusions

This chapter has provided an overview on the concepts of mass transport in electrochemistry, electrochemical equilibrium, and electrochemical kinetics. These concepts are the basis for the main electrochemical methods presented in the thesis. The next chapter shows the methodology of electrochemical simulation which is used through out the thesis.

# References

[1] R. G. Compton and C. E. Banks, *Understanding Voltammetry (2nd Edition)*. London, UK: Imperial College Press, 2011.

[2] A. J. Bard and L. Faulkner, *Electrochemical Methods: Fundamentals and Applications*. John Wiley and Sons, 2001.

[3] A. Fick *The London, Edinburgh, and Dublin Philosophical Magazine and Journal of Science*, vol. 10, no. 63, pp. 30–39, 1855.

[4] D. T. Gillespie and E. Seitaridou, *Simple Brownian Diffusion*. Oxford University Press, 2012.

[5] A. Einstein *Annalen der Physik*, vol. 322, no. 8, pp. 549–560, 1905.

[6] J. Newman and K. E. Thomas-Alyea, *Electrochemical systems*. John Wiley & Sons, 2012.

[7] R. B. Bird *Applied Mechanics Reviews*, vol. 55, no. 1, pp. R1–R4, 2002.

[8] *IUPAC. Compendium of Chemical Terminology, 2nd ed. (the "Gold Book"). Compiled by A. D. McNaught and A. Wilkinson. Blackwell Scientific Publications, Oxford (1997).*

[9] J. A. V. Butler *Trans. Faraday Soc.*, vol. 19, pp. 729–733, 1924.

[10] T. Erdey-Grúz and M. Z. Volmer *Physik. Chem.*, vol. 150, pp. 230–213, 1930.

[11] S. Arrhenius *Zeitschrift für Physikalische Chemie*, vol. 4, pp. 226–248, 1889.

[12] E. Laborda, M. C. Henstridge, C. Batchelor-McAuley, and R. G. Compton *Chem. Soc. Rev.*, vol. 42, pp. 4894–4905, 2013.

[13] U. Landau, *Electrochemistry in Industry: New Directions.* Springer Science & Business Media, 2012.

[14] F. Cottrell *Z. Phys. Chem.*, vol. 42, p. 385, 1903.

[15] S. Eloul and R. G. Compton *ChemElectroChem*, vol. 1, no. 5, pp. 917–924, 2014.

[16] S. Eloul and R. G. Compton *The Journal of Physical Chemistry C*, vol. 119, no. 49, pp. 27540–27549, 2015.

[17] W. Cheng, C. Batchelor-McAuley, and R. G. Compton *ChemElectroChem*, vol. 1, no. 4, pp. 714–717, 2014.

[18] Y. A. H. Matsuda *Z. Elecktrochem*, vol. 59, p. 494, 1955.

[19] D. Britz, *Digital Simulation in Electrochemistry*, vol. 666. Springer, 2005.

[20] R. G. Compton, E. Laborda, and K. R. Ward, *Understanding Voltammetry - Simulation of Electrode Processes.* Imperial College Press, 2013.

[21] A. M. Bond *Analyst*, vol. 119, no. 11, pp. 1R–21R, 1994.

[22] C. Amatore, M. R. Deakin, and R. M. M. Wightman *Journal of Electroanalytical Chemistry*, vol. 225, no. 1-2, pp. 49–63, 1987.

[23] C. Amatore, S. Arbault, Y. Bouret, M. Guille, and F. Lematre *ChemPhysChem*, vol. 11, no. 13, pp. 2931–2941, 2010.

[24] M. V. Mirkin, F.-R. F. Fan, and A. J. Bard *Journal of Electroanalytical Chemistry*, vol. 328, no. 1-2, pp. 47–62, 1992.

[25] R. W. Murray *Chemical Reviews*, vol. 108, no. 7, pp. 2688–2720, 2008.

[26] N. V. Rees, Y.-G. Zhou, and R. G. Compton *RSC Adv.*, vol. 2, pp. 379–384, 2012.

[27] R. J. Forster *Chemical Society Reviews*, vol. 23, no. 4, pp. 289–297, 1994.

[28] C. Amatore, E. Maisonhaute, and G. Simonneau *Electrochemistry Communications*, vol. 2, no. 2, pp. 81–84, 2000.

[29] Y. Saito *Review of Polarography*, vol. 15, no. 6, pp. 177–187, 1968.

[30] D. Shoup and A. Szabo *J. Electroanal. Chem.*, vol. 140, no. 2, pp. 237–245, 1982.

[31] A. Szabo, D. K. Cope, D. E. Tallman, P. M. Kovach, and R. M. Wightman *Journal of electroanalytical chemistry and interfacial electrochemistry*, vol. 217, no. 2, pp. 417–423, 1987.

# Chapter 2

# Electrochemical simulation

The numerical modelling of the current-time response from electrodes in physico-chemical systems is key to understanding mass transport and kinetics in electrochemical cells[1–3]. This especially includes the voltammetric and amperometric methods which were discussed in the previous chapter. Experimental electrochemical systems are known to be highly accurate and are widely used as sensitive and quantitative analytical methods, and in conjunction with accurate simulation, physical parameters can be extracted. These include diffusion coefficients, reaction mechanisms, kinetic constants, adsorption and catalytic parameters[4,5].

There are two main ways to approach the simulation of mass transport in electrochemistry. The first way is by random walk modelling. The second way, and more common for electrochemical systems, is by solving the diffusion equation in the continuous limit (Fick's second law). In this chapter, these methods are first reviewed. Second, the finite difference method, which is applied for many cases in this thesis, is discussed in detail.

## 2.1 Random walk modelling

In random walk models of Brownian motion, the path of individual particles are traced using a succession of random steps to simulate Brownian motion as described by Einstein theory[6]. For example, in a one dimensional space with a length $L$, the Brownian motion of a particle can be discretised to a 1D grid ($x_0 ... x_L$). The time step $\Delta t$ is chosen as a constant and small value. Thus the space grid can be defined by the mean square displacement at a single time step of a Brownian motion:

$$x_j - x_{j-1} = \Delta x = \sqrt{2D\Delta t} \tag{2.1}$$

(e.g. $x_0 = 0$, $x_1 = \sqrt{2D\Delta t}$, $x_2 = 2\sqrt{2D\Delta t}, ...,$ $x_L = L\sqrt{2D\Delta t}$). $\Delta x$ is needed to be sufficiently small[7] relative to the size of the space $L \gg \Delta x$. At each time step in the simulation, the position of each particle is updated from $x_j$ to $x_{j+1}$ or to $x_{j-1}$. The direction of the move of each particle at each time step is chosen via a random number generator. Using the random walk method, pathways of all particles that diffuse and undergo electrode reaction can be traced. This method has been successfully used to simulate electrochemical experiments of both chronoamperometry and cyclic voltammetry[8–11]. In particular, it is important for studying the response of ultra low concentrations of electro-active species[10]. The method is relatively simple to implement but computationally limited to small amount of particles (ultra low concentrations). The method is discussed further and applied to a study of ultra-dilute solution in chapter 4.

## 2.2 Numerical method for solving of the diffusion equation

The second way, and more common for simulating electrochemical systems, is by solving Fick's second law. In this way, a numerical method is applied to solve the partial differential equation over the space of the cell subject to specified boundary conditions. The simulation solves the concentration profiles which evolve in time. The model for simulation of the diffusion equation is specific to the geometry being simulated, and to the boundary conditions. This requires input of physical properties and specification of the type of experiment. This thesis discusses and develops simulations for various models. The appropriate form of Fick's second law, the simulation space, and the boundary conditions are defined for each case.

## 2.3 Finite difference method

### 2.3.1 Motivation

In electrochemistry, the two most popular methods for solving partial differential equations (PDE) are the finite element method (FEM)[12] and the finite difference method (FDM)[13].

In simple terms, in the finite element method the domain is subdivided into finite small cells. There is no restriction on the shape of the elements, but in triangles or rectangles are commonly employed in 2D geometries and tetrahedrons for 3D[14]. The method is a procedure that fits trial functions to the PDE for each finite element as a basis function. The basis function for each element forms a set of equations which can be solved in a matrix form. For example, the solution of the Fick's second law with appropriate boundary conditions gives the concentration profiles along each element in the domain[12]. The main advantage of the FEM in electrochemical simulations is the flexibility in using various shapes of element and using various basis sets, linear or higher orders to approximate the solution of each element. This flexibility allows the solution of an arbitrary geometry.

The finite element method is relatively difficult to implement, and therefore in cases of complex geometries, commercial software can be used[15,16]. The main limitation of using a commercial software is the inaccessibility to the algorithm. This is maybe not important in applicative studies, but crucial in fundamental studies. In general, commercial algorithms are tested and verified for known cases and therefore can be used to account geometrical modifications, or coupling complex physical behaviour such as electrochemical simulation of a battery[17] or a convection-diffusion problem[18]. However, in innovative fundamental studies the researcher optimistically seeks for new interesting behaviours which usually unseen before. This requires full control of the numeric in order to establish a careful research, and to eliminate any numerical artefacts.

Hence, in fundamental research, and especially for our case of diffusion in electrochemical cells, the finite difference algorithms are widely used[1,13,19,20]. This is due to the easy manipulation of the code to get a deep understanding of subtle effects on the transport, but in general, it involves the modelling of relatively simple geometries.

Additionally, the finite difference method allows fast and efficient simulation. Moreover, high performance computing can be implemented, and is developed fully for this study (see chapter 3). Throughout the thesis the finite difference method is employed to solve diffusion problems in the context of electrochemical systems. The main methodology is described next.

### 2.3.2 The numerical basis of finite difference simulation

In the general approach, the partial differential equation of interest, is approximated by finite differences. For example, the derivative of a function $f$ at a point $x$ can be defined by the limit:

$$f'(x) = \lim_{h \to 0} \frac{f(x+h) - f(x)}{h} \tag{2.2}$$

This is also called the forward difference approximation, where $h$ is a small finite difference. In the same way, this can also be defined as a backward difference:

$$f'(x) = \lim_{h \to 0} \frac{f(x) - f(x-h)}{h} \tag{2.3}$$

Using Taylor's theorem the error of these approximations can be investigated. For the forward difference:

$$f(x+h) = f(x) + \frac{f'(x)}{1!}h + \frac{f''(x)}{2!}h^2 + \frac{f'''(x)}{3!}h^3 + ... \tag{2.4}$$

and rearranging gives the first derivative to be:

$$f'(x) = \frac{f(x+h) - f(x)}{h} - \frac{f''(x)}{2!}h - \frac{f'''(x)}{3!}h^2 - ... \tag{2.5}$$

The first term on the right-hand side of the equation is the approximation of the forward finite difference. The error is therefore of the order of $h$:

$$\frac{f(x+h) - f(x)}{h} - f'(x) = O(h), \;\; O(h) \to 0 \, as \, h \to 0 \tag{2.6}$$

The same approach can be applied to find the error associated with the backward difference:

$$f(x-h) = f(x) - \frac{f'(x)}{1!}h + \frac{f''(x)}{2!}h^2 - \frac{f'''(x)}{3!}h^3 + ... \tag{2.7}$$

and the error is also of the order of $h$:

$$\frac{f(x) - f(x-h)}{h} - f'(x) = O(h), \;\; O(h) \to 0 \, as \, h \to 0 \tag{2.8}$$

However, another way to approximate the difference is via the central difference, which is more accurate:

$$f'(x) = \lim_{h \to 0} \frac{f(x+h) - f(x-h)}{2h} \tag{2.9}$$

The error can be evaluated by subtracting the Taylor expansions of the Forward and backward differences:

$$f(x+h) - f(x-h) = \frac{2f'(x)}{1!}h + \frac{2f'''(x)}{3!}h^3 + ... \tag{2.10}$$

Rearranging gives:

$$f'(x) = \frac{f(x+h) - f(x-h)}{2h} - \frac{f'''(x)}{3!}h^2 + ... \tag{2.11}$$

and the error is of the order of $h^2$ :

$$f'(x) = \frac{f(x+h) - f(x-h)}{2h} + O(h^2), \;\; O(h^2) \to 0 \, as \, h \to 0 \tag{2.12}$$

therefore the central difference more accurate ($h \ll 1$) than either of the forward and backward differences as $h$ tends to zero.

The second derivative of the function $f(x)$ can also be approximated via the central difference by summing the forward and backward differences:

$$f(x+h)+f(x-h)=2f(x)+f''(x)h^2+\frac{2f^4(x)}{4!}h^4+... \tag{2.13}$$

and by rearranging:

$$f''(x)=\frac{f(x+h)-2f(x)+f(x-h)}{h^2}+O(h^2) \tag{2.14}$$

with the same order of error ($O(h^2)$).

### 2.3.3 Explicit and implicit methods

The Fick's second law in one dimension is:

$$\frac{\partial c}{\partial t}=D\frac{\partial^2 c}{\partial x^2} \tag{2.15}$$

The space domain can be subdivided using a mesh $x_0, ..., x_N$ and the time domain using a mesh $t_0, ..., t_K$, choosing $\Delta x$ to be the difference between two consecutive space points and $\Delta t$ between two consecutive time steps. If the concentration in time point $t_k$ is known, the aim is to calculate the concentration at time point $t_{k+1}$, since the concentration at $t_0$ is specified by the relevant initial value, the forward difference for the time domain is used to approximate the time derivative of $c$ (at the space point $n$ and time point $k$):

$$\frac{\partial c}{\partial t}\sim\frac{c_n^{k+1}-c_n^k}{\Delta t} \tag{2.16}$$

The discretised diffusion equation can be solved in two ways; the explicit and implicit methods. In the explicit method, the concentrations at a later time are calculated from the known concentrations at the present time, $t_k$:

$$\frac{c_n^{k+1} - c_j^k}{\Delta t} = D\frac{c_{n+1}^k - 2c_n^k + c_{n-1}^k}{\Delta x^2} \tag{2.17}$$

In this way, $c_n^{k+1}$, can be found directly from the known concentration at the present state. However, the solution is stable only when $\Delta t$ is very small in comparison to $\Delta x^2$. The implicit method finds a solution by solving an equation involving both the current state of the system and the later one:

$$\frac{c_n^{k+1} - c_n^k}{\Delta t} = D\frac{c_{n+1}^{k+1} - 2c_n^{k+1} + c_{n-1}^{k+1}}{\Delta x^2} \tag{2.18}$$

In this case, only $c_n^k$ is known. In order to find a solution, a set of equations for each point in space is first constructed. This results in $N$ equations with $N$ unknown concentrations. Solving the set of equations takes much more computing time in the implicit method but has the advantage is that the method is unconditionally stable, regardless of the size of $\Delta t$.

An efficient algorithm to solve the equation system in the implicit method, is the Thomas algorithm[21], which is a specific case of Gaussian elimination that can be used to solve tridiagonal systems of equations. Each equation in the set can be re-written as:

$$\alpha_n c_{n-1}^{k+1} + \beta_n c_n^{k+1} + \gamma_n c_{n+1}^{k+1} = \delta_n c_n^k \tag{2.19}$$

where the coefficients are:

$$\alpha_n = -\frac{D}{\Delta x^2},\ \beta_n = \frac{1}{\Delta t} + \frac{2D}{\Delta x^2},\ \gamma_n = -\frac{D}{\Delta x^2},\ \delta_n = \frac{1}{\Delta t} \tag{2.20}$$

The set of the coefficients equations (eq. 2.19) forms the matrix $A$ which follows:

$$AU = b \tag{2.21}$$

where $U$ a vector of the unknown concentrations. In detail, the tridiagonal matrix is:

$$\begin{pmatrix} \beta_0 & \gamma_0 & & & & \\ \alpha_1 & \beta_1 & \gamma_1 & & \text{\huge 0} & \\ & \ddots & \ddots & \ddots & & \\ \text{\huge 0} & & \alpha_{n-1} & \beta_{n-1} & \gamma_{n-1} & \\ & & & \alpha_n & \beta_n & \end{pmatrix} \begin{pmatrix} c_0^{k+1} \\ c_1^{k+1} \\ \vdots \\ c_{n-1}^{k+1} \\ c_n^{k+1} \end{pmatrix} = \delta \begin{pmatrix} c_0^{k} \\ c_1^{k} \\ \vdots \\ c_{n-1}^{k} \\ c_n \end{pmatrix}$$

The first and last rows are subject to the boundary conditions, and the solution for the concentration profile at each time, can be found by knowing the initial concentrations (at t=0). The implicit method can be easily modified to solve electrochemical system of more than one species, or in non-uniform spaces[13], is modelled for various cases in this thesis.

### 2.3.4 Typical adaptations

#### Non-uniform grids

As discussed above, spatial and temporal grids are defined in each simulation in order to discretise the diffusion equation. The generated grids need to be dense enough in order to meet the high accuracy of electrochemical experiments[22]. However using a uniform grid would make the simulation impractical, especially in two dimensional (2D) spatial space due to the extreme computational cost. Instead, non-uniform grids are used. The non uniform spatial grid is defined to be selectively denser in locations where large gradients of concentration are expected, for example next to the electrode surface. Far away from the electrode, only small variations of concentration are expected, thus an expanding grid can be helpfully employed.

Similar considerations are necessary for the time grid. In the case of chronoamperometry, the potential step at zero time creates a large change in the concentration at short distances from the electrode. However, at long times the system reaches an almost steady state, particularly for microelectrodes, and therefore very large time steps leads to only small variations in the concentration profile. Therefore, an expanding time grid can be used to optimise the simulation time. Details about the definition of the grids are problem-specific and therefore are discussed separately for each case throughout the thesis.

### Dimensionless parameters

Once a physical model has been developed and appropriate equation with boundary conditions have been defined, a normalisation of the physical parameters is usually employed. For example, all distances are normalised to the characteristic radius/width of the electrode. Initial concentrations and diffusion coefficients are normalised to the bulk concentration, $\bar{D} = D/D^*$, $\bar{C} = c/c^*$. Dimensionless time is introduced to be $\tau = Dt/L^2$. Where $L$ is a characteristic value of the geometry. For example for Fick's second law (eq. 2.15) in a one dimension, this can be given as the length of the cell. Then the space coordinate can be defined as $\bar{X} = x/L$. Substituting the dimensionless parameters in the equation results in the form:

$$\frac{\partial \bar{C}}{\partial \tau} = \frac{\partial^2 \bar{C}}{\partial \bar{X}^2} \tag{2.22}$$

It is important to normalise the physical parameters for the following main reasons. First, it is convenient and more insightful to compare and test simulation results in a normalised parameters since it minimises the independent number of parameters. Second, unforeseen round-off errors can be introduced when using various dimensional parameters. Third, using dimensionless parameters generalises the solution, which can then be easily post-processed to compare various cases, without the need of re-solving the problem. All dimensionless parameters are listed and defined throughout the thesis.

### 2D algorithms

The above discussion considered only one dimensional systems. In many electrochemical models a two dimensional simulation is required, such as a microdisc electrode. For instance, in the case of two dimensional Cartesian space Fick's second law becomes:

$$\frac{\partial c}{\partial t} = D \left( \frac{\partial^2 c}{\partial x^2} + \frac{\partial^2 c}{\partial y^2} \right) \tag{2.23}$$

A common and efficient way to solve the two dimensional problem is the alternating direction implicit (ADI) method[23]. In this method, the PDE is solved for each time step in two half time sub-steps. At the first half time step the $x$ dimension is solved in the implicit way whilst the $y$ dimension is defined explicitly. In the second half time step $y$ is solved implicitly whilst the $x$ dimension is defined explicitly. This method is described in the representative example of the microdisc electrode in the next chapter.

### 2.3.5 Implementation

Implementation of electrochemical simulations using the FDM method can be made using various computer programming languages. However, taking into account the need for high accuracy, as well as the use of the program for various studies, it is highly necessary to build the tool on an object oriented programming language with a mixed high and low-level programming language. Accordingly, C++ can be an appropriate choice[13].

### 2.3.6 Conclusions

This introductory chapter has discussed numerical methods for electrochemical simulations which are employed in this study. Next, the new development of a high performance simulation is reported. The tool provides much higher efficiency in studying computationally costly electrochemical systems. More detail is also provided on the finite different model simulation in a case of the microdisc electrode.

# References

[1] D. Britz, *Digital Simulation in Electrochemistry*, vol. 666. Springer, 2005.

[2] H. Angerstein-Kozlowska, J. Klinger, and B. Conway *Journal of Electroanalytical Chemistry and Interfacial Electrochemistry*, vol. 75, no. 1, pp. 45–60, 1977.

[3] J. A. Alden and R. G. Compton *The Journal of Physical Chemistry B*, vol. 101, no. 44, pp. 8941–8954, 1997.

[4] A. J. Bard and L. Faulkner, *Electrochemical Methods: Fundamentals and Applications (2nd Edition).* John Wiley and Sons, 2001.

[5] R. G. Compton and C. E. Banks, *Understanding Voltammetry (2nd Edition).* Imperial College Press, 2011.

[6] A. Einstein *Annalen der Physik*, vol. 322, no. 8, pp. 549–560, 1905.

[7] D. T. Gillespie and E. Seitaridou, *Simple Brownian Diffusion.* Oxford university press, 2012.

[8] G. Nagy, Y. Sugimoto, and G. Denuault *Journal of Electroanalytical Chemistry*, vol. 433, no. 1, pp. 167–173, 1997.

[9] J. E. Baur and P. N. Motsegood *Journal of Electroanalytical Chemistry*, vol. 572, no. 1, pp. 29–40, 2004.

[10] I. J. Cutress, E. J. Dickinson, and R. G. Compton *Journal of Electroanalytical Chemistry*, vol. 655, no. 1, pp. 1–8, 2011.

[11] O. Sliusarenko, A. Oleinick, I. Svir, and C. Amatore *ChemElectroChem*, vol. 2, no. 9, pp. 1279–1291, 2015.

[12] T. Nann and J. Heinze *Electrochemistry Communications*, vol. 1, no. 7, pp. 289–294, 1999.

[13] R. G. Compton, E. Laborda, and K. R. Ward, *Understanding Voltammetry - Simulation of Electrode Processes.* Imperial College Press, 2013.

[14] J. N. Reddy, *An Introduction to the Finite Element Method*, vol. 2. McGraw-Hill New York, 1993.

[15] *COMSOL Multiphysics. www.comsol.com. COMSOL AB, Stockholm, Sweden.*

[16] *Ansys, www.ansys.com , Pennsylvania, United State.*

[17] S. Elul, Y. Cohen, and D. Aurbach *Journal of Electroanalytical Chemistry*, vol. 682, pp. 53 – 65, 2012.

[18] K. Ngamchuea, S. Eloul, K. Tschulik, and R. G. Compton *Analytical chemistry*, vol. 87, no. 14, pp. 7226–7234, 2015.

[19] J. Heinze *Journal of Electroanalytical Chemistry and Interfacial Electrochemistry*, vol. 124, no. 1, pp. 73–86, 1981.

[20] J. Heinze and M. Störzbach *Berichte der Bunsengesellschaft für physikalische Chemie*, vol. 90, no. 11, pp. 1043–1048, 1986.

[21] L. Thomas *Libraries, the Llewellyn Hilleth Thomas Papers*, vol. 1989, pp. 210–8, 1921.

[22] J. Heinze, M. Störzbach, and J. Mortensen *Journal of Electroanalytical Chemistry and Interfacial Electrochemistry*, vol. 165, no. 1, pp. 61–70, 1984.

[23] J. Crank and P. Nicolson in *Mathematical Proceedings of the Cambridge Philosophical Society*, vol. 43, pp. 50–67, Cambridge Univ Press, 1947.

# Chapter 3

# Implementing high performance voltammetry simulation using the implicit parallel algorithm

In this chapter, the numerical simulation of voltammetry and amperometry at a microdisc electrode is described and implemented with a parallel algorithm using the Graphic Processing Unit GPU (CUDA in C++) and adapting the implicit finite difference approximation with the ADI method. This leads to the high performance simulation of the current response whilst maintaining the high standard of accuracy required for such electrochemical systems. A maximum speed-up of 20 times with a standard graphic card specifications is realised. The simplified allocation and data flow allows an accessible code which produces a starting point for researchers to manipulate the code to study new problems in electrochemical and surface reaction systems that require high performance simulation. The work has been published in 'The Journal of Electroanalytical Chemistry'[1].

## 3.1 Introduction

The numerical modelling of the current-time response from electrodes in physico-chemical systems is key to understanding mass transport and kinetics in electrochemical cells[2,3]. One of the strongest tools is voltammetry, where a scanning potential applied to an electrode allows the investigation of surface kinetic processes and determination of the diffusion coefficient of electroactive species. In another important technique, amperometry, the investigation of mass transport and especially diffusion can be achieved by holding the electrode at a fixed potential to measure current over time from the oxidation or reduction of adsorbing or reacting entities.

Performance and accuracy are a significant part of the modelling methods, and uncompromising space grids or time steps[2,4], can make calculations be very long, even for relatively simple routine investigations. For example, the extraction of kinetic parameters and reaction mechanisms with a non-linear boundary condition problem[3,5] or studying the life cycle of thousand charge/discharge processes in a multi-dimensional battery cell[6,7]. Therefore, high performance simulation is important for making the problems practicable for study and application.

Recently, the simulation of voltammetry using the graphic processor unit (GPU) was introduced for the solution of finite difference problems via the explicit method[8]. Although the explicit method is a natural parallel problem, it is numerically unstable in comparison for the implicit method as shown for voltammetry problems by Bieniasz et al[9]. Thus, finite difference studies generally use the implicit method to avoid inaccuracy, and sometimes utilize the interface OpenMP (Open Multi-Processing) or the high performance implementation of MPI (Message Passing Interface) to gain a fair performance[4]. However, with growing interest in parallel algorithms using GPU, very recent computational studies show that changing the naturally sequential Thomas algorithm to solve the dominant diagonal matrix with the a less efficient but inherently parallel algorithm 'Parallel Cyclic Reduction' (PCR), enables a high performance in recent GPU architectures[10–12]. GPU implementations were reported for heat transfer[11] and are popular for fluid dynamics calculations[13], however, they have not yet introduced for electrochemical and surface kinetics either for research or applications.

I here introduce the Finite Difference simulation using the GPU for the implicit case of voltammetry at a disc electrode, using a two dimensional grid and kinetic boundary conditions for charge transfer in the case of redox reaction between species with equal diffusion coefficients. A simulation for the case of amperometry is also provided. The code provides a starting point for many other modelling systems that can be achieved by modifying and altering the code, such as the complex simulation of multi-species problems with unequal diffusion coefficients, multi-reaction mechanism, adsorption problems and non-linear boundary conditions, or arrays. The code itself [1] is written in an accessible way using CUDA with C++. That said, the code is optimised to be easy to understand rather than to be fully performance optimized. The results were also tested in comparison to the serial code with the Thomas algorithm and the analytical theoretical values for voltammetry.

## 3.2 Physical model

A representative electrochemical system is modelled for the case of statistical diffusion towards a disc electrode. This case is generally assumes a full supporting electrolyte, where migration is negligible. On the electrode surface, a kinetic and thermodynamic

---

[1] The program is provided by request at $http : //compton.chem.ox.ac.uk$.

boundary condition is employed with the widely used Butler-Volmer expression for the reaction mechanism on the disc surface[14].

The geometry is illustrated in figure 8.3a. Using axial symmetry around $r = 0$ (figure 8.3b), Fick's second law is solved for a cylindrical space[15]:

$$\frac{\partial c}{\partial t} = D\left(\frac{\partial^2 c}{\partial r^2} + \frac{\partial^2 c}{\partial z^2} + \frac{1}{r}\frac{\partial c}{\partial r}\right) \tag{3.1}$$

where $r$ and $z$ are the cylindrical coordinates, as shown in figure 8.3b. $D$ is the diffusion coefficient, $c$ is the concentration of the active species in an electrochemical cell with the redox couple ($A$ and $B$). Two distances are defined in the $r$ direction, the disc electrode radius ($r_d$) and the surface radius ($r_s$) as illustrated in figure 8.3.

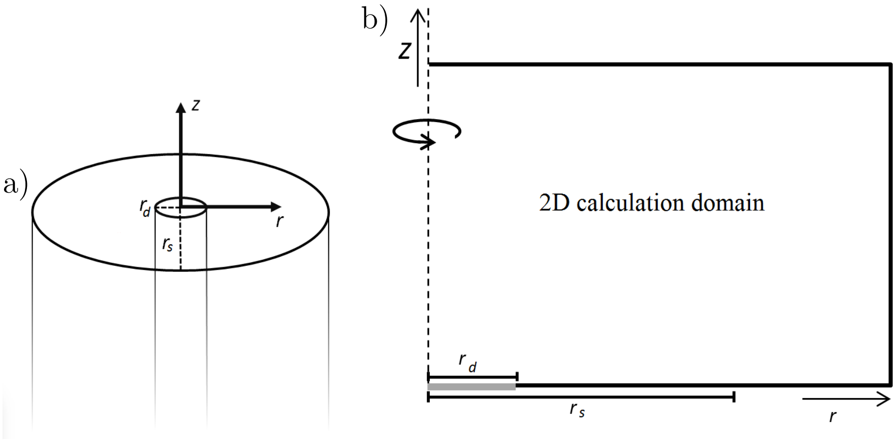

Figure 3.1: 3D Illustration of the microdisc electrode surrounded by an insulator (a) and the 2D system in the simulation model (b).

The electron transfer electrochemical reaction on the electrode $r \leq r_d$:

$$A \leftrightarrows B + e^- \tag{3.2}$$

The kinetics of the reaction on the electrode is defined by the boundary condition as shown below. Assuming equal diffusion coefficients for both species, $A$ and $B$, and a single step reaction of $A$ to $B$, equation 6.61 can be solved only for species $A$, and the concentration of species $B$ can be determined by:

$$1 = \frac{[B] + [A]}{[B]^* + [A]^*} \tag{3.3}$$

where $[A]^*$ is the initial concentration of species $A$, and $[B]^*$ is the initial concentration of $B$.

In the work reported below, $[B]^*$ is assumed to be zero.

### 3.2.1 Boundary Conditions

In voltammetry, the scanned potential $(E/V)$ is applied on the electrode with a scan rate $\nu(V/s)$. At $z = 0$ the kinetics at the adsorbing surface $(r_d < r \leq r_s)$ and the electrode boundary condition $(r \leq r_d)$ are defined. At the disc electrode, the latter is set to be the flux of each species related to the electrode potential $(E)$ according to the Butler-Volmer equation for an oxidation reaction[14]:

$$\begin{matrix} t \geq 0 \\ 0 < r \leq r_d \end{matrix} \qquad \left(\frac{\partial c_{A(r,0)}}{\partial z}\right)_{z=0} = k^0 \left[(1 - c_{A(r,0)})e^{-\frac{\alpha E}{RT}} - c_{A(r,0)}e^{\frac{(1-\alpha)E}{RT}}\right] \tag{3.4}$$

$F$ is the Faraday constant, and $R$ and $T$ are the gas constant and temperature, respectively. $k^0$ is the kinetic constant, and $\alpha$ is the transfer coefficients for the reaction.

In the case of voltammetry, $E$ depends on the potential scan rate $(\nu)$ which is applied on the electrode via:

$$\begin{aligned} &Forward\,scan \quad E_{min} \rightarrow E_{max} \quad E(t) = E\nu + E_{min} \\ &Backward\,scan \quad E_{max} \rightarrow E_{min} \quad E(t) = E_{max} - E\nu \end{aligned} \tag{3.5}$$

$E_{min,max}$ are the lowest negative and highest positive potentials in the (cyclic) voltammetry, respectively. The maximum time ($t_{\max}$) is chosen to be a full time of one cycle in the cyclic voltammetry:

$$t_{\max} = \frac{2(E_{max} - E_{min})}{\nu} \tag{3.6}$$

In the case of amperometry, the potential is adjusted to a constant high potential where no kinetic barrier exists and the current is then driven only by diffusion. In the case of a high potential, very small time steps must be included due to the large gradients in concentration adjacent to the electrode. However, since the long time steady state behaviour is of interest an expanding time grid must be used in order to solve the problem for short and long time, bearing in mind that this can be a source of instability[9] and thus the expanding factor should be adjusted carefully.

On the other boundaries of the cell, a wall/insulation boundary condition is defined for $A$ and $B$:

$$\begin{matrix} t \geq 0 \\ r_d < r \,,\, z = 0 \end{matrix} \qquad \left(\frac{\partial [A]}{\partial z}\right) = \left(\frac{\partial [B]}{\partial z}\right) = 0 \tag{3.7}$$

where $r_{max}$ and $z_{max}$ are set to be the cell boundaries which is generally far enough to affect diffusion in the time scale of experiment. Invariably, $r_{max}$ and $z_{max}$ are chosen to be large, such as $6\sqrt{Dt_{max}}$ in both directions $(r, z)$, to simulate an "infinite cell"[14].

From symmetry, the flux across the $z$ axes can be set to zero:

$$\left(\frac{\partial[A]}{\partial z}\right)_{r=0} = \left(\frac{\partial[B]}{\partial z}\right)_{r=0} = 0 \tag{3.8}$$

Finally, the edges in the outer space of the simulation set to the bulk concentration of species $A$:

$$c_{r_{\max}} = [A]^*, \quad c_{z_{\max}} = [A]^* \tag{3.9}$$

### 3.2.2 Current Calculation

The flux inward the disk electrode is given by:

$$0 < r \leq r_d \; j = \left(D\frac{\partial[A]}{\partial z}\right)_{Z=0} \tag{3.10}$$

Integrating the flux ($j$) over the disc, the net flux($J$) inward the disc electrode is obtained and thus the Faradaic current of the one electron redox reaction is:

$$I = 2\pi F[A]^* D \int_0^{r_d} j_{r,0,t} r \mathrm{d}r \tag{3.11}$$

## 3.3 Numerical Methods

The partial differential equation is discretised over a spatially expanding 2D grid with $m_{max}$ rows and $n_{max}$ columns $(r(n_{max}) \times z(m_{max}))$ which also gives the matrix sent for calculation. This space is meshed generally with an expanding grid around the nodes: $r_0, r_d, r_{max}, r_z$, where a large perturbation of flux and discontinuities are expected and high accuracy is needed to get a converged result. This can be seen in figure 3.2a which shows the grid points next to the edge of the electrode and the supporting insulator. The first differences around the nodes have minimum $\delta r$ and $\delta z$ values, after which the differences grow exponentially in space (r,z), before being compressed again around the boundaries $r = 0$, and $r_{max}$. The concentration equation is set for each species (in this case only for species $A$) in the space.

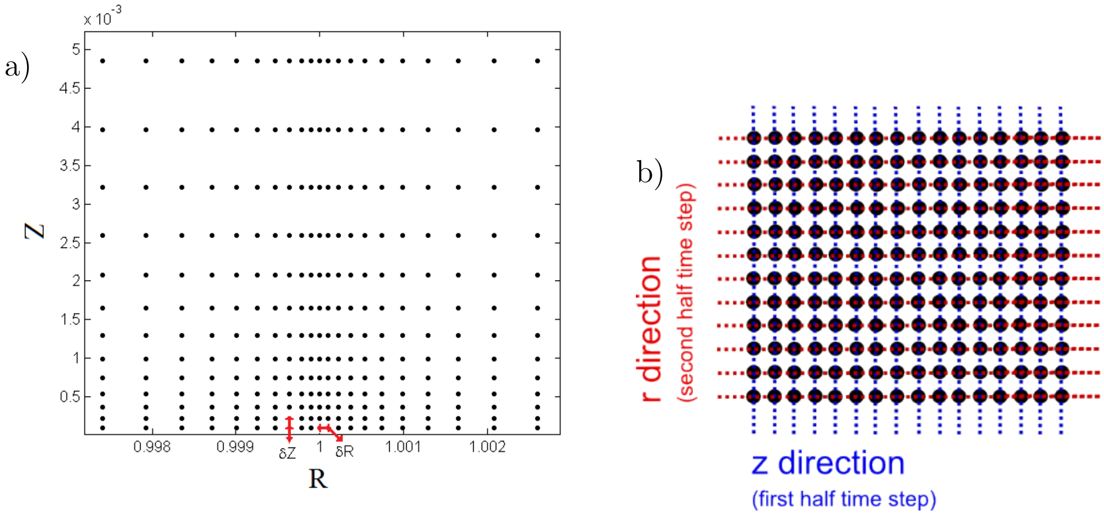

Figure 3.2: (a) The expanding grid next to the nodes. (b) Illustration of the ADI method algorithm.

The partial differential equations for both species, along with the boundary conditions are solved numerically with the finite difference method using the implicit Crank-Nicolson method[16], utilising the alternating direction implicit (ADI) method for solving the 2D space[4,11,17]. Within each time step the calculation is divided into two half time steps where at the first half step the $z$ direction is defined implicitly and the $r$ direction is defined explicitly and vice versa for the second half step[17]. The ADI method allows the solution of each column ($j$) in the $z$ direction or row ($i$) in the $r$ direction to be solved in parallel. At each row or column there is a set of equations that forms tri-diagonal matrices that need to be solved. In the algorithm the discretization of the set of equations is in the form:

$$\alpha_{i,j}c_{i,j-1} + \beta_{i,j}c_{i,j} + \gamma_{i,j}c_{i,j+1} = \delta_{i,j} \tag{3.12}$$

for the $z$ direction from $j = 0$ to $j = m$, or

$$\alpha_{i,j}c_{i-1,j} + \beta_{i,j}c_{i,j} + \gamma_{i,j}c_{i+1,j} = \delta_{i,j} \tag{3.13}$$

for the $r$ direction from $i = 0$ to $i = n$. (All coefficients for the domains and boundaries are shown in the literature[4]). The coefficients $\alpha, \beta, \gamma$ form a tridiagonal dominant matrix ($A$) which satisfies the equation (as discussed in chapter 2):

$$A^{-1}b = U \tag{3.14}$$

$U$ is the unknown concentration vector. The normal use of the Thomas algorithm for Gauss elimination in the case of a diagonal dominant matrix is carried out with linear efficiency ($O(n)$). OpenMP and MPI are good ways to increase the parallelism and create a better performance, optimizing several cores, when each core solves a full row or column in the concentration matrix. However, implementing the algorithm on GPU (to have many threads) usually makes the algorithm to be memory limited. Therefore, changing the algorithm to a less efficient but inherently parallel algorithm overcomes the memory traffic limit and a high performance calculation can be achieved. Parallel Cyclic Reduction (PCR) is an inherently parallel algorithm and is used to solve the diagonal dominant matrix in many previous finite difference models[10,12]. Its efficiency is linear-logarithmic, $O(nlogn)$, but can be easily spread to many threads in the current GPU architectures. It is therefore used to solve the set of concentration equations of each column in the $z$-direction and row in the $r$-direction. The PCR algorithm is a forward reduction of the tridiagonal matrix to half size at each iteration, until a matrix of only 2 unknowns is reached and determined. Then a backward substitution phase successively determines the other unknowns. The pseudo code and details on the PCR algorithm can also be found in the literature[10].

### 3.3.1 Memory allocation in the GPU device

In order to make the algorithm performance optimized to GPU processing, care needs to be taken when assigning arrays to the global or shared memory of every block. In some cases, in order to get better performance on the GPU it is necessary to divide the matrix to smaller matrices that can fit the ‘cache’ level, to fully utilize the traffic between the various cache levels and the wraps or blocks. This for example can be achieved by the technique of dividing the matrix into smaller sub matrices that can be efficiently calculated with the PCR algorithm and use the Thomas algorithm to connect back the sub-matrices into the original matrix[12]. For our purpose, a simplified memory allocation is used (discussed below) in order to make the shared code accessible as a starting point for high performance voltammetry calculations, so a scientist can relatively easy take the CUDA code, and alter the shared code further for their specific study. The allocation of the main pseudo 2D array of initial concentration values of size equals $m \times n$ is created on the host and is allocated in the global memory of the device along with the constant 1D array values of the $z$ grid ($z_0 - z_m$), and the constant 1D arrays along the $r$ grid ($r_0 - r_n$).

These arrays along with constant parameters, and ‘atomic-variable’ for integration summation, are used in the kernels, and the coefficient arrays are defined in the kernel with shared memory for each block of threads. In the memory allocation, each row or column is assigned to one block of threads. The mapping into the block is illustrated in figure 3.3. This limits the size of a direction to the maximum size of the blocks in the specific GPU architecture, but it is enough for most practical applications whilst keeping the coding fairly simple. In order to make larger grids, it is necessary to modify the mapping strategy with extra coding[10,12].

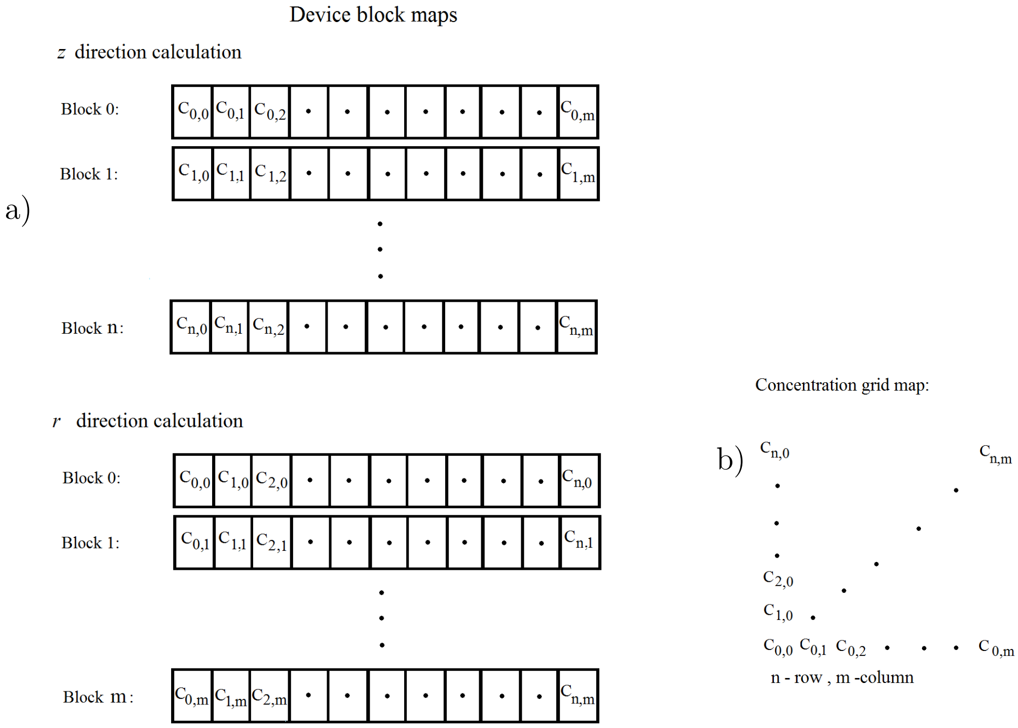

Figure 3.3: Illustration of allocation in the blocks (a), where each block is assigned to a row or a column in the concentration matrix (b).

### 3.3.2 Implementation

The parallelization of the ADI solver using NVIDIA CUDA was implemented through C++. The test machine was a Xeon E5-1650, 3.2GHz. The GPU tested is a NVIDIA Quadro K4000 with 4GB graphics memory and a 48KB shared memory (Kepler architecture), with 768 cores.

The algorithm uses the serial solving method where each direction is solved in a different kernel. Optimization for a better performance was found using the transpose of the array matrix between each direction, and using texture memory, but this alteration can be avoided in this stage[10]. The diagram in figure 3.4 shows the implementation on the GPU device. The calculation method is divided into three serial kernels to get synchronization between the blocks. The first is for solving the $z$ direction for each half time step by assigning the coefficients in the matrix including the respective boundary conditions, and using the PCR algorithm, it returns the new concentration maps. The second kernel makes the integration by using atomic addition to get global reduction and copy back the concentration to be used in the third kernel. In the same kernel, the $r$ direction is solved, and the results and parameters are updated. It is noted that at each time step the $z$ and $r$ calculation kernels re-assign the $\alpha, \beta$, and $\gamma$ coefficients which is not essential in this calculation. However in some other cases it would be needed as in the case of bulk or surface reaction and adsorption, or when adding a drift (migration) term to the diffusion equation[4].

## 3.4 Calculations

In the following, typical current responses are shown for voltammetry and amperometry simulations carried out on the GPU with the PCR algorithm. First, the validation of a voltammetry without any kinetic limitations is compared to the theoretical result. Second, simulation tests are shown for various electrochemical rates and for the case of potential step chrono-amperometry, in order to demonstrate the ability to implement common electrochemical simulations. Third, the performance of the GPU calculations are compared to calculations on the CPU at various matrix sizes.

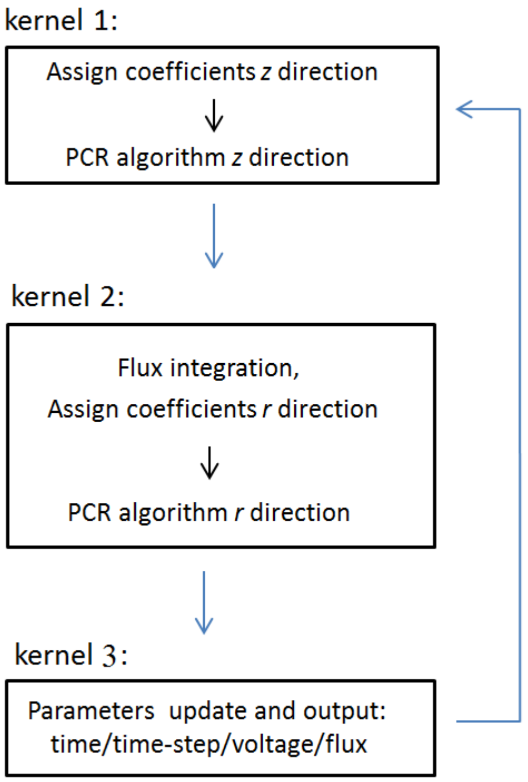

Figure 3.4: Illustration of the data flow at each time step.

It is convenient to convert the calculation and output results to dimensionless units where $\phi = EF/RT$ is a dimensionless potential, $\tau = Dt/r_d^2$ is the dimensionless time, and therefore the scan rate is defined as: $\sigma = \phi \cdot r_d^2/D^{15}$. The dimensionless flux is defined as : $J = I(A)/FD[A]^* r_d$, and lastly, the kinetic constant $k^0(m/s)$ is defined in dimensionless units as K=$k^0 r_d/D$, simplifying all calculations which are presented in dimensionless form.

### 3.4.1 Typical Voltammetry

The results of GPU calculations for typical voltammetry are shown in figure 3.5 for two dimensionless scan rates. This shows the net (dimensionless) flux response as function of (dimensionless) the potential applied to the electrode surface when there is no kinetic limitation on the electrode reaction (reversible process).

The results in figure 3.5 show high accuracy and can be validated by comparing with

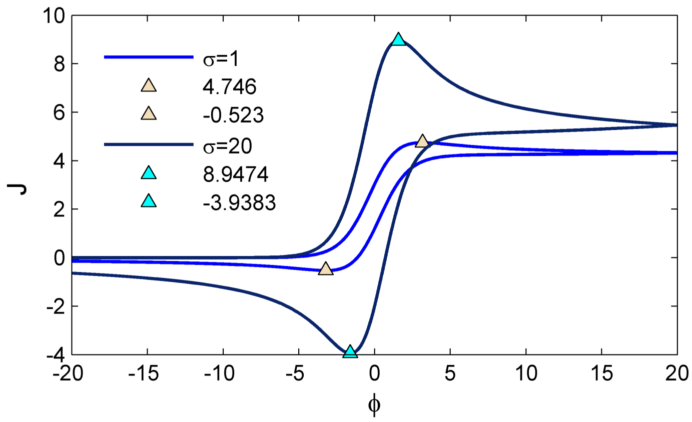

Figure 3.5: Calculation of a characteristic reversible voltammogram for two dimensionless scan rates, $\sigma = 20$, and $\sigma = 1$.

theoretical values of the peak values predicted by the formula[14]:

$$J_{peak} = -4r_d[A]^*(0.34\exp(-0.66\sqrt{\sigma}) + 0.66 - 0.13\exp(-11/\sqrt{\sigma}) + 0.351\sqrt{\sigma}) \tag{3.15}$$

The results of the simulation show a deviation up to 0.02% of the peak current in comparison to the theoretical $J_{peak}$. The simulations were also calculated in the CPU using the traditional method with the Thomas algorithm and show similar results, with a deviation of a maximum $2 \cdot 10^{-8}$ between the GPU and CPU calculations. This is a negligible error. However it is a crucial observation to validate the model due to the differences between the methods for eliminating the matrix. Note the PCR algorithm has a significantly larger amount of arithmetic operations per time step, that might have expressed more rounding errors from the approximations made in the model. In terms of performance, the calculation of voltammetry in the CPU with the Thomas algorithm took 22 minutes in comparison with 72s on the GPU, a speed up factor of 19 for this hardware configuration.

### 3.4.2 The simulation of kinetics in voltammetry, and of amperometry

The results for voltammetry calculated on the GPU for the case of various electron transfer dimensionless rate constants ($K = 1000, 100, 10$) are shown in figure 3.6a. The amperometry simulation of applying a potential step from zero current to a high potential is presented in figure 3.6b. The results are in full agreement with the simulation made on the CPU[18]. The maximum difference between the calculations (GPU to CPU algorithms) found to be bound to $5 \cdot 10^{-8}$ for the net currents at all times. It is important to note that when using an expanding time step, for achieving the steady state behaviour at very long time, the PCR algorithm found to be more sensitive to numerical oscillation than the Thomas algorithm for this model of amperometry. This is reasonable since many more arithmetic operations are made in the PCR algorithm.

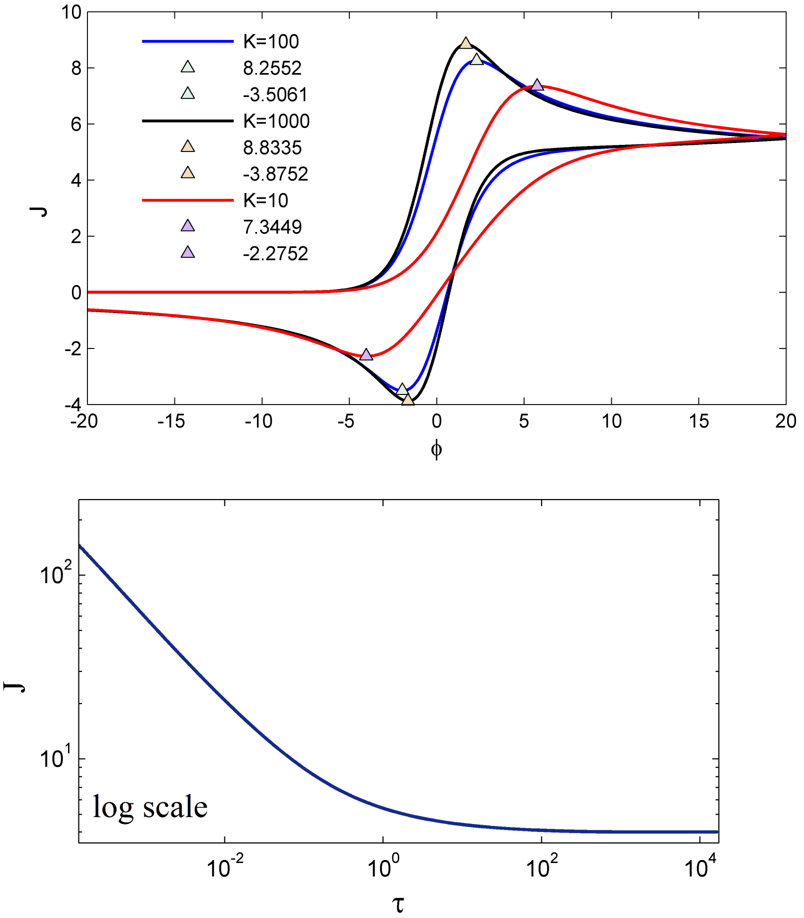

Figure 3.6: a) Calculation of a characteristic voltammogram for a various dimensionless electrochemical rate constants (K=100,10). b) Potential step Chrono-amperometry simulation plotted on a logarithmic scale.

### 3.4.3 Performance tests

The performance of the GPU implementation relative to the CPU for various concentration matrix sizes is evaluated in Table 3.1. The performance is measured for the cyclic voltammetry simulations. It is shown that a significant increase of speed is gained in small and large size matrices. The result for maximum speed up at a matrix size of 103X103 is specific to the GPU architecture used here (Kepler architecture and 768 cores). The different speed ups for various matrix sizes and the maximum speed up at 103X103 are due to the better time optimization between the memory traffic of the various cache memory levels to the computing time of the threads (in this GPU model). This keeps the maximum number of cores 'busy' during the calculations. The NVIDIA profiler analysis implies that increasing the number of cores would increase significantly the speed and therefore it is important to mention that the algorithm has been made on only single core CPU rather than using parallel CPU implementation, since both the number of cores in CPU often varies, and also the number of GPU cores tested is relatively low compared to other models. Bearing in mind that the serial Thomas algorithm is traffic limited, it was found that using the interface OpenMP (Open Multi-Processing) for eight cores in the ADI method increases the speed on average by a factor of three. Running the program in the NVIDIA visual profiler implies that most of the time is spent on arithmetic calculations which requires the assigning of the coefficients before the PCR algorithm. Therefore, higher performance can be achieved by pre-assigning parameters in the shared memory and/or using the texture memory.

| **Matrix size** | Speed up GPU/CPU | maximum difference in flux |
|---|---|---|
| 32X32 | 8.2 | $6.48 \times 10^{-8}$ |
| 45X45 | 13.3 | $1.08 \times 10^{-9}$ |
| 103X103 | 20.3 | $1.2 \times 10^{-8}$ |
| 400X400 | 12.09 | $2.0 \times 10^{-7}$ |
| 732X732 | 11.5 | $3.0 \times 10^{-8}$ |
| 1016X1016 | 14.5 | $8.0 \times 10^{-8}$ |

Table 3.1: Performance evaluation of cyclic voltammetry for a specific CPU 1 core Xeon E5-1650, 3.2Ghz, and GPU device with Kepler architecture and 768 cores.

## 3.5 Conclusions

Simulation code is introduced using CUDA NVIDIA for the parallel computing of voltammetry and potential step amperometry. The implementation is made via the implicit finite difference approximation with the ADI method and the PCR algorithm. This introduces high performance simulation of the current response whilst maintaining the high accuracy required in electroanalytical studies of mass transport and surface reaction. The simulation was validated and tested in comparison with the Thomas algorithm and with the litrature theoretical values of the peak and steady state current values. The performance tests show a 20 times faster simulation of voltammetry with a relatively standard graphic card (Quadro K4000) in comparison with a single core of Xeon 3.2GHz CPU. The simplified allocation and data flow used allows an accessible code which is a starting point for researchers to manipulate the code via C++ to study new models of electrochemical and surface reaction systems which require high performance, such as kinetic studies and highly cost simulations for many species with unequal diffusion coefficients.

# References

[1] S. Eloul and R. G. Compton *Journal of Electroanalytical Chemistry*, vol. 771, pp. 50–55, 2016.

[2] D. Britz, *Digital Simulation in Electrochemistry*, vol. 666. Springer, 2005.

[3] J. A. Alden and R. G. Compton *The Journal of Physical Chemistry B*, vol. 101, no. 44, pp. 8941–8954, 1997.

[4] R. G. Compton, E. Laborda, and K. R. Ward, *Understanding Voltammetry - Simulation of Electrode Processes*. Imperial College Press, 2013.

[5] H. Balslev and D. Britz *Acta Chemica Scandinavica*, vol. 46, pp. 949–955, 1992.

[6] S. Elul, Y. Cohen, and D. Aurbach *Journal of Electroanalytical Chemistry*, vol. 682, pp. 53 – 65, 2012.

[7] G. Ning, R. White, and B. Popov *Electrochimica Acta*, vol. 51, no. 10, pp. 2012–2022, 2006. cited By 109.

[8] I. J. Cutress and R. G. Compton *Journal of Electroanalytical Chemistry*, vol. 643, no. 1, pp. 102–109, 2010.

[9] L. K. Bieniasz, O. Østerby, and D. Britz *Computers & Chemistry*, vol. 19, no. 2, pp. 121 – 136, 1995.

[10] Y. Zhang, J. Cohen, and J. D. Owens *ACM Sigplan Notices*, vol. 45, no. 5, pp. 127–136, 2010.

[11] Z. Wei, B. Jang, Y. Zhang, and Y. Jia *Procedia Computer Science*, vol. 18, pp. 389 – 398, 2013. 2013 International Conference on Computational Science.

[12] M. Giles, E. László, I. Reguly, J. Appleyard, and J. Demouth in *Proceedings of the 7th Workshop on High Performance Computational Finance*, pp. 1–8, IEEE Press, 2014.

[13] N. Sakharnykh in *NVIDIA GPU Technology Conference, San Jose, CA, United State*, 2009.

[14] R. G. Compton and C. E. Banks, *Understanding Voltammetry (2nd Edition)*. Imperial College Press, 2011.

[15] J. Heinze *Journal of Electroanalytical Chemistry and Interfacial Electrochemistry*, vol. 124, no. 1, pp. 73–86, 1981.

[16] J. Crank and P. Nicolson in *Mathematical Proceedings of the Cambridge Philosophical Society*, vol. 43, pp. 50–67, Cambridge Univ Press, 1947.

[17] I. Lindemuth and J. Killeen *Journal of Computational Physics*, vol. 13, no. 2, pp. 181–208, 1973.

[18] E. Kätelhön and R. G. Compton *Analyst*, vol. 140, pp. 2592–2598, 2015.

# Chapter 4

# Diffusion in the stochastic limit - application for the impact method

This chapter investigates the diffusional impacts of particles on an electrode surface. The probability expressions for the average number of impact events on a surface are established using Fick's diffusion in the limit of a continuum flux. The number and the corresponding variance are calculated for the case of nanoparticles impacting on an electrode at which they are annihilated. Random walk simulations confirm that the variance follows a Poisson distribution for ultra-dilute and dilute solutions. The analytical expressions provide a straightforward way to predict the stochastics of impacts in a 'impact' experiment (also known as the 'nano-impatct' method) by using Fick's second law and assuming a continuum dilute flux. Therefore, the study's results are applicable to practical electrochemical systems where the number of particles are very small. Moreover, the presented analytical expression for the variance can be utilised to identify effects of particle inhomogeneity in the solution and is of general interest in all studies of diffusion processes towards an absorbing wall. This work, carried out in collaboration with Dr. E.

Kätelhön, Dr. C. Batchelor-McAuley, and Dr. K. Tschulik, and has been published in 'The Journal of Physical Chemistry C'[1].

## 4.1 Introduction

The detection of nano-particles is a rapidly growing area with implications for environmental, technological, and fundamental studies. The extensive use of nanoparticles in medicine, electronics and energy production as well as in the food and textile industries has vastly increased the demand for tracking and identifying the inevitable release of nanoparticle materials into the environment, and this is especially important since concerns have been raised regarding the possible toxicity of various nanoparticles towards humans[2,3]. Beyond analytical use, in both fundamental research and materials synthesis, understanding mechanisms that involve nanoparticles and their properties is critically required to sense and analyse them[4–9].

The electrochemical 'nano-impact' detection methodology has significant advantages over other techniques, including the ability to directly measure nanoparticles in-situ without the need for drying or modifying the solution[10]. In an electrochemical cell, nanoparticles diffuse freely and even at ultra-low concentrations can be detected via their random impacts on the electrode surface facilitated through Brownian motion[11]. When an impact occurs, an electrochemical reaction with a corresponding Faradaic current is measured, providing direct information about the individual nano-particle size. The statistical average number of impacts/hits[1] as a function of time can be described by Fick's diffusion equation allowing the concentration of nanoparticles in the sample to be in-

---

[1] Often the terminology for events of meeting a boundary/target due to diffusion is referred to as a 'hit' or 'passage'. Therefore, in the following I use the term 'hit' rather than 'impact' in most cases. However, when directly referring to the nano-impact method, the term 'impact' is also mentioned.

ferred[12]. With the increased accessibility of more sensitive potentiostats (high signal to noise ratio), and better understanding of the nano-particle role in electrochemical systems, the 'nano-impact' method has proved to be a valuable practical detection method for a range of particle sizes and various types of nanoparticles[12–14], organic molecules[15,16], and biomolecules[6,17]. Additionally, it provides fundamental understanding of chemical mechanisms[9,18,19], information about aggregation and agglomeration[9,20,21], and lately, the possibility of nano-particle detection at ultra-dilute concentrations, in the sub-pico-molar region[22].

The lower limit of detection in ultra-dilute nanoparticle solutions is experimentally constrained to situations in which a tiny number of impacts on the electrode are detected over an experimentally viable time-scale. Moreover, experiments with small data sizes exhibit deviations from the statistical average as described by Fick's diffusion equation. The magnitudes of these deviations are dependent upon the cell set-up, the sample concentration, the shape or size of the detecting electrode, and the nanoparticle of interest[22]. Physically, this deviation from Fickian behaviour occurs by virtue of the breakdown of continuous theory approximation inherent in Fick's second law. I expand the discussion on the application of Fick's second law in the transition between continuous and non-continuous media in the Appendix to this chapter.

In ultra-dilute media, the solution no longer behaves as a continuous media and instead of describing the space through an average concentration or concentration profile, probability density functions need to be introduced[23,24]. Evaluating expressions for the probability of an impact allows the determination of the expected deviation in the impact frequency, and is thus essential for the interpretation of analytical results in the 'nano-impact' method at various experimental set-ups. Additionally, comparisons between the theoretically expected variance and experimentally obtained measurements can be utilised to estimate the uncertainty in the concentration or the inhomogeneity of the nano-particle solution.

The 'nano-impact' method is a diffusion process towards an absorbing wall, and might be modelled with a continuous media approximation (see also Appendix), where it is reasonable to describe the system with a concentration, or as a non-continuous media at ultra-low concentrations, where stochastic processes occur and probability density needs to be introduced. Hence, the present study is important for understanding this system. Furthermore, there is a more general interest in such fundamental studies of the flux in Fickian diffusional processes. Fick's diffusion equation provides a practical way to mathematically describe the average number of many hits on an absorbing wall in the case of free diffusion. Therefore, Fick's second law is widely applicable to many systems, even for a very small diffusional flux. Among others, it is used to study the electrochemistry of small amounts of molecules[25–29], the growth of small particles[30,31], and diffusion towards a biological target[32]. However, since the obtained results are sensitive to the size of the absorbing wall and to the concentration, understanding the limitations of and the deviations from Fick's second law is critical. Moreover, using analytical expressions for the determination of the stochastic number of hits on an absorbing wall has an important practical advantage over computational stochastic methods such as random walk simulations: The analytical assessment provides a straight-forward way to analyse and predict experimental results, whilst random walk simulation is time consuming and computationally costly, especially in two or more dimensional coordinates[24].

Previous works in electrochemistry that focused on small amounts of molecules compared stochastic and statistical processes for single molecules[26], and for small current responses[27,33]. Recently, Boika and Bard[34] showed numerical simulation of first passage times of micro electrodes in ultra-dilute solutions. However, for the nano-impact method, it is required to find a practical method to derive probability expressions and the corresponding variance in order to study the influence of particle concentration and electrode shape or size on the analysis.

In this chapter, the stochastics of ultra dilute solutions (pM-fM) is investigated, where a very small but sufficient number of particles ($N_0 \gg 1$) are randomly distributed and independently diffuse in the cell. Fick's second law of diffusion is used to derive general expressions for the average number of impacts/hits and for the deviation from this average. These expressions are explicitly evaluated for the two representative and important cases of a macro electrode and for diffusion to a micro-sphere. The macro electrode represents the linear diffusion regime which is inherent to any large electrode or short time scale of electrochemical experiments. The micro sphere is a representative symmetric case, where a full convergent (radial) diffusion is obtained that results in enhanced mass transport as compared to the linear case. The difference between the cases of linear and convergent (radial) diffusion are explained and random-walk simulations are employed to support analytical expressions for the average number of hits in the case of linear diffusion regime.

## 4.2 Theory

The study is divided into the cases of (*i*) linear and (*ii*) convergent diffusion regimes. Both cases are investigated by starting with the Fick's diffusion equation:

$$\frac{\partial c}{\partial t} = D\nabla^2 c \tag{4.1}$$

where $c$ is the concentration and $D$ is the diffusion coefficient, and use the analytical solutions in one-dimensional linear and radial spaces[35,36]. Linear diffusion represents the case of semi-infinite diffusion and corresponds to a planar electrode in an infinite-sized cell. Radial diffusion represents the case of diffusion towards a finite-sized spherical electrode. Comparison calculations of the impact/hit probability for different electrode sizes and concentrations are provided. Additionally, in order to support the presented probability function and its variance, results of one-dimensional random walk simulations are shown in this study.

### 4.2.1 Linear diffusion - Macro-sized absorbing wall

For full and irreversible absorption, the continuous one-dimensional solution of Fick's second law gives the time dependent concentration profile as a function of the distance from the absorbing wall:

$$c(x,t) = c^{*}\mathrm{erf}(\frac{x}{2\sqrt{Dt}}) \tag{4.2}$$

which solves (eq. 5.1) with respect to the boundary conditions:

$$c(x=0, t \geq 0) = 0 \quad c(all\, x, t < 0) = c^{*}$$

$$c(x = \infty, t \geq 0) = c^*$$

where $c^*$ is the bulk concentration. For simplicity, the number concentration ($entities/m^3$) is used along this study. The flux towards the absorbing wall, which can for instance be a planar electrode, is then found by differentiation with respect to $x$ at $x = 0$:

$$j = -D\frac{\partial c}{\partial x}\bigg|_{x=0} = \frac{c^*\sqrt{D}}{\sqrt{\pi t}} \tag{4.3}$$

which is the Cottrell equation[37].

The conventional representation of Fick's second law as being applied to concentrations is meaningful in most chemical systems. However, the concentration which is defined as the number of entities per volume, can also be interpreted as the probability of finding an entity in space[38]. The underlying principle that allows such probability studies is the fact that the Brownian motions of different molecules or particles are independent of each other, as their diffusion is only caused by collisions with the fluid[38]. This principle enables us to find the probability of an individual particle hitting the absorbing wall, which can also be interpreted as an impact on an electrode surface. Using the summing rule of probabilities, the probability of $N_0$ particles hitting the absorbing wall as function of time is obtained.

The probability density ($p$) can be defined on all space ($x = 0$ *to* $\infty$) to be the probability of finding unity particle density in a one-dimensional space with length $L$ and at the initial time ($t_0$):

$$p^*(t_0) = \frac{1}{L} \quad 0 \leq x < \infty \tag{4.4}$$

$$p^*(t_0) = 0 \quad x < 0$$

Since this expression is a one-dimensional uniform probability density, $p$ has the units of $m^{-1}$. Substituting $p$ into Fick's second law, the probability density profile and probability density flux at $x = 0$ of a single particle are given by:

$$p(x,t) = p^*(t_0)\mathrm{erf}(\frac{x}{2\sqrt{Dt}}) = \frac{1}{L}\mathrm{erf}(\frac{x}{2\sqrt{Dt}}) \tag{4.5}$$

$$-D\frac{\partial p}{\partial x}\bigg|_{x=0} = \frac{p^*(t_0)\sqrt{D}}{\sqrt{\pi t}} = \frac{1}{L}\frac{\sqrt{D}}{\sqrt{\pi t}} \tag{4.6}$$

In the following, these two representations of the probability density function (eq. 4.5) and the probability density flux (eq. 4.6) are investigated to obtain an expression for the probability of a single particle hitting the absorbing wall. For the first representation, the probability density function is illustrated in figure 4.1a. Integration of $p(x,t)$ over $x$ yields the cumulative function density (CFD) which at $t_0$ equals the integration over $L$ and therefore, equals 1. At $t > 0$ the probability density along $x$ provides the fraction of the probability density that 'survived' at the time $t$. Thus, the complementary function of the 'CFD' presents the fraction of particle that absorbed (see figure 4.1). The hit-probability

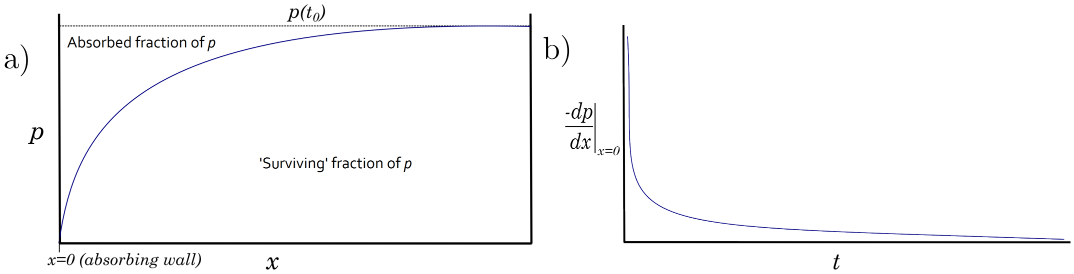

Figure 4.1: Illustration of the two representations of Fick's solution. a) The probability density functions along $x$ shows the surviving fraction and the absorbed fraction of particles. b) The flux probability density towards a fully absorbing wall (i. e. an electrode with the boundary condition, $c = 0$ at $x = 0$).

as a function of time is hence equal to:

$$p_{hit}(t) = \int_0^\infty \frac{1}{L} - \frac{1}{L}\mathrm{erf}(\frac{x}{2\sqrt{Dt}})dx \tag{4.7}$$

It is possible to integrate to infinity rather than to $L$ as $L$ is considered to be large but constant. This will be addressed below in the random-walk calculation. However, it is important to clarify that the probability density $1/L$ provides the average number of particles in a length $L$. The integration to infinity solves this general case for a constant probability density, and the application of this integral to experimental systems, therefore holds true as long as $L \gg 2\sqrt{(}Dt)$. The integral can be solved by substitution of the variable $x$:

$$z = \frac{x}{2\sqrt{Dt}}, \quad \int_0^\infty 2\sqrt{Dt}\frac{1}{L}\mathrm{erfc}(z)dz = \frac{1}{\sqrt{\pi}}\frac{2\sqrt{Dt}}{L} \tag{4.8}$$

Therefore,

$$p_{hit}(t) = \frac{2\sqrt{Dt}}{\sqrt{\pi}L} \tag{4.9}$$

The same conclusion can be achieved by using the Cottrell equation which is a representation of the flux at the boundary of the absorbing wall. Equation 4.6 describes the flux of the probability density at this boundary as a function of time. This provides the ‘amount of probability’ that dissipates at the absorbing wall per time, as plotted in figure 4.1b. Hence, integrating over time equally gives the hit probability (in dimensionless unit):

$$p_{hit}(t) = \int_0^t -D\frac{\partial p}{\partial x}dt = \int_0^t \frac{1}{L}\frac{\sqrt{D}}{\sqrt{\pi t}}dt = \frac{2\sqrt{Dt}}{\sqrt{\pi}L} \tag{4.10}$$

where $1/L$ is assumed to be constant over time as is discussed later.

It is observed that the integration of the flux over time gives the same result as the integration of the complementary CDF of the probability density over space. This identity is given as:

$$-\int_0^t D\frac{\partial p}{\partial x}dt = \int_0^\infty (p^*(t_0) - p)dx \tag{4.11}$$

and follows from mass conservation, and therefore also obeys Fick's 2nd law.

Using the summing rule of probabilities, the cumulative number of hits can be found by multiplying the probability of a unity particle density hit by the number of particles in one dimensional space ($p_{hit} \times N_0$). The expression for the one-dimensional case can be extended to a volumetric concentration in a cell with a planar electrode, by integrating the probability density of finding a particle in a volume above the surface area of the electrode (the absorbing wall):

$$N_0 \times p(x, t_0)(m^{-1}) = N_0 \times p(x, y, z, t_0)(m^{-3})) \int\int_A dA = c^*A \tag{4.12}$$

where $A$ is the area of the absorbing wall, $c^*$ is the concentration in number per unit volume ($N_0\, m^{-3}$). In other words, since the probability density solely depends on the distance from the surface, the probability of finding a particle in a volume that contains $N_0$ particles is $N_0/L$ in all space, and thus the cumulative number of hits (see table 4.1) on the wall as a function of time can be rewritten as:

$$\hat{N}_{hits}(t) = \frac{2N_0\sqrt{Dt}}{\sqrt{\pi}L} = \frac{2c^*A\sqrt{Dt}}{\sqrt{\pi}} \tag{4.13}$$

Table 4.1 summarises the relevant parameters.

| Symbol | Semantics | Description |
|---|---|---|
| $p^*(t_0)$ | Initial probability density (constant) $[m^{-1}]$ | Probability of finding particle in position x, at initial time $t_0$. |
| $p^*(r,t_0)$ | Radial initial probability density $[m^{-1}]$ | Probability of finding particle in radius r, at initial time $t_0$. |
| $p(x,t)$ | Probability density $[m^{-1}]$ | Probability of finding particle in position x, within the time t. |
| $p_{hit}(t)$ | Hit probability | Probability of one particle hitting the wall at time t. |
| $\hat{N}_{hits}(t)$ | Cumulative number of hits | The average accumulated number of hits from $t_0$ to $t$. |

Table 4.1: Definitions

The hit probability can be used to calculate the variance via the binomial distribution:

$$var(t) = N_0 p_{hit}(1 - p_{hit}) \tag{4.14}$$

where $p_{hit}$ is a probability of an independent event in a sample size of $n$.

Therefore, in this model the variance is given as:

$$var(t) = N_0\left[\frac{2\sqrt{Dt}}{L\sqrt{\pi}} - \frac{4Dt}{L^2\pi}\right] \tag{4.15}$$

The assumption that $L \gg \sqrt{4Dt}$ in practical experiments allows us to neglect the second term in the binomial variance which results in the Poisson limit and since the hit probability is low relative to the amount of particles in solution, and the distribution adopts the form of a Poisson distribution:

$$var(t) = N_0 p_{hit} = N_0\frac{2\sqrt{Dt}}{L\sqrt{\pi}} \tag{4.16}$$

It is later shown that random walk simulations for the linear case support the Poisson distribution for rare events out of large possibilities. It is noted that introducing statistical variance by applying mean probability is legitimate as long as there are sufficient particles ($N_0 \gg 1$). For a very few number of particles ($N_0 \sim 1$) in a very large cell, the probability of a hit cannot be considered Poisson and the distribution is related to the solution of a first passage time problem of a random walker[24,38–40].

Here, in a large number of particles ($N_0 \gg 1$), the corresponding estimated average first passage time [2] described as $T_1$, which defines the time until the first hit is expressed through

$$\hat{N}_{hit}(T_1) = 1 = \frac{2N_0\sqrt{DT_1}}{\sqrt{\pi}L} \tag{4.17}$$

This leads to an estimation of $T_1$ in the linear case to be:

$$T_1 = \frac{\pi L^2}{4DN_0^2} = \frac{\pi}{4D(c^*A)^2} \tag{4.18}$$

This type of square dependence on the concentration was also found for DNA transcription in a one-dimensional model by Socolov et al[32] who found the calculated mean first passage time for a boundary condition of first order kinetics. Note that here only a practical estimation is provided, see chapter 6 for more details about the calculation of the mean first passage time.

### 4.2.2 Validation using the 'random-walk' method

Examining the probability expression for the case where only one particle is present in a length $L$, it is found that the hit probability exceeds unity at a certain time, $t$:

$$p_{hit}(t) = \frac{2\sqrt{Dt}}{\sqrt{\pi}L} \tag{4.19}$$

---

[2] In chapter 4 and 5 I refer the 'estimated' average first passage time - the average time of one impact. The conventional definition of first passage time is used in chapter 6.

This is due to the fact that the integration over infinite distance allows particles in an initial distance greater than $L$ to reach the wall. However, in real cells and typical experiments, the following approximation holds true:

$$L \gg \sqrt{Dt} \tag{4.20}$$

This requirement equally applies to the Cottrell equation (chapter 1). However, in order to fully justify the expression for a real application in terms of the duration of experiment and the size of the cell, the result can be probed using a 'random walk' study. One-dimensional random walk simulations at dilute concentrations were performed to provide a verification of the probability expression and to validate the variance in the Poisson limit.

The random walk algorithm uses the Mersenne Twister pseudo random number generator[41]. A temporal step walk of $5 \cdot 10^{-4} s$ was chosen for two concentrations: $1.9 \cdot 10^{6}$ particles and 190 particles in 1mm length, corresponding to 0.1pM and 0.1fM concentrations. Representative diffusion coefficient of $D = 10^{-10} m^2 s^{-1}$ is used. The results are presented and discussed later in this chapter (in the discussion section).

### 4.2.3 Convergent (radial) diffusion - absorbing sphere

In a 'nano-impact' experiment, the size of the electrode must be small in order to minimize the occurrence of simultaneous impacts on the electrode and to reduce the capacitive noise so as to facilitate small charge measurements. Therefore micron-sized electrodes are commonly employed. Using Fick's second law, the concentration near a spherical fully absorbing wall follows[35,36]:

$$c(r,t) = c^* \left[1 - \frac{r_s}{r}\text{erfc}(\frac{r-r_s}{\sqrt{4Dt}})\right] \tag{4.21}$$

where $c^*$ is the bulk concentration and $r_s$ is the radius of the sphere. This concentration function can be used to determine the probability density of finding a particle in the distance $r$ from the centre of an absorbing sphere:

$$p(r,t) = p^*(r,t_0)\left[1 - \frac{r_s}{r}\text{erfc}(\frac{r-r_s}{\sqrt{4Dt}})\right] \tag{4.22}$$

For radial coordinates, the probability density of finding a particle in a radius $r$ at initial time is:

$$p^*(r,t_0) = 4\pi r^2 / V_{r_s \to R} \tag{4.23}$$

where $V_{r_s \to R}$ is the constant volume of the cell with a large radius $R$, excluding the volume of the absorbing sphere. The flux probability density at $r = r_s$ is then calculated as:

$$-D\frac{\partial p}{\partial r}\bigg|_{r_s} = p^*(r_s,t_0)D\left[\frac{1}{\sqrt{\pi Dt}} + \frac{1}{r_s}\right] \tag{4.24}$$

The flux equation consists of two terms. The first term corresponds to linear diffusion and the second term defines the constant flux of radial diffusion. At large $t$, the diffusional flux converges to the second term. It was shown earlier that is necessary to integrate either the probability or the flux probability density. The integration of both expressions gives:

$$p_{hit}(t) = \int_0^t -D\frac{\partial p}{\partial r}\bigg|_{r=r_s} = \int_0^\infty (p^*(r,t_0) - p(r,t))dr = \frac{4\pi r_s^2}{V_{r_s \to R}}\left[\frac{2\sqrt{Dt}}{\sqrt{\pi}} + \frac{Dt}{r_s}\right] \tag{4.25}$$

Note that in spherical coordinates, the probability of finding the particle is normalized from the three dimensional sphere volume to the spherical coordinate in one dimension (the integration over the area as done in the one dimensional linear case is inherent in the normalization). Thus, in order to find the cumulative number of hits in $N_0$ particles for three dimensional space, the sum rule of probability can be used:

$$\hat{N}_{hits}(t) = N_0 \times \frac{4\pi r_s^2}{V_{r_s \to R}} \left[ \frac{2\sqrt{Dt}}{\sqrt{\pi}} + \frac{Dt}{r_s} \right] = 4\pi r_s^2 c^* \left[ \frac{2\sqrt{Dt}}{\sqrt{\pi}} + \frac{Dt}{r_s} \right] \tag{4.26}$$

which results in the cumulative number of hits (average number of hits) as function of time:

$$\hat{N}_{hits}(t) = c^*(8r_s^2\sqrt{\pi Dt} + 4r_s\pi Dt) \tag{4.27}$$

In the case of small spheres the second term in the brackets dominates and the cumulative hits probability increases linearly with time. For large spheres the first term dominates and shows similar behaviour to the linear regime. The two components (the first and second term of the cumulative hits) can be treated separately. The variance of the first term as described in the linear regime, can be calculated through Poisson statistics. The second term, which describes the integration of the total flux obeys the physical model of 'shot' noise[33,42]. The 'shot' noise arises as a consequence of rare events in the Poisson limit, so that its variance follows a Poisson distribution:

$$var(t) = N_0 p_{hit} = \hat{N}_{hits}(t) = 4\pi r_s^2 c^* \left[ \frac{2\sqrt{Dt}}{\sqrt{\pi}} + \frac{Dt}{r_s} \right] \tag{4.28}$$

In the next section, the results of the probability expressions are discussed for the two cases as a function of the electrode/wall size, the concentrations, and the first passage time. The result of the 'random walk' simulations are also provided with the analytical expression for the linear case and probe the validity of the derived standard deviation for practical nano-impact experiments. Since the Poisson limit can be deduced from the linear case and the 'shot-Noise' model, a random walk simulation in radial coordinates is considered unnecessary for this study.

The discussed expressions for the cumulative number of hits in 'nano-impacts' experiments quantify fluctuations in a dilute continuum flux under Fickian diffusion. It should be noted that these expressions for the cumulative number of hits and the average first passage time are not related to the classic Pólya phenomena of small discrete sets of random walkers[24,43].

## 4.3 Discussion

### 4.3.1 Linear diffusion regime

The theoretical and simulations results of the cumulative number of hits on an electrode (wall), in a $1mm^2 \times 1mm$ cylinder are compared. Herein, a representative aqueous-media diffusion coefficient of $10^{-10}m^2s^{-1}$ is used. Figure 4.2 shows profiles for the cumulative number of hits, for four concentrations in the range of 1pM−0.1fM. The respective standard deviations ($\sqrt{var(t)}$) are also shown.

Figure 4.2 shows that above 1fM, many hits/impacts are observed during the time of experiment, which leads to Fickian behaviour. Below 0.1fM, the variance becomes significant and large deviations from the predicted number of hits are observed. Figure 4.3 shows a comparison between three different macro-sized walls ($3mm$, $1mm$, $0.5mm$) at a concentration of 0.1fM, the length of the cylinder is $1mm$ for all cases. It can be seen

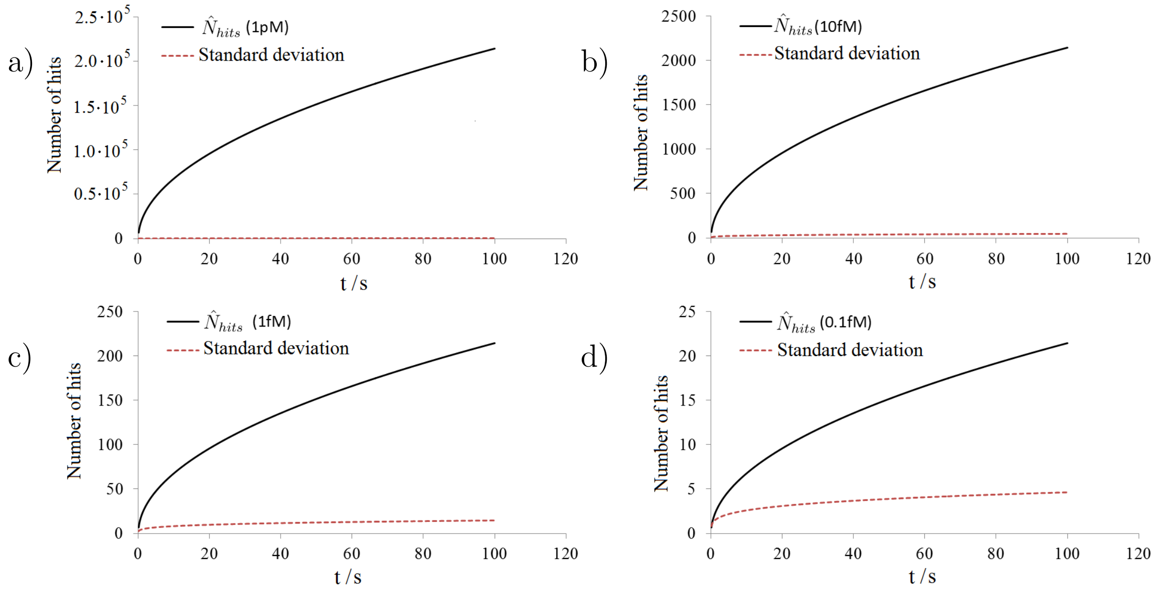

Figure 4.2: The cumulative number of hits and respective standard deviations as a function of time for various concentrations: a) 1pM, b) 10fM, c) 1fM, d) 0.1fM.

that by increasing the radius of the electrode from $1mm$ to $3mm$ the deviation becomes negligible. However, at a $0.5mm$ radius the standard deviation becomes significant, and the number of hits gets smaller, around 60 hits in 100 seconds.

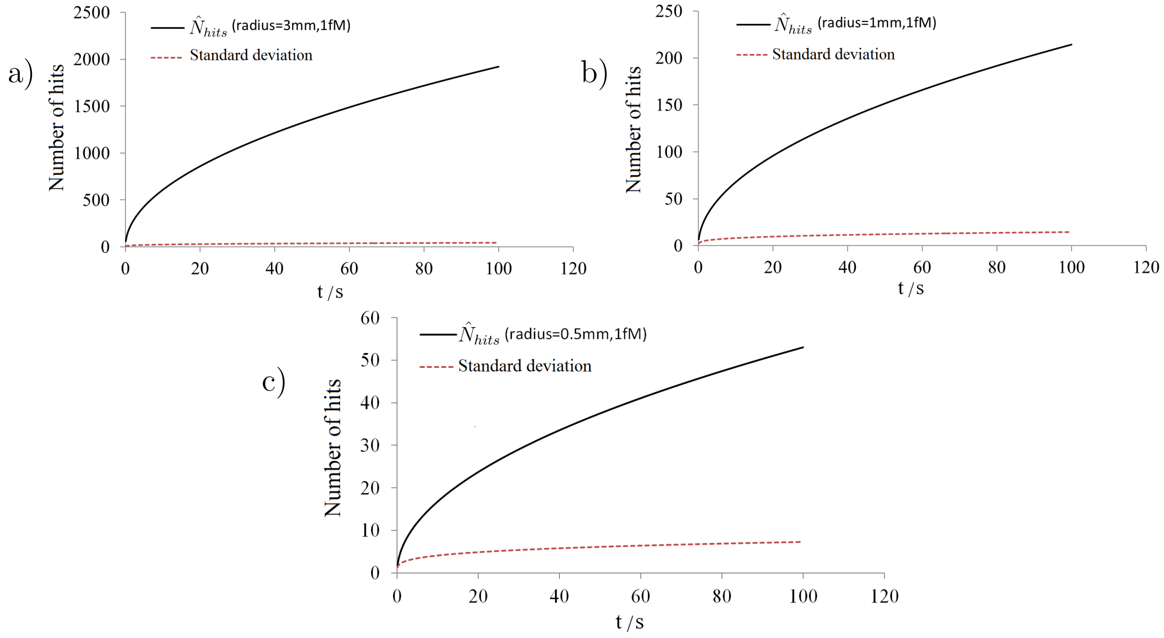

Figure 4.3: The cumulative hits (solid black line) as function of time for various radii: a) 3mm b) 1mm, and c) 0.5mm. The calculated standard deviation is provided in the red-dash line. $c = 1$fM.

Therefore, from figures 4.2 and 4.3, and from equations 4.13 and 4.15, it can be concluded that as the concentration decreases a linear decrease in the number of impacts occurs alongside a square root proportion for the deviation from the prediction. The same behaviour holds true for the electrode area, $A$, but subject to linear diffusion. The use of small electrodes and dilute solutions allows detection of impacts of individual particles. Hence, the first passage time is a crucial parameter for understanding the limit of detection. This is due to the fact that even in a case of a few expected impacts (which would yield large deviation), summing the number of impacts from $n$ repeated experiments minimizes the standard deviation by $\sqrt{n}$ (for the same reason that $N \times c^*$ and $N \times A$ reduce the standard deviation by $\sqrt{N}$). For this reason, the estimation of the first passage time gives an indication for the lower limit of concentration that can be used in experiments. Figure 4.4 shows the first passage time (first hit) at various radii. It can be seen that using a 0.1fM concentration often results in no impacts within the duration of a typical nano-impact experiment, which is in the range of few seconds to 1-2 minutes.

### 4.3.2 'Random-walk' study

Next the results of one dimensional random walk simulations are considered in a dilute solution (0.1pM) and in an ultra-dilute solution (0.1fM). Figure 4.5a shows the cumulative number of hits of a 0.1pM solution of randomly distributed particles in a cylindrical volume with a radius and a length of $1mm$ ($1.9 \cdot 10^6$ particles) within 100s in comparison with the analytical result. It can be seen that the analytical expression exactly predicts the result of the random walk simulation. Hence the random walk simulation confirms the validity of the hit probability expression and the approximation of $L \gg \sqrt{Dt}$ under realistic

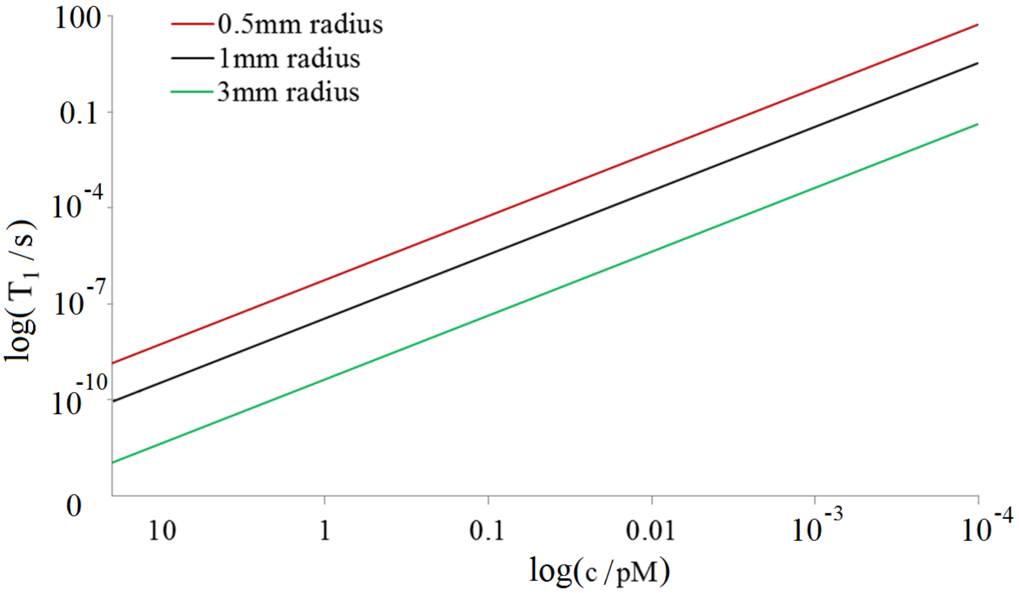

Figure 4.4: First passage time in linear diffusion regime as function of the particle concentration at various radii of absorbing wall: 3mm, 1mm, and 0.5mm (logarithmic scale).

experimental conditions.

Figure 4.5b provides a closer examination of the difference between the two curves, the hit probability and the random walk simulation. Since the deviation does not increase with time during the 100s, the boundary at $x = L$ is considered to be distant enough to be meaningful and thus allows the integration over space to infinity in the hit probability expression (eq. 4.7).

Moreover, figure 4.5b shows that the observed standard deviation is bounded within the calculated one-standard deviation, hence supporting the use of the Poisson limit. However, since many hits are observed in 0.1pM solution, the deviation is negligible and in order to examine the variance in the limit of detection, much lower concentrations should be considered. Therefore, an additional set of random walk simulations at ultra dilute solutions (0.1fM) was carried out to examine the cumulative number of hits and the variance observed.

Figure 4.6 shows the first 4 runs out of 400, providing a qualitative comparison between

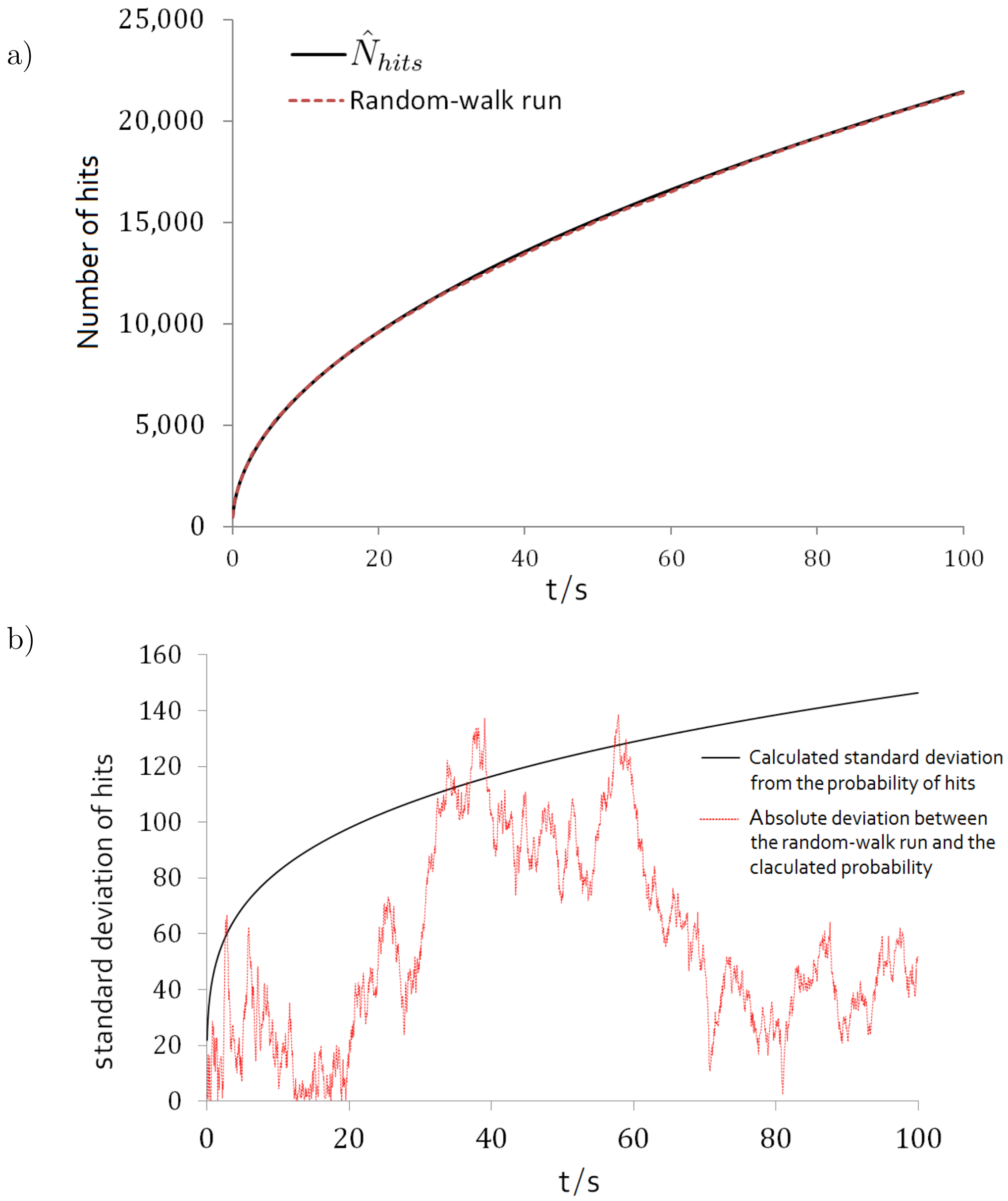

Figure 4.5: a)'Random-walk' simulation (dash red line) and hits probability expression (solid black line) as function of time. b) The calculated standard deviation from the hits probability (solid black line) and the absolute deviation between the random-walk simulation and the cumulative hits analytical expression(red dash line), $\sqrt{N_{analytical} - N_{simulation}}$. $c = 0.1pM$, $L = 1mm$.

the analytical hits probability and the random walk study. It shows that the analytical hits probability provides a good prediction at ultra-low concentrations, where only few hits are expected. The comparison also shows that the observed number of hits follows the calculated standard deviation over time. More statistical information is presented in figure 4.7 that shows 400 runs of the random walk simulation. The histograms show the

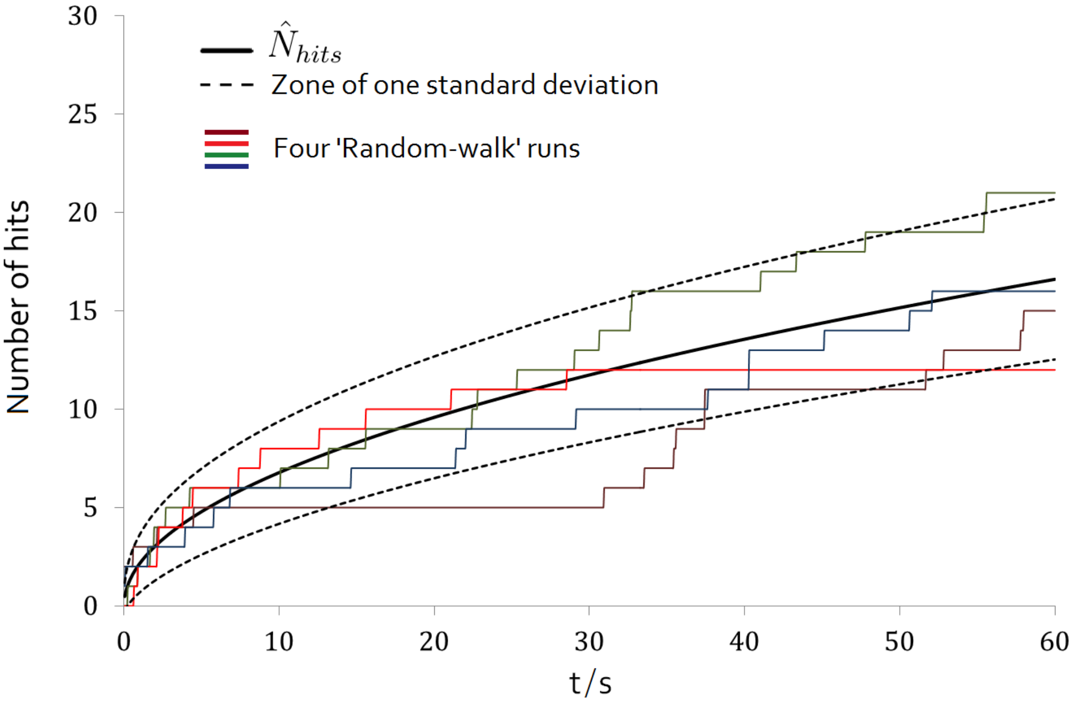

Figure 4.6: Random walk curves of 4 runs. The cumulative number of hits calculated from the analytical expression is plotted (solid black lines), as well as the zone of $+/-$ one standard deviation (dash black line). $c = 0.1fM$, $L = 1mm$.

distributions of the number of hits at specific times: 5s, 10s, and 100s. A clear match with the Poisson limit was observed at all times. At large times, when a large number of hits is expected, the Poisson distribution can also be approximated by a normal distribution. Note that the analytical expression for the hits probability at times 5s. 10s, and 100s yields the average number of hits, 5.2, 7.4, and 23.4, respectively. These values match well the mean of a Poisson distribution ($mode$ and $mode + 1$) fits; 5-6, 7-8, and 22-23 hits. The analytical expression for the variance provide a straightforward way to analyse nano-impact experiments beyond finding an unknown concentration or size distribution. The variance can be utilised to identify effects such as agglomeration and aggregation, or solution inhomogeneities by comparing the variance sampled in the experiment to the calculated variance of an ideal dispersed solution.

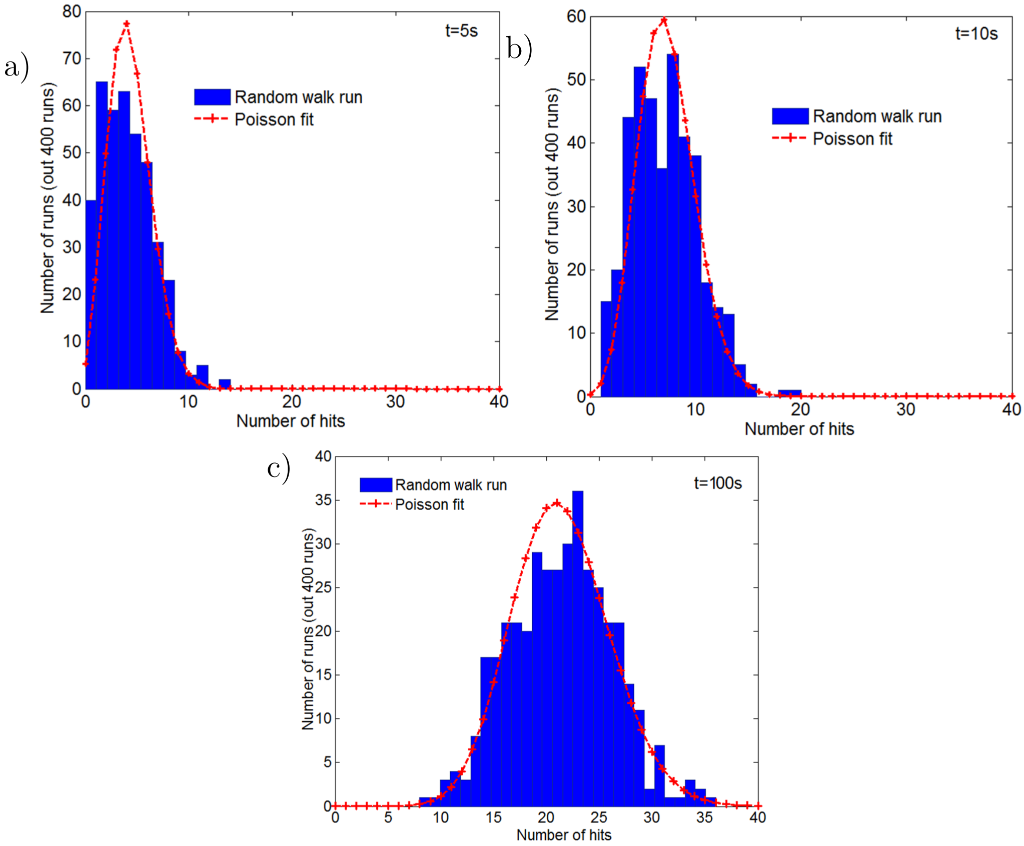

Figure 4.7: Distribution of the number of hits in 400 Random-walk runs at (a)t=5s, (b)10s, and (c)100s. The Poisson fits are plotted in the red dashed line.

### 4.3.3 Convergent (radial) diffusion regime

The results of the linear diffusion case, corresponding to macroscopic electrodes, showed that even at ultra-dilute concentrations, impacts might be detected. However the level of capacitive noise increases with area[44] and thus nano-impact events are commonly experimentally detected using micron-sized electrodes. Since $\hat{N}_{hits}(t)$ (eq. 4.27) depends on the surface area of the electrode/absorbing wall, the results change dramatically in the case of radial diffusion. Figure 4.8 shows the cumulative number of hits and the standard deviation in the case of a sphere of $1\mu m$ for various concentrations. It can be seen that the second term $4c^{*}r_s\pi Dt$ in eq. 4.27, is dominant on the time scale of the experiment and causes a linear increase in the number of hits. Moreover, the low number of hits

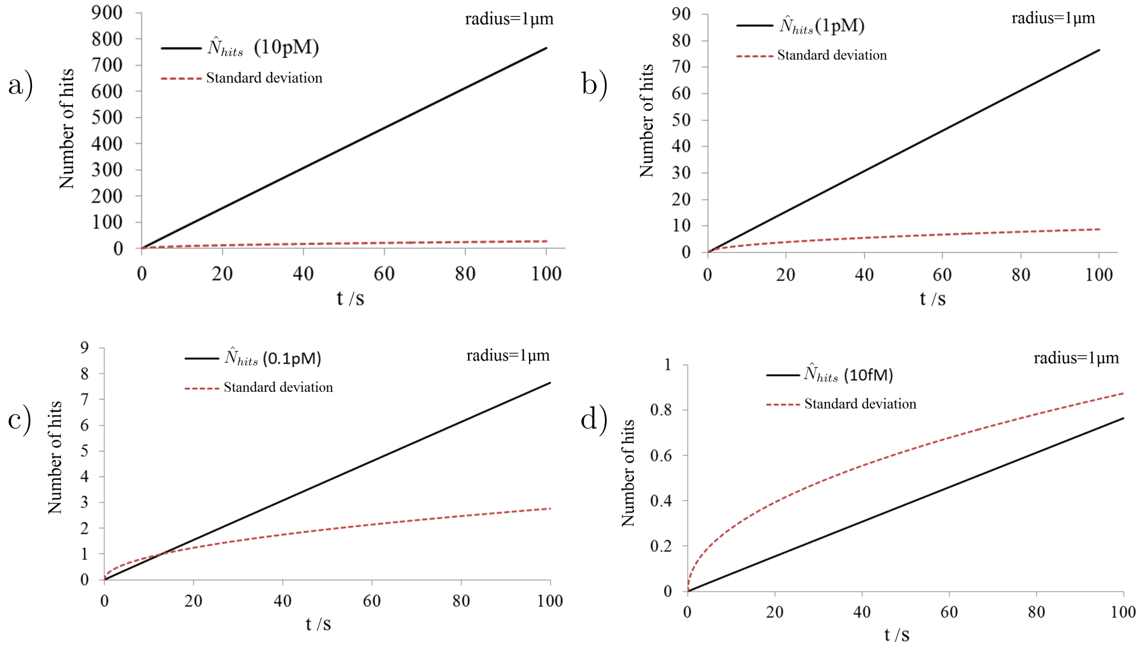

Figure 4.8: The hits probability (solid black line) as function of time for various concentrations: a)10pM, b) 1pM, c) 0.1pM and d) 10fM. The calculated standard deviation is shown by a red-dashed line. $(r_s = 1\mu m)$

implies that even at 1pM the standard deviation of the cumulative number of impacts is significant and at 10fM less than one hit is observed during 100 seconds.

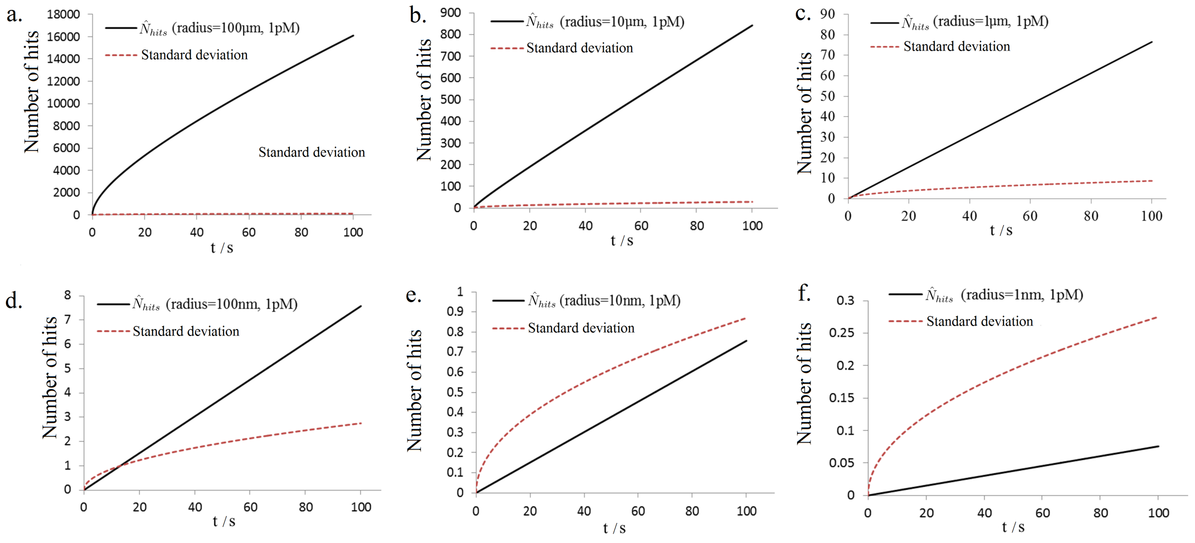

Figure 4.9: The hits probability in radial diffusion (solid black line) as function of time for various radii: a) $100\mu m$ b) $10\mu m$, c) $1\mu m$, d) $100nm$, e) $10nm$, and f) $1nm$. The calculated standard deviation is provided through the red-dash line. The particle concentration is $c =$1pM.

The effect of the sphere size (absorbing wall) is presented in figure 4.9. The hit probability is plotted for various sizes ranging from $100\mu m$ to $1nm$, in a solution of 1pM concentration. At large sizes, the number of hits is large enough to show negligible deviations from the expected cumulative frequency. The first term in the probability expression (eq. 4.27) is more dominant at the shorts times. For small spheres sizes, the number of hits over time decreases significantly, resulting in a large variance. It can be seen that below $1\mu m$, only a few hits are predicted and therefore the standard deviation becomes too large to obtain any meaningful information from a single experiment.

Finally, an estimation for the first passage time is presented for the convergent diffusion case. Equation (4.27) can be solved for the case of $\hat{N}_{hits}$ equals 1:

$$1 = c^*(8r_s^2\sqrt{\pi D T_1} + 4r_s\pi D T_1) \tag{4.29}$$

and figure 4.10 shows the first passage time ($T_1$) as function of the sphere size of an absorbing wall, for a particle concentration of 1pM (figure 4.10a) and as function of concentration (figure 4.10b) when the sphere size is $1\mu m$. This calculations show the importance of choosing the appropriate size of the electrode (figure 4.10a) in comparison with the concentration (figure 4.10b) of particles in the solution. The right balance between the solution concentration and the electrode size then allows the observation of a sufficient number of impacts for providing low variance. It can be seen that the first passage time increases linearly when the second constant term dominates (eq. 4.29) for small radii. Only when the radius of the absorbing sphere is large enough (figure 4.10a) does the dominance of the first term result in a larger gradient due to the non-linear proportion between radius and time (eq. 4.29). At large radii, $T_1 \propto 1/r_s^4$ and at small radii the linear diffusion term (first term) is negligible and thus $T_1 \propto 1/r_s$. Examining equation 4.29, at long times and for very small sphere sizes (steady state) the dependency of the first passage time is linear with concentration, as was shown in recent simulation studies by Boika and Bard[34]. However, from the analytical expression (eq. 4.29) it is also shown that the first passage time at short times and for larger radii has the influence of the linear diffusion regime ($T_1$ has a squared dependency of concentration). It is also necessary to take into account the specific size of nanoparticles in solution, since this will change the diffusion coefficient and will have a significant effect on the average number of impacts, the variance and the first passage time, as is shown in equation 4.27. Additionally, in Nano-impacts experiments, other effects should be taken into account. Such as shielding effects on surfaces, blocking species on the electrode, hindered diffusion, and aggregation[12,13]. The contribution of these effects on the expected number of impacts can be significant as reported in the literature, and therefore, understanding the diffusion process is crucial to quantify these effects. Hence, the next chapter aims to study various

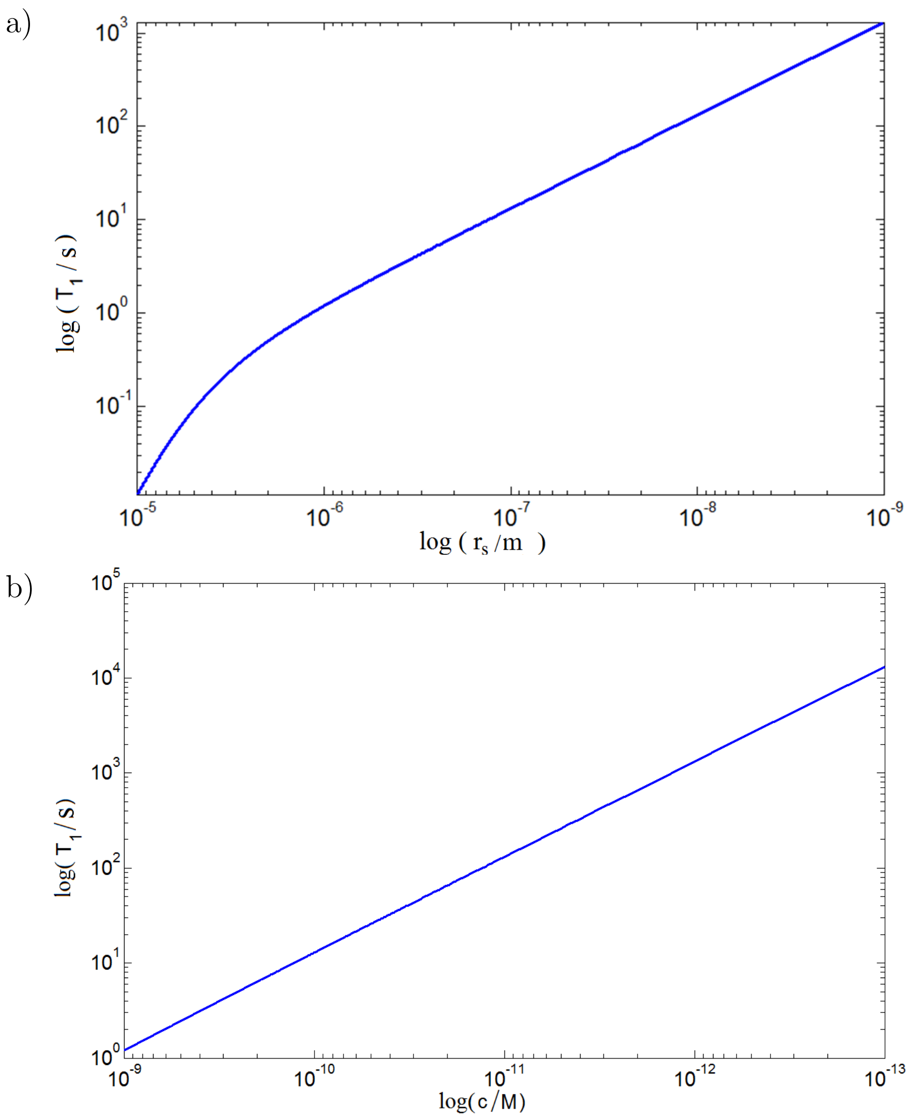

Figure 4.10: a) First passage time as a function of size of the absorbing sphere (also electrode) (logarithmic scale), $c$ =1pM. b) First passage time as a function of the concentration (logarithmic scale), $r_s = 1\mu m$.

geometries with more complex diffusion regimes but are used practically for nano-impact experiments; the micro-disc and the micro-cylinder.

## 4.4 Conclusions

Analytical expressions were derived for the average number of impacts in linear diffusion and convergent diffusion processes. The analytical expression shows the relation of the electrode area and the concentration to the number of impacts expected in nano-impact experiments. Random walk simulation confirms the analytical expression for linear diffusion, and shows that the variance accurately follows the Poisson limit for both dilute solution (0.1 pM) and ultra-dilute solutions (0.1 fM). It was found that even in the case of convergent diffusion towards a sphere, where there is a large increase in the number of hits/impacts due to efficient mass transport, the variance becomes significant for micro-sized electrodes and sub pM concentrations. The 'first passage time' was also estimated to provide a strong indication for the lower limit of detection in ultra-dilute solutions.

The analytical expressions provide a straightforward way to describe nano-impact experiments. Moreover, the calculated analytical expression for the variance can be utilised to identify solution inhomogeneities such as aggregation and agglomeration. Although this study is related to the 'nano impact' method, it further opens the opportunity to understand other diffusion mechanisms, where the variance in the Fickian diffusion is expected to be significant, such as in nano-growth[30,31] or in biological systems[32,45].

## 4.5 Appendix: Non-continuous media and the approximation of continuous media using Fick's second law

I further expand the discussion on the application of Fick's second law to continuous media and the origin of the deviation in non-continuous media. I begin with showing the solution of the diffusion equation for the stochastic case as it can be found in the literature[45,46](part A), then a short insight is provided to show how the Einstein solution can be related to Fick's second law and to this study (part B).

The importance of this appendix arises from the fact that probability density functions of individual particles as derived from Einstein's diffusion equation, are generally used in many fields of research for the calculation of diffusion problems. Therefore, the relation between the probability approach and Fick's second law is briefly emphasised in order to provide a clear explanation for the deviation of Fick's 2nd law in the non-continuous media. Fick's second law for one dimension is given by:

$$\frac{\partial c(x,t)}{\partial t} = D\frac{\partial^2 c(x,t)}{\partial x^2} \tag{4.30}$$

and Einstein's version of diffusion equation is:

$$\frac{\partial p_x(x,t|x_0,t_0)}{\partial t} = D\frac{\partial^2 p_x\left(x,t \mid x_0,t_0\right)}{\partial x^2} \tag{4.31}$$

**Part A**

It is important to note the logical difference between Fick's second law and Einstein's derivation. Whereas Fick's diffusion equation shows an approach for the determination of $p\ (x,\ \delta t)\ dx$, the *average number* of solute molecules in the interval $[x,\ x+\ dx]$ at a time $t$, Einstein determines $p_x(x{,}t\ \ |x_0{,}t_0)dx$, the *probability* that a *particular* solute molecule will be in the interval $[x,\ x\ +\ dx]$ at time $t$.[38]

When the diffusion of each individual part is taken into account, the stochastic solution of Einstein for many specific cases is based on Green functions and used to find the respective probability distributions in time and space for each particle. An appropriate numerical tool for solving stochastic problems is given by 'random walk' approaches or algorithms for the 'discrete stochastic approach'. However, the connection between Einstein and Fick can be shown directly, for example in a linear diffusion case with an absorbing boundary (one-dimensional half-space with full absorbing wall at $x = 0$).
Using Einstein diffusion equation (eq. 4.31), I consider a one-dimensional particle which diffuses freely in the presence of an absorbing wall at $x = 0$. The diffusion equation is solved with the initial condition:

$$p\,(x, t \to 0 \mid x_0, t_0) = \delta(x - x_0) \tag{4.32}$$

where $\delta$ is the Dirac delta function and the boundary condition at the wall is:

$$p\,(x = 0, t \mid x_0, t_0) = 0 \tag{4.33}$$

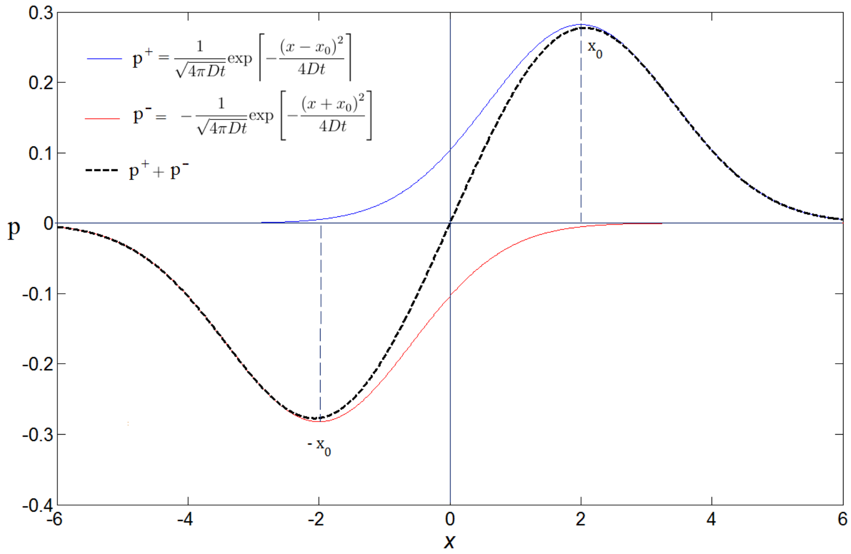

Figure 4.11: Calculation of the probability of finding a particle released in position $x_0 = 2$, at $t = 1$, when a fully absorbing wall is defined at $x = 0$. $D$ is normalized to 1.

The solution for the probability ($p$) is shown for many cases in the literature and is given by[46,47]:

$$p\left(x, t \mid x_0, t_0\right) = \frac{1}{\sqrt{4\pi Dt}}\exp\left[-\frac{\left(x - x_0\right)^2}{4Dt}\right] - \frac{1}{\sqrt{4\pi Dt}}\exp\left[-\frac{\left(x + x_0\right)^2}{4Dt}\right] \tag{4.34}$$

As shown in figure 4.11, the first term describes free diffusion without a wall. The second term shows the inverse term to enforce the boundary condition that the probability equals zero at the absorbing wall ($x = 0$). Since the number of particles that start in $x_0$ is not conserved, the fraction of particles that is left in the whole space (0<x) at any time by integration over space if the cumulative hits function is normalized to 1 at $t = 0$. The solution reflects previous works of Knudsen[45] and Schulten[47].

$$\frac{N}{N_{t=0}} = \int_0^\infty p\left(x, t \mid x_0, t_0 = 0\right) dx \tag{4.35}$$

where $N$ is the 'surviving' number of particles. Introducing the variable:

$$y = \frac{x}{\sqrt{4Dt}} \rightarrow \sqrt{4Dt}dy = dx \tag{4.36}$$

This gives:

$$\frac{N}{N_{t=0}} = \int_0^\infty \frac{1}{\sqrt{\pi}} \exp\left[-(y-y_0)^2\right] dy \; - \; \int_0^\infty \frac{1}{\sqrt{\pi}} \exp\left[-(y+y_0)^2\right] dy \tag{4.37}$$

The integration can be simplified by changing the integration limits (by constants):

$$\frac{N}{N_{t=0}} = \int_{-y_0}^\infty \frac{1}{\sqrt{\pi}} \exp\left[-(y)^2\right] dy \; - \; \int_{y_0}^\infty \frac{1}{\sqrt{\pi}} \exp\left[-(y)^2\right] dy \tag{4.38}$$

giving:

$$\frac{N}{N_{t=0}} = \int_{-y_0}^{y_0} \frac{1}{\sqrt{\pi}} \exp\left[-(y)^2\right] dy = \frac{2}{\sqrt{\pi}} \int_0^{y_0} \exp\left[-(y)^2\right] dy = \mathrm{erf} y_0$$

and by back substituting $y_0 \rightarrow x_0$[45]:

$$\frac{N}{N_{t=0}} = \mathrm{erf} \frac{x_0}{\sqrt{4Dt}} \tag{4.39}$$

This solution was shown previously[38,45,47]. Also the flux for the solution at $x \rightarrow 0$ gives the known Cottrell equation[37].

**Part B**

Here the solution is compared to the resembling structure of Fick's law for linear diffusion as is shown below. The concentration is obtained via Fick's law is:

$$\frac{c(x)}{c^*} = \operatorname{erf}\frac{x}{\sqrt{4Dt}} \tag{4.40}$$

However, there is a significant difference. Whilst the solution of Einstein's version shows the overall decay in the number of particles that started at $x_0$ in terms of the remaining fraction at the time $t$ *in all space*, Fick's solution shows the decay *at any location $x$ in space.* Thus Fick's result can be obtained from the Einstein solution. Considering the solution of the diffusion of one particle in equation 4.34, we can look at a certain constant point ($x_c$) and sum up all the probabilities in that point $x_c$ that arise from diffusion from all starting points $x_0, x_1, ...x_n$ in $\vec{x}$:

$$\sum_{n=0}^{\infty} p\left(x_c, t \mid x_n, t_0\right) = \sum_{n=0}^{\infty} \frac{1}{\sqrt{4\pi Dt}} \exp\left[-\frac{\left(x_c - x_n\right)^2}{4Dt}\right] \quad - \sum_{n=0}^{\infty} \frac{1}{\sqrt{4\pi Dt}} \exp\left[-\frac{\left(x_c + x_n\right)^2}{4Dt}\right] \tag{4.41}$$

When assuming a continuous space of starting points represented via dirac functions (i.e. sufficient amount of particles distributed in space), the sum can be rewritten as an integral:

$$\lim_{x_n - x_{n-1} \to 0} \sum_{0}^{n=\infty} p\left(x_c, t \mid x_n, t_0\right) = \int_0^{\infty} p\left(x_c, t \mid x, t_0\right) dx \tag{4.42}$$

and

$$\int_{n=0}^{\infty} p\left(x_c, t \mid x, t_0\right) dx = \int_0^{\infty} \frac{1}{\sqrt{4\pi Dt}} \exp\left[-\frac{\left(x_c - x\right)^2}{4Dt}\right] dx - \int_0^{\infty} \frac{1}{\sqrt{4\pi Dt}} \exp\left[-\frac{\left(x_c + x\right)^2}{4Dt}\right] dx \tag{4.43}$$

The parameters of the exponential functions have the symmetry:

$$\left(x_c - x\right)^2 = \left(x - x_n\right)^2 \; and \; \left(x_c + x\right)^2 = \left(x + x_n\right)^2 \; for \;\; x_c = x_n \tag{4.44}$$

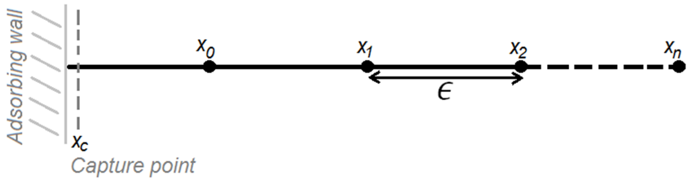

Figure 4.12: Illustration of the calculation of probability of finding particles in point $x_c$ close to the absorbing wall).

and therefore it gives:

$$\int_0^\infty p\left(\mathbf{x_0},t\mid\mathbf{x},t_0\right)dx=\int_0^\infty p\left(\mathbf{x},t\mid\mathbf{x_0},t_0\right)dx \tag{4.45}$$

Hence, the result of these integrations leads to the dependency discussed earlier in equations 4.39 and 4.40 in continuous media.

The limiting of the assumption of continuous media (eq. 4.42) can be showed by comparing the solution for Einstein's version (eq. 4.41) and Fick's (eq. 4.40) when getting from infinitesimal distances to finite distances between particles. The probability to find fraction of finite number of particles $(x_0, x_1 \dots x_n)$ by using equation 4.41 where $x = x_c$, and $\epsilon = x_{n+1} - x_n$ is:

$$\sum_{n=1}^{L} p\left(x=x_c,t\mid x_n,t_0\right)=\sum_{n=1}^{L}\frac{1}{\sqrt{4\pi Dt}}\exp\left[-\frac{\left(x-\epsilon\cdot n\right)^2}{4Dt}\right]-\sum_{n=1}^{L}\frac{1}{\sqrt{4\pi Dt}}\exp\left[-\frac{\left(x+\epsilon\cdot n\right)^2}{4Dt}\right] \tag{4.46}$$

$x_n = L$ is defined, so the number of particles that are taken into account to be $L/\epsilon$. We can observe at each time the probability to find particles at $x \approx 0$ and compare it to the solution of the Fick's concentration profile (eq. 4.40). $L$ was chosen to be far enough from $x_c$, $L - x_c \gg \sqrt{4Dt_{max}}$, this was checked by increasing $L$ until no change appeared to the graph.

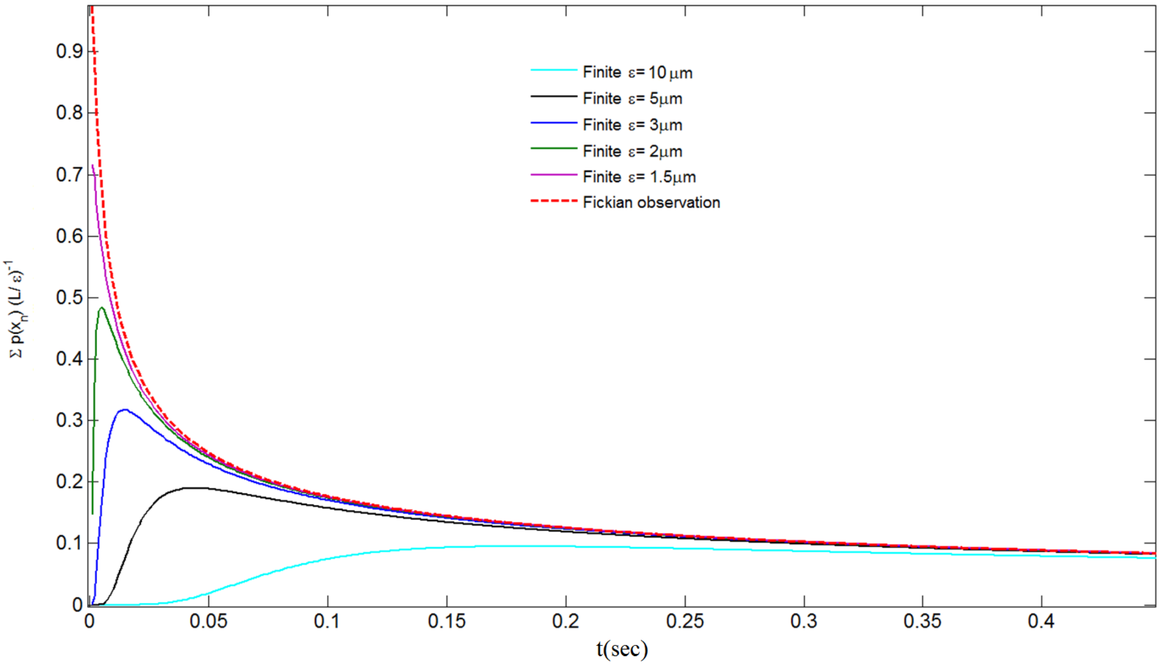

Figure 4.13: Calculations of the normalized probability of n particles to be found in the boundary as function t, for various distances, $\epsilon$. The Fick's profile is also provided in the red dash curve.

The calculation of the probability to find the fraction of particles for various distances, $\epsilon$ are shown in figure 4.13. The larger the distance $\epsilon$, the lower the probability to find particles in the short time than expected from Fick's second law. At smaller distances $\epsilon < 1.5\mu m$ the result shows Fick's observations. However, since the particles are randomly distributed, changing the distance of $x_0$ t be closer to the wall and $x_c$ to be far from the wall affects the profile as illustrate in figure 4.14. Therefore, calculations for various $x_0 - x_c$ when $\epsilon$ is constant $(10\mu m)$ are plotted in figure 4.15.

It shows that even-though the distance between particles is constant in average, the probability can be higher or lower than the expected Fickian profile depending on the starting position.

Since this calculation describes the case of a point as an absorbing wall, in 2D cell, this will be averaged over many distances distributed over $\epsilon$ (see figure 4.14) along the whole surface of the wall. Hence, if the particles are truly random distributed, the statistical

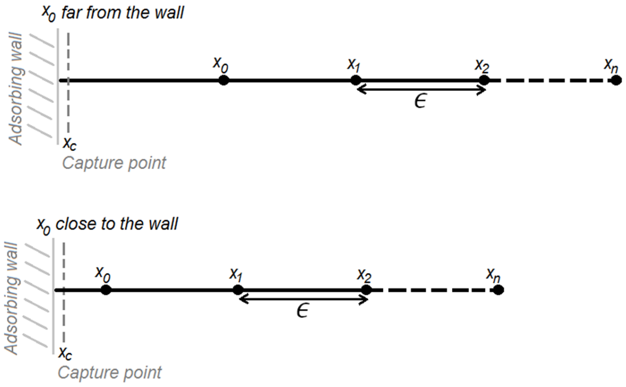

Figure 4.14: Illustration of the calculation of probability of finding particles in point $x_c$ close to the absorbing wall).

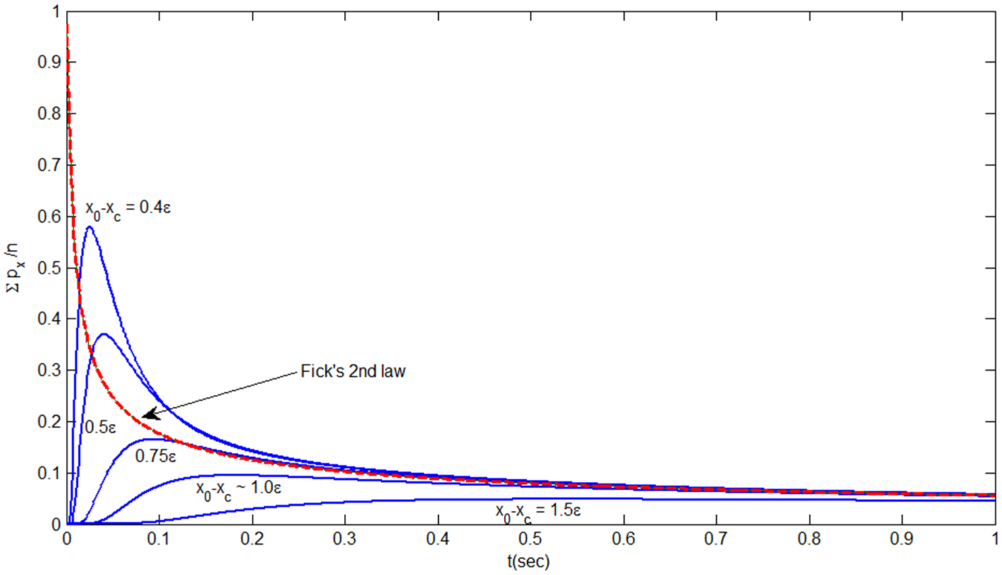

Figure 4.15: Calculations of the normalized probability of n particles to be found in the boundary for various positions $x_0 - x_c$, $\epsilon = 10\mu m$. The Fickian profile is also provided in the red dash curve.

Fickian behaviour is observed.

This shows that the deviation from the Einstein's approach occurs in the case of large distances between particles, i.e at low concentrations. However, this deviation varies with time due to the fact that particles in solution are randomly distributed and the distribution of the distances between nearest neighbours follows a spatial Poisson process. Hence, the deviation (or the variance) from Fick's solution can be introduced in order to study the stochastics of diffusion in non-continuous media.

# References

[1] S. Eloul, E. Kätelhön, C. Batchelor-McAuley, K. Tschulik, and R. G. Compton *The Journal of Physical Chemistry C*, vol. 119, no. 25, pp. 14400–14410, 2015.

[2] M. Ahamed, M. AlSalhi, and M. Siddiqui *Clin. Chim. Acta*, vol. 411, no. 23-24, pp. 1841–1848, 2010.

[3] N. Singh, B. Manshian, G. J. Jenkins, S. M. Griffiths, P. M. Williams, T. G. Maffeis, C. J. Wright, and S. H. Doak *Biomaterials*, vol. 30, no. 2324, pp. 3891 – 3914, 2009.

[4] L. Guo and D.-H. Kim *Chem. Commun.*, vol. 47, pp. 7125–7127, 2011.

[5] W. S. Hwang, P. L. Truong, and S. J. Sim *Anal. Biochem.*, vol. 421, no. 1, pp. 213 – 218, 2012.

[6] W. Cheng and R. G. Compton *Angew. Chem., Int. Ed.*, vol. 53, no. 50, pp. 13928–13930, 2014.

[7] A. Beyler, L. F. Marshall, O. Chen, D. K. Harris, D. D. Wanger, X. Brokmann, and M. G. Bawendi *Nat. Chem.*, vol. 5, pp. 602–606, 2013.

[8] L. Guo, A. R. Ferhan, K. Lee, and D.-H. Kim *Anal. Chem.*, vol. 83, no. 7, pp. 2605–2612, 2011.

[9] K. Tschulik and R. G. Compton *Phys. Chem. Chem. Phys.*, vol. 16, pp. 13909–13913, 2014.

[10] W. Cheng and R. G. Compton *TrAC Trends in Anal. Chem.*, vol. 58, pp. 79 – 89, 2014.

[11] W. Cheng, C. Batchelor-McAuley, and R. G. Compton *ChemElectroChem*, vol. 1, no. 4, pp. 714–717, 2014.

[12] E. J. E. Stuart, Y.-G. Zhou, N. V. Rees, and R. G. Compton *RSC Adv.*, vol. 2, pp. 6879–6884, 2012.

[13] Y.-G. Zhou, N. V. Rees, and R. G. Compton *Angew. Chem., Int. Ed.*, vol. 50, no. 18, pp. 4219–4221, 2011.

[14] N. P. Sardesai, D. Andreescu, and S. Andreescu *J. Am. Chem. Soc.*, vol. 135, no. 45, pp. 16770–16773, 2013.

[15] W. Cheng, C. Batchelor-McAuley, and R. G. Compton *ChemElectroChem*, vol. 1, no. 4, pp. 714–717, 2014.

[16] X.-F. Zhou, W. Cheng, and R. G. Compton *Nanoscale*, vol. 6, pp. 6873–6878, 2014.

[17] T. M. Alligrant, E. G. Nettleton, and R. M. Crooks *Lab Chip*, vol. 13, pp. 349–354, 2013.

[18] L. S. Y. Ly, C. Batchelor-McAuley, K. Tschulik, E. Kätelhön, and R. G. Compton *J. Phys. Chem. C*, vol. 118, no. 31, pp. 17756–17763, 2014.

[19] Y.-G. Zhou, N. V. Rees, and R. G. Compton *Phys. Chem. Chem. Phys.*, vol. 15, pp. 761–763, 2013.

[20] D. Qiu, S. Wang, Y. Zheng, and Z. Deng *Nanotechnology*, vol. 24, no. 50, p. 505707, 2013.

[21] J. C. Lees, J. Ellison, C. Batchelor-McAuley, K. Tschulik, C. Damm, D. Omanović, and R. G. Compton *ChemPhysChem*, vol. 14, no. 17, pp. 3895–3897, 2013.

[22] J. Ellison, C. Batchelor-McAuley, K. Tschulik, and R. G. Compton *Sensor Actuat B-Chem*, vol. 200, pp. 47 – 52, 2014.

[23] A. Einstein *Annalen der Physik*, vol. 322, no. 8, pp. 549–560, 1905.

[24] N. G. V. Kampen, *Stochastic Processes in Physics and Chemistry.* North-Holland, Amsterdam, 1992.

[25] C. Amatore, S. Arbault, I. Bonifas, and M. Guille *Biophys. Chem.*, vol. 143, no. 3, pp. 124 – 131, 2009.

[26] F.-R. F. Fan, J. Kwak, and A. J. Bard *J. Am. Chem. Soc.*, vol. 118, no. 40, pp. 9669–9675, 1996.

[27] I. J. Cutress, E. J. Dickinson, and R. G. Compton *J. Electroanal. Chem.*, vol. 655, no. 1, pp. 1–8, 2011.

[28] E. Kätelhön, K. J. Krause, K. Mathwig, S. G. Lemay, and B. Wolfrum *ACS Nano*, vol. 8, pp. 4924–4930, 2014.

[29] E. Kätelhön, K. J. Krause, K. Mathwig, P. S. Singh, S. G. Lemay, and B. Wolfrum *J. Am. Chem. Soc.*, vol. 135, pp. 8874–8881, 2013.

[30] J. van Embden, J. E. Sader, M. Davidson, and P. Mulvaney *J. Phys. Chem. C*, vol. 113, no. 37, pp. 16342–16355, 2009.

[31] N. T. K. Thanh, N. Maclean, and S. Mahiddine *Chem. Rev.*, vol. 114, no. 15, pp. 7610–7630, 2014.

[32] I. M. Sokolov, R. Metzler, K. Pant, and M. C. Williams *Phys. Rev. E*, vol. 72, p. 041102, Oct 2005.

[33] E. Kätelhön, K. J. Krause, B. Wolfrum, and R. G. Compton *ChemPhysChem*, vol. 15, no. 5, pp. 872–875, 2014.

[34] A. Boika and A. J. Bard *Analytical Chemistry*, vol. 87, no. 8, pp. 4341–4346, 2015.

[35] A. J. Bard and L. Faulkner, *Electrochemical Methods: Fundamentals and Applications.* John Wiley and Sons, 2001.

[36] R. G. Compton and C. E. Banks, *Understanding voltammetry.* London, UK: Imperial College Press, 2006.

[37] F. Cottrell *Z. Phys. Chem.*, vol. 42, p. 385, 1903.

[38] D. T. Gillespie and E. Seitaridou, *Simple Brownian Diffusion An Introduction to the Standard Theoretical Models.* Oxford University Press, 2012.

[39] P. L. Krapivsky and S. Redner *Am. J. Phys.*, vol. 64, pp. 546–551, 1996.

[40] A. Nagar and P. Pradhan *Physica A*, vol. 320, pp. 141–148, 2003.

[41] M. Matsumoto and T. Nishimura *ACM Transactions on Modeling and Computer Simulation*, vol. 8, pp. 3–30, 1998.

[42] W. Schottky *Annalen der Physik*, vol. 362, no. 23, pp. 541–567, 1918.

[43] G. Pólya *Math. Ann.*, vol. 84, p. 149, 1921.

[44] J. Yao and K. D. Gillis *Analyst*, vol. 137, pp. 2674–2681, 2012.

[45] O. Sten-Knudsen, *Biological Membranes: Theory of Transport, Potentials and Electric Impulses.* Cambridge University Press, 2007.

[46] K. S. Attila Szabo and Z. Schulten *J. Chem. Phys.*, vol. 72, pp. 4350–4357, 1980.

[47] K. Schulten and I. Kosztin, *Lectures in Theoretical Biophysics: Non-Equilibrium Statistical Mechanics- Einstein Diffusion Equation- Chapter 3.* Department of Physics and Beckman Institute University of Illinois at Urbana-Champaign, 2000.

# Chapter 5

# Diffusional impacts of nanoparticles on microdisc and microwire

The previous chapter investigated diffusional impacts for a planar and spherical electrodes. In this chapter, approximate expressions are derived for the average number of diffusive impacts/hits of nanoparticles on microdisc and microwire electrodes for the case where the impact leads to the loss of the nanoparticles from solution either via irreverisble adsorption or complete electro-dissolution. The theory can also be applied to sub-micrometer size electrodes (nano-electrodes). The resulting equations can be utilized to analyse the number of impacts and its variance in the 'nano-impact' experiment. Expressions for estimated first passage time are also provided for dilute nanoparticle solutions in the continuum limit of Fickian diffusion. The expressions for the first passage times are used to estimate the lower limit of detection in ultra-dilute nanoparticle solutions for typical nano-impact experiments, and show the advantage of using microwire electrodes in ultra-dilute solutions or solutions containing larger nano-particles. This work, carried out in collaboration with Dr. E. Kätelhön, Dr. C. Batchelor-McAuley, and Dr. K. Tschulik, and has been published in 'The Journal of Electroanalytical Chemistry'[1].

## 5.1 Introduction

The 'nano-impact' method offers significant advantages over conventional optical techniques, including the ability of analysing nanoparticles in-situ without the need for drying or modifying the investigated solution[2,3]. The nano-impact method has been used to identify various types of nanoparticles[2,4–7], and to provide fundamental insights into chemical mechanisms[8–12], agglomerations and aggregations[13,14], and sensing at low nanoparticle concentrations for environmental studies[5].

In the 'nano-impact' method, nanoparticles diffuse freely in an electrochemical cell, and are detected via their stochastic hits on an electrode, which may also be referred to as an 'impact'. Typically, micrometer sized electrodes are used to avoid large capacitance noise[15,16] or simultaneous impacts.

Previously in the thesis (chapter 4), probability expressions have been derived using Fick's second law to predict the number of diffusional impacts of nanoparticles that are fully dissolved on spherical and planar electrodes[17]. It was also shown how the variance of the probability expressions behaves in the Poisson limit[17]. Furthermore, expressions were derived for the first passage time (estimated for one impact as discussed in chapter 4) as an indication of the lower concentration limit of detection. Having reported in depth the comparison between the radial and linear diffusion regime for the case of spherical and planar electrodes, in the present chapter this method is employed to microdisc and microcylinder geometries, as the importance of such electrodes for nano-impacts is enormous: The use of microdisc electrodes is the common way of measuring impacts in the radial diffusion regime[2,4,5,18], and by utilizing microwire (microcylinder) electrodes the detection of nano-particles in the femto-molar concentration region is enabled[19]. This study is focused on impacts which lead to the loss of the nanoparticles from solution, either via irreversible adsorption or electro-dissolution. This assumption allows us to investigate the case of diffusion towards a fully absorbing wall[17].

## 5.2 Theory

This study is divided into the cases of (*i*) microdisc and (*ii*) microwire electrodes. In both cases Fick's diffusion equation is used:

$$\frac{\partial c}{\partial t} = D\nabla^2 c \tag{5.1}$$

where $c$ is the concentration and $D$ is the diffusion coefficient of the nanoparticles. Previously known analytical expressions, which are approximate solutions for the mass transport in chronoamperometry, are employed as a starting point.

### 5.2.1 Microdisc electrode

In cylindrical coordinates the diffusion equation is given by:

$$\frac{\partial c(r,z,t)}{\partial t} = D\left(\frac{\partial^2 c(r,z,t)}{\partial r^2} + \frac{\partial^2 c(r,z,t)}{\partial z^2} + \frac{1}{r}\frac{\partial c(r,z,t)}{\partial r}\right) \tag{5.2}$$

Since the considered system features a symmetry with respect to the z-axis, the angular terms of the Laplacian can be neglected. Further assuming destructive impacts, the boundary conditions are given by a fully absorbing surface, where the concentration

$c(r,0,t) = 0$, on the electrode surface and $\partial c/\partial z = 0$ at all other boundaries. Far from the electrode, at $z, r \to \infty$, the bulk concentration is set to $c = c^*$ at any time and the concentration in all space is also set to $c^*$ at $t = 0$. Saito found the steady state flux towards a disc electrode under such conditions to be[20]:

$$J(t \to \infty) = 4Dc^* r_d \tag{5.3}$$

where $r_d$ is the disc radius. An approximate solution valid for all time is given by the Shoup and Szabo equation[21]:

$$J = 4Dc^* r_d f(\tau) \tag{5.4}$$

where

$$f(\tau) = 0.7854 + 0.8862\tau^{-1/2} + 0.2146\exp(-0.7823\tau^{-1/2}) \tag{5.5}$$

and $\tau$ is a dimensionless time parameter, which is defined as:

$$\tau = 4Dt/r_d^2 \tag{5.6}$$

This convenient expression is widely used and provides accuracy to within 0.6 % compared to simulations by Heinze[22]. Via the discussed approach in chapter 4, this solution is utilised to study the probability of finding $\hat{N}_{hits}(t)$ (the term 'hits' is used in the symbol for consistency with previous work[17], and in the text 'hit' is referred to an 'impact') within the time $t$ after the experiment was started. In particular, the concentration can be replaced with the probability density ($p^*$) of finding a particle at $t_0$ at a given position and the flux with the accumulated number of impacts ($\hat{N}_{hits}(t)$) in a dilute solution:

$$J = \frac{d\hat{N}_{hits}(t)}{dt} = 4Dp^{*}r_{d}f(\tau) \tag{5.7}$$

Integrating over time gives the accumulated number of impacts:

$$\hat{N}_{hits}(t) = \int_{0}^{t} 4Dp^{*}r_{d}f(\tau)dt \tag{5.8}$$

In order to solve this equation, the integration variable $t$ is transformed to $\tau$:

$$\hat{N}_{hits}(t) = \int_{0}^{\tau} p^{*}r_{d}^{3}f(\tau)d\tau \tag{5.9}$$

The integration of the Shoup-Szabo equation can be calculated via a power series expansion of the exponential term:

$$\beta\exp(-\alpha\tau^{-1/2}) = \beta(1 - \alpha\tau^{-1/2} + \frac{\alpha^{2}}{2!}\tau^{-1} - \frac{\alpha^{3}}{3!}\tau^{-3/2} + ... + \frac{(-\alpha)^{n}}{n!}\tau^{-n/2}) \tag{5.10}$$

Integration then gives:

$$\hat{N}_{hits}(t) = p^{*}r_{d}^{3}F(\tau) \tag{5.11}$$

where:

$$F(\tau) = \tau + 1.437\sqrt{\tau} + 6.567\cdot 10^{-2}\ln\tau + \frac{3.425\cdot 10^{-2}}{\sqrt{\tau}} - \frac{3.349\cdot 10^{-3}}{\tau} \tag{5.12}$$

when taking into account the five first terms. This expression was derived previously and is used for determining concentrations in the ‘nano-impact’ experiment[5]. Under common experimental conditions, $\tau \gg 0$, it is only necessary to use the first three terms of the Taylor series, as the fourth and above terms add less than 0.6 % to the accuracy. Therefore, the solution for the average number of impacts is:

$$\hat{N}_{hits}(t) = p^* r_d^3(\tau + 1.437\sqrt{\tau} + 6.567 \cdot 10^{-2} \ln \tau), \quad \tau = 4Dt/r_d^2 \tag{5.13}$$

The estimation for the first passage time can then be found by solving $\hat{N}_{hits}(t) = 1$:

$$\frac{1}{p^* r_d^3} = \tau + 1.437\sqrt{\tau} + 6.567 \cdot 10^{-2} \ln \tau \tag{5.14}$$

Boika and Bard recently suggested an approach for finding the first passage time of impacts on a microdisc electrode[23] and predict an inverse proportionality between the number of impacts and the nanoparticle concentration. The above analytical solution agrees with this finding under certain experimental conditions: At large $\tau$, i.e. $\tau \gg 100$, equation 5.14 can be simplified to an inverse linear relation of concentration with time:

$$\frac{1}{4Dp^* r_d} = t \tag{5.15}$$

If, however, $\tau$ is calculated for a typical nano-impact experiment using a microdisc electrode of the radius $5\mu m$ and a particle concentration of 5pM, the average first passage time is found to be $\tau = 1.12$ using the presented approach, while neglecting the non-linear terms in equation 5.14 leads to a value of $\tau = 2.65$, which deviates by more than 100%. The dependency of the first passage time on concentration is detailed later in the discussion section.

The duration of 'nano-impact' experiments is limited for experimental reasons[24], thus the first passage time provides an indication for the overall time needed to conduct an experiment. In the previous chapter it was shown that the variance of the number of impacts detected in an experiment can be modelled in the Poisson limit[17]. This means that the standard deviation (SD) follows the square root of the expected number of impacts and the standard deviation of one hit is hence 100%. Therefore, the duration of an experiment must be significantly longer than the expected first passage time.

### 5.2.2 Microwire electrode

Szabo[25] found an expression for the transient flux towards a semi-infinite hemicylinder, which is accurate to within 1.3% for short and long times:

$$J(t) = \pi D c^* l f(\tau) \tag{5.16}$$

where $l$ is the length of the cylinder and $f(\tau)$ is:

$$f(\tau) = \frac{e^{-\sqrt{\pi\tau}/10}}{\sqrt{\pi\tau}} + \frac{1}{ln[(4e^{-\gamma}\tau)^{1/2} + e^{5/3}]} \tag{5.17}$$

$\tau$ is defined as $Dt/r_c^2$, where $r_c$ is the radius of the cylinder, and $\gamma = 0.5772$ is the Euler-Mascheroni constant. Again, time integration is obtained to find the average number of impacts on a cylinder (twice the surface of a hemi-cylinder):

$$\hat{N}_{hits}(t) = \int_0^t 2\pi D p^* l f(\tau) dt = \pi D p^* l \int_0^t \frac{e^{-\sqrt{\pi\tau}/10}}{\sqrt{\pi\tau}} + \frac{1}{ln[(4e^{-\gamma}\tau)^{1/2} + e^{5/3}]} dt \tag{5.18}$$

Changing the variable $t$ to $\tau$ gives:

$$\hat{N}_{hits}(t) = \int_0^{\tau} 2\pi p^* l r_c^2 f(\tau) d\tau \tag{5.19}$$

The integration of the Szabo equation can be solved as follows. The integral of the first term can be found by substituting $-\sqrt{\pi\tau}/10 = x$:

$$\int_0^{\tau} \frac{e^{-\sqrt{\pi\tau}/10}}{\sqrt{\pi\tau}} d\tau = -20 \frac{e^{-\sqrt{\pi\tau}/10}}{\pi}\Bigg|_0^{\tau} \tag{5.20}$$

The second term has the form:

$$\frac{1}{ln[(4e^{-\gamma}\tau)^{1/2} + e^{5/3}]} d\tau = \frac{1}{ln[\alpha\tau^{1/2} + \beta]} d\tau \tag{5.21}$$

where $\alpha = 2e^{-\gamma/2}$ and $\beta = e^{5/3}$. Substitution of $\alpha\tau^{1/2} + \beta = e^x$ gives:

$$\tau = \frac{(e^x - \beta)^2}{\alpha^2}, \; d\tau = \frac{2e^x(e^x - \beta)}{\alpha^2} dx \tag{5.22}$$

Substitution in equation (5.21) yields:

$$\int_0^{\tau} \frac{1}{ln[\alpha\tau^{1/2} + \beta]} d\tau = \int_{ln(\beta)}^{ln(\alpha\tau^{1/2}+\beta)} \frac{2}{\alpha^2} \frac{e^x(e^x - \beta)}{x} dx = \frac{2}{\alpha^2}(Ei(2x) - \beta Ei(x))\Bigg|_{ln(\beta)}^{ln(\alpha\tau^{1/2}+\beta)} \tag{5.23}$$

where $Ei(x)$ is the exponential integral:

$$Ei(x) = \int_{-x}^{\infty} \frac{e^x}{x} dx = \gamma + ln(x) + \sum_{k=1}^{\infty} \frac{x^k}{k \cdot k!} \tag{5.24}$$

The integration of $F(\tau)$ then gives:

$$F(\tau) = \frac{\hat{N}_{hits}(t)}{2\pi p^* l r_c^2} = \int\limits_{\tau_0}^{\tau} f(\tau) d\tau = -20 \frac{e^{-\sqrt{\pi\tau}/10}}{\pi} + \frac{2}{\alpha^2}\left(Ei(2x[\tau,\tau_0]) - \beta Ei(x[\tau,\tau_0])\right) \quad (5.25)$$

and substituting the Ei (exponential integral), gives:

$$F(\tau) = 11.69 - 20\frac{e^{-\sqrt{\pi\tau}/10}}{\pi} + \frac{2(1-\beta)}{\alpha^2} lnx + \frac{2}{\alpha^2}\sum_{k=1}^{\infty}\frac{(2^k - \beta)[lnx]^k}{k \cdot k!} \quad (5.26)$$

where

$$x = ln(\alpha\tau^{1/2} + \beta), \;\; \alpha = 2e^{-\gamma/2}, \;\; \beta = e^{5/3}, \gamma = 0.5772 \quad (5.27)$$

The numerical integration of $f(\tau)$ and the approximate expression for $F(\tau)$ (eq. 5.26) are compared in figure 5.2. The figure shows that in order to reach good accuracy in the range $\tau = 0$ to 1000 many terms are needed, which makes this expression impractical. Therefore as a more realistic approach a fit is proposed for the numerical integration of $f(\tau)$, from within the range from $\tau_0 = 0$ to $\tau = 1000$:

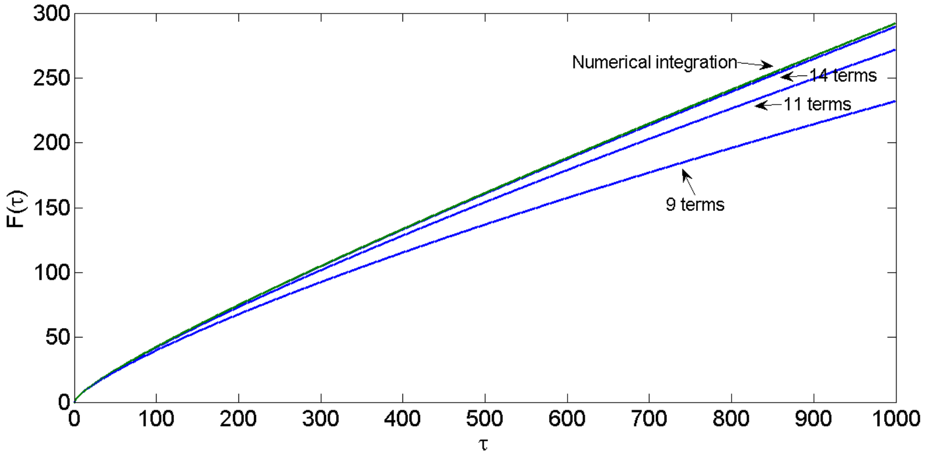

Figure 5.1: Comparison between the numerical integration of Shoup's $f(\tau)$ and the analytically found expression using the first terms of the infinite sum.

$$F^*_{short}(\tau < 1000) = 0.60\tau - 20\frac{e^{-\sqrt{\pi\tau}/10}}{\pi} - 0.1591\tau^{1.1} - 3.5e^{-0.02\tau} + 9.866 \tag{5.28}$$

This expression is in good agreement with the numerical integration of Szabo's equation. The numerical integration was solved in Matlab by using quadratic adaptive integration with an absolute error tolerance of $10^{-10}$ and a relative error tolerance of $10^{-6}$. Figure 5.2 shows the agreement between the numerical integration of Shoup's equation and $F^*(\tau)$ in the considered range of $0 < \tau < 1000$. However for sub-micrometre sized electrodes and nano-electrodes $\tau$ can easily exceed 1000 in a typical experiment. Therefore, another fit to Szabo's integration is applied in the range $\tau \geq 1000$:

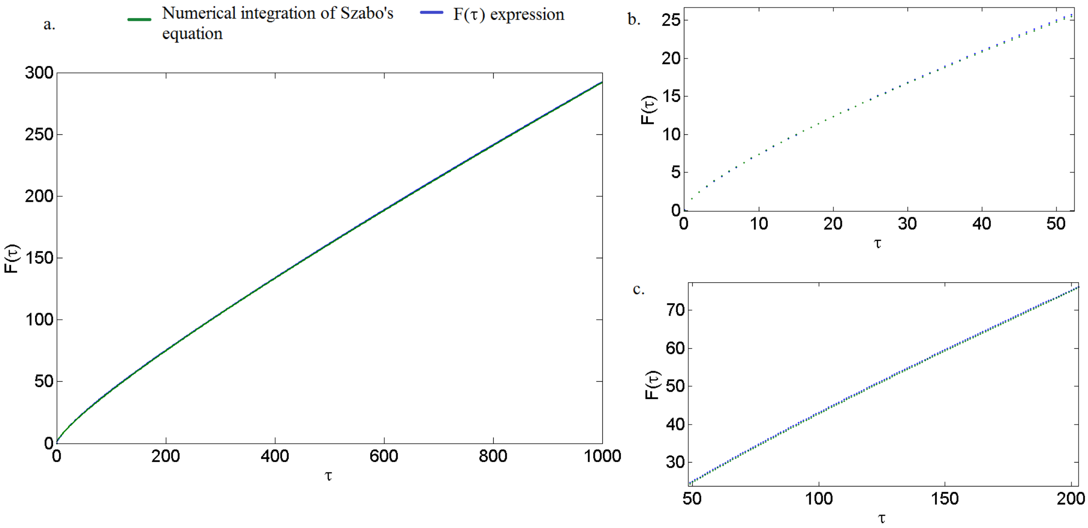

Figure 5.2: Comparison between the numerical integration of Shoup's $f(\tau)$ and the suggested function $F^*(\tau)$. Two sections of the graphs are amplified in plots b) and c).

$$F^*_{long}(\tau \geq 1000) = 292.2 + \frac{2.03(\tau - 1000)}{ln(\tau)} - 0.7\sqrt{\tau - 1000}e^{-\frac{1000-\tau}{40000}} \tag{5.29}$$

This function was found to be accurate for $\tau \geq 1000$ [1].

The final expression for the average number of impacts on a cylinder is hence given by:

$$\hat{N}_{hits}(t) = 2\pi p^* l r_c^2 F^*(\tau), \;\; \tau = Dt/r_c^2 \tag{5.30}$$

where $p^*$ is the particle number concentration, $l$ is the length of the cylinder and $r_c$ is the cylinder radius. The standard deviation follows $\sqrt{\hat{N}_{hits}(t)}$ and the average first passage time can be calculated by choosing $\hat{N}_{hits}(t) = 1$. $F^*(\tau)$ is defined through equations 5.28 and 5.29 for the ranges $0 < \tau < 1000$ and $\tau \geq 1000$, respectively.

## 5.3 Discussion

In this section, the above calculated expressions are applied to find the average number of impacts in a given time in the 'nano-impact' experiment. The results are divided into the case of a microdisc electrode and the cases of a wire electrode. Additionally, estimated first passage times are discussed as functions of the electrode size and the nanoparticle concentration.

### 5.3.1 Microdisc electrode

The number of impacts was calculated for a representative electrochemical cell containing a microdisc electrode, a nanoparticle concentration of $c^* = 1pM$, and diffusion coefficient of $10^{-10} m^2 s^{-1}$. Plots of the average number of impacts as a function of time are shown in figure 5.3 for various disc radii. It can be seen that within the typical duration of an experiment (100s), a linear increase in the number of impacts is observed for sufficiently

---

[1] The agreement with the numerical integration method used is better than 1% for all $\tau$, except for $0.1 < \tau < 12$ where the error can be up to 2.4%

small radii electrodes ( $\sim 1\mu m$ and below) due to the radial diffusion regime, where the expression for the number of impacts can be reduced to:

$$\hat{N}_{hits}(t) = 4Dp^{*}r_{d}t \tag{5.31}$$

However, in the case of a larger radius $r_d = 10\mu m$, the transient behaviour is slightly visible. The same trend can be seen as function of the particles diffusion coefficient as shown in figure 5.4 for a $1\mu m$ disc electrode. Since the particle size is inversely proportional to the diffusion coefficient (as described by the Stokes-Einstein equation[26]), the number of impacts gradually decreases with the particle size. For instance, at $D = 10^{-10}m^2s^{-1}$, which corresponds to a particle radius of $\sim 2nm$ in water, many impacts are predicted. On the other hand side, particles featuring sizes larger than $\sim 100nm$ are likely to exhibit few or no impacts during a 100s test period. It is noted, that the convergent diffusion regime which result in linear increase of the number of impacts with time is valid when $4Dt/r^2 \gg 1000$ according to equation 5.14. However, the first event is likely to happen also in the transient limit even in the sub-pM region, as is shown next.

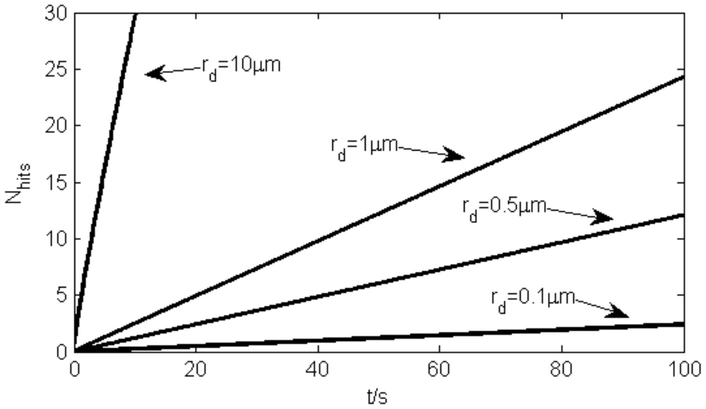

Figure 5.3: Average number of impacts on a microdisc calculated for various electrode radii. The nanoparticle concentration and the diffusion coefficient are $c^{*} = 1pM$ and $10^{-10}m^2s^{-1}$, respectively.

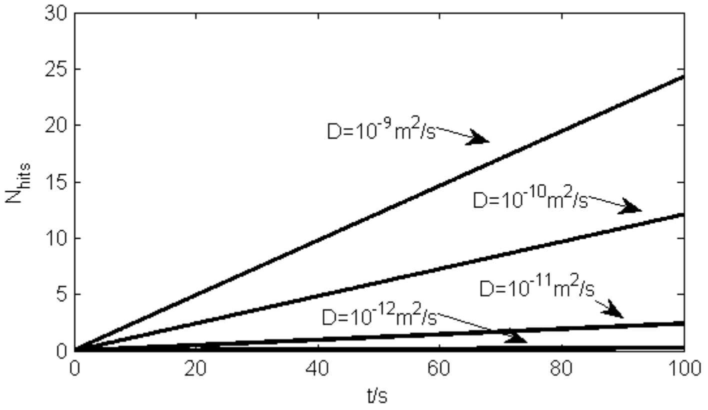

Figure 5.4: Average number of impacts on a microdisc electrode featuring a radius of $1\mu m$ in a solution of particles at a concentration of $c^* = 1pM$ for various diffusion coefficients.

Figure 5.5 shows an estimation of the lower limit of detection on the basis of the first passage time. The first passage time as a function of the initial concentration and indicate areas is plotted, in which the standard deviation (SD) exceeds the expected number of impacts. The graphs in figure 5.5 indicate the lowest concentration that can be detected for a given size of a microdisc and a given diffusion coefficient. For example, in figure 5.5a, in the case of an electrode featuring a radius of $1\mu m$ and a diffusion coefficient of $D = 10^{-10}m^2/s$, the first impact occurs on average after 50s for concentrations below 0.1pM. Figure 5.5b shows that the limit of detection can be improved by enlarging the electrode surface. Both figures, 5.5a and 5.5b show the non-linearity behaviour of the first passage time with concentration in the pM and sub-pM regions. However, inside the fM region a linear relation can be assumed as found by Boika and Bard[23].

### 5.3.2 Microwire electrode

A microwire (microcylinder) electrode features a macro dimension in terms of its length $l$ and a micro dimension in terms of its radius $r_c$. The relation between the exposed length and the number of detected impacts is linear and can hence be utilized to adjust the

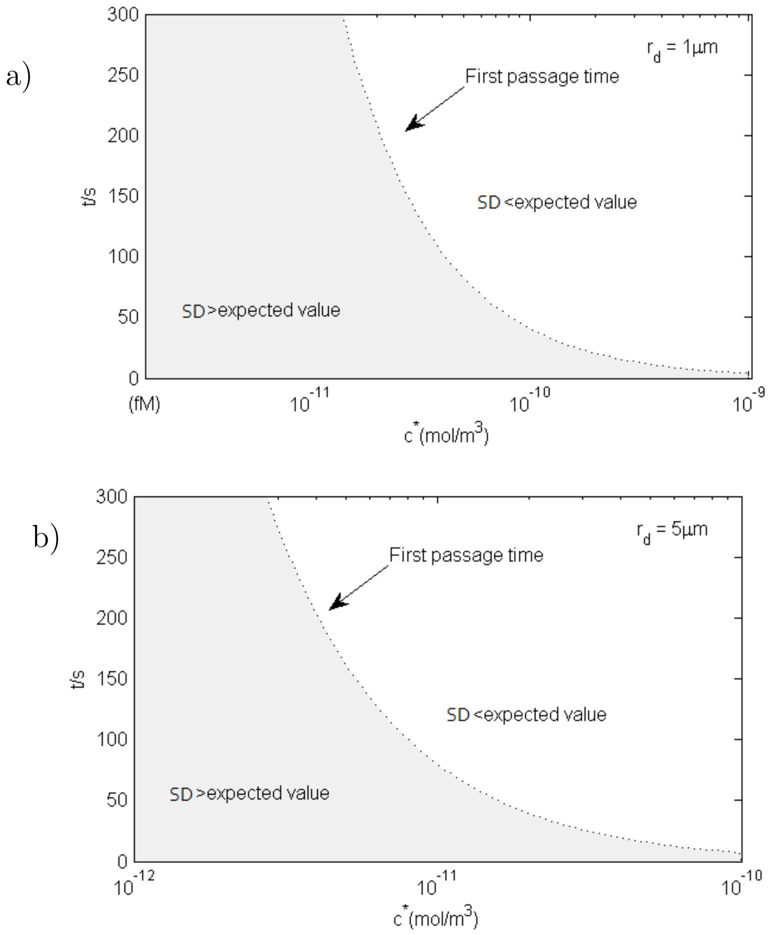

Figure 5.5: The limit of detection as a function of the concentration is estimated via the first passage time for a radius of $r_d = 1\mu m$ (a) and $r_d = 4\mu m$ (b). The areas in which the standard deviation(SD) is larger than the expected value are coloured grey.

sensitivity in the case of small concentrations by simply increasing the exposed length.

In the figures 5.6 and 5.7, the number of impacts on a wire ($l = 1mm$) as function of time is plotted for various radii and various diffusion coefficients, respectively. The large number of impacts within 100s at a concentration of 1pM indicates the system's ability to detect nanoparticles even at ultra low concentrations, in the fM-region. It is also shown that the number of impacts gradually increases due to the large contribution of the convergent diffusion within the 100s of the experiment. For larger wire radii a non-linearity is observed, which can be realised through considering the significant contribution of the macro-size diffusion layer that is established within the first seconds of the experiment.

At small radii ($0.5 - 1\mu m$), however, the accumulated number of impacts is almost linear within the 100s of the experiment. Moreover, from the plots for various diffusion coefficients in figure 5.7, it can be seen that the microwire geometry exhibits good sensitivity in the detection of particle sizes larger than $\sim 200nm$ in water.

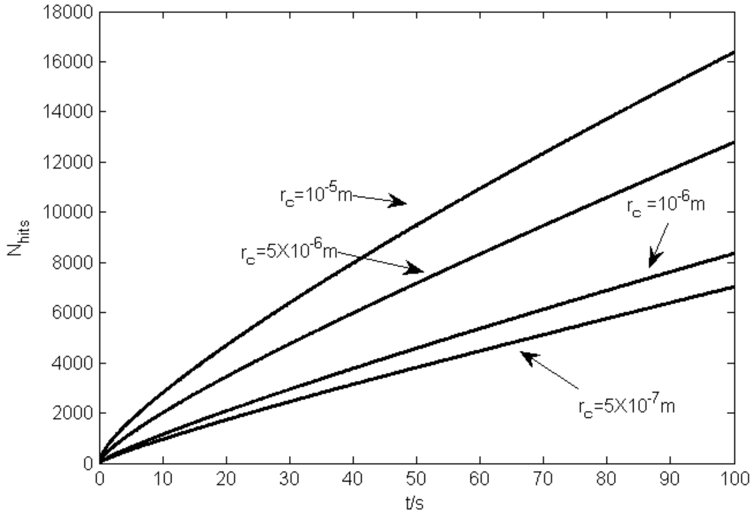

Figure 5.6: Average number of impacts on a microwire electrode at various cylinder radii. The calculation employs the following parameters: $c^* = 1pM$,$l = 1mm$ and $D = 10^{-10}m^2s^{-1}$.

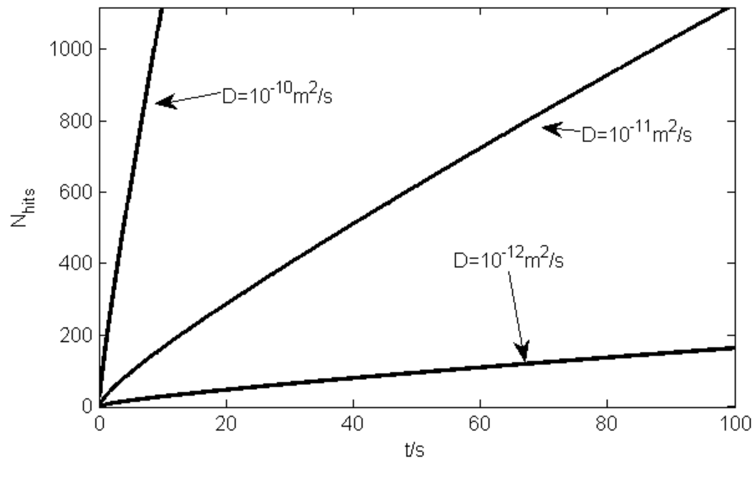

Figure 5.7: Average number of impacts on a microwire electrode at a concentration of $c^* = 1pM$ and various diffusion coefficients. The length of the wire is set to $l = 1mm$ and wire's radius is set to $r_c = 1\mu m$.

The lower limit of detection of a microwire electrode can be discussed in terms of ‘estimated’ first passage time (as shown in chapter 4). The first passage times as a function of the concentration for various radii are plotted in figure 5.8. The results show the possibility of observing a large number of impacts even at ultra low concentrations sub fM regions. As the microwire geometry provides a mixed behaviour between the transient- and the steady state regime, it is particularly useful for the ‘nano-impact’ method. Its geometry also allows the avoidance of shielding effects arising from the electrode support[27,28].

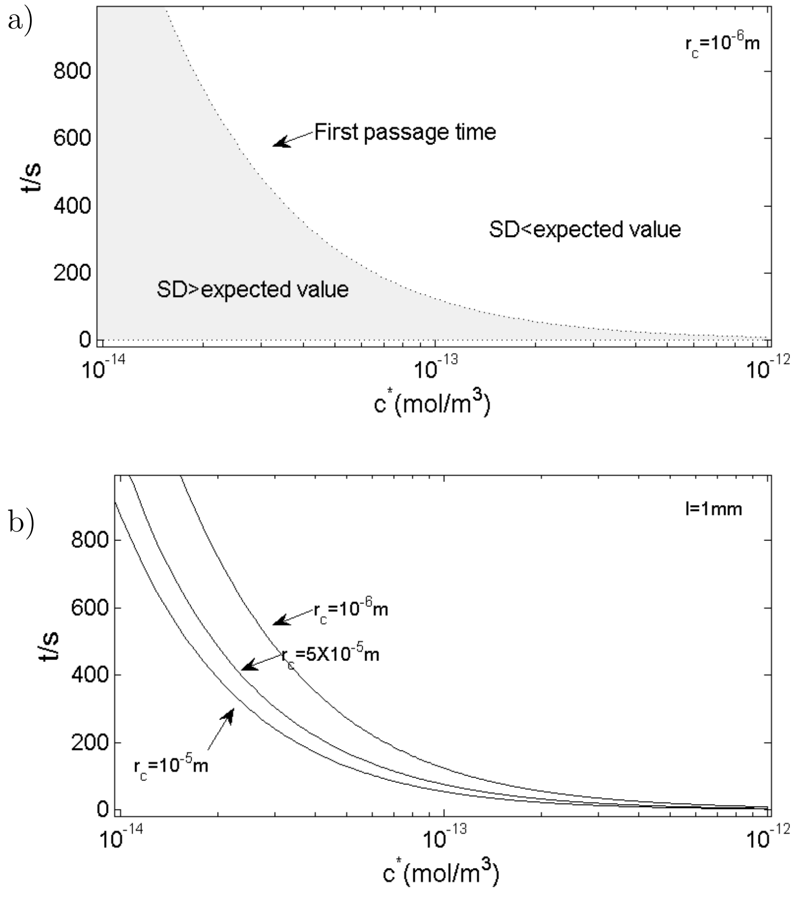

Figure 5.8: a) The limit of detection as function of concentration is estimated via the first passage time for $r_c = 1\mu m$ and $r_d = 4\mu m$. The area where the standard deviation (SD) greater than the expected value for the average number of impacts are coloured grey. b) The first passage time for various microwire radii, where $l$=1mm and $D = 10^{-10} m^2/s$.

### 5.3.3 Comparison between microdisc and microwire geometries

Comparing the previous two sections, it is shown that there are significant advantages arising from the use of microwire electrodes over the use of microdisc electrodes. As the average number of expected impacts in a given time interval is proportional to a microdisc's electrode radius as well as to a wire-electrode's length, the sensitivity of both systems can be adjusted via one or the other parameter. However, in the case of the microdisc, the electrode area increases quadratically with the electrode radius, while the electrode area only increases linearly with the length of the microwire electrode. Since the overall electrode area is proportional to the capacitance background noise[15,16], it is relevant to examine the 'limit of detection' of both geometries as function of the electrode area. Figure 5.9a-b shows the results of the estimated average first passage time as a function of the area of the cylinder and disc electrodes at ultra-dilute solutions. Figure 5.9a shows the results for 10fM solution and figure 5.9b) for 1fM. The thickness of the microwire is fixed to a representative value of $1\mu m$ whilst the length ($l$) varies with the areas.

The significantly lower values for the microwire electrode reveals the advantage of using microwire electrodes in 'nano-impact' experiment at ultra-low concentrations and large sizes of nano particles. Moreover, in the case of a very ultra dilute solution, 1fM (figure 5.9b), only the microwire case shows practical values of first passage times for carrying out a 'nano-impact' experiment. For instance, if a microwire electrode featuring a length of $1mm$ and a radius of $1\mu m$ is compared with a microdisc electrode that has the same total surface area (radius of a disc set to $44.7\mu m$) of $6.28nm^2$ in a concentration of 1fM and a diffusion coefficient of $10^{-11}m^2s^{-1}$, it is found that the first passage time is 90s in the microwire electrode case, but taken an impractical value of 660s in the microdisc

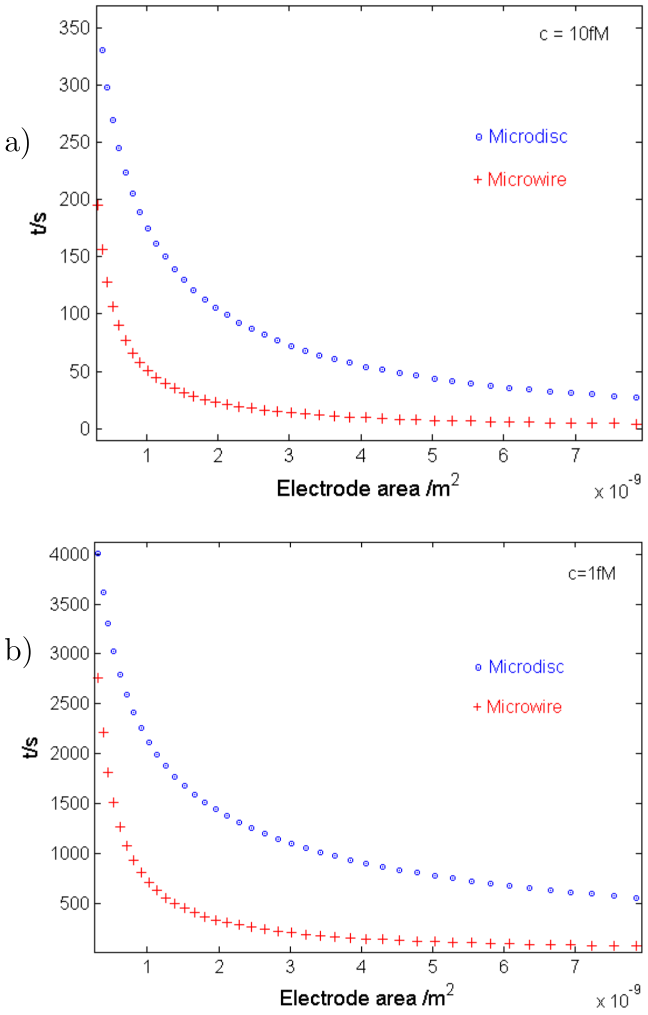

Figure 5.9: Comparison of the first passage times as function of the electrode area of a cylinder and a disc in ultra dilute solutions, 10fM (a) and 1fM (b). The diffusion coefficient is set to $10^{-11}m^2s^{-1}$ and the thickness of the cylinder is set to $1\mu m$ for all areas.

electrode case, as also observed from figure 5.9b.

## 5.4 Conclusions

Approximated analytical expressions were derived for the average number stochastic particle impacts on microdisc- and microwire electrodes. The presented analytical expressions can be applied to ‘nano-impact’ experiments and provide the relation between the electrode geometry, its size, the concentration, and the number of observed impacts expected.

Expressions for the estimated ‘first passage time’ are also provided, which can be used as a indication for the lower limit of detection in ultra-dilute solutions. The results for the number of hits/impacts and the estimated first passage time in the case of microwire electrodes reveal advantages over the use of microdisc electrodes as better statistics can be achieved even at ultra-low concentrations in the fM region while the overall electrode area and hence the capacitive background noise remains relatively small.

# References

[1] S. Eloul, E. Kätelhön, C. Batchelor-McAuley, K. Tschulik, and R. G. Compton *Journal of Electroanalytical Chemistry*, vol. 755, pp. 136–142, 2015.

[2] W. Cheng and R. G. Compton *TrAC Trends in Analytical Chemistry*, vol. 58, pp. 79 – 89, 2014. New Nanobiosensing Techniques and Bioanalysis.

[3] A. J. Bard, H. Zhou, and S. J. Kwon *Israel Journal of Chemistry*, vol. 50, no. 3, pp. 267–276, 2010.

[4] W. Cheng, X.-F. Zhou, and R. G. Compton *Angewandte Chemie International Edition*, vol. 52, no. 49, pp. 12980–12982, 2013.

[5] E. J. E. Stuart, Y.-G. Zhou, N. V. Rees, and R. G. Compton *RSC Adv.*, vol. 2, pp. 6879–6884, 2012.

[6] L. Sepunaru, K. Tschulik, C. Batchelor-McAuley, R. Gavish, and R. G. Compton *Biomater. Sci.*, vol. 3, pp. 816–820, 2015.

[7] X.-F. Zhou, W. Cheng, C. Batchelor-McAuley, K. Tschulik, and R. G. Compton *Electroanalysis*, vol. 26, no. 2, pp. 248–253, 2014.

[8] X.-F. Zhou, W. Cheng, and R. G. Compton *Nanoscale*, vol. 6, pp. 6873–6878, 2014.

[9] T. M. Alligrant, E. G. Nettleton, and R. M. Crooks *Lab Chip*, vol. 13, pp. 349–354, 2013.

[10] D. Qiu, S. Wang, Y. Zheng, and Z. Deng *Nanotechnology*, vol. 24, no. 50, p. 505707 (7pp), 2013.

[11] K. Tschulik, W. Cheng, C. Batchelor-McAuley, S. Murphy, D. Omanović, and R. G. Compton *ChemElectroChem*, vol. 2, no. 1, pp. 112–118, 2015.

[12] W. Cheng and R. G. Compton *Angewandte Chemie International Edition*, vol. 53, no. 50, pp. 13928–13930, 2014.

[13] J. C. Lees, J. Ellison, C. Batchelor-McAuley, K. Tschulik, C. Damm, D. Omanović, and R. G. Compton *ChemPhysChem*, vol. 14, no. 17, pp. 3895–3897, 2013.

[14] K. Tschulik and R. G. Compton *Phys. Chem. Chem. Phys.*, vol. 16, pp. 13909–13913, 2014.

[15] J. Yao and K. D. Gillis *Analyst*, vol. 137, pp. 2674–2681, 2012.

[16] C. Batchelor-McAuley, J. Ellison, K. Tschulik, P. L. Hurst, R. Boldt, and R. G. Compton *Analyst*, 2015.

[17] S. Eloul, E. Kätelhön, C. Batchelor-McAuley, K. Tschulik, and R. G. Compton *The Journal of Physical Chemistry C*, vol. 119, no. 25, pp. 14400–14410, 2015.

[18] Y.-G. Zhou, N. V. Rees, and R. G. Compton *Angewandte Chemie International Edition*, vol. 50, no. 18, pp. 4219–4221, 2011.

[19] J. Ellison, C. Batchelor-McAuley, K. Tschulik, and R. G. Compton *Sensors and Actuators B: Chemical*, vol. 200, pp. 47 – 52, 2014.

[20] Y. Saito *Review of Polarography*, vol. 15, no. 6, pp. 177–187, 1968.

[21] D. Shoup and A. Szabo *Journal of Electroanalytical Chemistry and Interfacial Electrochemistry*, vol. 140, no. 2, pp. 237–245, 1982.

[22] J. Heinze *Journal of Electroanalytical Chemistry and Interfacial Electrochemistry*, vol. 124, no. 1, pp. 73–86, 1981.

[23] A. Boika and A. J. Bard *Analytical Chemistry*, vol. 87, no. 8, pp. 4341–4346, 2015.

[24] E. Kätelhön, W. Cheng, C. Batchelor-McAuley, K. Tschulik, and R. G. Compton *ChemElectroChem*, vol. 1, no. 6, pp. 1057–1062, 2014.

[25] A. Szabo, D. K. Cope, D. E. Tallman, P. M. Kovach, and R. Wightman *Journal of Electroanalytical Chemistry and Interfacial Electrochemistry*, vol. 217, no. 2, pp. 417 – 423, 1987.

[26] D. T. Gillespie and E. Seitaridou, *Simple Brownian Diffusion An Introduction to the Standard Theoretical Models*. Oxford University Press, 2012.

[27] S. Eloul and R. G. Compton *ChemElectroChem*, vol. 1, no. 5, pp. 917–924, 2014.

[28] J. Ellison, S. Eloul, C. Batchelor-McAuley, K. Tschulik, C. Salter, and R. G. Compton *Journal of Electroanalytical Chemistry*, vol. 745, pp. 66 – 71, 2015.

# Chapter 6

# Hindered diffusion towards small targets

The diffusion of a particle is slowed as it moves close to a surface, and therefore can influence the predictions of the stochastic impacts of particles as it was discussed in the previous (chapters 4 and 5). In this chapter, I identify the conditions under which this hindered diffusion is significant and show that is strongly dependant on the sizes of both the particle and the target. The study focuses particularly on the transport of nanoparticles to a variety of targets including a planar surface, a sphere, a disc and a wire, and provide data which allows the frequency of impacts to be inferred for a variety of experimental conditions. Equations are given to estimate the particle fluxes explaining literature observations reported on the detected frequency of impacts. Finally a drastic effect is observed on the calculation of the mean first passage time of a single particle impacting a sub-micron sized target, showing the importance of this effect in biological systems. This work, carried out in collaboration with Dr. E. Kätelhön, and has been accepted for publication in 'The Journal of Physical Chemistry Chemical Physics'.

## 6.1 Introduction

Predicting the events of single particles stochastically hitting a target by virtue of their Brownian motion is of great interest in understanding numerous biophysical and chemical processes. Over the past decade, growing attention has been given to processes involving single particles impacting on electrodes.

Particles are usually considered to diffuse freely in solution and stochastically impact at micro- or smaller electrodes[1–3]. During an 'impact', the particle may undergo a direct charge transfer reaction or may mediate a reaction between the electrode and a solution phase species[4,5]. The average number of impacts as function of time and the individual particles' first passage times of reaching the electrode can be described by the diffusion equation as it was discussed previously in chapter 5[6,7], on which basis models can be developed providing important tools to verify experiments and to measure the concentration of nano-particles in ultra-dilute samples for example for environmental studies[8]. The impact method has recently opened new ways to identify and model nano-particle agglomeration in solution[9–11], to study chemical mechanisms[12–14], and to characterise the composition of modified nano-particles[15,16]. In general, studying stochastic arrivals of particles to small targets and the mean first passage time of a single particle, is of large interest in many processes. These include the interaction of biological macromolecules[17] and nano-particles[18], modelling drug delivery[19], and in biological processes such as rate regulation[20].

The transport of particles, from bulk solution to a reaction zone close to the surface of a target is usually described solely by Brownian motion. Thus the frequency of observed impacts can be estimated by solving the diffusion equation:

$$\frac{\partial c}{\partial t} = \nabla \cdot (D \cdot \nabla c) \tag{6.1}$$

with mixed Dirichlet-Neumann boundary conditions for the adsorption at the surface of a small target, such as an electrode, and reflection elsewhere.

In bulk solution, each particle has a characteristic isotropic diffusion coefficient $D_0$ that reflects its size and shape. The Stokes-Einstein relation gives the bulk diffusion coefficient of a spherical particle in the limit of low Reynolds numbers, which is found to be a good estimation even for particles in water of radii $r_p$ of only a few nanometres[21]:

$$D_0 = \frac{k_B T}{6\pi\eta r_p} \tag{6.2}$$

where $\eta$ is the dynamic viscosity, $k_B$ is the Boltzmann constant, and T is the temperature. When the space available for diffusion is confined, the particle's hydrodynamic mobility must be taken into account when modelling its diffusive transport. Brenner[22] and Faxén[23] have calculated the corrections to the Stokes-Einstein relation for the normal- and parallel diffusion coefficients near a wall. The expressions agree well with experiments[24,25]. Bevan and Prieve have approximated the analytical solution made by Brenner for the case of hindered diffusion normal to a wall for a sphere with a radius $r_p$, separated by a distance $h$:

$$D(h) = \frac{6h^2 + 2r_p h}{6h^2 + 9r_p h + 2r_p^2} \cdot D_0 \tag{6.3}$$

where $h$ is the separation distance between the wall and the closest point of the particle surface. The same study reported an experiment to quantify diffusion coefficients of microbeads at very close distances to walls. Using optical measurements they produced results that followed the above expression for a ratio of separation ($h$) to the particle radius, $h/r_p = 40\text{nm}/3.5\mu\text{m} \sim 0.01$. The hindering of diffusion due to space confinement (also referred to as "geometrically constrained Brownian motion") is also evident in porous media such as zeolites[26], and is crucial in various models of biological systems[27,28] such as for the delivery of nano-medicine in the confined zone of a tumour rich in collagen[29].

When modelling the diffusive mass transport of particles from the bulk, far from any boundaries, to an active site on a surface, the effect of hindered diffusion is however often legitimately neglected in experimental studies. For instance, in nano-impact experiments, the observed mass transport of silver nano-particles showed good agreement with free diffusion without any consideration of hindered diffusion[7,30]. Also, a previous model for diffusion towards a sphere showed only minor differences in comparison to experiments with nickel nano particles of radius $26nm$[31]. On the other hand, previous stochastic calculations of the duration of an impact event at an electrode showed the necessity of including hindered diffusion for predicting the residence time of an impact[32]. Additionally, a very recent study modelled the case of a convection-diffusion system for a rotating electrode in a nano-impact experiment and showed that hindered diffusion significantly affects the flux towards a rotating electrode[33].

This work shows that when the target is small, hindered diffusion becomes important for the prediction of the particle flux and the estimation of the number of impacts in experiments. I show that this effect is due to convergent diffusion[34], where the diffusion field is confined to a small space near the surface (not centre) and regardless of the cell size. This confinement of the diffusion field defines the influence of hindered diffusion on the flux and the first passage time of a particle searching for a target. The flux is found to be a function of the size of the target and its geometry. Approximate functions are provided and can be used directly to estimate the flux of particles towards electrode. It is shown below that the effect becomes important for nano-particles searching for a target of the order of a micrometre or less.

The study has also importance for various nano-particle or macromolecule attachment models[18,19] (see also illustration in figure 6.1). Moreover, first passage statistics are important to understand biological processes such as the synapse regulation of the exit rate through an ultra small window in a bounded domain[20] and how viruses travel towards a nuclear pore[35]. These types of diffusion problem are analogous to that examined below and known as the 'Narrow escape time' problem[36,37]. It is shown here, that in such systems the estimation of the first passage time, is changed drastically as a function of the target size due to the hindering of diffusion.

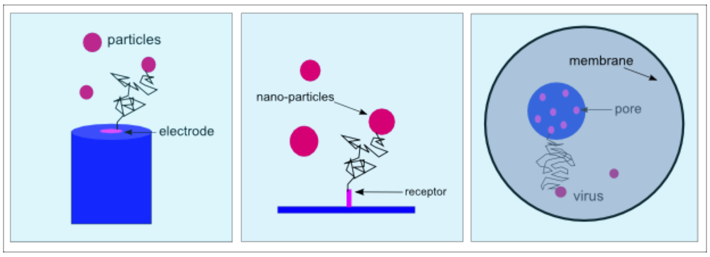

Figure 6.1: Hindered diffusion is strongly dependant on the sizes of both the particle and the target.

In this chapter, the importance of the effect is first examined on the steady state flux at small targets, by solving the diffusion equation for a simplified one-dimensional (1D) model. It is shown that the transport is strongly influenced by the hindering of diffusion in the case of sufficiently small targets. Then the results of a numerical study are provided for a variety of targets including spherical, disc and wire electrodes. Approximate but applicable functions are given for the steady state flux and data for the expected number of impacts in various experimental conditions.

## 6.2 Simplified model

For the purpose of explaining when hindered diffusion has an influence on the diffusion flux, I examine the analytical solution of diffusion towards a small sphere. In the context of the 'nano-impact' method, the size of the electrode must be small in order to minimize the occurrence of simultaneous impacts on the electrode and to reduce the capacitive noise so as to facilitate small charge measurements. Therefore micron-sized electrodes, or smaller, are commonly employed[8]. First, neglecting hindered diffusion, the diffusion equation results in Fick's second law in radial coordinates:

$$\frac{\partial c}{\partial t} = D_0 \left( \frac{\partial^2 c}{\partial r^2} + \frac{2}{r} \frac{\partial c}{\partial r} \right) \tag{6.4}$$

$r$ is the radial coordinate with r=0 corresponds to the centre of the sphere. Along with the boundary conditions of a fully adsorbing sphere with the radius $r = r_s, c = 0$ and $r = r_\infty, c = c^*$ this solves to give[34,38]:

$$c(r,t) = c^* \left[ 1 - \frac{r_s}{r} \mathrm{erfc}(\frac{r - r_s}{\sqrt{4Dt}}) \right] \tag{6.5}$$

and the flux at the surface is:

$$-D_0 \frac{\partial c}{\partial r}\bigg|_{r=r_s} = c^*(r_s, t_0) D_0 \left[ \frac{1}{\sqrt{\pi D_0 t}} + \frac{1}{r_s} \right] \tag{6.6}$$

For the convenience of the reader, the derivation is supplied in Appendix. The flux towards a sphere illustrates the convergent behaviour of the diffusion field. The time dependent term is dominant at short times and vanishes at larger time, whilst the $1/r_s$ term is size-dependent but constant with time. At large electrodes and practical time scales, the transient is dominant and the second convergent term can be neglected.

An insightful exercise to understand the influence of hindered diffusion on such a system is to add a distance-dependent diffusion coefficient in a form of a simplified function. This allows the analytical study of the hindered-diffusion effect on the flux. To this end, a simple function is used instead of the more complex approximation given in eq. (6.3):

$$D_{trial}(r) = D_0 \mathrm{e}^{-Br_s/r} \sim D(r) \tag{6.7}$$

where $r$ is the distance between the centre of the sphere ($r = 0$) to the closest point of the particle surface. $r_s$ is the sphere radius and a positive point in $r$ direction. $B$ is a fitting parameter that might be fitted to various $r_p$ and has no units. The dimensional parameters are given in table 1. It can be seen in figure 6.2 that the function closely follows the Bevan's and Prieve's approximation for this purpose. For the simplicity of the present exercise, the function depends on the distance from $r = 0$, the centre of the small sphere target. This means that the function is finite when $r_s/r = 1$ and not zero, thus is less valid for very small $B$ (see also figure 6.2).

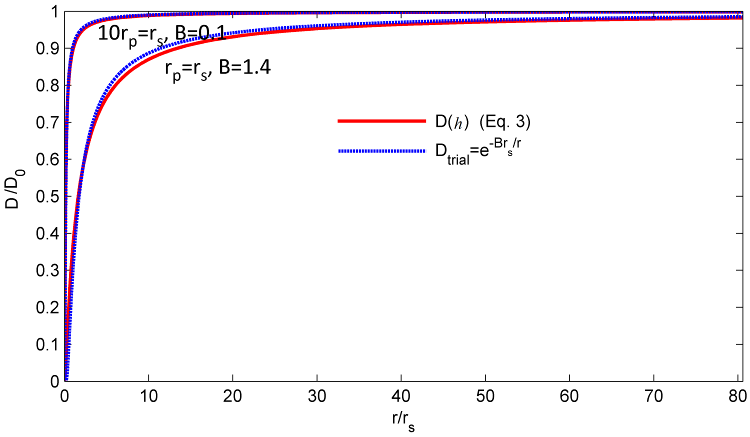

Figure 6.2: Example of the behaviour of the approximate exponential function compared to $D(h)$ when $r_s = r_p \rightarrow B = 1.4r_s$ and $r_s = 10r_p \rightarrow B = 0.1r_s$. For simplicity of the model, the distance is taken from r=0 the centre of the small target.

Substitution of the function into the diffusion equation, and simplifying to steady state, the diffusion equation becomes:

$$0 = \frac{\partial^2 c}{\partial r^2} + \left(\frac{2}{r} + \frac{Br_s}{r^2}\right)\frac{\partial c}{\partial r} \tag{6.8}$$

By reducing order and substituting the boundary condition $c(x = 0, t) = 0$ and $c(x = \infty, t) = c^*$, the flux solves to (see also Appendix):

$$J_{ss} = \frac{D_0 c^*}{r_s}\left[\frac{B}{(1 - \mathrm{e}^B)}\right] \tag{6.9}$$

It can be seen that when $B \to 0$, (when the particle is very small relative to $r_s$,) the term in the squared brackets tends to unity. This results in the same steady state current found for non-hindered mass transport (eq. 6.6). When $B$ is greater than 0, the steady state flux decreases and at very large $B$ ($B \to \infty$), the steady state flux tends to zero. *This shows that the effect of limited diffusion on the steady state flux strongly depends on the ratio $r_p/r_s$.* For example, when $r_s = r_p$, $B$ is fitted to 1.4 and the steady state current is reduced to $0.45 D_0 c^*/r_s$, which is 45% of the steady state flux found without hindered diffusion. When $r_s = 10r_p$, however, the steady state flux is only reduced to 95 %, demonstrating that when the target is sufficiently large, hindered diffusion can be neglected in the steady state.

## 6.3 Numerical study

The numerical study is divided into three parts. First, the results for a 1D and macro-scale target are reported in order to show in which cell size the contribution of hindered

Table 6.1: Dimensional parameters

| Parameter | Description | Units |
|---|---|---|
| $r_p$ | Radius of a particle | $m$ |
| $r_c$ | Radius of a cell | $m$ |
| $r_d$ | Radius of a target disc | $m$ |
| $r_s$ | Radius of a target surface | $m$ |
| $r_w$ | Radius of a target wire | $m$ |
| $l$ | Length of a wire | $m$ |
| $L$ | Length of a 1D cell | $m$ |
| $D_0$ | Diffusion coefficient from the Stokes-Einstein eq. | $m^2s^{-1}$ |
| $D$ | Diffusion coefficient, distance dependant | $m^2s^{-1}$ |
| $c$ | Number concentration | $particles/m^3$ |
| $c^*$ | Bulk number concentration | $particles/m^3$ |
| $j$ | Flux density | $particles/(m^2s)$ |
| $J_{ss}$ | Steady state flux | $particles/s$ |
| $\tau_0$ | First passage time for non-hindered diffusion | $s$ |
| $\tau_D$ | First passage time for hindered diffusion case | $s$ |
| $P_{impact}$ | Probability of impact | |
| $N_{impact}$ | Average number of impacts | |
| $X_t$ | Average tunnelling distance | $m$ |

diffusion can be neglected as function of the particle size. Second, the results for the flux towards a small sphere are shown for a cell of arbitrary size, and show a strong decrease in the flux which depends on the ratio between the particle size and the target size. I also report the drastic effect of the hindered diffusion on the first passage time calculations for very small targets. Third, the study of two important experimental systems is reported, the diffusion of particles towards a microdisc and a wire.

### 6.3.1 1D cell and a macro-scale target

The study of a 1D linear system is a starting point that shows the domination of near-wall hindered diffusion as function of a confined cell with a length $L$. The target is located at $x = 0$ and a fixed wall at $x = L$. The cell is schematically shown in figure 6.3. When a particle hits the target, a full adsorption is assumed. For instance, in the case of the 'impact' method, a high over-potential is applied on the electrode as a target and metal-particles that arrive by diffusion are fully oxidised. The cell in figure 6.3 shows the typical diffusion field (layer) that propagates from the adsorbing target and reaches the wall at long times. The non-homogeneous hydrodynamic loss is a particle size dependent function and assumed to be small in comparison to a macro-target, thus it is illustrated as a thin layer next to the adsorbing surface (figure 6.3). Additionally, the effect of hindered diffusion on the upper wall can be neglected, though in a very small confined space this effect would be significant.

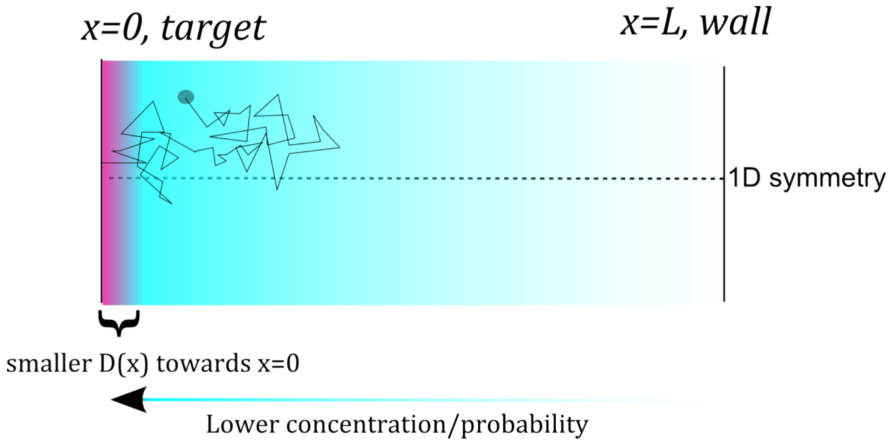

Figure 6.3: Confined 1D geometry featuring a large target. The drawing illustrates the diffusion field (cyan to white gradient) and the non-homogeneous reduction in the diffusion coefficient (violet to blue). Changes in the diffusion coefficient next to the upper wall ($x = L$) are neglected.

### Model

The diffusion equation in 1D has the form:

$$\frac{\partial c}{\partial t} = \nabla \cdot (D(x) \cdot \nabla c) \tag{6.10}$$

where $D(x)$ follows Bevan and Prieve approximation shown earlier (eq. 6.3).

It is noted that the expression (eq. 6.3) tends to zero at the surface of the wall. Moreover, at very small distances from the wall the continuous model is not valid due to surface attraction or repulsion forces, double layer interactions, or even the wall roughness[23]. However, in a Faradaic reaction, the charge is transported from the surface of the particle to the electrode via electron tunnelling. Thus, an average tunnelling distance of the order of $X_t = 1nm$ is assumed, and locates the adsorbing boundary at this point[31], so that on this boundary, $c(x = X_t, t \geq 0) = 0$. As a result, the diffusion coefficient is finite on the adsorbing boundary. In the results below for the quantitative studies, an explicit expression is used for the tunnelling distribution function as is discussed later in this chapter. At the upper boundary a reflection boundary condition is set:

$$t \geq 0, \quad \left. \frac{\partial c(x,t)}{\partial x} \right|_{x=L} = 0 \tag{6.11}$$

At $t = 0$ the concentration is set to the initial concentration $c^*$. The flux is evaluated numerically through mass balance to avoid numerical errors in the calculation of the diffusion coefficient next to the wall:

$$J(t) = \int_{X_t}^{L} \frac{\partial c}{\partial t} \mathrm{d}x \tag{6.12}$$

In the case of small cells, instead of presenting the flux of particles, it is more informative to calculate the cumulative probability of an impact from a single particle searching the adsorbing boundary in a finite cell:

$$P_{impact}(t) = c^* L - \int_{X_t}^{L} c(x,t) \mathrm{d}x \tag{6.13}$$

where $c^*$ is the initial probability density to find a single particle in size $L$ and equals $1/L$. The model is solved numerically using the Implicit-Finite Difference Method which is detailed in the Appendix.

## Discussion

The results of the probability of an impact at different sizes of confined cells are presented in figure 6.4 for representative $r_p$ of $100nm$. The results are also compared to calculations of the 'non-hindered' case. It is shown that the effect becomes smaller as the cell gets larger, and negligible in cells which are above $100\mu m$ in length.

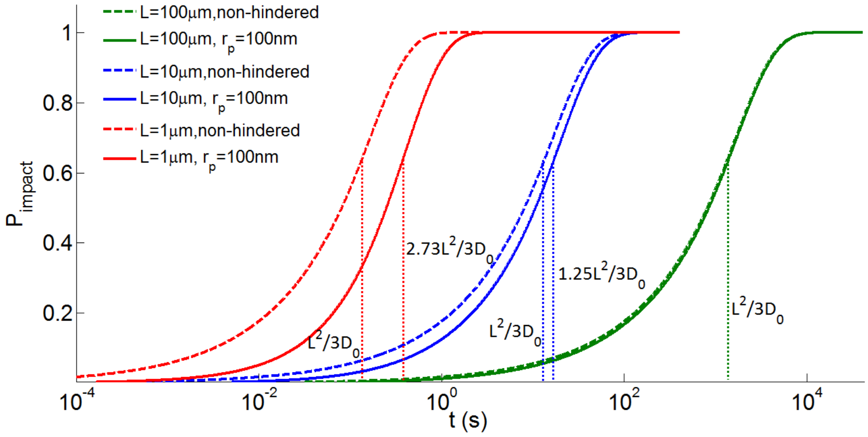

Figure 6.4: The influence of hindered diffusion on the probability of impact, in a confined space for large targets and various cell sizes $L$=100$\mu$m,10$\mu$m,1$\mu$m. The dashed lines presents the non-hindered calculations, and the solid lines the calculations with hindered diffusion.

The analytical solution of the mean time for impact with no consideration of hindered-diffusion follows $L^2/3D$ in such a geometry [4]. This value is compared to the mean time of impact in the 'hindered' case which is calculated numerically (also referred to the 'mean first passage time')[39]:

$$\tau_0 = \int_0^{\infty} \int_{X_t}^{L} c(x,t) \mathrm{d}x \mathrm{d}t \tag{6.14}$$

As shown in figure 6.4. Only at very small $L = 1\mu$m, is a significant effect on the expected time for impact observed for the $100nm$ particles. It is concluded from these results that for a macro electrode as a target, the effect of hindered diffusion can be legitimately

---

[4] $L^2/3D$ is calculated directly from the integration of the mean passage time: $D_0 \Delta\tau(x) = -1$ with the boundary conditions, $\tau(0) = 0$ and $\partial_x \tau(L) = 0$, for a particle with a initial uniform probability density in all $x$ (from 0 to L).

neglected unless the cell is confined to a very small size. This is easily explained by the fact that in a non-confined cell the diffusion layer gets much further away from the hindered diffusion zone and therefore most of the time the particle 'searches' for the target with a bulk diffusion coefficient (as illustrated in figure 6.3). Hence, the expectation time or the flux in a many-particle system are in such cases not much influenced by hindered diffusion. This behaviour is valid only in the case of large targets as discussed in the previous section. I next provide the calculations for the case of a finite sphere where near-wall hindered diffusion can play an important role regardless of the cell size.

### 6.3.2 1D cell - a finite sphere target

The diffusion of a particle towards a sphere is schematically shown in figure 6.5. In this case, the diffusion layer is convergent (also confined to a small distance), depends on the particle size and can be comparable to the hindered diffusion zone. As a result, the particle diffusion coefficient is hindered for a significant fraction of its searching time.

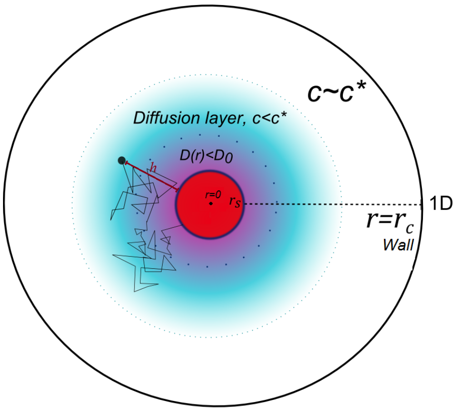

Figure 6.5: Bounded cell of a size $r_c$ with 1D radial symmetry (solid circle), featuring a finite sphere electrode as a target ($r_s$). The drawing illustrates the diffusion field/layer (cyan to white gradient, limited by the denser-doted circle) and the hindered diffusion layer near the spherical target (violet to blue, limited by the space-doted circle).

## Model

The non-homogeneous diffusion problem is solved numerically in spherical coordinates and 1D radial symmetry:

$$\frac{\partial c(r,t)}{\partial t} = D(r - r_s)\left(\frac{\partial^2 c}{\partial r^2} + \frac{2}{r}\frac{\partial c}{\partial r}\right) + \frac{\partial D(r - r_s)}{\partial r}\frac{\partial c}{\partial r} - P \tag{6.15}$$

where $D(r - r_s)$ is the hindered diffusion coefficient calculated in accordance with eq. (6.3), where $h$ equals $r - r_s$.

In order to get a better accuracy for very small targets and particle sizes, instead of using a fully adsorbing boundary, an electron tunnelling approximation is used via a sink term ($P$), to model the impact of a particle as a fast reaction at a very small distance from the surface. This follows an exponential fall off of the tunnelling probability with distance:

$$P = c(r,t)\nu \mathrm{e}^{-\beta(r-r_s)} \tag{6.16}$$

$\nu$ is the tunnelling rate ($s^{-1}$) of the process which is chosen to be sufficiently large to provide invariable convergent values. $\beta$ is the electron decay factor ($m^{-1}$) which is solvent dependent and from scanning tunnelling microscope measurements is thought to be $1.59\mathring{A}^{-1}$ in aqueous media[40,41]. It is noted that our calculation is found to be insensitive to small changes in the value of this parameter, however the effect of the tunnelling distance varies for various sizes of targets as is discussed next in the dimensionless analysis and in the result.

### Dimensionless form

The diffusion equation can be transformed into a dimensionless form in order to reduce the number of dependant parameters. The $r$ coordinate, the particle radius, and the cell size are normalised to the radius of the sphere:

$$R = r/r_s, \;\; R_p = r_p/r_s, \;\; R_c = r_c/r_s \tag{6.17}$$

A dimensionless time is introduced:

$$\tau = D_0 t/r_s^2 \tag{6.18}$$

and the diffusion coefficient and the concentrations can be normalised to:

$$D^*(R) = D(R)/D_0 \tag{6.19}$$

$$C = c/c^* \tag{6.20}$$

This results in the dimensionless form of the diffusion problem:

$$\frac{\partial C}{\partial \tau} = D^*(R-1)\left(\frac{\partial^2 C}{\partial R^2} + \frac{2}{R}\frac{\partial C}{\partial R}\right) + \frac{\partial D^*(R-1)}{\partial R}\frac{\partial C}{\partial R} - P^* \tag{6.21}$$

where the dimensionless sink term is given as:

$$P^* = \frac{C r_s^2}{D_0}\nu \mathrm{e}^{-\beta^*(R-1)} \tag{6.22}$$

and $\beta^* = \beta r_s$.

Reflection boundary conditions are used everywhere, at the surface of the electrode sphere and at the upper boundary of the cell.

The dimensionless total flux of particles impacting the sphere is calculated through the mass balance as follows:

$$J_0(\tau) = 4\pi \int_1^{R_c} \frac{\partial C}{\partial \tau} R^2 \mathrm{d}R \tag{6.23}$$

The dimensional flux is therefore:

$$J(t) = J_0(\tau) c^* r_s D_0 \tag{6.24}$$

A full parametric study is carried out to quantify the time dependence and the steady state flux. Details on the numerical solution and convergence tests are provided in the computational methods (see Appendix).

### Discussion

The effect of hindered diffusion on the transient flux of particles for various ratios $R_p$ ($r_p/r_s$) impacting on a sphere is shown in figure 6.6. In order to provide a clear estimation of the effect at different ratios ($r_p/r_s$), the net flux ($molm^{-2}$) is normalised to the theoretical steady state flux towards a sphere ($4\pi c^* r_s D_0$).

The results show a strong dependence of the expected flux on the ratio $r_p/r_s$. The results also suggest that the transient flux is strongly influenced by hindered diffusion at all times. At very short times this is due to the arrival of particles from very short distances, where $D(r) << D_0$. In contrast with the case of a macro-scale flat target, the steady-state flux strongly depends on the particle size.

Since $\beta^*$ depends on $r_s$, $\beta^*$ can also affect the flux response. Figure 6.7 shows the

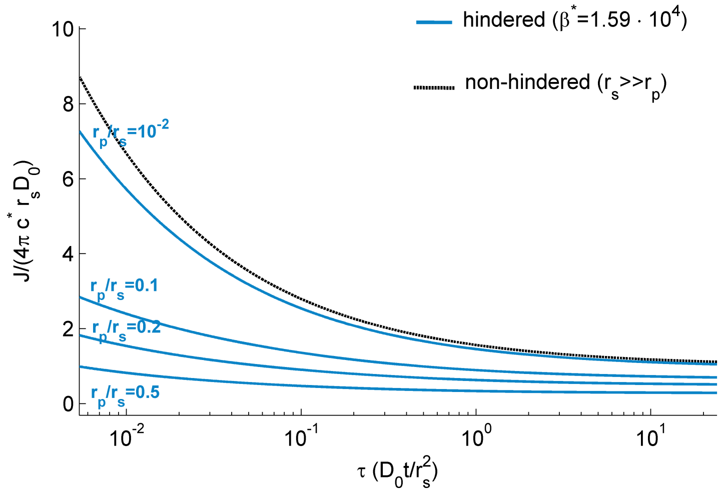

Figure 6.6: Flux of particles of various $R_p$ ($r_p/r_s$), normalised to steady state and as function of dimensionless time. $\beta^* = 1.59 \cdot 10^4$, which corresponds to $r_s = 1\mu m$ and $\beta = 1.59\mathring{A}^{-1}$ in aqueous media.

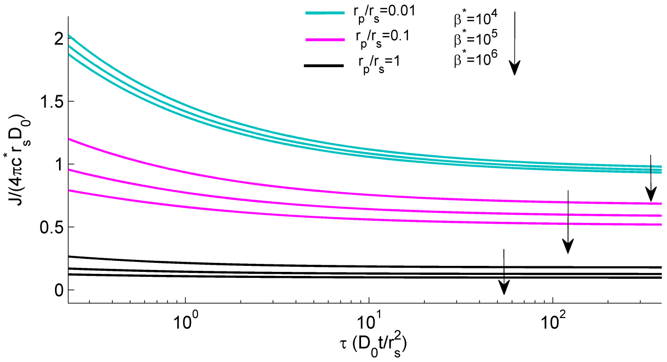

Figure 6.7: Flux of particles of various $R_p$ ($r_p/r_s$=0.01,0.1,1), and for various $\beta^* = 10^4, 10^5, 10^6$. The flux is normalised to steady state and as function of dimensionless time.

behaviour of the normalised flux of particles for various ratios $r_p/r_s$ and for a large range of $\beta^* = 10^4 - 10^6$. The figure shows that the flux depends also on $\beta^*$ and therefore is a function of the absolute value of the tunnelling size. When the tunnelling distance is smaller (larger $\beta^*$), the effect of hindered diffusion layer is more dominant since the diffusion coefficient is damped to a lower value before charge transfer occurs. Accordingly, it is observed from the dimensionless analysis that for a given $r_s/r_p$, when $r_s$ is larger, the flux is reduced and tends to be more affected by the hindered diffusion. Figure 6.7 also shows that when $r_s/r_p$ is large (0.01) the effect of $\beta^*$ is moderated. When the particle is very small relative to the target, the effect of hindered diffusion is reduced since the hindered diffusion layer becomes comparable in size to the size of the tunnelling zone.

For practical use, the results using dimensional sizes of $r_s$ and $r_p$ are also presented. The effect of hindered diffusion on the transient flux of particles impacting on a sphere is shown in figure 6.8. In order to provide a clear estimation of the effect at different sizes of electrodes and particles, the flux is normalised to the theoretical steady state flux of each case, and the time is given in dimensionless units.

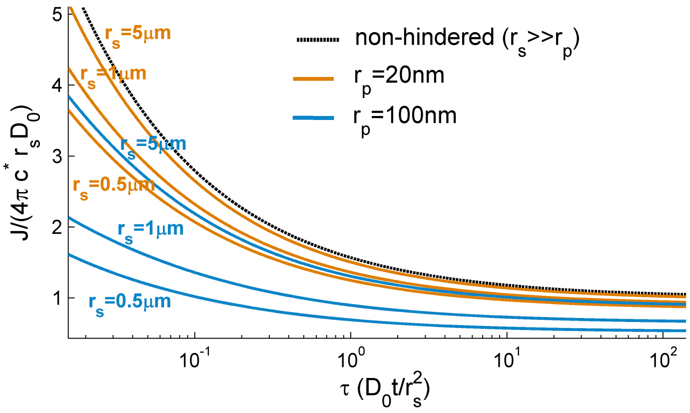

Figure 6.8: Flux of particles of radius $20nm$ (orange curves) and $100nm$ (blue curves) normalised to steady state and as function of dimensionless time.

The results show a large reduction of the expected flux for $100nm$ particles and a moderate effect on the flux of $20nm$ particles. The effect found to be significant for target sizes in the order of $1\mu m$ and below.

In many systems for single particle detection such as the 'impact' method, the diffusive flux of particles is at steady state. I have conducted a parametric study of the steady state flux ($J_{ss}$), to find the correlation between the size of the target and the particle size. The map of the flux relative to the flux under non-hindered diffusion was simulated for a set of 4000 parameters and is given in figure 6.9. The least-square method is used to fit the steady state flux map to an exponential function, relying on the behaviour found earlier, and the knowledge of the asymptotic solutions ($r_p/r_s \to \infty, J \to 0$ and $r_p/r_s \to 0, J \to 1$). The steady state equation in the case of particles impacting a sphere can be approximated as:

$$sphere: \; J^{fit}_{ss,D(r)} = 4D_0\pi c^* r_s (0.57\mathrm{e}^{-2.34\frac{r_p}{r_s}} + 0.43\mathrm{e}^{-0.21\frac{r_p}{r_s}} \pm Er) \tag{6.25}$$

The equation is fitted with an r-square value of 0.996, and can be used to estimate of the effect of hindered diffusion towards a sphere. The function provides a good fitting for most ratios of $r_p/r_s$, with a maximum deviation $Er = \pm 0.08$. A residual map is provided for better accuracy in the Appendix. The equation along with the residual map can be used directly to estimate the flux of particles towards a sphere or a hemi-sphere.

The map in figure 6.9 and eq. (6.25) show the strong relation of the hindered diffusion as function of the ratio $r_p/r_s$. It is also shown that the effect is significant for micrometre targets and large nano-particles of a few hundreds nanometre sizes.

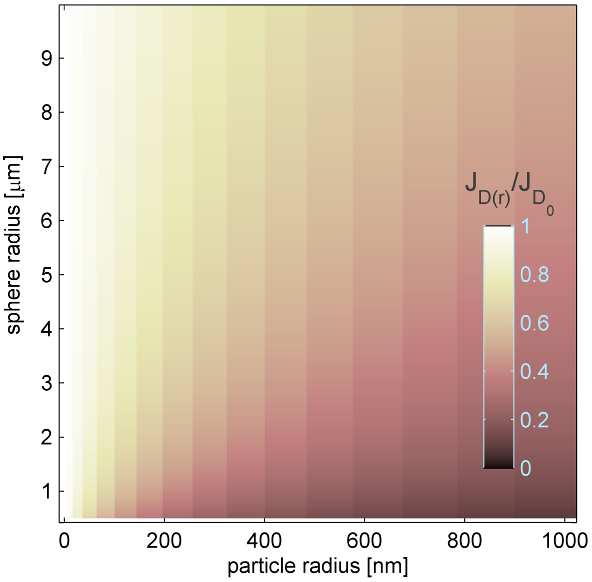

Figure 6.9: The steady state flux map as a function of the nano-particle and sphere size.

Note that the results of the map presented in figure 6.9 and eq. (6.25) hold when the target is large in comparison to the particle size. When the particle size is comparable or larger than the target, the hydrodynamic mobility is less influenced by the target and would result in a deviation from the steady state flux calculated.

I next address the result of the mean first passage time (MFPT) of a particle searching for a sphere, bounded in a spherical cell of the order of a few micrometres. In such cells the target can be of the sub-micron size. This is relevant for biological processes involve with calculations of the mean first passage times, for instance in the case of biomolecules searching for small targets[35,36] and in nano-electrode systems[3]. The MFPT is calculated directly through the temporal integration of the survival density function:

$$\tau_D = \int_0^{\infty} \int_{r_s}^{r_c} 4\pi c(r,t) r^2 \mathrm{d}r \mathrm{d}t \tag{6.26}$$

for one particle in a bounded sphere with radius $r_c$. Parametric study was carried out to find how the MFPT changes under the influence of near-wall hindered diffusion. For all cases $r_c = 100 r_s$ is selected to be far enough from the target. The ratio between the calculation of the MFPT for non-hindered case $\tau_0$ to the calculation of the 'hindered' case $\tau_{D(r)}$ are presented in the colour-map in figure 6.10. The map shows the deviation from the mean first passage time can be significant. For instance, when the target is in the order of a few hundreds nanometres, even considering a small radius of particle, such as $20nm$, the expected MFPT is five times smaller than that calculated when including hindered diffusion. The map shows that the first passage time can be reduced drastically for small targets even when considering the problem of small nano-sized particles searching for small targets.

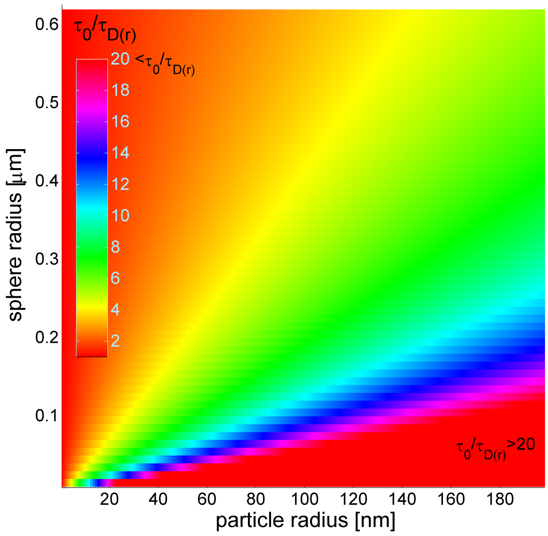

Figure 6.10: The mean first passage time (MFPT) of a particle searching for a sphere for the ‘non-hindered’ case relative to the MFPT of the ‘hindered’ case.

## 6.4 Near-wall Hindered diffusion of particles towards a finite disc and a wire

In impact experiments or in general in sensing applications, microdisc or wire target[8] geometries are generally used. These behave as fully adsorbing surfaces in the case of electrodes when a sufficiently high potential is applied. The number of expected impacts in these systems is determined from the diffusion flux. Here the deviation from the expected flux is quantified as function of the disc radius or the wire radius in comparison to the particle size.

### 6.4.1 Hindered diffusion of particles towards a finite disc

Microdisc electrodes are typically fabricated by insulating a metal wire with a radius $r_d$ of the order of microns in a glass sheath with a radius $r_c$. The 2D symmetry is illustrated in figure 6.11.

When particles arrive close to the surface of the sheath the hydrodynamic mobility

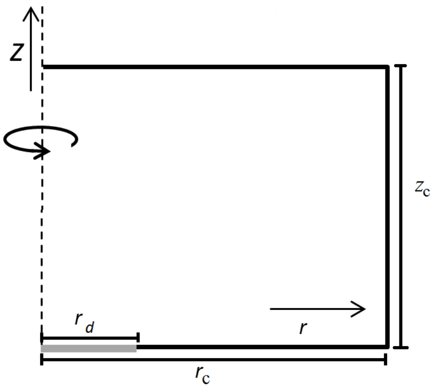

Figure 6.11: Microdisc electrode with a radius $r_d$ insulated with a sheath of a size $r_c(\gg r_d)$ in a cell size of $z_c(\gg r_d)$.

loss is anisotropic in the normal ($\hat{\mathbf{z}}$) and parallel directions ($\hat{\mathbf{r}}$). In cylindrical coordinates, the diffusion equation has the form[42]:

$$\frac{\partial c}{\partial t} = \nabla \cdot \{D \cdot (\frac{\partial c}{\partial r}\hat{r} + \frac{1}{r}\frac{\partial c}{\partial \phi}\hat{\phi} + \frac{\partial c}{\partial z}\hat{z})\} \tag{6.27}$$

and the diffusion coefficient is represented by a second rank tensor:

$$D = D_0 \begin{bmatrix} \sigma_{rr} & \sigma_{r\phi} & \sigma_{rz} \\ \sigma_{\phi r} & \sigma_{\phi\phi} & \sigma_{\phi z} \\ \sigma_{zr} & \sigma_{z\phi} & \sigma_{zz} \end{bmatrix} \tag{6.28}$$

For an axisymmetric system like the ones considered, the anisotropic diffusion equation simplifies to:

$$\frac{\partial c}{\partial t} = D_0 \left( \sigma_{rr}\frac{\partial^2 c}{\partial r^2} + \frac{\sigma_{rr}}{r}\frac{\partial c}{\partial r} + \sigma_{zz}\frac{\partial^2 c}{\partial z^2} + \frac{\partial \sigma_{zz}}{\partial z}\frac{\partial c}{\partial z} \right) - P \tag{6.29}$$

(More details are provided in the Appendix). $\sigma_{zz}(z)$ follows the Bevan and Prieve approximation(eq. (6.3)) and for the parallel diffusion coefficient, $\sigma_{rr}(z)$, Faxén's approximation can be used[23]:

$$\begin{aligned}\sigma_{rr}(h) = 1 - \frac{9}{16}\left(\frac{r_p}{h+r_p}\right) + \frac{1}{8}\left(\frac{r_p}{h+r_p}\right)^3 \\ -\frac{45}{256}\left(\frac{r_p}{h+r_p}\right)^4 - \frac{1}{16}\left(\frac{r_p}{h+r_p}\right)^5\end{aligned} \tag{6.30}$$

Anisotropic diffusion in this system is considered for the disc and for the insulating sheath surrounding it. Hindered diffusion for the cell boundaries far from the electrodes is neglected. Instead of using an adsorbing boundary on the disk, a sink term $P$ is added, as is discussed for the case of a sphere. Here the electron tunnelling zone is implemented as a function of the distance $z$ from the surfaces. Reflection boundary conditions are considered everywhere, on the insulating sheath, on the cell boundaries, and on the disk electrode. The cell boundaries in the case of the microdisc are generally far enough to affect diffusion in the time scale of experiment. Invariably, $r_c$ and $z_c$ are chosen to be larger than $6\sqrt{D_0 t}$[34]. At zero time, the concentration in all space is set to the bulk concentration, $c(x, t = 0) = c^*$.

The 2D anisotropic diffusion equation is solved numerically (see methods in Appendix) in order to calculate the flux and the accumulated number of impacts on a microdisc surface. The value of $\beta$ selected is $\beta = 1.59\mathring{A}^{-1}$ and therefore assume that the zone of electron transfer is tiny in comparison to the size of the hindered diffusion layer and diffusion layer. The effects of hindered diffusion on the transient flux and the number of impacts on a micro-disc are presented in figure 6.12a and figure 6.12b, respectively. In order to provide a clear estimation of the effect at different sizes of electrodes and particles, the flux is normalised to $J/c^* r_s D_0$, and the time is in dimensionless units $(tD_0/r_s^2)$. The number of impacts in 6.12b is further normalized to $c^* r_s^3$. The transient curves for the different target sizes and for 100$nm$ and 20$nm$ particle sizes are compared to the flux for non-hindered case. The results show the different behaviour of the flux and the expectation of the number of impacts is influenced by the disc size in the case of a particle of size 100$nm$ but only a moderate deviation is expected for small size nano-particles, even at ultra-small electrodes.

The result explains the fit to Fick's diffusion (non-hindered case) of experimental measurements to determine concentrations of silver nano-particles and for Nickel nano-particles via 6.9$\mu$m microdisc electrodes[30]. In their work, the frequency of impacts was measured for various dilute concentrations, and found to increase linearly with the concentration. Moreover, for each concentration they fitted the accumulative number of impacts to the theoretical number of impacts from Fick's diffusion which was found to be with good agreement (less then 5% deviation in a 5s measurement).

The result shows an example of the importance of this analysis for the determination of nano-particles in environmental applications.

The steady-state response is examined further by a parametric study in a similar way as discussed for the sphere. The colour map of the ratio between the steady state flux to the steady-state flux in non-hindered case is presented in figure 6.13. It is also assumed that $\beta = 1.59\mathring{A}^{-1}$ and show the result for the dimensional case where $r_s$ and $r_p$ is varied. The map shows no significant differences from the sphere case. This is due to the fact that the solution for a sphere is also the solution of hemisphere lying on a large reflecting surface which closely resembles the case of the disc[43]. However, the steady state flux is found to be fitted to a similar function with different coefficients:

$$disc: \quad J^{fit}_{ss,D(r)} = 4D_0c^*r_d(0.57\mathrm{e}^{-3.37\frac{r_p}{r_s}} + 0.43\mathrm{e}^{-0.26\frac{r_p}{r_s}} \pm Er) \tag{6.31}$$

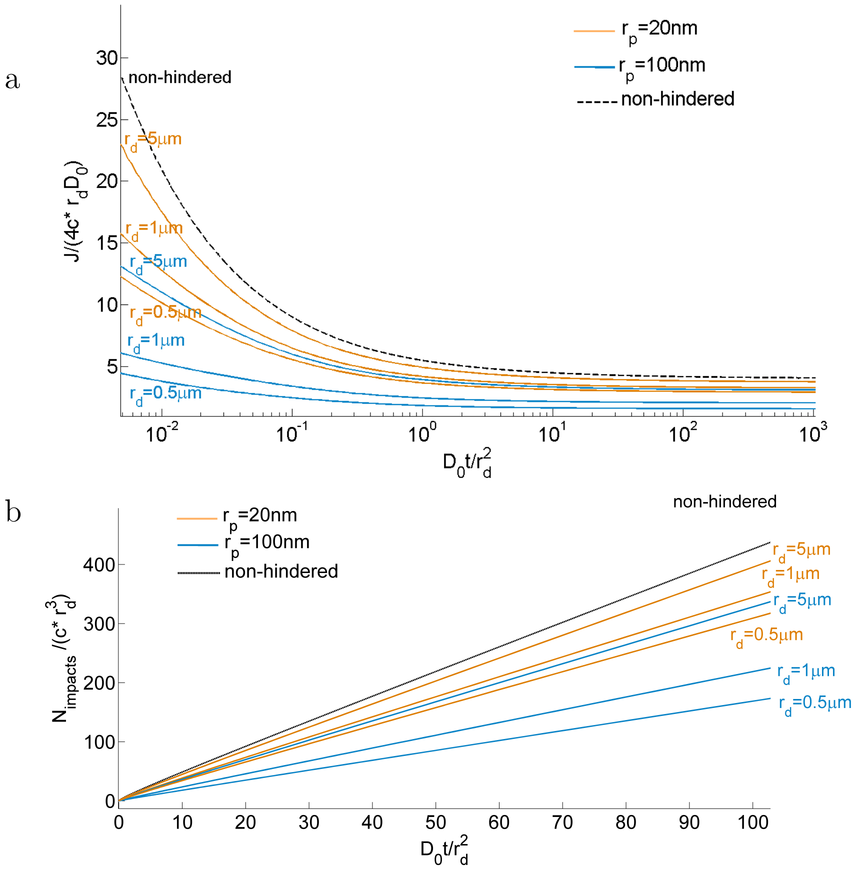

Figure 6.12: The influence of hindered diffusion on the normalised flux (a), and on the number of impacts expected (b) on a microdisc target for various disc radii ($0.5\mu m$-$5\mu m$), and for particles of $20nm$ (orange curves) and $100nm$ (blue curves). The dashed & black curves represent the cases of neglecting hindered diffusion. $\beta$ is chosen to be $1.59\mathring{A}^{-1}$.

The goodness of the fitting (r-square=0.9943) is shown by the residual map ($Er$) in the Appendix. The functions along with the residual map can also be used directly by experimentalist for the prediction of the hindered diffusion effect on the flux of particles and for an estimation of the number of impacts.

Examining the coefficients of the exponentials in the functions of the spherical case in equation 6.25 (-2.34,-0.21) and the disc case (-3.37,-0.26) reveals the contribution of the anisotropic transport. The significantly larger coefficients for the disc function indicates a stronger reduction of the flux in comparison to the steady state flux. This is due to the additional hydrodynamic loss in the lateral direction ($r$) when a particle arrives at the sheath surface.

Note that for the disc as a target, the size of the wall that hinders the hydrodynamic mobility is the size of the target as well as the usually large insulating sheath, and therefore, the model holds also when the target size is comparable to the size of the particle.

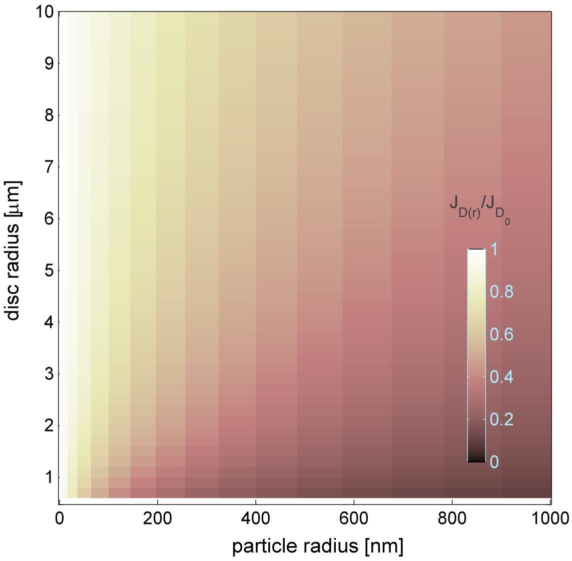

Figure 6.13: The hindered diffusion steady state flux as a fraction of the non-hindered flux ($J_{D(r)}/J_{D_0}$) map as a function of the nano-particle size and the disc size. The map present the case of $\beta = 1.59\mathring{A}^{-1}$.

### 6.4.2 Hindered diffusion towards a wire

An important electrode is the wire electrode which is recommended for the particle impact experiments. The wire electrode consists of a micro-sized radius $r_w$ and a length $l$, typically $l \gg r_w$. The wire electrode geometry provides a higher number of impacts for the same electrode area of a disc[6]. In addition, impact experiments of large particle sizes, usually only become feasible with wire electrodes[8,44]. Here it can be seen that the effect of near-wall hindered diffusion is much reduced in comparison to the case of a sphere or disc due to the changed characteristic diffusion field towards the wire. The diffusion layer characterised with a mixed behaviour of small and large scale targets. The diffusion equation can be solved by assuming axial symmetry; The diffusion equation is therefore:

$$\frac{\partial c(r,t)}{\partial t} = D(r-r_w)\left(\frac{\partial^2 c}{\partial r^2} + \frac{1}{r}\frac{\partial c}{\partial r}\right) + \frac{\partial D(r-r_w)}{\partial r}\frac{\partial c}{\partial r} - P \tag{6.32}$$

where $r_w$ is the micro-size radius of the wire. The same methodology and boundary conditions are used in this case and described earlier for the spherical geometry.

The results for the number of impacts for various sizes of particles are presented for 1$\mu$m and for 5$\mu$m radii in figure 6.14a and figure 6.14b, respectively. The number of impacts is normalized to $2\pi c^* l r_w^2$. The results can easily be converted for experimental purposes. The curves show a significantly reduced effect of hindered diffusion in comparison with the disk or sphere as targets. This is due to the semi 'macro' behaviour of the wire. The diffusion layer propagates into a much larger space than in the case of fully convergent diffusion due to the large length of the wire. Hence, the number of impacts is less influenced by hindered diffusion.

This observation explains the surprising high number of impacts reported for large particles (E.coli bacteria)[44] of size $> 1.0\mu$m impacting a wire electrode with a radius of $3.5\mu m$. A frequency of $\sim 0.25s^{-1}$ which is $\sim 60\%$ of the expected frequency from pure Fickian diffusion was reported. This observation agrees with the calculated average frequency with the inclusion of hindered diffusion $\sim 0.21s^{-1}$ for a $1\mu m$ particle size (for simplicity approximating the bacteria a spherical particle). This proportion can also be inferred by looking at figure 6.14b for the case of $5\mu m$. The lower calculated frequency can be related to the fact that the bacteria size ($> 1.0\mu$m) is in the order of the size of the wall ($3.5\mu m$).

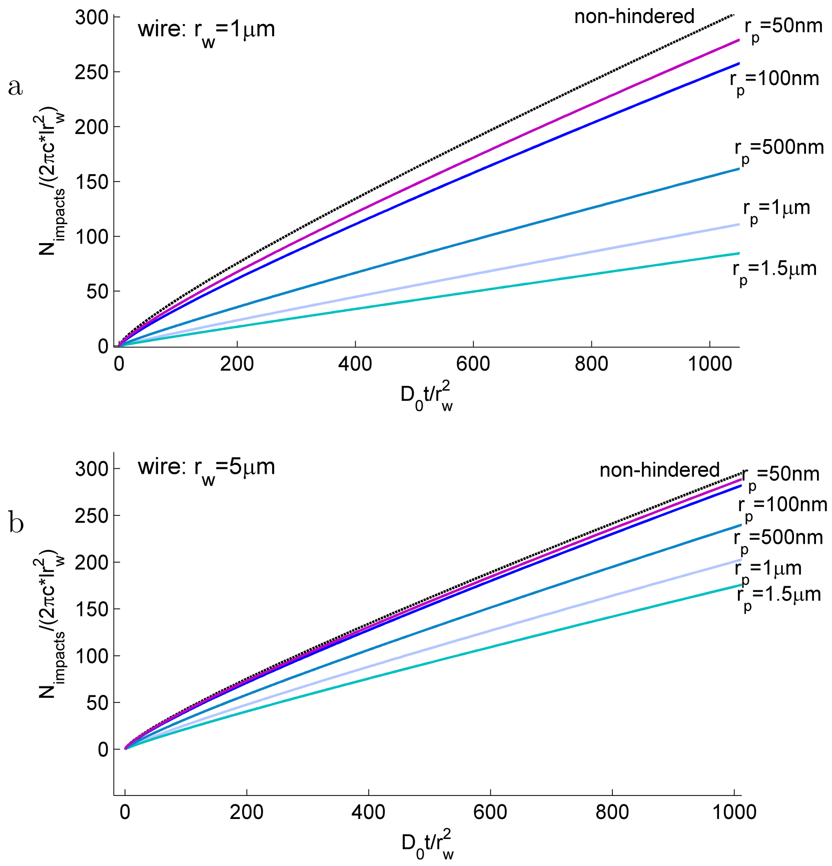

Figure 6.14: The number of impacts expected on a wire for various sizes of particles ($50nm$-$1.5\mu m$) compared to the 'non-hindered' case. The results are presented for a wire of a radius $r_w = 1\mu m$ (a), and $r_w = 5\mu m$ (b), $\beta = 1.59\mathring{A}^{-1}$.

It is also useful to discuss the result of the dimensionless form problem, in the same manner it is discussed earlier for the sphere. In this case the coordinates are normalised to $r_w$, so the diffusion equation becomes:

$$\frac{\partial C}{\partial \tau} = D^*(R-1)\left(\frac{\partial^2 C}{\partial R^2} + \frac{1}{R}\frac{\partial C}{\partial R}\right) + \frac{\partial D^*(R-1)}{\partial R}\frac{\partial C}{\partial R} - P^* \tag{6.33}$$

$$P^* = \frac{C r_w^2}{D_0}\nu \mathrm{e}^{-\beta^*(R-1)} \tag{6.34}$$

and $\beta^* = \beta r_w$.

Figure 6.15 shows the normalised flux towards the wire for two different ratios $r_p/r_w = 0.01, 0.1$ and as function of $\beta^*$. The results show that the effect of $\beta^*$, (a measure of the tunnelling distance) on the flux is smaller at small ratios as observed in the case of the sphere. However, it is also observed that the effect of $\beta^*$ on the flux is reduced strongly at long times. This is due to the reduced effect of the hindered diffusion layer towards a wire.

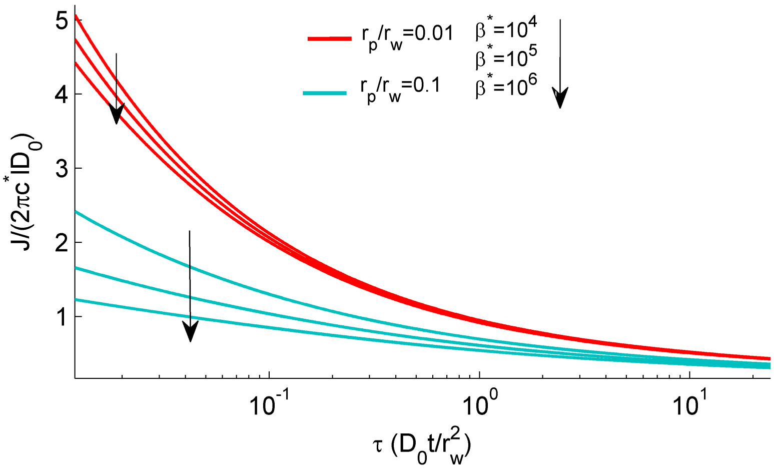

Figure 6.15: Flux of particles of various $R_p$ $(r_p/r_w)$ and $\beta^*$. The flux is normalised to steady state and presented as a function of dimensionless time.

## 6.5 Conclusions

When a particle diffuses from bulk solution towards a target it is slowed close to the target. It has been shown that although in a non-confined space hindered diffusion can be legitimately neglected, for sufficiently small targets the transport is effectively confined by the diffusion field. Subsequently, the flux strongly depends on the size of the particle and the size of the target regardless of the cell size. The numerical study has also shown a significant reduction of the flux at targets of the order of a micrometre.

Parametric studies have enabled the development of equations that show the flux dependency on the ratio between the size of the target and the size of the particle assuming that the zone of hindered diffusion is larger than that of electron transfer. The functions estimate the flux of particles in experimental studies such as of the electrochemical 'impact' method and can be used to estimate the stochastic number of impacts. For instance, the calculation of 'impacts' towards a wire target as an electrode could explain the high number of particle impacts despite the large size of the particles[44] and the close fitting to pure Fickian diffusion with a bulk diffusion coefficient at a 5$\mu$m microdisc[30].

Additionally, calculations of the mean first passage time towards a sphere and a hemisphere have shown a large deviation from the non hindered case. I found that when the window is in the order 100 hundreds nanometers, the expected mean first passage time is ca five times shorter than the calculated hindered diffusion for a particle of a size of $20nm$. Hence it is particularly important for the understanding of diffusion processes such as of biomolecules searching for sub-micrometre size targets. This includes synapse regulation of the exit rate, drag delivery applications and modelling viruses travel towards a nuclear pore.

## 6.6 Appendix

The appendix for this chapter includes details on the computational methods (1), the solution of the diffusion equation towards a sphere (2), further details on the anisotropic 2D diffusion equation (3), and a discussion on the residual maps of the steady state flux equations (4).

### 6.6.1 Computational methods

Numerical calculations of the non-homogeneous and anisotropic diffusion equations were carried out using the Implicit Finite difference method for 1D cases and combined with the

ADI method for the 2D anisotropic case. The Thomas algorithm was employed to solve the discrete concentration equations[45,46]. For the 2D parametric study, which contains thousands of runs for each case, a GPU high-performance solver is utilised using the implicit parallel algorithm as is discussed in chapter 3[47].

The mesh was created using an expanding grid to provide sufficiently small differences next to the walls and the target surface. The near-wall hindered diffusion problem is very sensitive to meshing and the convergence of the result varies for different sizes of particles due to the diffusion coefficient profile close to the wall. Therefore, a careful convergence test was carried out to evaluate the minimum difference ($10^{-7} \cdot r_s$) and the expansion factors (1.06 in both $r$ and $z$ directions) required for achieving an accurate simulation in the near-wall hindered diffusion simulation for $r_p > 5nm$.

### Accuracy and convergence tests

Initial tests were carried out using non-hindered cases to provide a full agreement (within 0.6 % for all time) of the mass balance equations with theoretical transient flux towards the disc and a sphere[48]. The expansion factor parameter, the minimum difference, and the tunnelling rate coefficient ($\nu$) for the non-hindered case were varied until the result for the flux converged to the value for the simplified model of no-tunnelling but fully adsorbing surface. In the parametric study, which contained 4000 runs to find the steady state, a global convergence approach was used as follows: The simulation was run and then fitted to the function to find the coefficients (eq. 6.25, 6.31). Thereafter, the mesh parameters were varied until the coefficients of the fitted equation remained constants.

### Implementation

All simulations were implemented using C++. For the parametric study, the parallelization of ADI solver was implemented using NVIDIA CUDA. The processor was a Xeon E5-1650, 3.2GHz, and 16GB of RAM. The GPU is a NVIDIA Quadro K4000 (Kepler architecture). Least squares fittings using the 'general-model' fit function as well as post-processing procedures were carried out in Matlab software.

## 6.6.2 Diffusion to a finite sphere

### Non-hindered diffusion case

The solution of diffusion towards a sphere or an hemi-sphere can be found through solving the diffusion equation in one dimensional radial coordinates system:

$$\frac{\partial c}{\partial t} = D(\frac{\partial^2 c}{\partial r^2} + \frac{2}{r}\frac{\partial c}{\partial r}) \tag{6.35}$$

with boundary conditions of a full adsorbing surface on the sphere with a radius $r_s$, and bulk concentration is assumed at infinite distance:

$$t \geq 0, \quad r = r_s, \quad c = 0 \tag{6.36}$$

$$t \geq 0, \quad r = \infty, \quad c = c^* \tag{6.37}$$

Changing the variable:

$$u = -cr \tag{6.38}$$

gives the equation

$$\frac{\partial u}{\partial t} = D\frac{d^2u}{dr^2} \tag{6.39}$$

It requires the introduce of a new variable:

$$\eta = \frac{r}{2\sqrt{Dt}} \tag{6.40}$$

and the diffusion equation becomes:

$$\frac{d^2u}{d\eta^2} + 2\eta\frac{du}{d\eta} = 0 \tag{6.41}$$

This gives the solution to be of the form:

$$\frac{du}{d\eta} = ae^{-\eta^2} \tag{6.42}$$

Integrating and applying the bulk boundary condition at infinity gives:

$$\int\limits_{u}^{u^*} du = a\int\limits_{\eta}^{\infty} e^{-\eta^2} d\eta \tag{6.43}$$

$$u^* - u = a(\frac{\sqrt{\pi}}{2} - e^{-\eta^2} d\eta) \tag{6.44}$$

Using the boundary condition of a fully adsorbing surface at $r = r_s$, we get:

$$a = -(\frac{2}{\sqrt{\pi}})rc^* \tag{6.45}$$

and substituting back:

$$c = c^*\{1 - \frac{r_s}{r}(1 - erf(\frac{r - r_s}{\sqrt{4Dt})})\} \tag{6.46}$$

$$c = c^*\{1 - \frac{r_s}{r}(1 - \frac{2}{\sqrt{\pi}}\sum_0^\infty \frac{(-1)^n z^{2n+1}}{n!(2n+1)})\} \ where \ z = \frac{r - r_s}{\sqrt{4Dt}} \tag{6.47}$$

Finding the flux:

$$D\frac{dc}{dr}\mid_{r=r_s} = Dc^*\{\frac{r_s}{r}\frac{2}{\sqrt{\pi}}(\sum_0^\infty \frac{(-1)^n z^{2n}}{n!}\frac{dz}{dr}) + \frac{r_s}{r^2}(1 - \frac{2}{\sqrt{\pi}}\sum_0^\infty \frac{(-1)^n z^{2n+1}}{n!(2n+1)})\} \tag{6.48}$$

where

$$z = \frac{r - r_s}{\sqrt{4Dt}}, \ \ \frac{dz}{dr} = \frac{1}{\sqrt{4Dt}} \tag{6.49}$$

Expanding the Taylor series:

$$D\frac{dc}{dr}\mid_{r=r_s} = Dc^*\{\frac{2}{\sqrt{\pi}}(1 - z^2 + \frac{z^4}{2} - ...)(\frac{1}{\sqrt{4Dt}}) + \frac{2}{\sqrt{\pi}}(-z + \frac{z^3}{3} - ...) + \frac{1}{r_s})\} \tag{6.50}$$

Since $z = \frac{r - r_s}{\sqrt{4Dt}} = 0$ at $r = r_s$

$$D\frac{dc}{dr}\mid_{r=r_s} = Dc^*(\frac{1}{\sqrt{\pi Dt}} + \frac{1}{r_s}) \tag{6.51}$$

### Hindered diffusion steady-state case

Substitution of the function into the diffusion equation, in radial coordinates yields:

$$\frac{\partial c}{\partial t} = \nabla \cdot (D(r)\nabla c) = D_0 \mathrm{e}^{-Br_s/r}\frac{\partial^2 c}{\partial r^2} + D_0 \mathrm{e}^{-Br_s/r}\left(\frac{2}{r} + \frac{Br_s}{r^2}\right)\frac{\partial c}{\partial r} \tag{6.52}$$

This expression can be simplified by limiting our analysis to the steady-state of the system:

$$0 = \frac{\partial^2 c}{\partial r^2} + \left( \frac{2}{r} + \frac{Br_s}{r^2} \right) \frac{\partial c}{\partial r} \tag{6.53}$$

By reducing order and substituting the boundary condition $c(x = 0, t) = 0$ and $c(x = \infty, t) = c^*$, the homogeneous ordinary differential equation directly solves to:

$$c = \frac{c^*}{\mathrm{e}^{Br_s/r} - 1} \left( 1 - \mathrm{e}^{Br_s/r} \right) + c^* \tag{6.54}$$

and the steady state flux at the sphere to:

$$J_{ss} = -D_{trial}(r) \frac{\partial c}{\partial r}\bigg|_{r=r_s} = \frac{D_0 c^*}{r_s} \left[ \frac{B}{(1 - \mathrm{e}^B)} \right] \tag{6.55}$$

### 6.6.3 Anisotropic hindered diffusion towards a disc:

In cylindrical coordinates, the hindered diffusion is represented only by the normal stresses for the coordinates r and z. The gradient of the scalar field of concentration in the anisotropic diffusion equation gives the vector:

$$\frac{\partial c}{\partial t} = \nabla \cdot \{ D( \frac{\partial c}{\partial r} \hat{r} + \frac{1}{\phi} \frac{\partial A}{\partial \phi} \hat{\phi} + \frac{\partial c}{\partial z} \hat{z} ) \} \tag{6.56}$$

and the diffusion coefficient is represented by a second rank tensor:

$$D = D_0 \begin{bmatrix} \sigma_{rr} & \sigma_{r\phi} & \sigma_{rz} \\ \sigma_{\phi r} & \sigma_{\phi\phi} & \sigma_{\phi z} \\ \sigma_{zr} & \sigma_{z\phi} & \sigma_{zz} \end{bmatrix} \tag{6.57}$$

Recall the divergence of a vector field (A) in cylindrical coordinates:

$$\nabla \cdot A = \left( \frac{1}{r} \frac{\partial (r \cdot A_r)}{\partial r} + \frac{1}{r} \frac{\partial A_\phi}{\partial \phi} + \frac{\partial A_z}{\partial z} \right) \tag{6.58}$$

In axial symmetry $\frac{\partial A}{\partial \phi} = 0$. By combining the above equations we get:

$$\frac{\partial c}{\partial t} = D_0 \left( \frac{1}{r} [r \sigma_{rr} \frac{\partial^2 c}{\partial r^2} + \frac{\partial c}{\partial r} (\sigma_{rr} + r \frac{\partial \sigma_{rr}}{\partial r})] + \sigma_{zz} \frac{\partial^2 c}{\partial z^2} + \frac{\partial \sigma_{zz}}{\partial z} \frac{\partial c}{\partial z} \right) \tag{6.59}$$

$$\frac{\partial c}{\partial t} = D_0 \left( \sigma_{rr} \frac{\partial^2 c}{\partial r^2} + \frac{\sigma_{rr}}{r} \frac{\partial c}{\partial r} + \frac{\partial c}{\partial r} \frac{\partial \sigma_{rr}}{\partial r} + \sigma_{zz} \frac{\partial^2 c}{\partial z^2} + \frac{\partial \sigma_{zz}}{\partial z} \frac{\partial c}{\partial z} \right) \tag{6.60}$$

The $D \perp$ and $D \parallel$ are functions of the distance z from the electrode, or the wall adjacent to the electrode (at z=0). Therefore, $\partial \sigma_{rr} / \partial r = 0$ and the diffusion problem becomes:

$$\frac{\partial c}{\partial t} = D_0 \left( \sigma_{rr} \frac{\partial^2 c}{\partial r^2} + \frac{\sigma_{rr}}{r} \frac{\partial c}{\partial r} + \sigma_{zz} \frac{\partial^2 c}{\partial z^2} + \frac{\partial \sigma_{zz}}{\partial z} \frac{\partial c}{\partial z} \right) \tag{6.61}$$

### 6.6.4 Residual maps of the flux towards a sphere and a disc

Here the results of the fitting are discussed, and residual maps are provided for further accuracy of the flux estimation that can be used along with the approximated functions. This chapter provided the approximate steady state functions in the case of particles impacting a sphere and a disc:

$$sphere: \; J^{fit}_{ss,D(r)} = 4 D_0 \pi c^* r_s (0.57 \mathrm{e}^{-2.34 \frac{rp}{rs}} + 0.43 \mathrm{e}^{-0.21 \frac{rp}{rs}} \pm Er) \tag{6.62}$$

$$disc: \quad J^{fit}_{ss,D(r)} = 4 D_0 c^* r_d (0.57 \mathrm{e}^{-3.37 \frac{rp}{rs}} + 0.43 \mathrm{e}^{-0.26 \frac{rp}{rs}} \pm Er) \tag{6.63}$$

The functions, with an r-square value of 0.996 for sphere and 0.943 for disc, also were used as a method to find global convergence of the spatial mesh for the numerical solution as discussed in the computational methods. The local goodness of the fitting is shown by the residual map $(Er)$ $(Er = J_{ss}(fit) - J_{ss}(simulation))$ in figure 6.16a for the sphere and in figure 6.16b for the disc. The functions provide a good fitting in most ratios of $r_p/r_s$, within a value of ±0.08. The fit shows that at small targets and small particles the deviation of the simulated flux from the fitted function is relatively large $J_{ss}(fit) - J_{ss}(simulation) \sim -0.08$ which underestimates the flux. This deviation is found to be partly due to the tunnelling distance which becomes important for very small particles and targets; For very small targets the diffusion layer thickness becomes comparable to the tunnelling distance, thus small particles are being consumed before they loose a significant fraction of their hydrodynamic mobility, and a deviation from the behaviour of the exponential decay is observed. It was found that increasing artificially the $\beta$ value in the tunnelling function $(P)$ by an order of magnitude results in a maximum residual of ±0.05. The functions along with the residual map can also be used directly by experimentalist for the prediction of the hindered diffusion effect on the flux of particles and for an estimation of the number of impacts.

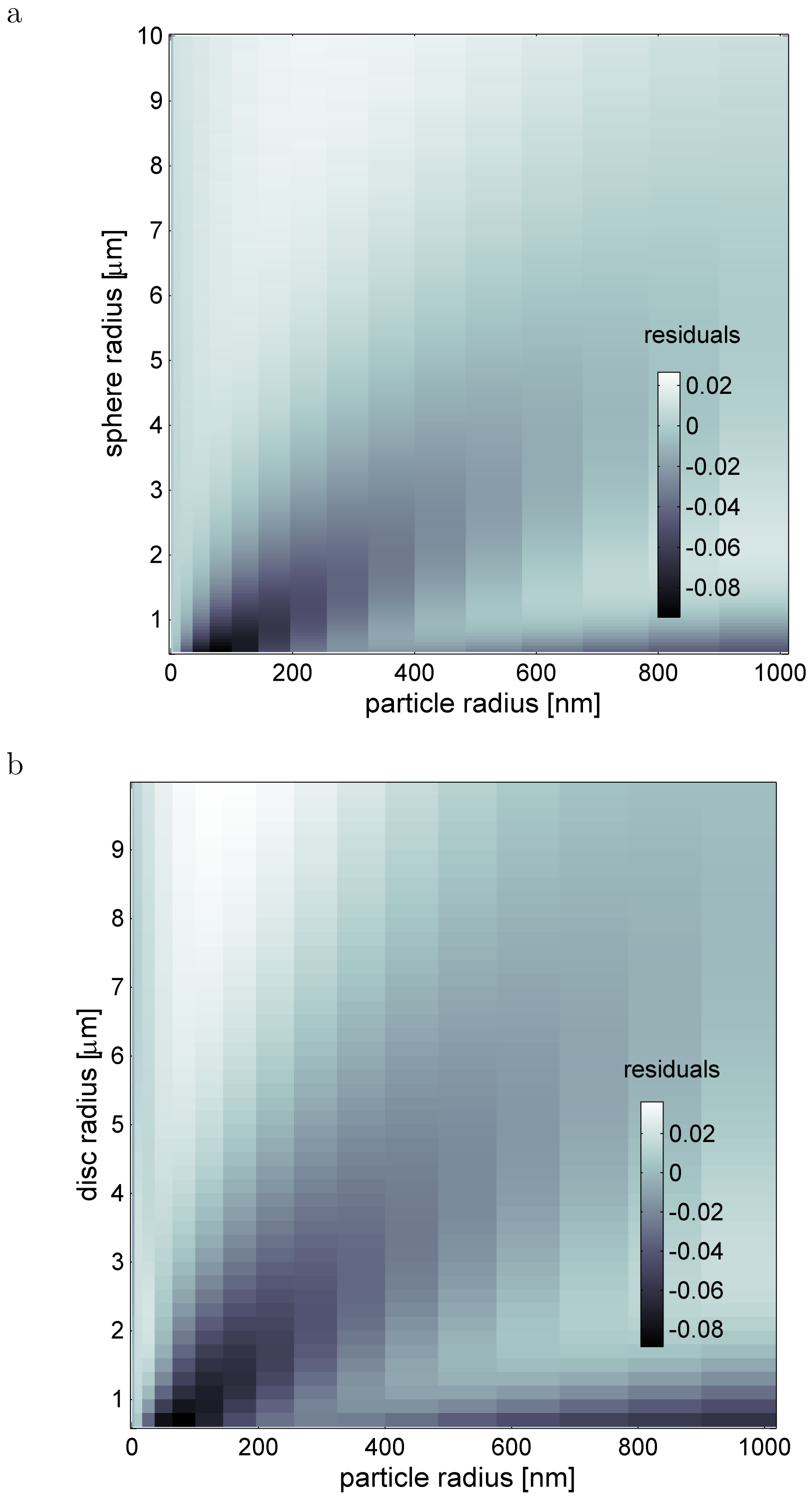

Figure 6.16: The residuals map ($Er$) of the fitted function for the sphere (a) and the disc (b) cases, $J_{ss}(fit) - J_{ss}(simulation)$.

# References

[1] X. Xiao and A. J. Bard *J. Am. Chem. Soc.*, vol. 129, no. 31, pp. 9610–9612, 2007.

[2] N. V. Rees, Y.-G. Zhou, and R. G. Compton *RSC Adv.*, vol. 2, pp. 379–384, 2012.

[3] F.-R. F. Fan and A. J. Bard *Science*, vol. 277, no. 5333, pp. 1791–1793, 1997.

[4] E. Kätelhön and R. G. Compton *ChemElectroChem*, vol. 2, no. 1, pp. 64–67, 2015.

[5] A. J. Bard, H. Zhou, and S. J. Kwon *Israel Journal of Chemistry*, vol. 50, no. 3, pp. 267–276, 2010.

[6] S. Eloul, E. Kätelhön, C. Batchelor-McAuley, K. Tschulik, and R. G. Compton *J. Electroanal. Chem.*, vol. 755, pp. 136–142, 2015.

[7] A. Boika and A. J. Bard *Analytical Chemistry*, vol. 87, no. 8, pp. 4341–4346, 2015.

[8] J. Ellison, C. Batchelor-McAuley, K. Tschulik, and R. G. Compton *Sensor Actuat B-Chem*, vol. 200, pp. 47 – 52, 2014.

[9] K. Tschulik and R. G. Compton *Phys. Chem. Chem. Phys.*, vol. 16, pp. 13909–13913, 2014.

[10] D. Qiu, S. Wang, Y. Zheng, and Z. Deng *Nanotechnology*, vol. 24, no. 50, p. 505707, 2013.

[11] S. V. Sokolov, E. Kätelhön, and R. G. Compton *J. Phys. Chem. C*, vol. 119, no. 44, pp. 25093–25099, 2015.

[12] T. M. Alligrant, E. G. Nettleton, and R. M. Crooks *Lab Chip*, vol. 13, pp. 349–354, 2013.

[13] H. Zhou, F.-R. F. Fan, and A. J. Bard *J. Phys. Chem. Lett.*, vol. 1, no. 18, pp. 2671–2674, 2010.

[14] W. Cheng and R. G. Compton *Angew. Chem., Int. Ed.*, vol. 53, no. 50, pp. 13928–13930, 2014.

[15] L. R. Holt, B. J. Plowman, N. P. Young, K. Tschulik, and R. G. Compton *Angew. Chem., Int. Ed.*, vol. 55, no. 1, pp. 397–400, 2016.

[16] N. P. Sardesai, D. Andreescu, and S. Andreescu *J. Am. Chem. Soc.*, vol. 135, no. 45, pp. 16770–16773, 2013.

[17] K. Pappaert, P. V. Hummelen, J. Vanderhoeven, G. Baron, and G. Desmet *Chemical Engineering Science*, vol. 58, no. 21, pp. 4921 – 4930, 2003. International Symposium on Mathematics in Chemical Kinetics and Engineering.

[18] V. P. Zhdanov and F. Höök *European Biophysics Journal*, vol. 44, no. 4, pp. 219–226, 2015.

[19] F. Danhier, O. Feron, and V. Préat *Journal of Controlled Release*, vol. 148, no. 2, pp. 135–146, 2010.

[20] A. Singer, Z. Schuss, and D. Holcman *Phys. Rev. E*, vol. 78, no. 5, p. 051111, 2008.

[21] J. T. Edward *Journal of Chemical Education*, vol. 47, no. 4, p. 261, 1970.

[22] H. Brenner *Chemical Engineering Science*, vol. 16, no. 3-4, pp. 242–251, 1961.

[23] A. Goldman, R. Cox, and H. Brenner *Chemical Engineering Science*, vol. 22, no. 4, pp. 653–660, 1967.

[24] P. Huang and K. S. Breuer *Phys. Rev. E*, vol. 76, no. 4, p. 046307, 2007.

[25] M. A. Bevan and D. C. Prieve *J. Chem. Phys.*, vol. 113, no. 3, pp. 1228–1236, 2000.

[26] J. Karger and D. M. Ruthven, *Diffusion in Zeolites and Other Microporous Solids.* Wiley, New York, 1992.

[27] S. L. Dettmer, S. Pagliara, K. Misiunas, and U. F. Keyser *Phys. Rev. E*, vol. 89, no. 6, p. 062305, 2014.

[28] S. Pagliara, C. Schwall, and U. F. Keyser *Advanced Materials*, vol. 25, no. 6, pp. 844–849, 2013.

[29] R. K. Jain and T. Stylianopoulos *Nature Reviews Clinical Oncology*, vol. 7, no. 11, pp. 653–664, 2010.

[30] E. J. E. Stuart, Y.-G. Zhou, N. V. Rees, and R. G. Compton *RSC Adv.*, vol. 2, pp. 6879–6884, 2012.

[31] E. O. Barnes, Y.-G. Zhou, N. V. Rees, and R. G. Compton *J. Electroanal. Chem.*, vol. 691, pp. 28–34, 2013.

[32] E. Katelhon and R. G. Compton *Chem. Sci.*, vol. 5, pp. 4592–4598, 2014.

[33] S. V. Sokolov, E. Kätelhön, and R. G. Compton *The Journal of Physical Chemistry C*, vol. 120, no. 19, pp. 10629–10640, 2016.

[34] R. G. Compton and C. E. Banks, *Understanding Voltammetry (2nd Edition)*. London, UK: Imperial College Press, 2011.

[35] D. Holcman *Journal of Statistical Physics*, vol. 127, no. 3, pp. 471–494, 2007.

[36] Z. Schuss, A. Singer, and D. Holcman *Proceedings of the National Academy of Sciences*, vol. 104, no. 41, pp. 16098–16103, 2007.

[37] O. Bénichou and R. Voituriez *Phys. Rev. Lett.*, vol. 100, no. 16, p. 168105, 2008.

[38] A. J. Bard and L. Faulkner, *Electrochemical Methods: Fundamentals and Applications*. John Wiley and Sons, 2001.

[39] P. L. Krapivsky and S. Redner *Am. J. Phys.*, vol. 64, pp. 546–551, 1996.

[40] M. Hugelmann and W. Schindler *Surface Science*, vol. 541, no. 1, pp. L643–L648, 2003.

[41] P. P. Edwards, H. Gray, M. Lodge, and R. J. Williams *Angew. Chem., Int. Ed.*, vol. 47, no. 36, pp. 6758–6765, 2008.

[42] R. B. Bird *Applied Mechanics Reviews*, vol. 55, no. 1, pp. R1–R4, 2002.

[43] K. B. Oldham and C. G. Zoski *Journal of electroanalytical chemistry and interfacial electrochemistry*, vol. 256, no. 1, pp. 11–19, 1988.

[44] L. Sepunaru, K. Tschulik, C. Batchelor-McAuley, R. Gavish, and R. G. Compton *Biomaterials Science*, vol. 3, no. 6, pp. 816–820, 2015.

[45] L. K. Bieniasz, O. Østerby, and D. Britz *Computers & Chemistry*, vol. 19, no. 2, pp. 121 – 136, 1995.

[46] R. G. Compton, E. Laborda, and K. R. Ward, *Understanding Voltammetry - Simulation of Electrode Processes*. Imperial College Press, 2013.

[47] S. Eloul and R. G. Compton *J. Electroanal. Chem.*, vol. 771, pp. 50 – 55, 2016.

[48] E. Kätelhön and R. G. Compton *Analyst*, vol. 140, pp. 2592–2598, 2015.

# Chapter 7

# Shielding of a microdisc electrode surrounded by an adsorbing surface

The previous chapter has described how hindered diffusion can be important to the prediction of impacts of particles on electrodes. This chapter investigates another surface effect that can strongly influence the experimental results of the 'impact' method in the case of microdisc electrodes. Microdisc electrodes are usually made by surrounding a metal wire of a diameter of a few microns in a flat insulating sheath made of glass or other insulating material. The latter may be as much as millimeter in size. The sheath is generally assumed to play no role in the voltammetry observed at the microdisc electrode. However, in some cases, and especially for experiments with nano-particles, significant adsorption can occur on the sheath so perturbing the current response measured at the disc. I report theoretical calculations of the effect of 'shielding' by the insulating sheath of micro electrodes and show that this can significantly influence the magnitude of the current even for relatively small levels of adsorption, not least because of the typically very large area of the insulation relative to the electrode size. The work has been published in 'The

Journal of Chem-Electro-Chem'[1].

## 7.1 Introduction

Microelectrodes have transformed the dynamic range of electrochemistry since their introduction and popularization dating from the 1970s and 1980s[2–5]. The diversity and range of their application continue to expand[6–9]and their advantages have been discussed in chapter 1.

Microelectrodes are typically fabricated by insulating a metal wire of a micron diameter by a sheath made of glass or some other electrically non conducting material[10]. The end of the structure is polished flat in practical use so as to expose a metal microdisc surrounded by a concentric ring of insulation. The latter is usually of the millimetre size. In analysing the current response seen at the microdisc electrode, it is usually assumed that the insulating sheath plays no role other than to provide a non-conducting surround and at which no material fluxes arrive or leave. This is undoubtedly an excellent assumption for molecular voltammetry conducted in conventional media. However, in the context of the study of biological media, functionalized surfaces, or nano-particles, this may no longer be the case. In particular, if the species of interest (by virtue of their voltammetry at the microdisc surface) adsorb on the insulation sheath, then, because of the large relative area of this potential material 'sink', a significant perturbation of the microdisc current can arise. Such considerations may play an important role in the area of 'nano-impacts' where the microelectrode preparation is extremely important for the quantitative analysis of nano-particles and some evidence of 'shielding' has been noted[11,12].

In this chapter, I report simulations that quantify the effect of shielding caused by adsorption on the insulating sheath of the microelectrodes, and demonstrate that this can have a very significant influence on the currents measured at microdisc electrodes.

## 7.2 Theory

A model is developed to simulate the shielding effect on the flux of electroactive species, towards a microdisc electrode surrounded by an insulating but sticking surface. This study is made via simulating Fickian diffusion under chronoamperometry in the presence of supporting electrolyte to assume diffusion controlled transport. By approximating the transport to behave in a statistical manner[13–15], complex stochastic modelling can be avoided and Fick's second law can be numerically solved[17]. For the microdisc geometry, Fick's second law is solved for cylindrical space using axial symmetry around $r = 0$[18]:

$$\frac{\partial c}{\partial t} = D\left(\frac{\partial^2 c}{\partial r^2} + \frac{\partial^2 c}{\partial z^2} + \frac{1}{r}\frac{\partial c}{\partial r}\right) \tag{7.1}$$

where $D$ is the diffusion coefficient, $c$ is the concentration, and $r$ and $z$ are cylindrical coordinates. In this space, the axis $z$ passes through the centre of the disc and is perpendicular to its plane. Therefore, two distances are defined in the $r$ direction, the disc electrode radius ($r_d$) and the surface radius ($r_s$) as illustrated in figure 7.1.

Dimensionless parameters are used in the simulation to simplify the analysis[18]. Coordinates are normalized to the surface radius ($R = r/r_s, Z = z/r_s$) and concentrations are defined relative to the bulk concentration of the electroactive species ($C = c/c^*$). A dimensionless time parameter ($\tau$) is defined as:

$$\tau = \frac{D}{r_s^2}t \tag{7.2}$$

All the dimensional and dimensionless symbols are summarized in Table 7.1. In the transformed coordinates the radius of the surface is unity and the microdisc lies between: $0 < R_d < 1$. Converting Fick's second law into a dimensionless form gives[19]:

$$\frac{\partial C}{\partial \tau} = \left( \frac{\partial^2 C}{\partial R^2} + \frac{\partial^2 C}{\partial Z^2} + \frac{1}{R}\frac{\partial C}{\partial R} \right) \tag{7.3}$$

The dimensionless mass transport equation must be solved over all space with the appropriate boundary conditions which define the kinetics and fluxes on the surfaces of the simulation space.

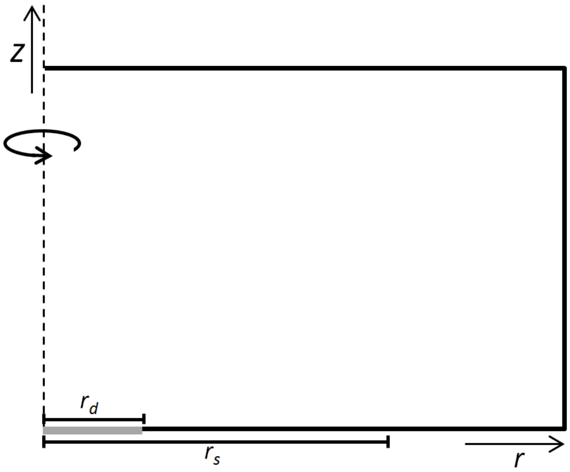

Figure 7.1: Schematic of the 2D calculation area of the microdisc electrode with radius $r_d$ and the adsorbing surface with radius $r_s$.

### 7.2.1 Boundary Conditions

At $z = 0$ the kinetics of the sticking surface and the electrode boundary condition are defined. At the disc electrode, the concentration is set to zero, assuming mass transport control:

$$at \quad \tau \geq 0 \quad and \quad R \leq R_d, C_{R,0} = 0 \tag{7.4}$$

Next the boundary condition for the sticking surface is considered[13,20]. The concentration adjacent to the surface drops due to adsorption. This boundary condition is assumed to be a first order kinetic irreversible adsorption according to the Langmuirian model[20,21]. Therefore, the flux on the sticking surface is given by:

$$D\left(\frac{\partial c}{\partial z}\right)_{z=0} = k_0\,(1-\theta)\,c_{r,0} \tag{7.5}$$

where ($\theta$) is the fractional coverage and varies between 0-1. The adsorption rate constant ($cm\,s^{-1}$) is denoted by $k_0$. The rate constant $k_0$ can be related to a 'sticking coefficient' which is experimentally accessible in some cases e.g.[22]. Converting $k_0$ to a dimensionless rate constant gives $K$:

$$K = \frac{k_0 r_s}{D} \tag{7.6}$$

Rewriting the flux equation in a dimensionless form gives the surface boundary condition:

$$\begin{matrix} \tau \geq 0 \\ R_d < R \leq R_s \end{matrix} \qquad \left(\frac{\partial C}{\partial Z}\right)_{Z=0} = K\,(1-\theta)\,C_{R,0} \tag{7.7}$$

The surface coverage ($\Gamma / mole\,cm^{-2}$) is defined as the density of the maximum coverage. Hence, the variation of $\theta$ with $t$ can be defined as:

$$\Gamma\frac{\partial\theta}{\partial t} = k_0(1-\theta)c_{r,0} \tag{7.8}$$

Converting into dimensionless form gives:

$$\frac{\partial\theta}{\partial\tau} = K(1-\theta)\frac{C_{R,0}}{\gamma} \tag{7.9}$$

| Parameter | Description | Units |
|---|---|---|
| $A$ | Electrode area | $m^2$ |
| $r_d$ | Electrode radius | $m$ |
| $r_s$ | Surface radius | $m$ |
| $D$ | Diffusion coefficient | $m^2 s^{-1}$ |
| $c$ | Concentration | $molm^{-3}$ |
| $c^*$ | Bulk solution concentration | $molm^{-3}$ |
| $\theta$ | Fractional surface coverage | |
| $\Gamma$ | Surface coverage of a full monolayer | $molcm^{-2}$ |
| $k^0$ | Adsorption rate constant | $ms^{-1}$ |
| $t$ | Time | $s$ |
| $j^D$ | Flux per unit area | $molm^{-2}s^{-1}$ |
| $J^D$ | Net Flux | $mols^{-1}$ |
| $j$ | Dimensionless flux density | |
| $J$ | Dimensionless net flux | |
| $C$ | $c/c^*$ | |
| $R$ | $r/r_s$ | |
| $R_d$ | $r_d/r_S$ | |
| $R_s$ | 1 | |
| $Z$ | $z/r_s$ | |
| $\tau$ | $Dt/r_s^2$ | |
| $K$ | $k_0 r/D$ | |
| $\gamma$ | $\Gamma k^0/(c^* D)$ | |

Table 7.1: Dimensional and dimensionless parameters

where $\gamma$ is a dimensionless coverage defined by:

$$\gamma = \Gamma/(c^{*}D/k_0) \tag{7.10}$$

Beyond the sticking surface, at $Z = 0$, an insulation boundary condition is applied:

$$R_s < R \leq R_{max} \qquad \left(\frac{\partial C}{\partial Z}\right)_{Z=0} = 0 \tag{7.11}$$

The edges in the outer space of the simulation set to the bulk concentration:

$$C_{R_{\max}} = 1, \quad C_{Z_{\max}} = 1 \tag{7.12}$$

where $R_{max}$ and $Z_{max}$ are set to be arbitrarily far enough from the root mean squared displacement according to the Einstein equation[23,24]:

$$\begin{aligned} R_{\max} &= 1 + 6\sqrt{\tau_{\max}} \\ Z_{\max} &= 6\sqrt{\tau_{\max}} \end{aligned} \tag{7.13}$$

$\tau_{\max}$ is chosen to be sufficiently large to achieve a full convergence of the flux in chronoamperometry. From symmetry, the flux across the $Z$ axisymmetric boundary can be set to zero:

$$\left(\frac{\partial C}{\partial R}\right)_{R=0} = 0 \tag{7.14}$$

The dimensionless flux inward the disk or the electrode is given by:

$$\begin{array}{ll} disk: & 0 < R \leq R_d \\ surface: & R_d < R \leq R_s \end{array} \qquad j = \left(\frac{\partial C}{\partial Z}\right)_{Z=0} \tag{7.15}$$

By integrating the flux ($j^D$) over the disc and the surface, the net flux($J^D$) inward the disc electrode and the adsorbing flux to the surface become:

$$J_d^D = 2\pi \int_0^{r_d} j_{r,0}^D r \mathrm{d}r \,, \quad J_s^D = 2\pi \int_{r_d}^{r_s} j_{r,0}^D r \mathrm{d}r \tag{7.16}$$

In dimensionless form:

$$J_d = 2\pi \int_0^{R_d} j_{R,0} R \mathrm{d}R \,, \quad J_s = 2\pi \int_{R_d}^{R_s} j_{R,0} R \mathrm{d}R \tag{7.17}$$

Assuming a single electron transfer, the dimensional Faradaic current inward the microdisc electrode is obtained as follows:

$$I_d = 2\pi F c^* D r_s \int_0^{R_d} j_{R,0} R \mathrm{d}R \,, \tag{7.18}$$

The shielding effect then can be derived and compared to analytical calculations of a full sticking or non-sticking surface at different radius ratios, $R_{sd}$:

$$R_{sd} = \frac{R_s}{R_d} \tag{7.19}$$

### 7.2.2 Numerical Methods

The finite difference approximation is used along with the Crank-Nicolson method[25] to solve a set of concentration equations simultaneously over the 2D space at each point in time. These equations are discritized over an expanding spatial 2D grid with $m$ rows and $n$ columns ($R(n) \times Z(m)$) and dimensionless time 1D grid ($\tau(k)$). The spatial grid is generated over the space with 3 nodes ($N_{1-3}$) at: $\delta R, R_d, R_s$. The neighbours points around these nodes are set to be with the smallest differences $\delta R$ and $\delta Z$, after which the grid differences grow exponentially to achieve full cover of all the space according to the following definitions:

$$\begin{aligned}
&R\ grid:\\
&N_1 = \delta R,\ \ N_2 = R_d,\ \ N_3 = R_s,\\
&R_{n+1} = R_n \gamma_R \qquad N_j < R_n < \tfrac{N_j + N_{j+1}}{2},\ \ R_s < R_n < R_{max}\\
&R_{n+1} = R_n / \gamma_R \qquad \tfrac{N_j + N_{j+1}}{2} < R_n < N_{j+1}
\end{aligned} \tag{7.20}$$

$$\begin{aligned}
&Z\ grid:\\
&Z_{m+1} = Z_m \gamma_Z \qquad 0 < Z_m < Z_{max}
\end{aligned}$$

where $\gamma_R$ and $\gamma_Z$ are the expansion factors between two adjacent cells in the rows $R_{n+1}$ to $R_n$ and in the columns $Z_{n+1}$ to $Z_n$, respectively. An illustration of the spatial grid around any node is provided in figure 7.2.

The $\delta\tau$ in the dimensionless time grid is constant at the beginning of the chronoamperometry process where the change in flux is large. However, when the following criteria is achieved ($\tau_s$), an exponential growth is applied for the dimensionless time step $\Delta\tau$[26]:

$$\frac{\Delta J}{\Delta \tau} < \left(\frac{\Delta J}{\Delta \tau}\right)_{\tau=0} \times 0.001 \tag{7.21}$$

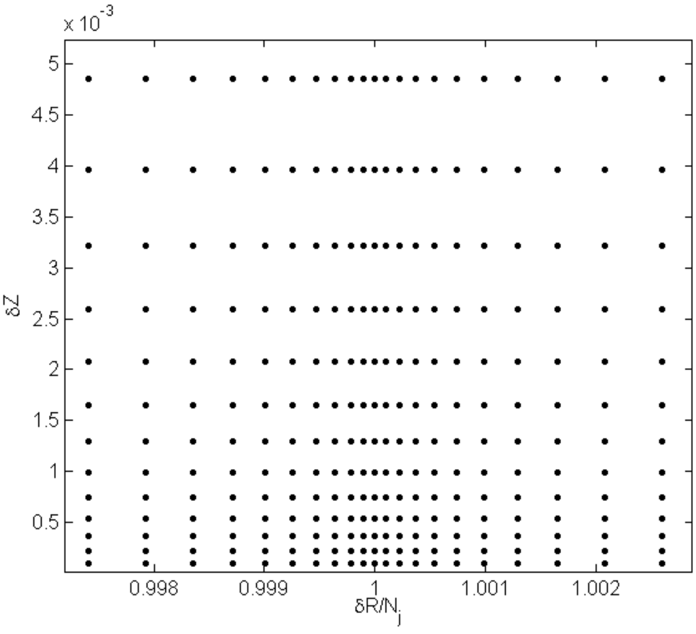

Figure 7.2: The discretization around the nodes in the spatial grid.

Therefore:

$$
\begin{aligned}
&\tau_0 = 0 \\
&\tau_{k+1} = \tau_k + \delta\tau \qquad 0 < \tau_k \le \tau_s \\
&\tau_{k+1} = \gamma_\tau \tau_k \qquad\quad \tau_s < \tau_k
\end{aligned}
\tag{7.22}
$$

where $\gamma_\tau$ is the expansion factor between two adjacent time steps ($k+1$ and $k$). The convergence criterion for the flux is defined to be:

$$\left| \frac{J_{k+1}}{J_k} - 1 \right| < 1 \times 10^{-9} \tag{7.23}$$

The 2D mass transport system is solved using parallel computing of the alternating direction implicit (ADI) method. Each individual direction ($R_n, Z_m$) in the ADI method is solved with the Thomas Algorithm for direct solving the using the Thomas algorithm as discussed in chapters 2 and 3. This allows the solution of the equations in a form of a tri-diagonal matrices to be obtained in $O(n)$ operations. Numerical convergence study of the steady state flux with ensuring that the calculations are sufficiently accurate with the following values : $\delta R = 1 \times 10^{-5}, \delta Z = 1 \times 10^{-5}, \delta\tau = 1 \times 10^{-9}, \gamma_R = 1.1, \gamma_Z = 1.3, \gamma_\tau$ =1.001.

Simulations were coded in C++ (as discussed in chapter 2 and 3) with the OpenMP(Open Multi-programming) API (no GPU acceleration is needed). The simulations preformed on an Intel (R) Xeon (R) 3.2Ghz, with approximately usage of 0.5GB RAM, and runtime between 5-20 minutes.

## 7.3 Results and discussion

The simulations are divided into three parts. I first report a case study of chronoamperometry at a simple microdisc electrode with an infinite insulating and non sticking surrounding surface. This allows validation of the code by examining the behaviour of the chronoamperometry curve, and comparing the values of the transient current with analytical and numerical results from previous works of Szabo[27] and Heinze[28]. Second in this section, simulation results are presented for a fully sticking surface where the concentration is set to zero both on the microdisc electrode and on the surface (sheath). This simulation was made with different ratios of $R_{sd}$ to extract the relation of the shielding current to $R_{sd}$. These results for transport controlled sticking at the surrounding sheath can also be derived analytically to further validate the simulations. Third, results are discussed for intermediate sticking kinetics reflecting an intermediate case between a full sticking and non-sticking surrounding surface (sheath) where its controlled by finite adsorption kinetics ($k_0$). This later study is made with representative ratios of $R_{sd} = 10$, $R_{sd} = 10^2$, and $R_{sd} = 10^3$.

### 7.3.1 Model validation - simple microdisc electrode chronoamperometry

The model described above is used to generate the results of the dimensionless steady state current in a chronoamperometry process. The concentration at the disc electrode is set to zero. No sticking occurs on the sheath. Figure 7.3 shows the decay of the dimensionless flux at the microdisc as function of dimensionless time. The steady state flux is normalized to the theoretical value of the steady state flux at a microdisc electrode ($J/4CDR$) and for large $\tau$ is converged to a satisfying value of 1.001. To assess the accuracy, I compare all the results with earlier simulation literature[27,28], and also to the Shoup−Szabo approximate equation for chronoamperometry at a microdisc[27] (which is reported to be accurate to within 0.6%[27] ), where:

$$I = 4nFDc^{*}r_{d}f(\tau^{*}) \tag{7.24}$$

$$f(\tau^{*}) = 0.7854 + 0.8862\tau^{*-1/2} + 0.2146e^{-0.7823\tau^{*-1/2}} \tag{7.25}$$

For comparison purposes, $\tau^{*} = 4\tau$ was defined in order to follow the Shoup−Szabo definition of the dimensionless time parameter. The variation of $f(\tau^{*})$ with $\tau^{*}$ is presented in Table 7.2. The results show a good agreement with the simulation literature and the analytical approximation. It is worth mentioning that at short times the deviation from the other works shown here, can reach up to 0.4% but as time tends to large values, the deviation from the literature approaches zero. Overall this accuracy, validates the grid parameter chosen for the numerical 2D calculation of the chronoamperometry process and gives a reliable basis to for the further calculations reported in this work.

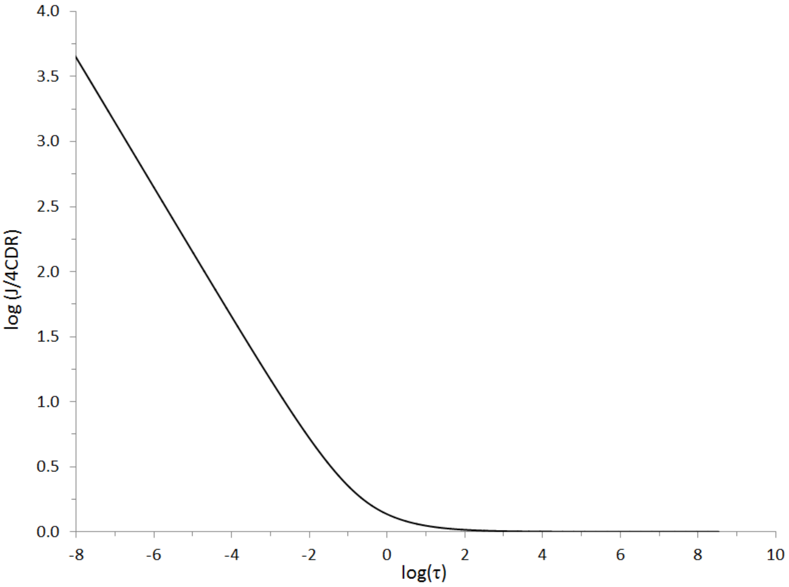

Figure 7.3: Simulation of CA process at a microdisc electrode. Note that the curve is presented with logarithmic scales.

| $\tau^* = 4 \times \tau$ | $f(\tau^*)$ | | | |
|---|---|---|---|---|
| | This work | Heinze[28] | Shoup and Szabo[27] | Shoup and Szabo[27] (approximation) |
| 0.01 | 9.677 | 9.66 | 9.632 | 9.647 |
| 0.04 | 5.246 | 5.237 | 5.226 | 5.221 |
| 0.09 | 3.777 | 3.772 | 3.768 | 3.755 |
| 0.25 | 2.612 | 2.609 | 2.602 | 2603 |
| 0.64 | 1.969 | 1.969 | 1.969 | 2.008 |
| 1.21 | 1.689 | 1.688 | 1.68 | 1.695 |
| 2.25 | 1.496 | 1.495 | 1.491 | 1.496 |
| 4.00 | 1.367 | 1.367 | 1.366 | 1.374 |
| 6.76 | 1.280 | 1.28 | 1.279 | 1.285 |

Table 7.2: Validation of the chronoamperometric currents at different dimensionless times versus other simulations in the literature.

### 7.3.2 The shielding effect - full sticking on the surrounding surface (sheath)

Further simulation was next carried out to describe the shielding current on a microdisc electrode surrounded by a ”full” sticking surface at when adsorption occurs at a mass transport controlled surface, so the concentration on both the surrounding insulating surface and on the electrode was set to zero. In this case, in the simulation the flux is integrated along the radius of the disc ($r_d$) according to equation 8.28. However, the sought result can also be obtained using the exact expression for the mass transport controlled flux distribution along the radius[29–31]:

$$j = \frac{2}{\pi}\frac{c^*D}{\sqrt{r_s^2 - r^2}} \tag{7.26}$$

By integrating the flux density from 0 to $R_d$ over the disc area, the shielded dimensionless flux can be derived as:

$$J^s = 2\pi \int_0^{R_d} \frac{2}{\pi}\frac{1}{\sqrt{R_s^2 - R^2}} R\mathrm{d}R = -4(\sqrt{R_s^2 - R_d^2} - R_s) \tag{7.27}$$

Rearranging and approximating the root with a Taylor series, the relation of the shielding flux with $R_d$ and $R_s$ is:

$$J^s = 4R_s\left(\frac{R_d^2}{2R_s^2} - \frac{R_d^4}{8R_s^4} + \frac{R_d^6}{16R_s^6} - ...\right) \approx \frac{2R_d^2}{R_s} + O\left(\frac{R_d^4}{8R_s^3}\right) \approx \frac{2R_d^2}{R_s} \tag{7.28}$$

Values of $J^s$ from the above relation and from simulation have been calculated for three different radius ratios, $R_{sd}$ and the results are summarized in Table 7.3. Excellent agreement is evident. This results shows that the current shielded by a fully sticking surface

| $R_d$ | $R_{sd}$ | $J^s$ (simulation) | $J^s$ (expression) | J without sticking surface ($J = 4CDR_d$) |
|---|---|---|---|---|
| 0.1 | 10 | $1.99 \times 10^{-2}$ | $2.0 \times 10^{-2}$ | 0.4 |
| 0.01 | 100 | $1.98 \times 10^{-4}$ | $2.0 \times 10^{-4}$ | 0.04 |
| 0.001 | 1000 | $2.00 \times 10^{-6}$ | $2.0 \times 10^{-6}$ | 0.004 |

Table 7.3: Numerical and analytical values of the dimensionless shielding flux at various radius ratios.

can be simply generated by:

$$I^s = 2Fc^*D\frac{R_d^2}{R_s} \qquad for\ R_d << R_s \tag{7.29}$$

In the following section I use this model to simulate the current shielded by a surface when adsorption occurs with finite absorption kinetics.

### 7.3.3 Shielding effect - kinetically controlled adsorption

Chronoamperometry simulation was first carried out for various adsorption rates at a representative ratio of $R_{sd} = 1000$. Other ratios are discussed later in this section. This ratio of 1000 describes a typical case where a microelectrode of the order of $1\mu m$ is surrounded by an insulating surface of the order of $1mm$ radius. The chronoamperometry curves are presented in figure 7.4.

The results in figure 7.4 show the shielding effect on the flux/current ($J = I/nF$) when the surface is active toward adsorption. For low rates of adsorption, the curves have the typical profile of chronoamperometry on an unshielded microdisc, except for a slight deviation in the absolute values; close examination of the quasi-steady state flux absolute values shows that the dimensionless flux decreases by 7.5% from 4.02 for a non-sticking surface (the upper black thicker curve) to 3.71 for relatively low adsorption rate of $K = 1 \times 10^{-4}$. It is important to note that this value is simulated for $R_d = 1 \times 10^{-3}$. Therefore, in order to derive the dimensionless flux, I normalized the flux and K by $R_d$ to get the dimensionless form since the dimensionless J and R are defined using $r_s$ and $r_d$.

It can be seen that for intermediate rates of adsorption ($K = 0.1 - 1000$), the curves are characterized by two relaxations. The first is due to the disc and the second later one is

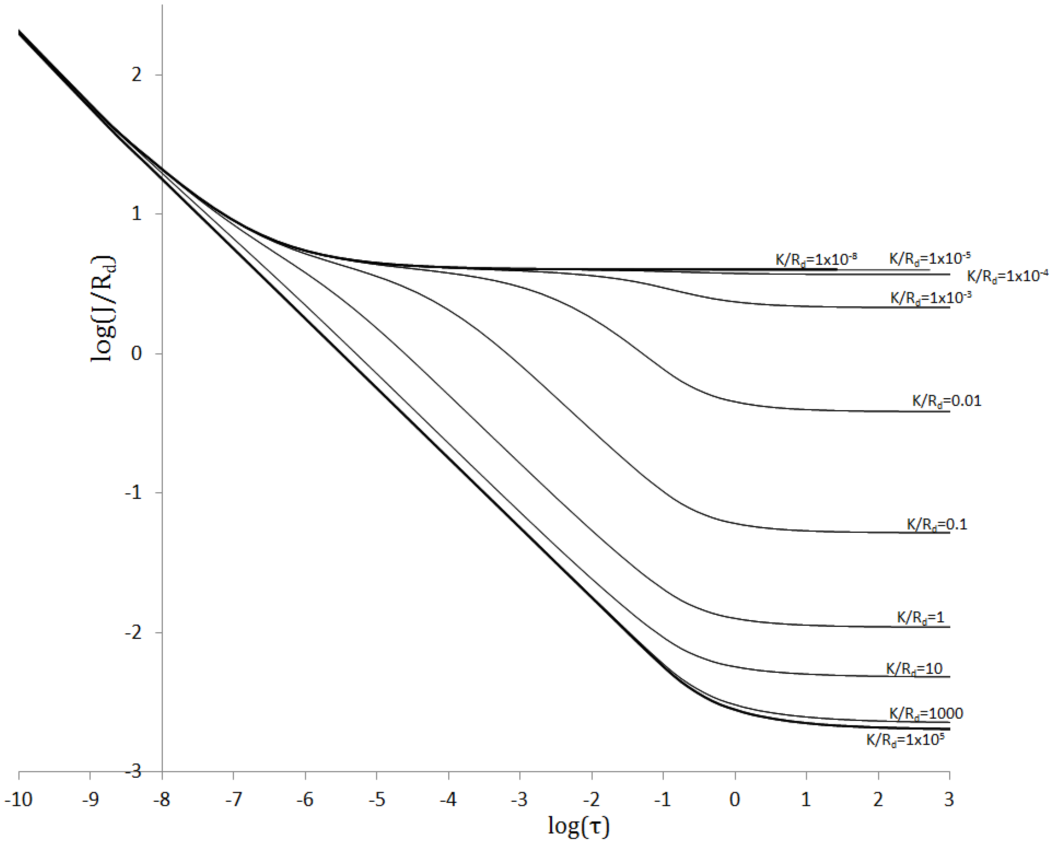

Figure 7.4: Chronoamperometry curves at the total flux simulated on the microdisc surrounded by adsorbing surface with a wide range of K (from $1 \times 10^{-8}$ to $1 \times 10^{5}$).

related to the surrounding surface. This behaviour sharply increases with the adsorption rate constants over the range $10^{-3} < K/R_d < 1$.

At very high adsorption rates ($K/R_d > 1$), the chronoamperometry profile suggests that the adsorption surface behaves as a full sticking surface and therefore the microdisc and the adsorbing surface can effectively be considered as a united surface, yielding one current relaxation on the electrode where the quasi-steady state flux value ($2 \times 10^{-6}$) can also be derived from the analytical relation described earlier (equation 7.29). For the purposes of comparison, all the quasi-steady states values at different adsorbing rates and radius ratios are summarized in Table 7.4. Converting these values to dimensional currents using equation 8.29 can be very useful to determine the surrounding sheath activity and the shielded disc current by comparing these values with an experimental measured current at microdisc electrode.

| $K/R_d$ | $R_{sd} = 10$ | $R_{sd} = 100$ | $R_{sd} = 1000$ |
|---|---|---|---|
| $1 \times 10^{-5}$ | 4.013 | 4.015 | 3.985 |
| $1 \times 10^{-4}$ | 4.010 | 3.972 | 3.707 |
| 0.001 | 3.983 | 3.664 | 2.143 |
| 0.01 | 3.733 | 2.022 | 0.385 |
| 0.1 | 2.312 | 0.343 | 0.0521 |
| 1 | 0.619 | 0.0621 | 0.0109 |
| 10 | 0.263 | 0.0274 | 0.00481 |
| 100 | 0.211 | 0.0213 | 0.00311 |
| 1000 | 0.203 | 0.0204 | 0.00227 |
| $1 \times 10^{4}$ | 0.202 | 0.0202 | 0.00206 |
| $1 \times 10^{5}$ | 0.201 | 0.0201 | 0.00203 |

Table 7.4: Quasi-steady state values at various $R_{sd}$ and dimensionless K.

Figure 7.5 compares the behaviour of the flux/current measured from the electrode with the ratio between the adsorbing surface and the electrode, where $R_{sd} = 10$, $10^2$ and $10^3$. The profiles show that when the adsorbing surface becomes active, at higher $R_{sd}$ ratios the flux gets lower value and the relaxation time due to the adsorption surface becomes longer compared to larger $R_{sd}$ ratios. It can be seen that at $R_{sd} = 10$ the relaxation time to the quasi-steady state is fast and thus adsorption has a relatively smaller effect on the shape of the chronoamperometry curves. The profiles of the very low and high adsorption rates (figure 7.5a and figure 7.5c) particularly show the behaviour of a non-sticking and fully-sticking surface, and their absolute values (table 7.4) are in good agreement with the analytical expression described earlier.

In order to better understand the interaction between the adsorbing surface and the disc current, it is helpful to generate concentration profiles of the electrolyte/ adsorbing species in solution. Since the non-uniform diffusion flow generates different coverages across the insulating surface (sheath), it is necessary to choose $\Gamma$ to be artificiality large

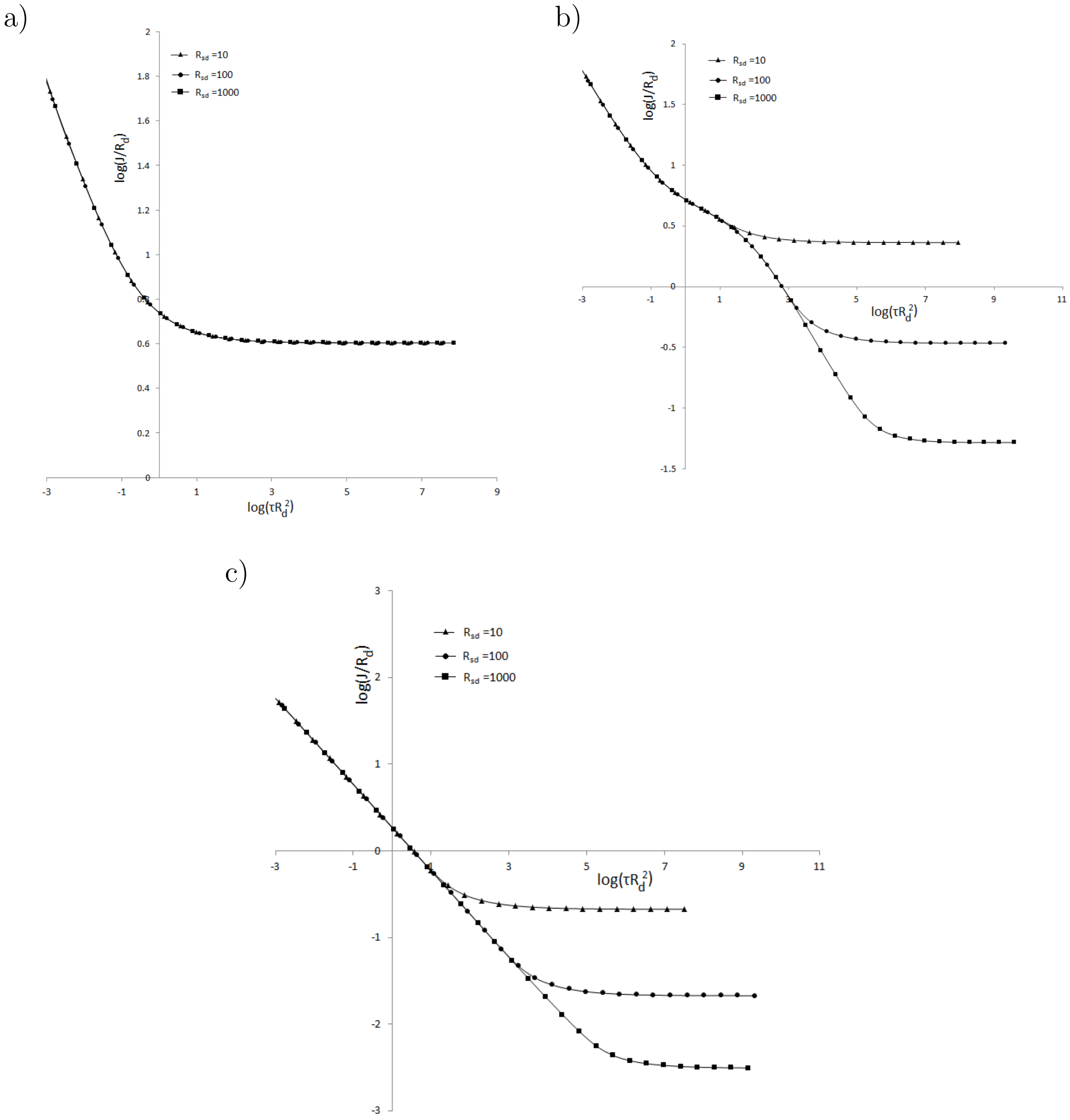

Figure 7.5: A comparison of chronoamperometry curves in different $R_{sd}$ (1000,100,10) at (a) K= $1 \times 10^{-3}$, (b) $K = 1$, and (c) $K = 1000$. In order to compare between the results of the chronoamperometry curves for different $R_{sd}$, I normalize the flux, $\tau$ and $K$ relative to the calculated $R_d$.

enough, so that $\theta << 1$ at all $\tau$. Consequently, the coverage is small enough to not affect the kinetics within the chronoamperometry process (since $(1 - \theta) \approx 1$), allowing a quasi-steady state to be achieved. In order to determine the variation of adsorption uptake across the surface, the coverage rate ($d\theta/d\tau$) is examined along the surface ($R_d < R \leq R_s$)

as shown in figure 7.6. The profiles of coverage rates also describes the flux profiles on the surface from equations 7.7 and 7.9. These results (figure 7.6) show how the rate of coverage develops with time for the chronoamperometry process with a representative ratio of $R_{sd} = 10$. Concentration maps in two dimensions are also provided in figure 7.7 to give a complementary view of the adsorption behavior. These concentrations maps were generated in two dimensions at quasi-steady state, near the electrode and the adsorption surface ($0 \leq R \leq 1,\ 0 \leq Z \leq 0.6$ ). At lower adsorbing rates of the surface (figure 7.6a), it can be seen that the coverage is dominated mostly by the disc concentration gradient. Therefore, near the disc edge ($R_d$) where the concentration is diluted, the flux and the coverage on the surface are lower, whereas on moving away from the disc radially towards the bulk solution, the concentration increases until it approaches the bulk concentration. In the same manner, the adsorption rate gradually increases along the surface. For intermediate rates (figure 7.6b), the surface becomes active, and thus higher rates of adsorption are observed at the edge of the surface typical for non-linear diffusion to the microelectrode surface[31]. Figure 7.6c and 7.7b suggest that the surface almost fully controls the shape of the profile for the high adsorbing rate constant of $K = 1000$. Moreover, figure 7.6 shows that a quasi-steady state is achieved for all the range of adsorbing rates as the gap between two consequent curves approaches to zero (the time grows approximately exponentially with each curve). These quasi-steady state profiles give the coverage profiles that would be observed at a long chronoamperometry process, as long as the coverage fraction can be neglected ($\theta \gg 1$).

Figure 7.8 shows the flux along the microdisc electrode. Since the boundary condition on the disc is assumed to be zero, the flux profile along the disc follows the behaviour of mass transport in a microdisc system. Comparing the values of the flux in the low and

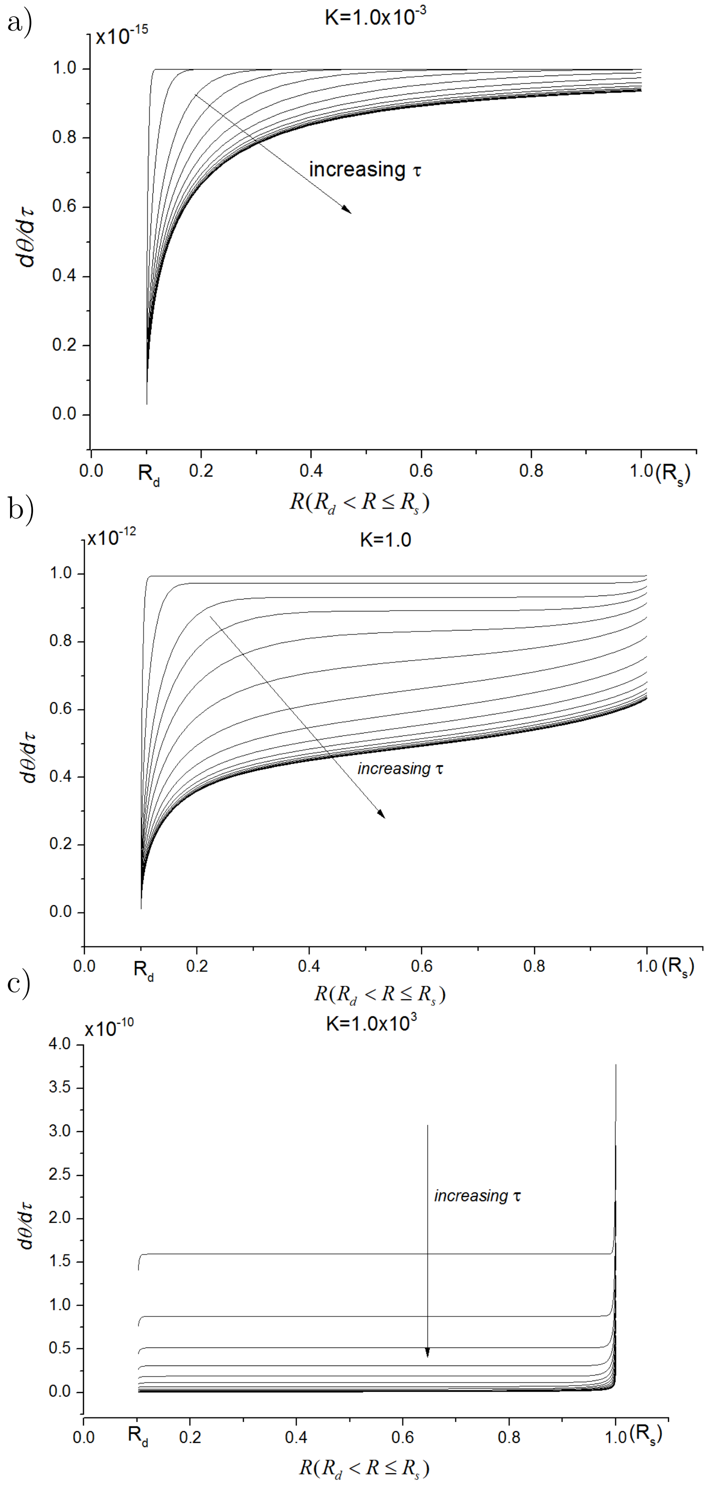

Figure 7.6: The rate of coverage ($d\theta/d\tau$) along the surface ($R_{sd} = 10$) at various $\tau$ in three different adsorbing coefficient rates: $K = 10^{-3}$(a), $K = 1.0$(b), and $K = 10^{3}$(c). The $\tau$ values from the upper to the downer curves are: $1.6 \cdot 10^{-6}$, $6.0 \cdot 10^{-6}$, $1.80 \cdot 10^{-5}$ , $5.05 \cdot 10^{-5}$, $1.39 \cdot 10^{-4}$, $3.79 \cdot 10^{-4}$, $1.03 \cdot 10^{-3}$, $2.80 \cdot 10^{-3}$, $7.62 \cdot 10^{-3}$, $2.07 \cdot 10^{-2}$, $5.62 \cdot 10^{-2}$, 0.15, 0.42, 1.12, 3.06, 8.32, and the thick line is $\tau = 9099$.

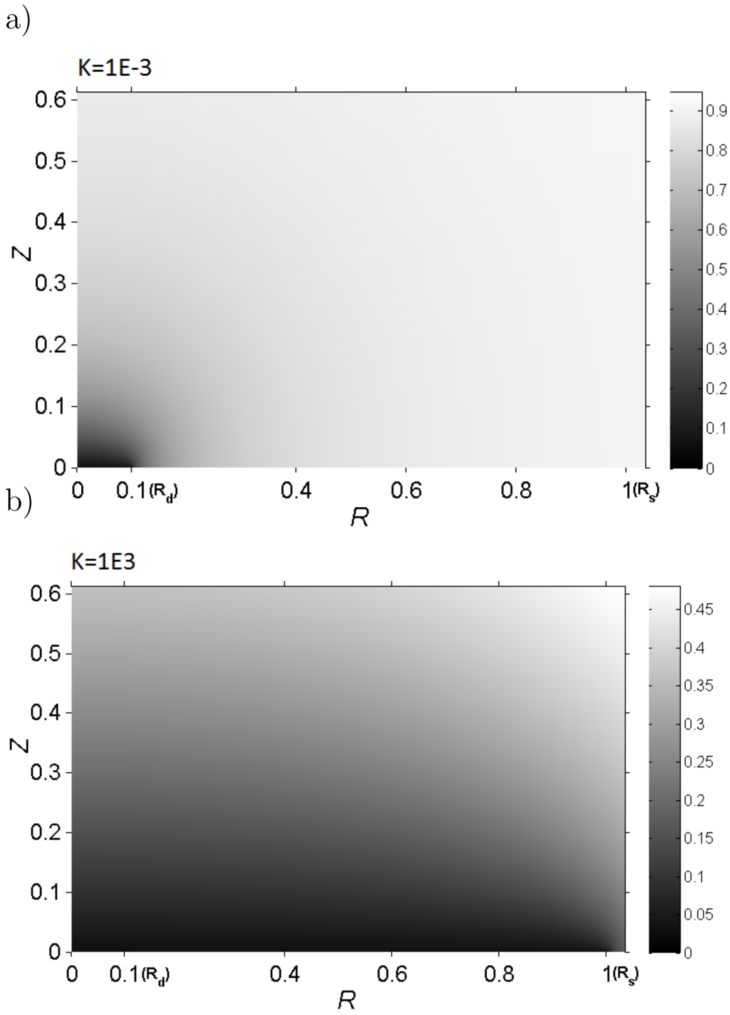

Figure 7.7: Concentration maps of the electrode and surface area ($R_{sd} = 10$) in low adsorbing rate, $K = 0.001$ (a) and high adsorbing rate, $K = 1000$ (b)

high adsorbing rates(figure 7.8a-b) suggests that the ”edge effect” of high flux density in the edge of the microdisc, is moderated at high adsorbing rates as expected when the surface becomes fully active.

## 7.4 Conclusions

The simulations shown in this chapter indicate that if significant adsorption occurs on the sheath used to insulate a microdisc electrode, then this can have a high impact on the measured current-time data because of a significant ’shielding effect’. It was shown that this effect is reflected both in the characteristic shape of the relaxation in

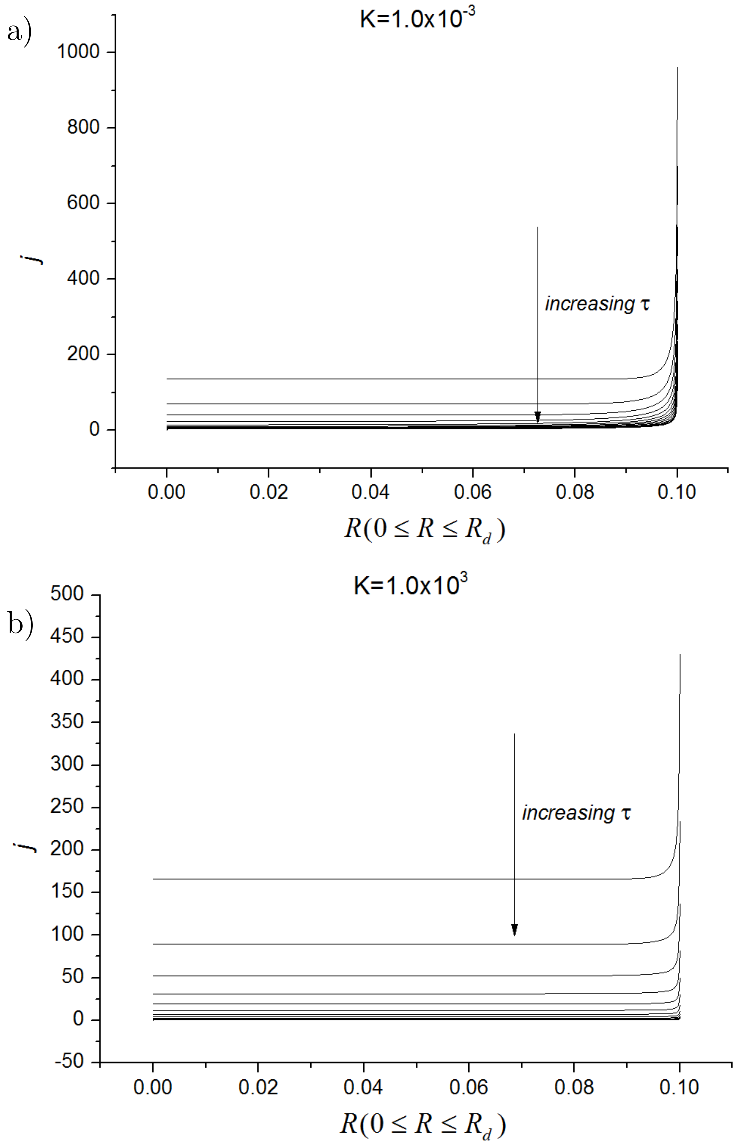

Figure 7.8: The flux density ($j$) inward the disc at various $\tau$ in two adsorbing coefficient rates: $K = 10^{-3}$(a) and $K = 10^{3}$(b), $R_{sd} = 10$. The $\tau$ values from the upper to the downer curves are: $1.6 \cdot 10^{-6}$, $6.0 \cdot 10^{-6}$, $1.80 \cdot 10^{-5}$, $5.05 \cdot 10^{-5}$, $1.39 \cdot 10^{-4}$, $3.79 \cdot 10^{-4}$, $1.03 \cdot 10^{-3}$, $2.80 \cdot 10^{-3}$, $7.62 \cdot 10^{-3}$, $2.07 \cdot 10^{-2}$, $5.62 \cdot 10^{-2}$, 0.15, 0.42, 1.12, 3.06, 8.32, and the thick line is $\tau = 9099$.

chronoamperometry and in the quasi-steady state current values. Moreover, the observed quasi-steady state currents are a function of the sheath to disc electrode radius ratio and the adsorption rate, and the data reported can be directly used in experimental systems to determine this effect on the current responds measured at microdisc electrode surrounded by an insulating but simultaneously adsorbing sheath.

# References

[1] S. Eloul and R. G. Compton *ChemElectroChem*, vol. 1, no. 5, pp. 917–924, 2014.

[2] C. Amatore, M. R. Deakin, and R. Wightman *Journal of Electroanalytical Chemistry and Interfacial Electrochemistry*, vol. 225, no. 12, pp. 49 – 63, 1987.

[3] C. Amatore, N. Da Mota, C. Lemmer, C. Pebay, C. Sella, and L. Thouin *Anal. Chem.*, vol. 80, pp. 9483–9490, Dec. 2008.

[4] M. R. Deakin, R. Wightman, and C. Amatore *Journal of Electroanalytical Chemistry and Interfacial Electrochemistry*, vol. 215, no. 12, pp. 49 – 61, 1986.

[5] A. Bond, M. Fleischmann, and J. Robinson *Journal of Electroanalytical Chemistry and Interfacial Electrochemistry*, vol. 168, no. 12, pp. 299 – 312, 1984.

[6] C. Amatore, S. Arbault, I. Bonifas, and M. Guille *Biophysical Chemistry*, vol. 143, no. 3, pp. 124 – 131, 2009.

[7] C. Amatore, S. Arbault, Y. Bouret, M. Guille, and F. Lematre *ChemPhysChem*, vol. 11, no. 13, pp. 2931–2941, 2010.

[8] R. W. Murray *Chemical Reviews*, vol. 108, no. 7, pp. 2688–2720, 2008.

[9] M. V. Mirkin, F.-R. F. Fan, and A. J. Bard *Journal of Electroanalytical Chemistry*, vol. 328, no. 12, pp. 47 – 62, 1992.

[10] A. M. Bond *Analyst*, vol. 119, pp. 1R–21R, 1994.

[11] K. Tschulik, C. Batchelor-McAuley, H.-S. Toh, E. J. E. Stuart, and R. G. Compton *Phys. Chem. Chem. Phys.*, vol. 16, pp. 616–623, 2014.

[12] Y.-G. Zhou, N. V. Rees, and R. G. Compton *Angewandte Chemie International Edition*, vol. 50, no. 18, pp. 4219–4221, 2011.

[13] E. O. Barnes and R. G. Compton *Journal of Electroanalytical Chemistry*, vol. 693, pp. 73–78., 2013.

[14] K. R. Ward, N. S. Lawrence, R. S. Hartshorne, and R. G. Compton *Journal of Electroanalytical Chemistry*, vol. 683, pp. 37–42., 2012.

[15] I. J. Cutress and R. G. Compton *Chemical Physics Letters*, vol. 508, pp. 306–313, May 2011.

[16] H. Brenner *Chemical Engineering Science*, vol. 16, no. 3, pp. 242–251, 1961.

[17] I. J. Cutress, E. J. Dickinson, and R. G. Compton *Journal of Electroanalytical Chemistry*, vol. 655, pp. 1–8, May 2011.

[18] I. Streeter and R. G. Compton *The Journal of Physical Chemistry C*, vol. 111, no. 49, pp. 18049–18054, 2007.

[19] J. Crank, *The mathematics of diffusion.* Oxford university press, 1979.

[20] R. G. Compton and K. L. Pritchard *J. Chem. Soc., Faraday Trans.*, vol. 86, no. 1, pp. 129–136, 1990.

[21] I. Langmuir *Journal of the American Chemical Society*, vol. 40, no. 9, pp. 1361–1403, 1918.

[22] Y.-G. Zhou, N. V. Rees, and R. G. Compton *Chemical Physics Letters*, vol. 514, no. 4, pp. 291–293, 2011.

[23] A. Einstein *Annalen der Physik*, vol. 322, no. 8, pp. 549–560, 1905.

[24] D. Gavaghan *Journal of Electroanalytical Chemistry*, vol. 456, no. 1, pp. 13–23, 1998.

[25] J. Crank and P. Nicolson in *Mathematical Proceedings of the Cambridge Philosophical Society*, vol. 43, pp. 50–67, Cambridge Univ Press, 1947.

[26] D. Gavaghan *Journal of Electroanalytical Chemistry*, vol. 420, no. 12, pp. 147 – 158, 1997.

[27] D. Shoup and A. Szabo *Journal of Electroanalytical Chemistry and Interfacial Electrochemistry*, vol. 140, no. 2, pp. 237–245, 1982.

[28] J. Heinze *Journal of Electroanalytical Chemistry and Interfacial Electrochemistry*, vol. 124, no. 1, pp. 73–86, 1981.

[29] Y. Saito *Review of Polarography*, vol. 15, no. 6, pp. 177–187, 1968.

[30] M. A. Bender and H. Stone *Journal of Electroanalytical Chemistry*, vol. 351, no. 12, pp. 29 – 55, 1993.

[31] R. Compton and C. Banks, *Understanding voltammetry.* Imperial College Press, 2006.

# Chapter 8

# Voltammetric sensitivity enhancement by using pre-concentration

In this chapter, the study of a ’sticking‘ surface (discussed in chapter 7) is expanded to the interesting case of a reversible adsorbing surface. in particular a popular approach to enhancing the sensitivity of voltammetry is the surface modification of electrodes so as to provide adsorption sites which allow pre-concentration of target species, so as to promote sensitivity and reduced limits of detection. The surface modifier is typically inert other than providing enhanced adsorption and hence pre-concentration and non-conductive so that after pre-concentration the adsorbent must desorb and diffuse to the electrode before detection. A simulation of an idealized model is reported for this type of voltammetry, focusing in particular on the effects of adsorption coverage and binding strength on the surface on the voltammetry response. The work has been published in ‘The Journal of Physical Chemistry C’[1].

## 8.1 Introduction

Chemically modified electrodes have found enormous application in electrochemistry following the pioneering work of Murray and colleagues[2–5]. In one recent and popular variant the electrode is modified with insulating particles, often nanoparticles, which serve to enhance voltammetry signals by means of pre-concentrating target species prior to voltammetric detection. Table 8.1 provides a range of illustrative examples[6–16]. The approach for particular analytes is generally developed empirically. The aim of the present chapter is to explore the parameters underpinning the method using an idealized model. In particular it can be anticipated that the two step process in which adsorption on particles or surfaces adjacent to the detection electrode prior to voltammetry requires the subsequent desorption and diffusion of the target to the electrode. See illustration in figure 8.1.

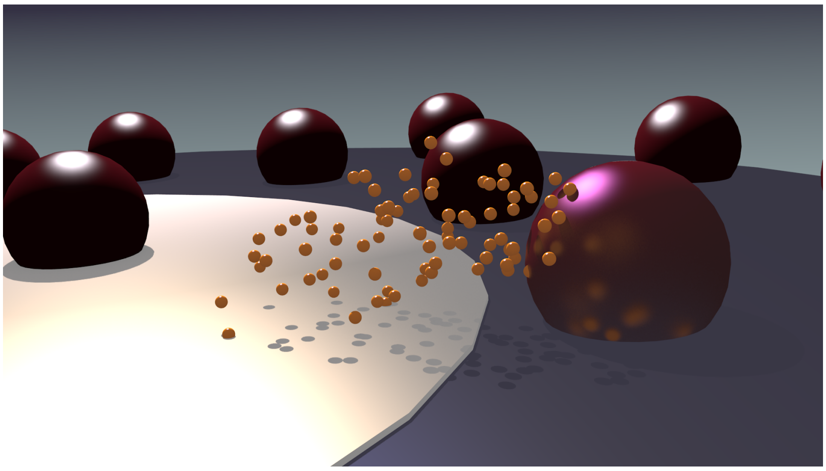

Figure 8.1: Illustration of the of pre-concentrated species (yellow spheres) on the modifier (red spheres) surrounding a disc electrode.

It follows then that the strategy requires a delicate balance of adsorption strength in order to be useful. In particular very strong irreversible adsorption will simply provide a 'sink' for the analyte and no useful signals, whilst slow adsorption and/or slow desorption will be similarly useless by virtue of offering little pre-concentration. In order to probe the balance, I adopt the idealized model shown in figure 8.2. Here the study considers a disc electrode surrounded by a concentric ring ('sheath') on which adsorption occurs exclusively, allowing to pre-concentrate the target analyte, $A$. After the pre-concentration, simulations are carried out to explore the effect on the voltammetry of species $A$ at the disc electrode. In this way the thermodynamics and kinetics of the process:

$$A(aq) \leftrightarrows A(ads) \tag{8.1}$$

are shown to strongly influence the current response only under very carefully selected conditions.

In the previous chapter, it was reported that the supporting sheath surrounding a micro-disc electrode can significantly shield the current response when the electro-active species irreversibly adsorbs on the surface[17]. It was found that in case of irreversible adsorption on the supporting sheath, the measured current reflecting the adsorbing rate and the radius ratio between the disc and the surface. This shielding effect was also discussed in nanoparticle impact analysis[18] and other evidence of 'shielding' has been noted[19,20]. Following that, in this study, new interest has arisen in studying the case where a *reversible* adsorption takes place on the surface surrounding an electrode as a model for the chemically modified electrodes described above. Transient voltammetry measurements such as cyclic voltammetry (CV) can be dramatically affected by this adsorbing surface, since, when scanning the potential, a diffusional transport of material towards or away from the disc electrode changes of concentration distribution in the cell local to the electrode which can potentially trigger desorption of material from the surface towards the electrode.

This study reveals insights of how electrochemical behaviour can be influenced by the surface surrounding a disc electrode and underpinning sensitive analytical methods and applications related to physical adsorption of nanoparticles or molecules on modified surfaces (see Table 8.1). Additionally, the basic understanding of how an adjacent surface can control the behaviour of the voltammetry, providing a novel way to make responsive controlled released electrochemical systems and high sensitive detection[21,22]. For example, it can boost the Faraday current when the concentration drops in the solution near the electrode, or release particles of interest from the surface to the solution when a reaction on the disc electrode occurs.

This chapter reports the effect of an annular sheath concentric with a working electrode as a reversible adsorbing surface in voltammetry measurements. The model retains the essential features of modelling the adsorption system of interest whilst having a two dimensional geometry of the diffusion field which allows extensive simulation to explain all parameters which would be impossible for any three dimensional model. It is shown that the adsorption effect can have strong influence on the current value as well as the shape of the respond of the voltammogram, and is therefore generally important for studies using electro-active particles that can potentially be adsorbed on the surface surrounding the electrode.

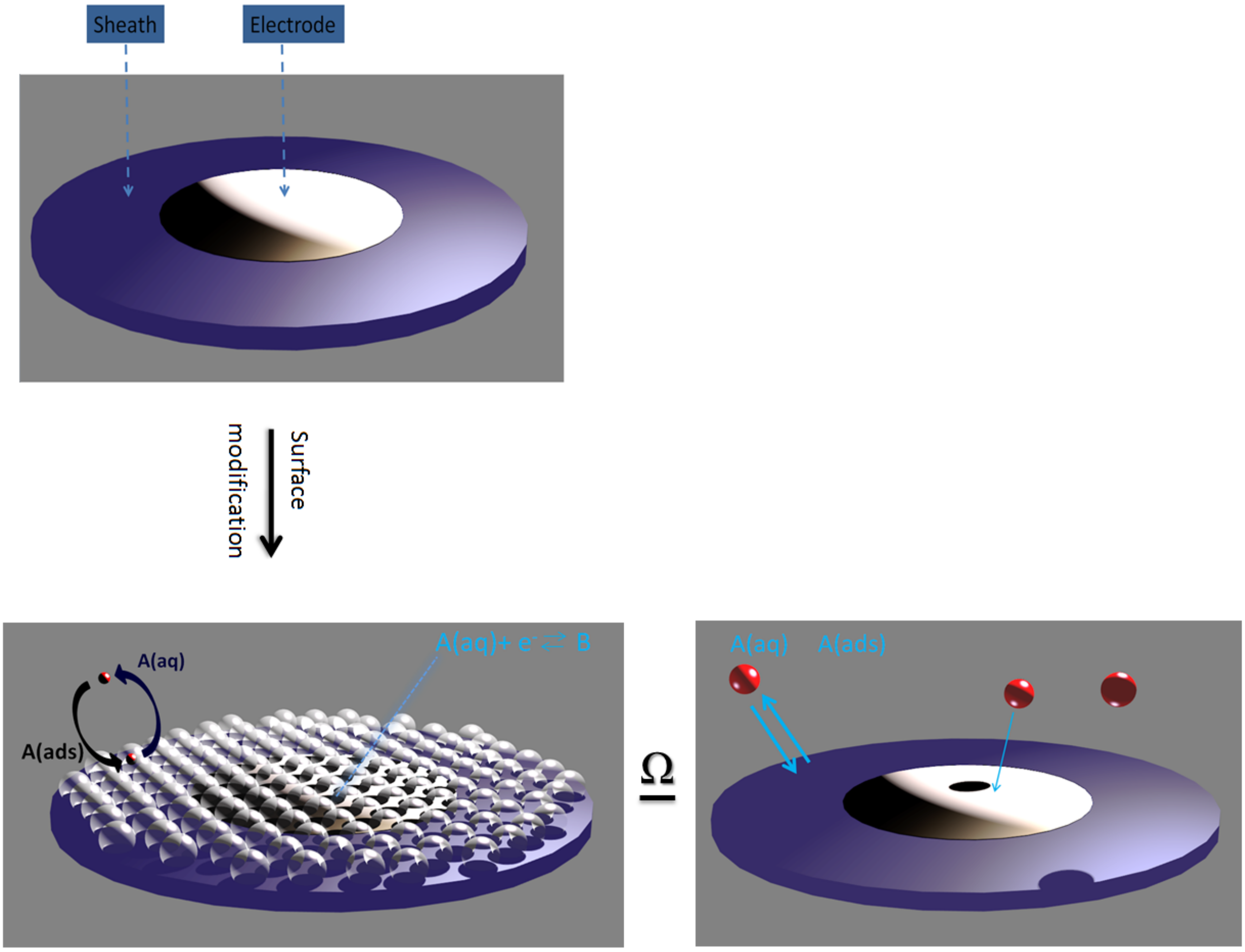

Figure 8.2: Illustration of the idealized model for the simulation of pre-concentrated species $A$ (red spheres) on the modifier (white spheres) around the electrode.

| Publication | Modifying substrate | Target species |
|---|---|---|
| [6] Kaur & Srivastava, 2014 | nanocrystalline metallosilicate | Riboflavin, Rutin, Pyrodoxine |
| [7] Yu et al. , 2013 | $Co_3O_4$ nanocrystals | Pb(II) |
| [8] Zhang et al. , 2013 | $\alpha - MnO_2$ | Zn(II), Cd(II), Pb(II), Cu(II), Hg(II) |
| [9] Xu et al. , 2013 | hollow nano-spheres of magnesium sillicate | Cd(II), Pb(II), Cu(II), Hg(II) |
| [10] Liu et al. , 2013 | porous $Co_3O_4$ microsheets | Pb(II) |
| [11] Herzog et al. , 2013 | mesoporous organosilica | Hg(II) |
| [14] Zhang et al. , 2011 | nano-wall arrays of $CaCO_3$ chitosan | organophosphate pesticides |
| [12] Mbouguen et al. , 2011 | bilayer of organoclay overcoating sublimed ferrocene layer | ascorbic acid, uric acid |
| [15] Zhang et al. , 2011 | flower-like hydroxyapatite | Cd(II), Pb(II) |
| [13] Tonlé et al. , 2010 | thiol-functionalized clay | Pb(II) |
| [16] Yin et al. , 2010 | nano-'shuttles' of copper oxide (CuO) | Hg(II) |

Table 8.1: Illustrative examples of modified surfaces to provide pre-concentration of target analytes.

## 8.2 Theory

A cyclic voltammetry simulation is considered for a system containing small finite disc electrode surrounded by an insulating but adsorbing/desorbing sheath. The sheath is assumed to behave according to the reversible Langmuir model of surface adsorption[23]. This study is made via simulating Fickian diffusion under the presence of supporting electrolyte, allowing a diffusion controlled transport. By approximating the transport to behave in a statistical manner[24–26], the Fick's second law can be numerically solved[27,28]. For a finite disc geometry (figure 8.3a), Fick's second law is solved for a redox couple in a cylindrical space using axial symmetry around $r = 0$[29]:

$$\frac{\partial c_A}{\partial t} = D_A \left( \frac{\partial^2 c_A}{\partial r^2} + \frac{\partial^2 c_A}{\partial z^2} + \frac{1}{r}\frac{\partial c_A}{\partial r} \right) \tag{8.2}$$
$$\frac{\partial c_B}{\partial t} = D_B \left( \frac{\partial^2 c_B}{\partial r^2} + \frac{\partial^2 c_B}{\partial z^2} + \frac{1}{r}\frac{\partial c_B}{\partial r} \right)$$

where $r$ and $z$ are the cylindrical coordinates, $D$ is the diffusion coefficient, $c$ is the concentration, and the symbols $A$ and $B$ are the redox couple species in the one step one electron electrochemical reaction:

$$A \leftrightarrows B + e^- \tag{8.3}$$

Two distances are defined in the $r$ direction, the disc electrode radius ($r_d$) and the surface radius ($r_s$) as illustrated in figure 8.3.

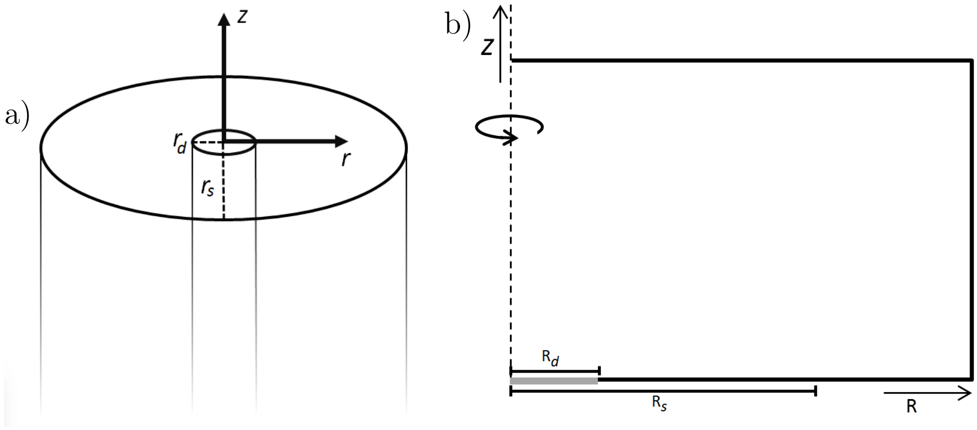

Figure 8.3: 3D Illustration of the microdisc electrode surrounded by a sheath (a) and the 2D dimensionless system in the simulation model (b).

### 8.2.1 Dimensionless coordination representation

Dimensionless parameters are used in the simulation to simplify the analysis[29]. All the dimensional and dimensionless symbols presented in this work, are also summarized in Table 8.2. Coordinates are normalized to the surface radius ($R = r/r_s, Z = z/r_s$) and concentrations are defined relative to the bulk concentration of the electroactive species ($C = c/c^*$). The diffusion coefficient of the product species ($B$) can be related to the diffusion coefficient of species $A$ by:

$$d_B = D_B/D_A \tag{8.4}$$

Further, a dimensionless time parameter ($\tau$) is defined as:

$$\tau = \frac{D_A}{r_s^2}t \tag{8.5}$$

In the transformed coordinates, the radius of the surface is unity and the microdisc electrode lies between: $0 < R_d < 1$. Converting Fick's second law into a dimensionless form gives[30]:

$$\begin{aligned} \frac{\partial C_A}{\partial \tau} &= \left( \frac{\partial^2 C_A}{\partial R^2} + \frac{\partial^2 C_A}{\partial Z^2} + \frac{1}{R}\frac{\partial C_A}{\partial R} \right) \\ \frac{\partial C_B}{\partial \tau} &= d_B \left( \frac{\partial^2 C_B}{\partial R^2} + \frac{\partial^2 C_B}{\partial Z^2} + \frac{1}{R}\frac{\partial C_B}{\partial R} \right) \end{aligned} \tag{8.6}$$

The dimensionless mass transport equations must be solved over all space with the appropriate boundary conditions which define the kinetics and fluxes on the surfaces; the disc and the sheath (figure 8.3b).

| Parameter | Description | Units |
|---|---|---|
| Dimensional parameters | | |
| $A$ | Electrode area | $cm^2$ |
| $r_d$ | Electrode radius | $cm$ |
| $r_s$ | Surface radius | $cm$ |
| $D$ | Diffusion coefficient | $cm^2 s^{-1}$ |
| $c$ | Concentration | $mol\, cm^{-3}$ |
| $c^*$ | Bulk solution concentration | $mol\, cm^{-3}$ |
| $\theta$ | Fractional surface coverage | |
| $\theta_{eq}$ | Initial coverage state | |
| $\Gamma$ | Surface coverage of a full monolayer | $mol\, cm^{-2}$ |
| $k^0$ | Standard electrochemical rate constant | $cm\, s^{-1}$ |
| $k_0$ | Adsorption rate constant | $cm\, s^{-1}$ |
| $k_1$ | Desorption rate constant | $mol\, cm^{-2}\, s^{-1}$ |
| $t$ | Time | $s$ |
| $j^D$ | Flux | $mol\, cm^{-2}\, s^{-1}$ |
| $J^D$ | Rate | $mol\, s^{-1}$ |
| $\alpha$, $\beta$ | Symmetry coefficients | |
| $R$ | Gas constant | $J\, mole^{-1} K^{-1}$ |
| $E$ | Potential | V |
| $E_f^0$ | Formal potential | V |
| Dimensionless parameters | | |
| $j$ | Dimensionless flux density | |
| $J$ | Dimensionless net flux | |
| $C_{A,B}$ | $c_{A,B}/c^*_{A,B}$ | |
| $R$ | $r/r_s$ | |
| $Z$ | $z/r_s$ | |
| $d_B$ | $D_B/D_A$ | |
| $\tau$ | $D_A t/r_s^2$ | |
| $K_{BV}^0$ | $k^0 r_s/D_A$ | |
| $K_0$ | $k_0 r_s/D_A$ | |
| $K_1$ | $\frac{k_1 r_s}{D c_A^*}$ | |
| $\gamma$ | $\Gamma(\frac{1}{c^*_{A(r,0)} r_s})$ | |
| $\phi$ | F(E-$E_f^0$ )/RT | |
| $\sigma$ | Dimensionless scan rate, $r_s^2 \frac{F}{D_A RT}$ | |

Table 8.2: Dimensional and dimensionless parameters

### 8.2.2 Boundary conditions

At $z = 0$, the kinetics of the adsorbing surface ($R_d < R \leq R_s$), and the electrode boundary condition ($R \leq R_d$ ) are defined. At the disc electrode, the boundary condition is set to be the flux of each species correlated to the electrode potential (E) according to the Butler-Volmer equation (for the oxidation reaction):

$$\begin{matrix} \tau \geq 0 \\ 0 < R \leq R_d \end{matrix} \qquad \left(\frac{\partial C_{A(R,0)}}{\partial Z}\right)_{Z=0} = K^0_{BV}\left(C_{B(R,0)}e^{-\alpha\phi(\tau)} - C_{A(R,0)}e^{\beta\phi(\tau)}\right) \tag{8.7}$$

$K^0_{BV}$ is the dimensionless rate constant given by $k^0 r_s/D_A$ where $k^0$ is the standard heterogeneous rate. $\alpha$ and $\beta$ are the symmetry parameters, and $E^0_f$ is the formal potential. $\phi(\tau)$ is equal to $F(E - E^0_f)/RT$. The potential depends on the scan rate and time via:

$$\begin{aligned} Forward\,scan: &\quad E < E_{max} \quad E = t\nu + E_{min} \\ Backward\,scan: &\quad E > E_{min} \quad E = E_{max} - t\nu \end{aligned} \tag{8.8}$$

and in dimensionless form depends on the dimensionless scan rate ($d\phi/d\tau$) applied in a cyclic voltammetry measurement:

$$\begin{aligned} Forward\,scan: &\quad \phi < \phi_{max} \quad \phi(\tau) = \tau\sigma + \phi_{min} \\ Backward\,scan: &\quad \phi > \phi_{min} \quad \phi(\tau) = \phi_{max} - \tau\sigma \end{aligned} \tag{8.9}$$

$\sigma$ is therefore the dimensionless scan rate, and $\phi_{min,max}$ are the lowest negative and highest positive dimensionless potentials in the cyclic voltammetry, respectively. In this study, $\phi_{min}$ set to -20 and $\phi_{max}$ to +20, far enough from the expected redox peaks. $K_{BV}$ is also considered to be fast enough to simplify the model, and since its role is not of primary importance in this study.

Applying mass conservation of the electrochemical reaction, the flux boundary condition of species B is set to:

$$\begin{matrix} \tau \geq 0 \\ 0 < R \leq R_d \end{matrix} \qquad \left(\frac{\partial C_A}{\partial Z}\right)_{Z=0} = -d_B \left(\frac{\partial C_B}{\partial Z}\right)_{Z=0} \tag{8.10}$$

Boundary condition is considered for the adsorption of species on the sheath surface[24,31]. The process is described as a first order reversible reaction, according to the Langmuirian model[23]. Therefore, the dimensional flux of species $A$ on the adsorbing surface is given by:

$$\begin{matrix} \tau > 0 \\ r_d < R \leq r_s \end{matrix} \qquad D_A \left(\frac{\partial c_A}{\partial z}\right)_{z=0} = k_0 \left(1 - \theta\right) c_{A(r,0)} - k_1 \theta \tag{8.11}$$

where $\theta$ is the fractional coverage and varies between zero to unity. The adsorption and desorption rate constants are denoted by $k_0 (cm\, s^{-1})$ and $k_1 (mole\, cm^{-2} s^{-1})$, respectively. Converting $k_0$ and $k_1$ to dimensionless rate constants gives:

$$K_0 = \frac{k_0 r_s}{D_A},\ K_1 = \frac{k_1 r_s}{D_A c_A^*} \tag{8.12}$$

Following that the flux equation is rewritten in a dimensionless form to define the surface boundary condition:

$$\begin{array}{ll} \tau > 0 & \\ R_d < R \leq R_s & \end{array} \qquad \left(\frac{\partial C_A}{\partial Z}\right)_{Z=0} = K_0\,(1-\theta)\,C_{A(R,0)} - K_1\theta \tag{8.13}$$

$\Gamma\,(mole\,cm^{-2})$ is defined as the maximum coverage. Hence, the variation of $\theta$ with $t$ can be denoted as:

$$\Gamma\frac{\partial\theta}{\partial t} = k_0\,(1-\theta)\,c_{A(r,0)} - k_1\theta \tag{8.14}$$

and in dimensionless form:

$$\gamma\frac{\partial\theta}{\partial\tau} = K_0\,(1-\theta)\,C_{A(R,0)} - K_1\theta \tag{8.15}$$

where $\gamma$ is a dimensionless coverage. By combining equation 8.12 and equation 8.15, and substituting $\tau$ and $C_A$ with $D_A t/r_s^2$ and $c_A/c_A^*$, respectively :

$$\gamma\frac{r_s^2}{D_A}\frac{\partial\theta}{\partial t} = \frac{k_0 r_s}{D_A}\,(1-\theta)\,\frac{c_{A(r,0)}}{c^*_{A(r,0)}} - \frac{k_1 r_s}{D_A c^*_{A(r,0)}}\theta \tag{8.16}$$

Rearranging,

$$c^*_{A(r,0)} r_s \gamma\frac{\partial\theta}{\partial t} = k_0\,(1-\theta)\,c_{A(r,0)} - k_1\theta \tag{8.17}$$

and by using equation 8.14 and equation 8.17 the dimensionless maximum coverage is obtained:

$$\gamma = \Gamma(\frac{1}{c^*_{A(r,0)} r_s}) \tag{8.18}$$

For species $B$, on the sheath surface ($R_d < R \leq R_s$), a wall boundary condition is set:

$$R_d < R \leq R_s \qquad \left(\frac{\partial C_B}{\partial Z}\right)_{Z=0} = 0 \tag{8.19}$$

It is important to note that it is reasonable to assume that only species $A$ can adsorb/desorb since in the case where species B does adsorb, only a very small effect on the result is seen for the forward peak which is the basis of the sensing application described in the introduction. Moreover, since oxidation/reduction changes the charge on $A$ it is likely that neutral $A$ molecules would adsorb more than charged $B$ molecules.

Beyond the adsorbing/desorbing surface, at $Z = 0$, a wall boundary condition for both species $A$ and $B$ is set:

$$R_s < R \leq R_{max} \qquad \left(\frac{\partial C_{A,B}}{\partial Z}\right)_{Z=0} = 0 \tag{8.20}$$

From symmetry, the flux across the $Z$ axisymmetric boundary can be set to zero:

$$\left(\frac{\partial C_{A,B}}{\partial R}\right)_{R=0} = 0 \tag{8.21}$$

The edges in the outer space of the simulation set to the bulk concentration:

$$C_{R_{\max}} = 1, \quad C_{Z_{\max}} = 1 \tag{8.22}$$

where $R_{max}$ and $Z_{max}$ are set to be far enough from the root mean squared displacement according to the Einstein equation[32,33]:

$$R_{\max} = 1 + 6\sqrt{\tau_{\max}} \tag{8.23}$$
$$Z_{\max} = 6\sqrt{\tau_{\max}}$$

and $\tau_{\max}$ is chosen to be a full time of one cycle in the CV:

$$\tau_{\max} = \frac{2(\phi_{max} - \phi_{min})}{\sigma} \tag{8.24}$$

### 8.2.3 Initial conditions

The initial dimensionless concentration of the electro-active species ($C_A$) is set to 1, and for the oxidized form (species $B$), the concentration is set to 0. It is assumed that before carrying out the cyclic voltammetry measurement, the surface of the sheath adsorbs particles until an equilibrium on the surface is achieved before applying a potential. Therefore, rearranging equation 8.13 where $C$ equals to 1 and the flux equals to 0, gives the initial coverage of the adsorbing/desorbing surface of the sheath in the equilibrium state corresponding to the familiar Langmuir isotherm:

$$\begin{array}{l} \tau = 0 \\ R_d < R \leq R_s \end{array} \qquad \theta_{eq} = \frac{K_0}{K_0 + K_1} \tag{8.25}$$

### 8.2.4 Current calculation

The dimensionless flux inward the disk electrode is given by:

$$\begin{array}{ll} disk: & 0 < R \leq R_d \\ surface: & R_d < R \leq R_s \end{array} \qquad j^D = \left(\frac{\partial C_A}{\partial Z}\right)_{Z=0} \tag{8.26}$$

By integrating the flux ($j^D$) over the disc and the surface, the net fluxes are obtained (inward the disc electrode and the adsorbing/desorbing flux on the surface surrounding it) :

$$J_d^D = 2\pi \int_0^{r_d} j_{r,0}^D r \mathrm{d}r\,, \quad J_s^D = 2\pi \int_{r_d}^{r_s} j_{r,0}^D r \mathrm{d}r \tag{8.27}$$

In dimensionless form:

$$J_d = 2\pi \int_0^{R_d} j_{R,0} R \mathrm{d}R\,, \quad J_s = 2\pi \int_{R_d}^{R_s} j_{R,0} R \mathrm{d}R \tag{8.28}$$

Assuming a single electron transfer, the dimensional Faradaic current inward the microdisc electrode is obtained as follows:

$$I_d = 2\pi F c_A^* D r_s \int_0^{R_d} j_{R,0} R \mathrm{d}R = F J_d^D \tag{8.29}$$

### 8.2.5 Numerical methods

The partial differential equations for both species, along with the boundary conditions are solved numerically with the finite difference method for each time step, using the implicit Crank-Nicolson method[34]. These equations are discritized over an expanding spatial 2D grid with $m_{max}$ rows and $n_{max}$ columns ($R(n_{max}) \times Z(m_{max})$). This space is meshed with an expanding grid around 3 nodes: $\delta R, R_d, R_s$, where a large perturbation of flux is expected. The first differences around the nodes are set to be with the minimum $\delta R$ and

$\delta Z$ values, after which the differences grow exponentially to cover all the space as follows:

$$\begin{aligned}
&R\ grid:\\
&R_{n+1} = R_n \rho_R \qquad \delta R < R_n < \tfrac{R_d}{2},\ \ R_d < R_n < \tfrac{R_s+R_d}{2},\ \ R_s < R_n < R_{max}\\
&R_{n+1} = R_n/\rho_R \qquad \tfrac{R_d}{2} < R_n < R_d,\ \ \tfrac{R_s+R_d}{2} < R_n < R_s\\
&Z\ grid:\\
&Z_{m+1} = Z_m \rho_Z \qquad 0 < Z_m < Z_{max}
\end{aligned} \tag{8.30}$$

where $\rho_R$ and $\rho_Z$ are the expansion factors between two adjacent cells in the rows $R_{n+1}$ to $R_n$ and in the columns $Z_{n+1}$ to $Z_n$, respectively. The concentration equations is set to each species ($A$ and $B$) in the space.

Using the alternating direction implicit (ADI) method, the 2D mass transport system is solved. Each individual direction $(R_n, Z_m)$ in the ADI method is solved for the two species. This allows the solution of the finite difference equations in a form of tri-diagonal matrices to be obtained in $O(2 \cdot m_{max} \cdot n_{max})$ operations at each time step. In the Z directions where species $A$ is coupled with species $B$ (on the electrode boundary), one tri-diagonal matrix solves the set of concentration equations for both species[35].

Numerical convergence was achieved with the following values: $\delta R = 1 \times 10^{-5}, \delta Z = 1 \times 10^{-8}$ (the minimal differences next to the nodes), and $\rho_R = 1.15, \rho_Z = 1.15$ (the expanding factors of the grid) ensuring that the calculations are sufficiently accurate at a practicable solving time. It is important to minimize $\delta Z$ relative to $\tau_{max} \times (\theta/\Gamma)$ in order to avoid numerical error accumulation in the coverage. As will be mentioned also in the result section, in cases of very fast coverage changes $(d\theta/d\tau)$, the numerical parameters chosen for the simulation are insufficient for achieving a smooth cyclic voltammetry (CV), or even not applicable. Hence in order to stay in practical calculation time and real systems zone, the upper range of $K_0$ and $K_1$ was limited to a maximum value of 10,000.

Simulations were coded in C++ with the OpenMP. The simulations preformed on an Intel (R) Xeon (R) 3.2Ghz, with approximately usage of 0.5GB RAM, and runtime between of 20 minutes for each CV calculation (no needs for GPU simulation).

## 8.3 Results and discussion

At first, a representative case is discussed, where a reversible adsorption/desorption occurs on the surface of the supporting sheath under typical practical conditions of cyclic voltammetry. This introduces the basic physical effects on the voltammetry and discusses the main roles of a reversible surface in the CV measurement. Following that, a parametric study shows trends in the voltammetry as function of various important physical parameters.

It is worth mentioning that all CVs start assuming a fully equilibrated state of the adsorbing/desorbing surface with the solution. This would likely be also the case in mostly all the electro-analytical systems mentioned, except if the particles of interest are not present in the system before applying the potential[36].

### 8.3.1 Cyclic voltammetry with a reversible adsorbing sheath - a representative case

A simulation was carried out to describe the effect of the reversible adsorbing/desorbing surface of the sheath ('active surface'), using the following parameters $K_{eq}(K_0/K_1) = 0.1$, $K_0 = 10$ and a radius ratio of $1 : 10(R_d/R_s)$. The surface maximum density $\gamma$ was chosen to be 100. In practice, typical values for $D(10^{-9}m^2\, s^{-1}), c(1mM)$, and $r_s(10\mu m)$, would give $k_0$ and $k_1$ to be $10^{-2} m\, s^{-1}$ and $10^{-3} mole\, s^{-1}\, m^{-2}$, respectively, and this corresponds to realistic values of $\Gamma = 10^{-9} mole\, cm^{-2}$. The dimensionless scan rate of the CV has set to an intermediate value of ($\sigma = 10$), so other effects of interest, notably from the supporting sheath's surface can be clearly captured. For comparison, a 'blank CV' was simulated for the case of a disc with the same conditions, only without any adsorption/desorption ('non-active surface'), $K_0$ and $K_1$ were equal to zero.

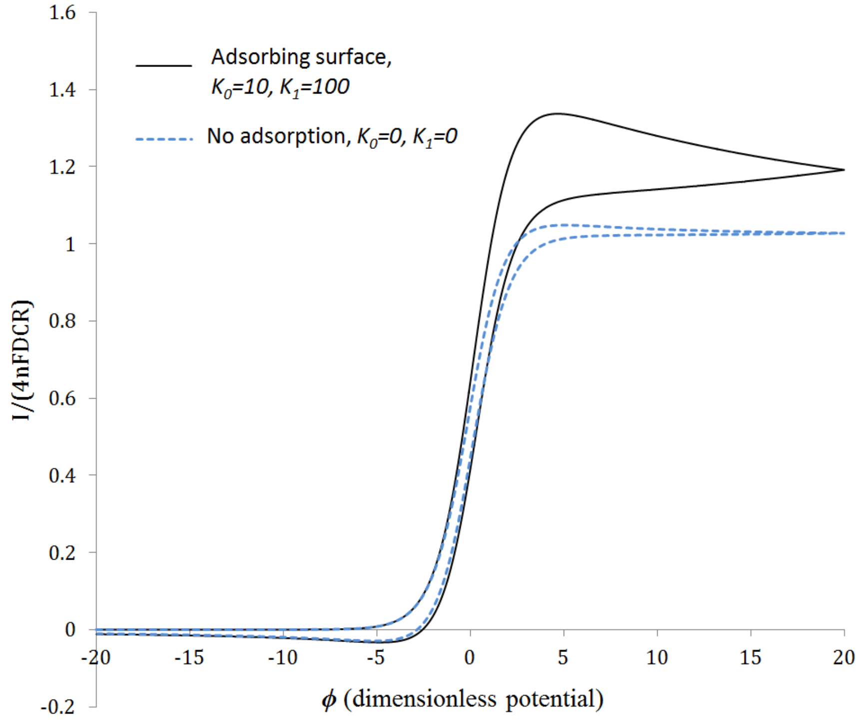

Figure 8.4: Cyclic voltammetry at a non-adsorbing surface (dashed curve), and cyclic voltammetry in a reversible case(solid curve). Other conditions: $\sigma = 10$, $R_s/R_d = 10$, $D_A = D_B = 1$

.

Figure 8.4 presents the voltammograms for both cases. In the 'non-active surface' , the CV shows the expected behaviour of the current response of a disc electrode. Since the scan rate is intermediate, a small peak is observed and the voltammogram is shifted from true steady state behaviour, towards a partial transient behaviour. It is also observed that the normalized current approaches the steady state value, 1, $(I/4nFDC^{*}R)^{37}$. However, under the condition of an 'active surface', a large oxidation peak is observed that evolves during the forward scan, whilst the reduction peak remains almost unchanged. The oxidation peak is clearly a result of the large extra amount of species $A$ that can be released from the surface and flow towards the disc electrode, in the zone of the diffusion layer, where the concentration of species $A$ is otherwise more depleted. The back reduction peak is not strongly influenced by the 'active surface' as observed from figure 8.4, since species $B$ is assumed to not have an interaction with the surface of the sheath.

A "snapshot" of the concentration maps for the two cases were taken in the forward scan at the dimensionless potential of 2.0, slightly before the peak gets to full height. These maps are presented in figure 8.5a. A difference concentration map is also provided in figure 8.5b to emphasis the concentration changes between the two cases. In comparison between the 'non-active surface' and the 'active surface', it is seen that the diffusion layer in the $R$ direction is significantly narrower for the case of an active adsorbing/desorbing surface. For the 'non-active surface', the radial diffusion layer has an expected normal shape and is expanded in the same size along the $R$ and $Z$ directions, while in the case of the 'active surface', as desorption occurs, a compensation of accessible material that is released from the supporting surface creates a sharper and narrower gradient in the $R$ direction, and therefore alters the peak measured in the CV. Another way to understand the role of the surface is to examine the change in the coverage on the surface. Figure 8.6 shows coverage as a function of potential at $R = 0.1$ and 1.0 and reveals that most of the contribution of the current is via desorption from the inner side of the surface close to the disc. The area far from the disc shows only a small change in the coverage along the CV. Since the sheath is defined via the Langmuir model, it can be seen that when the coverage gets to low values with increasing $\phi$, the desorption becomes moderated, and as a consequence, the compensation of access material towards the disc becomes limited for

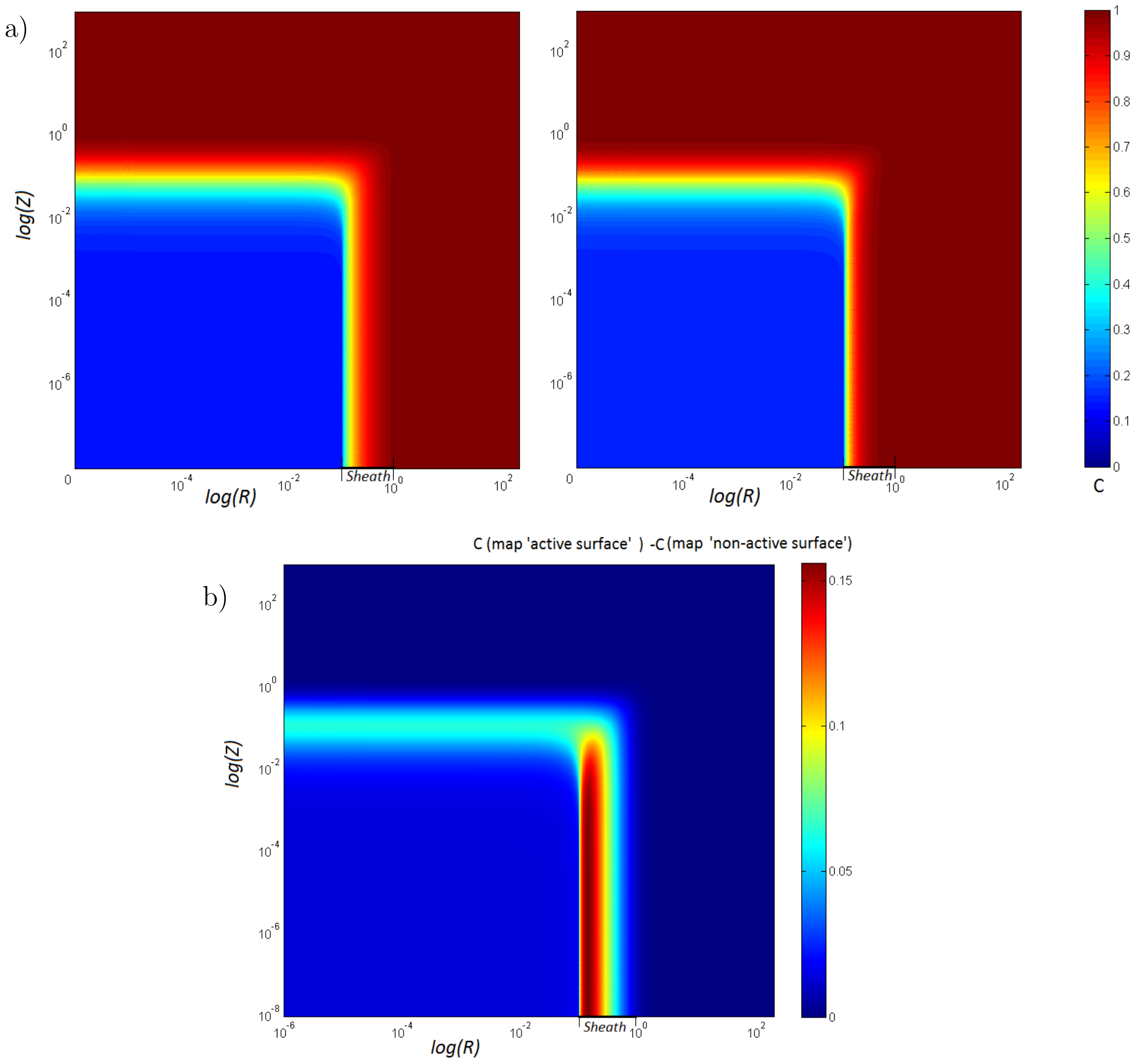

Figure 8.5: a) Concentration maps in logarithmic scaled space, at $\phi = 2.0$ in the forward scan. The left colour map is with a non-active surface, the right colour map is for 'active surface' where: $K_1 = 100$ and $K_0 = 10$. b) difference concentration maps between the absolute concentration values of the 'active surface' map and the 'non-active surface' map. Other conditions: $\sigma = 10$, $R_s/R_d = 10$, $D_A = D_B = 1$. The sheath corresponds to $R_s - R_d$.

the high potentials, thus resulting in a peak shape at the CV observed in figure 8.4.

From the results for this representative case, I report that a reversibly adsorbing sheath, not only can increase the current response significantly, but also may alter the shape of the voltammogram from steady state to transient 'peak like' shape. These effects

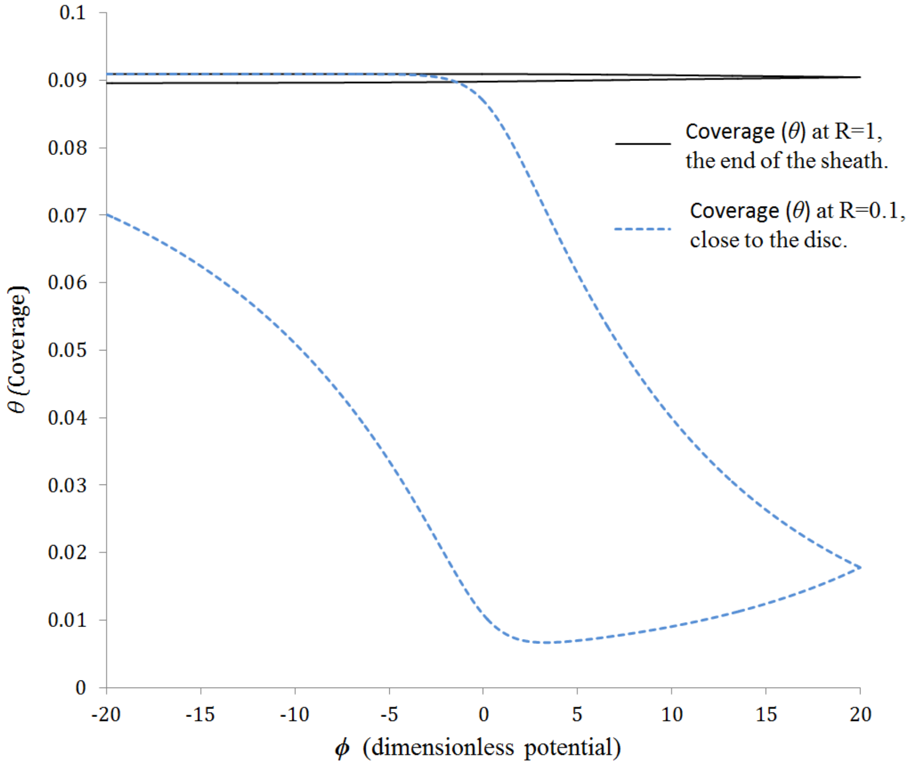

Figure 8.6: Coverage ($\theta$) profiles in the reversible adsorbing/desorbing surface as a function of potential. The dashed curve stands for the beginning of the sheath closest to the disc ($R = 0.1(R_d)$). The solid line shows the coverage in the end of the sheath at $R = 1(R_s)$. Other conditions: $\sigma = 10$, $R_s/R_d = 10$, $D_A = D_B = 1$.

on the current values and the shape, are controlled by the sheath properties and also by the voltammetry parameters, as is discussed next.

### 8.3.2 Parametric study

In order to understand the influence of the adsorbing/desorbing surface properties on the CV measurements, a series of CV simulations are carried out with changing the sheath parameters: $K_0, K_1, \gamma$, and $R_{sd}$.

#### Adsorption / desorption rates

This study shows how the CV is affected due to the change of the surface rate constants, $K_0$ and $K_1$. Same values are used for $\gamma = 100$ ,$\sigma = 10$, and for the radius ratio ($R_s/R_d = 10$).

Figure 8.7 shows the voltammograms for variable $K_1$ and constant $K_0$ (figure 8.7a), and for constant $K_1$ and variable $K_0$ (figure 8.7b).

In figure 8.7a, it is shown that the oxidation current is altered significantly as the desorbing rate increases. However, at a high rate of $K_1$ and relative low rate of $K_0$ ($K_0 = 100, K_1 = 1000$, figure 8.7a), the current decreases. This is explained as follows; due to the fast rate of desorption and low initial coverage ($\theta_{eq}$) the surface of the sheath is drastically diluted within the time scale of the CV at this particular scan rate, leading to insufficient available material for desorption before fully exploiting the diffusion transport towards the disc electrode. Subsequently, it results in a significant relaxation of the current and also a clear transient oxidation peak.

Moreover, figure 8.7b shows that increasing $K_0$ also alters the oxidation current. The starting point of the measurement corresponds to an equilibrium coverage ($\theta_{eq}$), and therefore faster $K_0$ results in higher $\theta_{eq}$. Consequently, the surface has a larger amount of material, accessible for desorption, during the CV. However, in the highest presented value of $K_0 = 1000$ and $K_1 = 100$, the current decreases. This means that the adsorption term in equation 8.13, $K_0 \left(1 - \theta\right) C_{A(R,0)}$ becomes more dominant, and it implies that faster mass transport (higher scan rate) can reduce back this term and alter the current for this kinetic rates. In effect there is stronger adsorption on the surface.

It is important to mention that at extremely high rates, the simulated voltammograms become "noisy" due to large changes in the coverage along the adsorbing sheath relative to the spacing of the simulation mesh. The noise can be reduced by significantly reducing the values of $\rho_R$ and $\rho_Z$. However, for larger rates it becomes impossible to have a fully smooth simulation unless $\delta\tau$ is decreased significantly (by orders of magnitudes), which would make the calculation impracticable even for significantly powerful computers. This

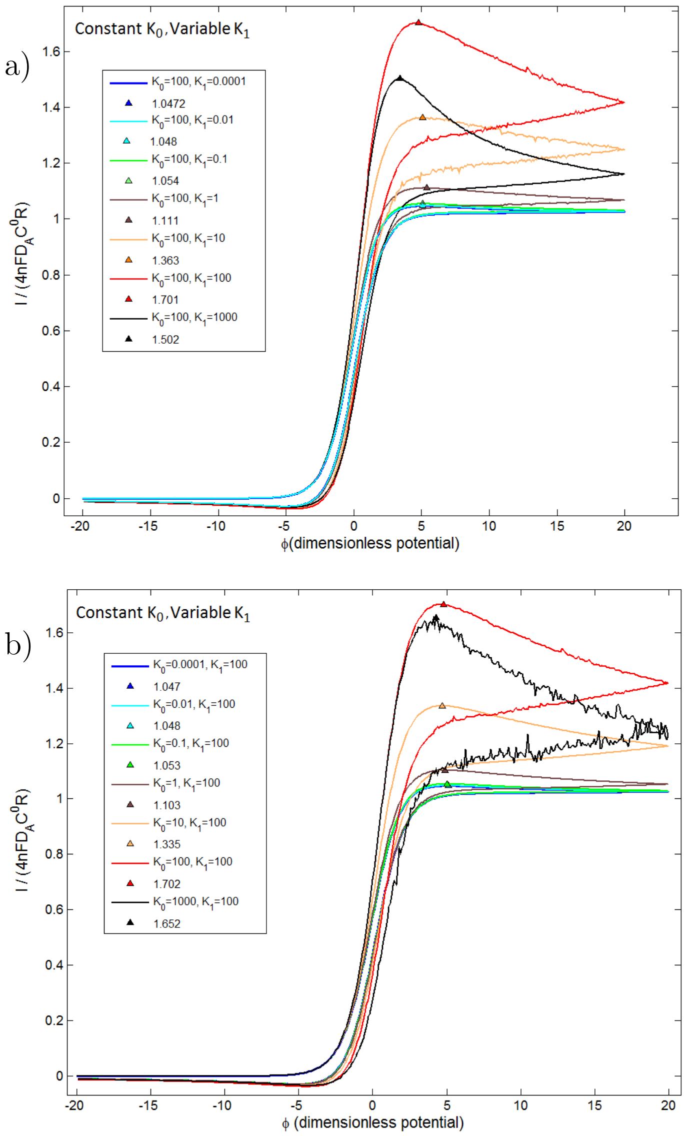

Figure 8.7: Voltammograms for constant $K_1$ and variable $K_0$ (a) and voltammograms for variable $K_1$ and constant $K_0$ (b), under the conditions: $\sigma = 10$, $\gamma = 100$, $R_s/R_d = 10$, and $D_A = D_B = 1$.

instability is also inversely proportional to $\gamma$ and thus when higher $\gamma$ is applied, larger kinetic rates can be investigated for these numerical calculations. It can be seen from figure 8.7, that the CV measurement not only depends on the surface rate constants $K_0$ and $K_1$ independently, but also with their ratio, $K_{eq} = K_0/K_1$. In order to clarify more this dependency, a set of simulations were performed, scanning $K_0, K_1$ in the range between $10^{-4}$ to $10^4$. The peak of each voltammogram was mapped into a surface plot

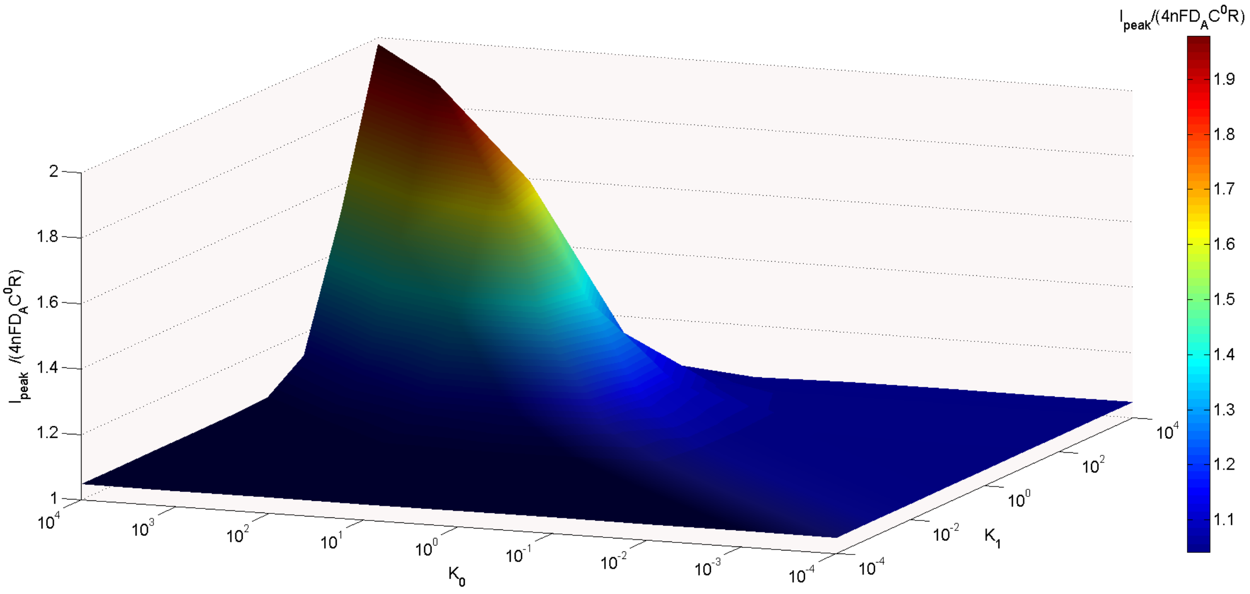

Figure 8.8: Surface map of the oxidation peak in a set of CV simulations, when $K_1$ and $K_2$ are scanned between $10^{-4}$ to $10^4$. The map consists 9x9 matrix of the oxidation peaks. The CVs were carried out for the following conditions: $\sigma = 10$, $\gamma = 100$, $R_s/R_d = 10$, and $D_A = D_B = 1$.

presented in figure 8.8. The surface map shows that when $K_0$ is of the same order of $K_1$, the oxidation peak gives higher values. The maximum current is not exactly when $K_{eq} = 1$, but varies in the range of $K_0/K_1 = 1.5 - 3$; the surface map is not fully symmetric. The implication of these observations for practical analysis using adsorptive pre-concentration is firstly that the optimum surface requires a delicate balance of kinetics and thermodynamics that is likely to be beyond rational prediction, implying the essential need for empiricism in this area. Secondly, the maximum change of current is less than an order of magnitude implying that pre-concentration via surface adsorption has limited analytical value. In principle, only optimizing *all* the following parameters; $K_1$, $K_0$ and $\gamma$ results in further significant enhancement of the current, but an order of magnitude is unlikely for practical situations.

**Maximum surface coverage($\gamma$)**

The maximum surface coverage is an essential parameter for predicting the effect of desorption on the CV measurement. Figure 8.9 presents the voltammograms at various $\gamma$ and figure 8.10 shows the coverage on the sheath near the disc electrode at $R = 1 + \delta R$.

It is shown in figure 8.9 that when $\gamma$ gets to large values, the oxidation current increases significantly, due to the high amount of species $A$ on the surface that is available for desorption. Nevertheless it can be seen that the reduction peak is not influenced by $\gamma$. Furthermore, it is observed that the voltammogram shape varies from transient behaviour with a clear peak to a steady state plateau (8.9). This can be explained by looking at the coverage changes in figure 8.10. At large $\gamma$, the coverage ($\theta$) is only slightly changed during the CV, whilst for low $\gamma$, the contribution of flux towards the disc becomes limited after achieving low coverage during the forward scan.

It can be inferred from comparison between these figures (8.9, 8.10) that when the coverage remains unchanged during the CV, as in the case of $\gamma = 10^7$, the voltammograms have a steady state shape in the forward potential scan. Figure 8.9 also shows that when $\gamma$ reaches high values the current approaches a finite value. This is because $\theta$ remains $K_0/(K_0 + K_1)$ for all $\tau$, and therefore, the maximum flux from the surface in the case of high $\gamma$, is limited to:

$$J_s = -\frac{(1 - C_{R,0})K_0 K_1}{K_0 + K_1}, \quad for\ all\ \tau\ where\ \ \gamma \longrightarrow \infty. \tag{8.31}$$

For lower values of $\gamma = 10^2, 10^5$, a gradual decreasing of the coverage occurs during the CV (figure 8.10), and the oxidation current is also characterized with a gradual drop (figure 8.9). In the cases of drastic and non linear drops of the coverage, an oxidation peak evolves ($\gamma = 10, 5, 2$). These results imply that the surface should be relatively accessible for adsorption sites in order to have a significant effect. At $\gamma = 10^{-2}$ or below, the influence of the surface is negligible, and the voltammetry has the same behaviour of a 'non-active surface'.

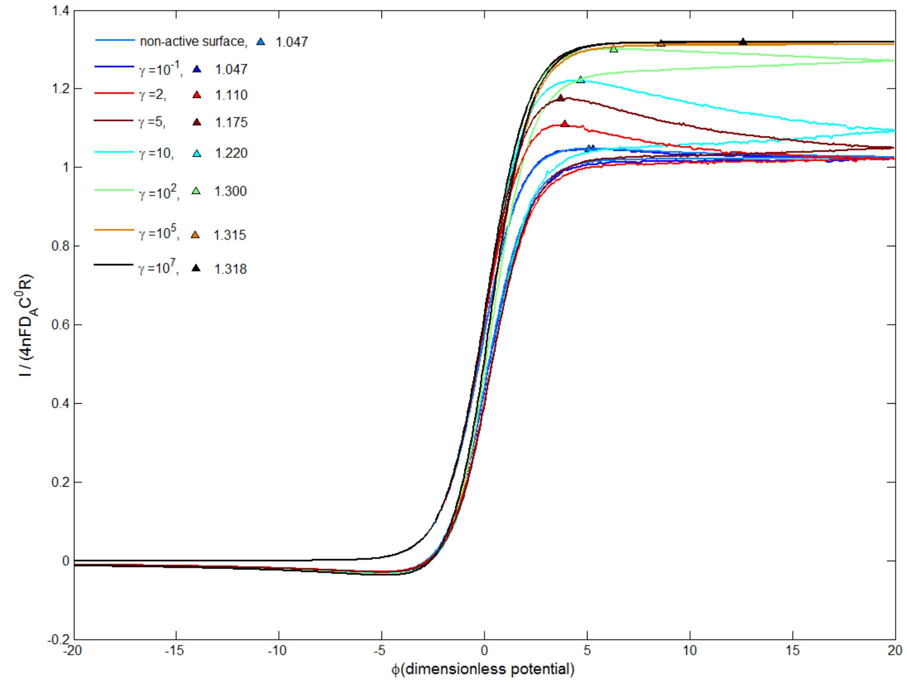

Figure 8.9: A comparison of voltammograms (coloured solid line, —) in various maximum surface adsorbing density ($\gamma$) and their oxidation peaks ( coloured triangle, ▲). The CV simulations were carried out under the following conditions: $\sigma = 10$, $K_0 = 10$, $K_1 = 10$, $R_s/R_d = 10$, and $D_A = D_B = 1$.

### Radius ratio ($R_s/R_d$)

Next the radius of the sheath is considered. In the model described earlier, the sheath is described as the modifier in which analytes $A$ can adsorb or desorb. The sheath size varies a lot for various electrochemical systems comprising micro and sub-micro disc electrodes, and can be in the range of less than one micrometre to an order of a millimetre. Here, in dimensionless system, the sheath size is reflected through the ratio of $R_s/R_d$. Therefore, cyclic voltammetry (CV) simulations were carried out in various ratios and present the

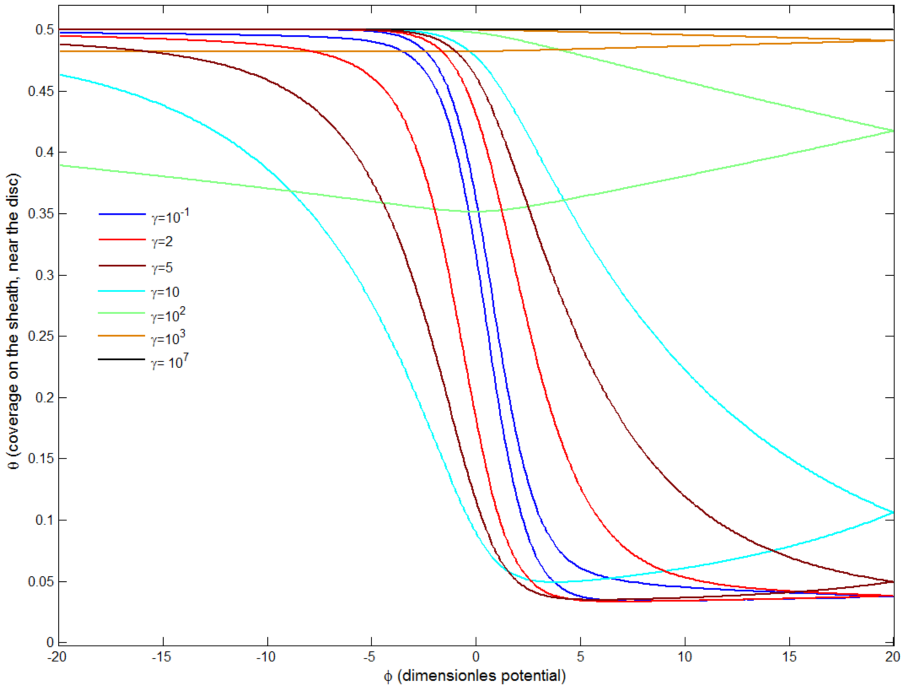

Figure 8.10: A comparison of the coverage during the CV simulations on the sheath, near the disc ($R = 1 + \delta R$). The comparison shows the coverage at various maximum surface adsorbing density ($\gamma$) in the range of $\gamma = 10^{-1}$ to $10^7$). The CV simulations were carried out under the following conditions: $\sigma = 10$, $K_0 = 10$, $K_1 = 10$, $R_s/R_d = 10$, and $D_A = D_B = 1$.

influence of the sheath radius size on the CV measurement, in the case of reversible adsorption on the surface. In terms of using the disc/sheath geometry as a model for modified electrodes the study reflects the effect of changing the amount of modifier.

Figure 8.11 shows the voltammograms at various radius ratio ($R_s/R_d$), for representative simulations made at $K_1 = 100$ and $K_0 = 10$. $\gamma$ is chosen to be 100, and $\sigma = 10$. It is observed that for ratios above 5, the voltammetry does not change. This is due to the fact that far from the electrode the concentration gets close to the bulk concentration, and therefore little desorption flux occurs. This can also be studied from the coverage examination shown previously at figure 8.6. It was shown that the coverage at $R = R_s$ for the simulation of $R_s/R_d = 10$ remains almost unchanged during the CV. An interesting observation is that even at $R_s/R_d = 1.1$ a reasonable alteration of the oxidation peak is

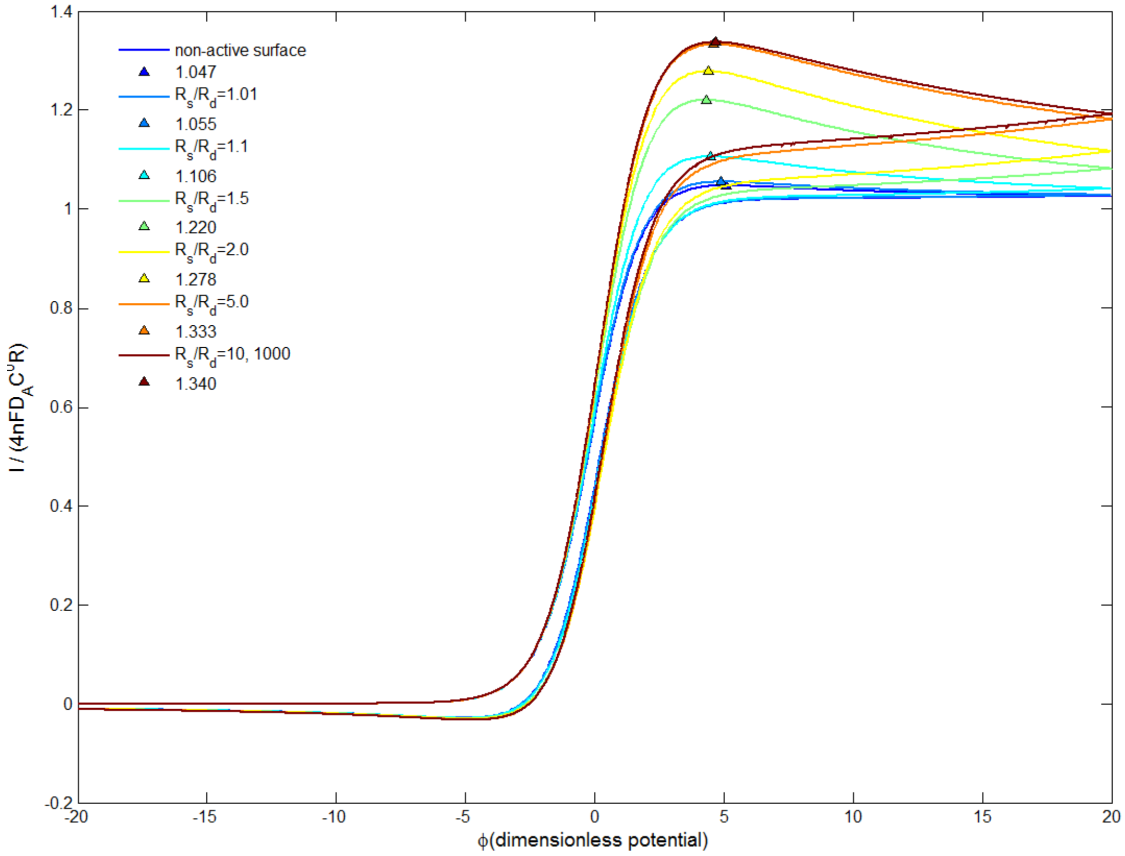

Figure 8.11: A comparison of the coverage during the CV simulations on the sheath, near the disc ($R = 1 + \delta R$). The comparison shows the coverage at various maximum surface adsorbing density ($\gamma$) in the range of $\gamma = 10^{-1}$ to $10^{7}$). The CV simulations were carried out under the following conditions: $\sigma = 10$, $K_0 = K_1 = 10$, and $D_A = D_B = 1$.

still seen (figure 8.11 ). It implies that even a 100nm coat surrounding a microdisc electrode can cause a significant effect on the current response in CV measurements. At the same time the implication for modified electrodes is that the benefits of modifing layers are confined to the case of relatively thin coats; the value of increasing the film thickness becomes progressively less with increasing size.

### Scan rate ($\sigma$)

Lastly, the scan rate parameter $\sigma$ is considered, since it can change dramatically the behaviour of the voltammetry. By changing the scan rate, two dominant physical properties reflect the surface response in the CV measurement of the disc electrode. The first is the mass transport that changes the concentration distribution around the disc as discussed earlier. The second is the time duration requires to scan the voltammogram. That said, when increasing the scan rate and reducing the time scale, a fast desorption for the surface can operate without reaching a low coverage that could limit the desorption.

The observations can be studied by examining two different scan rates for particular adsorbing/desorbing rate constants. Figure 8.12 compares CVs in $\sigma = 10$ (figure 8.12a) $\sigma = 100$ (figure 8.12b) of a 'non-active surface' and an 'active surface', where $K_0, K_1$ equals to 100 and 1000 (figure 8.12a summarizes certain voltammograms showed previously in figure 8.7). Additionally, concentration profiles for species $A$ in both scan rates, as well as extreme cases of a fast scan rate ($\sigma = 625$) and a very slow scan rate ($\sigma = 0.2$), along Z=0 around the potential of oxidation and reduction peaks are provided in figure 8.13.

The result in figure 8.12 for the case where $K_0, K_1 = 100$ clearly shows that a higher scan rate results in a greater compensation of species $A$ flux from the adsorbing surface and alteration of the current significantly. The concentration profiles of the forward scan at figure 8.13 imply again that only the very close sites to the electrode are dominant, since, even-though the averaged concentration along the surface is higher relative to the case of slower mass transport (broader diffusion layer), the greater concentration gradient close to the disc causes a larger alteration of the current via desorption of species $A$ from the inner side of the surface. It can be seen that the concentration profiles of the very fast and slow scan rates also follow this trend.

It was shown above that for $\sigma = 10$, when $K_0$ or $K_1$ are increased from 100 to 1000 the current is reduced, since in this case, the surface coverage gets to very low values that limits the desorption from the surface towards the electrode. However, when increasing the scan rate from 10 to 100 figure 8.12b, the surface does not reach the limitation of low

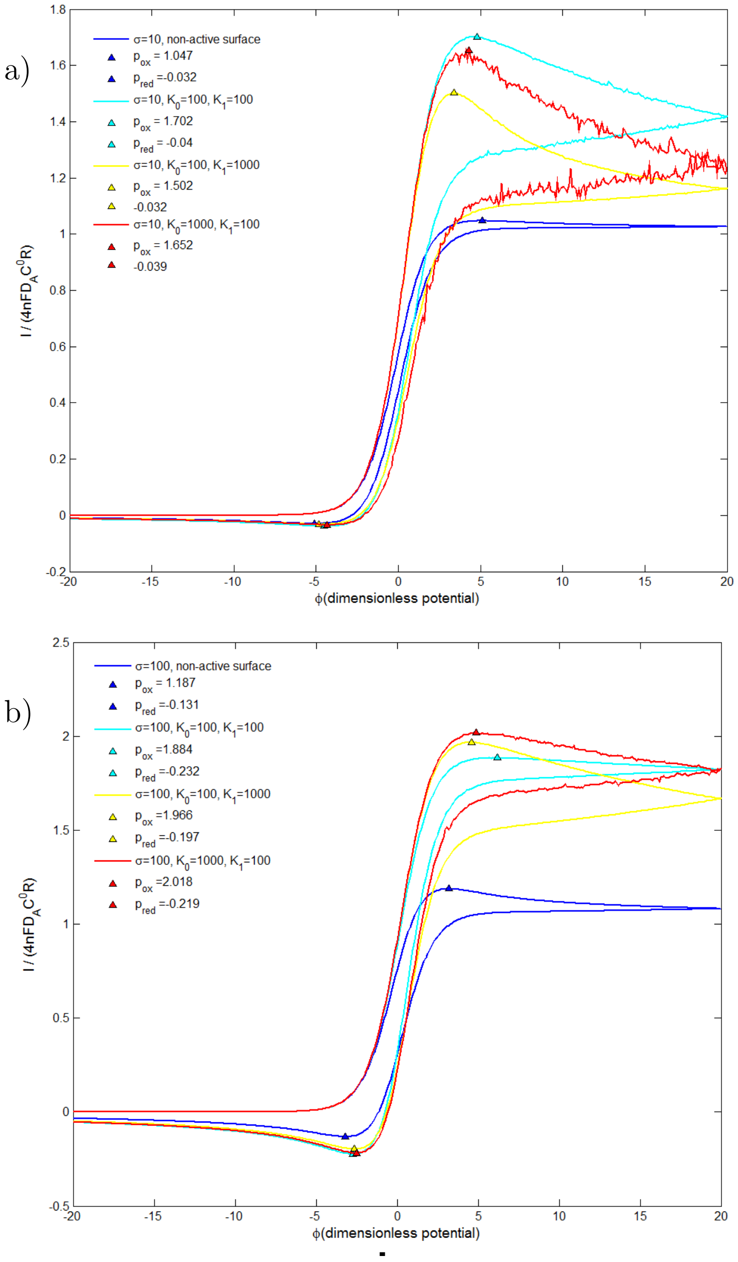

Figure 8.12: Comparison of two scan rates in CV measurements on a disc electrode surrounded by a reversible adsorption surface. (a) Voltammograms at $\sigma = 10$ and various $K_1$ and $K_0$. (b) Voltammograms at $\sigma = 100$ and various $K_1$ and $K_0$. $\gamma = 100$ for both (a) and (b). Other conditions: $R_s/R_d = 10$, $D_A = D_B = 1$.

coverage in the shorter time scale. As a consequence, the peaks get to higher values when $K_0$ or $K_1$ are increased from 100 to 1000, and the relaxation of the current following the peak is moderated in comparison to the case of the lower scan rate ($\sigma = 10$).

The results also show that at $\sigma = 100$ and $K_0 = 1000$ or $K_1 = 1000$ the reduction

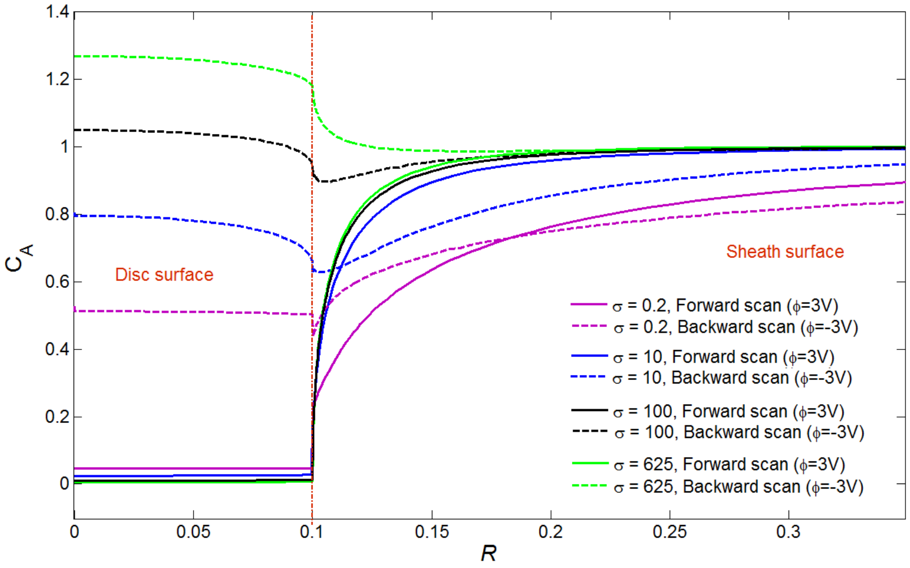

Figure 8.13: Concentration profiles of species $A$ on Z=0, at $\sigma = 10$ (blue lines) and $\sigma = 100$ (black lines), and also for extreme cases of $\sigma = 0.2$ and $\sigma = 625$. The profiles were taken in the forward oxidation peaks (solid lines) and backward reduction peaks (dashed lines). The CV simulations were carried out under the following conditions: $K_0 = 100$ and $K_1 = 100$, $\gamma = 100$. Other conditions: $R_s/R_d = 10$, $D_A = D_B = 1$.

peak is increased. From examining the concentration profiles of the backward peaks of both scan rates, it suggests that in the reverse scan, a significant higher concentration value of species $A$ is observed in the solution adjacent to the disc for faster scan rates. These high values arise from the large desorption occurring during the CV, leading to the concentration of species $A$ even in excess of the initial concentration (8.13). The latter shifts the reversible electrochemical reaction further to the reduction side. It is worth mentioning, that from examination of the concentration profiles of the extreme cases (very fast and slow scan rates) at $R = 0.1$, we can see the importance of choosing very small finite differences ($\delta R$) at the edge of the electrode to obtain stable calculations in very large concentration gradients.

Finally, the influence of the scan rate on the voltammogram can be generalised in a system with a disc surrounding a reversible adsorbing surface. Figure 8.14 shows CVs of an 'active-surface' and 'non-active surface' over a range of scan rates ($\sigma = 0.2 - 625$). The results show different stages of the voltammogram shape that evolves when changing the scan rate with an 'active surface'. At a very low scan rate (figure 8.14a), the effect of the surrounding surface on the voltammogram is negligible due to the slow mass transport towards the disc electrode. Increasing the scan rate to an intermediate values (figure 8.14b-c) causes a peak, due to desorption of species $A$ from the 'active surface'. This is in contrast to the steady state shape expected from the voltammetry on a microdisc electrodes. A further increase of the scan rates (figure 8.14d-e) results in another alteration of the voltammogram; in the case of an 'active surface' this stage is characterised by a significant increase of the current and the voltammogram shape transforms to a steady state behaviour, as opposed to a transient behaviour observed in the 'non active surface'. This is due to the domination of the fast desorption of the species $A$ towards the disc electrode. At high scan rates (figure 8.14f), the desorption from the surrounding surface at these constant rates, is limited by the very fast mass transport occurring on the disc, and the transient behaviour of the voltammogram starts to evolve and then dominate the shape of the voltammogram.

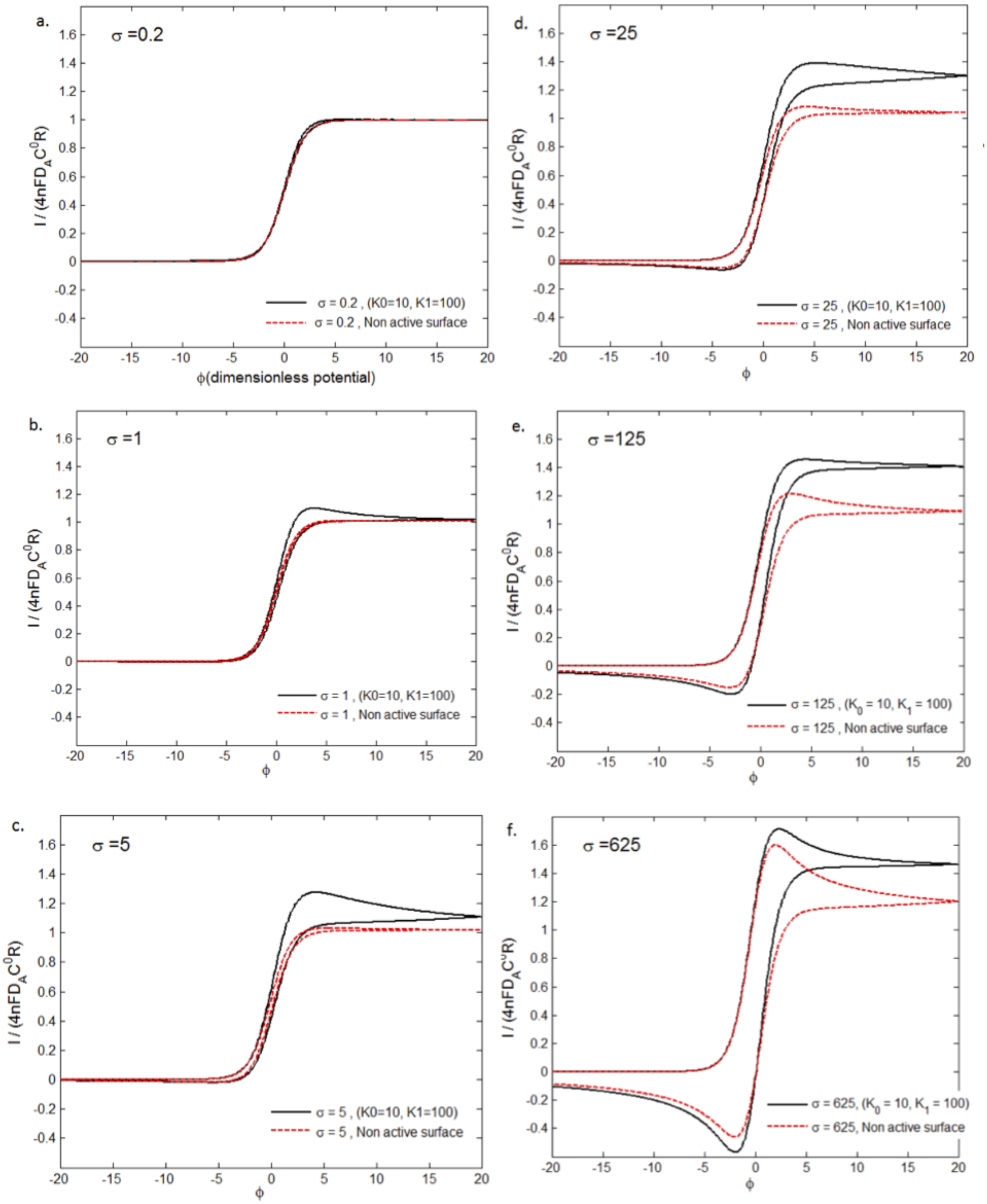

Figure 8.14: CVs of an 'active-surface'(black curves) and 'non-active surface' (red curves) in a range of scan rates: (a) $\sigma = 0.2$ , (b) $\sigma = 1$ ,(c) $\sigma = 5$ ,(d) $\sigma = 25$, (e) $\sigma = 125$, (f) $\sigma = 625$. The CV simulations for the 'active surface' were carried out under the following conditions: $K_0 = 10$ and $K_1 = 100$, $\gamma = 100$. Other conditions: $R_s/R_d = 10$, $D_A = D_B = 1$.

## 8.4 Conclusions

It has been shown that an adsorbing surface adjacent to the disc electrode can provide an enhancement of the voltammetry signal. This may be useful analytically but the current enhancements are limited because of the need for the both high surface coverage *and* fast desorption kinetics. It was specifically observed that the desorption to adsorption rate ratio ($K_{eq}$) should be close to unity in order to achieve maximum enhancement of the signal.

The result shows that only the close sites to the electrodes dominate the surface response, and thus it implies that even a very thin coat on a disc electrode can strongly effect the measurement. It can be suggested that in modified electrode surfaces, as discussed earlier in figure 8.2, the most important sites are those near the edge of the disc electrode where the current density is much higher due to the edge effect of transport towards the finite disc. Equally the benefits of greatly increasing the thickness of modifying layers becomes progressively less the greater the thickness, tending to zero for thick coats.

Finally, the scan rate parameter was shown to have a dramatic influence on the behaviour of the adsorbing surface, and the voltammetry shape can vary from transient to steady state shape dependant on the surface kinetics and coverage. The easy variation of the scan rate parameter in experimental systems can therefore give information about the kinetics of the surface and the ability to achieve efficient signal enhancement.

# References

[1] S. Eloul and R. G. Compton *The Journal of Physical Chemistry C*, vol. 118, no. 42, pp. 24520–24532, 2014.

[2] S. Ranganathan, R. Guo, and R. W. Murray *Langmuir*, vol. 23, no. 13, pp. 7372–7377, 2007.

[3] J. N. Richardson, S. R. Peck, L. S. Curtin, L. M. Tender, R. H. Terrill, M. T. Carter, R. W. Murray, G. K. Rowe, and S. E. Creager *J. Phys. Chem-US*, vol. 99, no. 2, pp. 766–772, 1995.

[4] S. Chen *J. Am. Chem. Soc.*, vol. 122, no. 30, pp. 7420–7421, 2000.

[5] R. W. Murray *Chem. Rev.*, vol. 108, no. 7, pp. 2688–2720, 2008.

[6] B. Kaur and R. Srivastava *Electroanal*, vol. 26, no. 5, pp. 1078–1089, 2014.

[7] X.-Y. Yu, Q.-Q. Meng, T.-J. Luo, B. Yong-Sun, Q.-X. Li, J.-H. Liu, and X.-J. Huang *Sci. Rep.*, vol. 3, no. 2886, pp. 1–7, 2013.

[8] Q.-X. Zhang, D. Peng, and X.-J. Huang *Electrochem. Commun.*, vol. 34, pp. 270 – 273, 2013.

[9] R. X. Xu, X. Y. Yu, C. Gao, Y. J. Jiang, D. D. Han, J. H. Liu, and X. J. Huang *Anal. Chim. Acta*, vol. 790, pp. 31 – 38, 2013.

[10] Z.-G. Liu, X. Chen, J.-H. Liu, and X.-J. Huang *Electrochem. Commun.*, vol. 30, pp. 59 – 62, 2013.

[11] G. Herzog, N. A. Vodolazkaya, and A. Walcarius *Electroanal*, vol. 25, no. 12, pp. 2595–2603, 2013.

[12] J. C. K. Mbouguen, I. T. Kenfack, A. Walcarius, and E. Ngameni *Talanta*, vol. 85, no. 1, pp. 754 – 762, 2011.

[13] I. K. Tonlé, S. Letaief, E. Ngameni, A. Walcarius, and C. Detellier *Electroanal*, vol. 23, no. 1, pp. 245–252, 2011.

[14] J. Gong, W. Zhang, T. Liu, and L. Zhang *Nanoscale*, vol. 3, pp. 3123–3131, 2011.

[15] Y. Zhang, Y. Liu, X. Ji, C. E. Banks, and W. Zhang *J. Mater. Chem.*, vol. 21, pp. 7552–7554, 2011.

[16] Z. Yin, J. Wu, and Z. Yang *Microchim. Acta*, vol. 170, no. 3-4, pp. 307–312, 2010.

[17] S. Eloul and R. G. Compton *ChemElectroChem*, vol. 1, no. 5, pp. 917–924, 2014.

[18] J. Ellison, C. Batchelor-McAuley, K. Tschulik, and R. G. Compton *Sensor. Actuat. B - Chem.*, vol. 200, pp. 47 – 52, 2014.

[19] K. Tschulik, C. Batchelor-McAuley, H.-S. Toh, E. J. E. Stuart, and R. G. Compton *Phys. Chem. Chem. Phys.*, vol. 16, pp. 616–623, 2014.

[20] Y. G. Zhou, N. V. Rees, and R. G. Compton *Angwe. Chem. Int. Edit.*, vol. 50, no. 18, pp. 4219–4221, 2011.

[21] H. Liu, Y. Li, K. Sun, J. Fan, P. Zhang, J. Meng, S. Wang, and L. Jiang *J. Am. Chem. Soc.*, vol. 135, no. 20, pp. 7603–7609, 2013.

[22] E. Kätelhön, K. J. Krause, K. Mathwig, S. G. Lemay, and B. Wolfrum *ACS Nano*, vol. 8, no. 5, pp. 4924–4930, 2014.

[23] I. Langmuir *J. Am. Chem. Soc.*, vol. 40, no. 9, pp. 1361–1403, 1918.

[24] E. O. Barnes and R. G. Compton *J. Electroanal. Chem.*, vol. 693, pp. 73–78., 2013.

[25] H. Brenner *Chem. Eng. Sci.*, vol. 16, no. 3, pp. 242–251, 1961.

[26] I. J. Cutress and R. G. Compton *Chem. Phys. Lett.*, vol. 508, pp. 306–313, May 2011.

[27] I. J. Cutress, E. J. Dickinson, and R. G. Compton *J. Electroanal. Chem.*, vol. 655, no. 1, pp. 1–8, 2011.

[28] K. R. Ward, N. S. Lawrence, R. S. Hartshorne, and R. G. Compton *J. Electroanal. Chem.*, vol. 683, pp. 37–42., 2012.

[29] I. Streeter and R. G. Compton *J. Phys. Chem. C*, vol. 111, no. 49, pp. 18049–18054, 2007.

[30] J. Crank, *The mathematics of diffusion.* London, UK: Oxford University Press, 1979.

[31] R. G. Compton and K. L. Pritchard *J. Chem. Soc., Faraday Trans.*, vol. 86, no. 1, pp. 129–136, 1990.

[32] A. Einstein *Ann. Phys.*, vol. 322, no. 8, pp. 549–560, 1905.

[33] D. Gavaghan *J. Electroanal. Chem.*, vol. 456, no. 1, pp. 13–23, 1998.

[34] J. Crank and P. Nicolson in *Math. Proc. Cambridge; Cambridge University Press*, vol. 43, pp. 50–67, Cambridge Univ Press, Cambridge University Press, 1947.

[35] R. G. Compton, E. Laborda, and K. R. Ward, *Understanding Voltammetry - Simulation of Electrode Processes*. Imperial College Press, 2013.

[36] C. Amatore, S. Arbault, I. Bonifas, and M. Guille *Biophys. Chem.*, vol. 143, no. 3, pp. 124 – 131, 2009.

[37] D. Shoup and A. Szabo *J. Electroanal. Chem. Interfacial Electrochem.*, vol. 140, no. 2, pp. 237–245, 1982.

# Chapter 9

# Charge diffusion on the surface of particles with simple geometries

Chapters 4-6 discussed the transport of particles impacting electrode surfaces and focused on geometrical influences of the electrode surface. This chapter discusses shape effects and the surface coverage of insulating particles modified with an electroactive surface layer and immobilized on an electrode surface. A model is developed to describe diffusion of charge transfer between electro-active sites on the surface of insulating particles assuming charge injection from the electrode supporting the particles. The current-time responses are studied for particles with various shapes namely a cylinder, a sphere, and a cube, and can be used directly to determine the coverage of sites on the particle surface. In practice, chrono-amperometry measurements can be made in which the particles impact an electrode held at a suitable potential. It is shown that the current response has a characteristic behaviour reflecting the particle shape and aspect ratio which allows the transient to distinguish between the various shapes and their orientations on the electrode. It is clearly shown that spherical particles have a non-Cottrellian behaviour whilst cylinders, and cubes have a characteristic Cottrellian current at sufficiently short times. Additionally, various aspect ratios of cylinders such as flake-like, tubular or bamboo-like particles, change the current-response and the shape can be assumed by comparing the current values at the short and long times. The work has been published in 'The Journal of Physical Chemistry C'[1].

## 9.1 Introduction

The current-time response of an electrochemical reaction has been studied for more than one hundred years and serves as a central tool to analyse and understand electrochemical systems[2]. In studying mass transport, the 'chronoamperometry' technique is utilized, where a large over-potential step is applied at the electrode-solution interface and electroactive species next to the electrode react on the electrode and are immediately consumed. With a large enough overpotential, and in controlled conditions of fully supporting electrolyte and with no convection, the current response reveals the diffusion of species in space adjacent to the electrode[3,4].

In general for electrochemical cells, the current-time response is described by the diffusion of species towards the electrode. For example at a planar (large area) electrode, the current decays with $1/\sqrt{(t)}$, which results from one dimensional (1D) diffusion process, follows the widely known 'Cottrell' equation[2]:

$$I_d = \frac{nFADc^*}{\sqrt{\pi t}} \tag{9.1}$$

where $I_d$ is the diffusion current measured, $F$ is the Faraday constant, $A$ is the electrode area, $D$ is the diffusion coefficient, $n$ is the number of electrons transferred and $c^*$ is the initial bulk concentration of the redox species. Nevertheless, the Cottrellian behaviour is a spacial case of solving the diffusion equation for an infinite one-dimensional cell. In general, the time current relationship is unique to the electrode size or shape. For instance, using a micron sized electrode disc[5], or spherical-cap electrode[6], a convergent-radial diffusion regime is obtained.

Beside the common use of 'chrono-amperometry' to measure the diffusion of electro-active species in solution towards an electrode, many works have utilized the technique to understand diffusion in various spaces. The deviation from the Cottrellian behaviour can give valuable information on diffusional process, for instance, understanding thin-layer cells[3] and thin-film electrodes[7], or modelling neurotransmitter diffusion detection in the cases of a poorly supported electrolyte solutions such as in vivo experiments of dopamine release[8].

Further, the current transient analysis has also an important role in particle identification and detection via the so-called 'nano-impacts' method (chapters 4 and 5). The advantage of the mass transport towards microdisc and microwire electrodes, enables the detection of single impacts of various type of nano-particles by their oxidation or reduction[9,10]. Their frequency of impacts is fitted to a radial and non-Cottrellian diffusion[11] process to quantify the concentration in various media[12,13] as it was discussed in chapters 4 and 5. In another case, the particles can hit the electrode and not react but rather mediate a reaction of another species in the interface between the surface of the particle and the solution[14,15], and this can change significantly the mass transport and the current-time response.

In both cases of direct oxidation of the particle or mediated reaction, the particles used are typically conductors. However, Quinn et al.[16] have shown that chronoamperometry can be used to study indirect detection of insulating particles, by measuring the reduction of current due to the blocking of sites on the electrode surface by the insulating particles.

Recently, the current response from a chemically modified surface of insulating spherical particles have studied by Thompson et al.[17]. In their system, they measured a redox reaction on the modified surface of insulating spherical particles. The particles were immobilised on the electrode, and a current response could be measured from applying a potential step. The current decay was suggested to correspond to a charge hopping mechanism[18] around the spherical particles, where an active redox reaction on the interface particle solution can take place. The mechanism has been modelled via diffusion of charge to the redox sites around the surface of a sphere, and the simulated current time response fitted to the coverage density of the modified redox sites, and to the diffusion coefficient of charge between the sites.

Very recent work by Lin and Compton[19], showed a ‘particle-impact’ experiment to quantify the adsorption of catechol on a single modified alumina particle. Using the theory for charge diffusion over the surface of an insulating sphere, individual impact spikes arising from the electro-oxidation of adsorbed catechol could be modelled to find the surface coverage ($mole/m^2$) of the adsorbed catechol.

The applicability of this model to study charge transfer as a random hopping of electrons on surface with a simple current response analysis, encouraged us to extend this model to consider other particle shapes.

In both studies mentioned above, the particles considered were spherical particles. However, with different particle geometries such as flakes, tubes, or cubical particles, the current behaviour is expected to behave differently due to the different space of charge diffusion. Thus the aims of the present chapter are to investigate if the current-time spike seen in nano impact experiments can be used to identify the shape of the impacting particles.

In this chapter, I show the ability to utilize the method for measuring charge transfer on a surface of particles with different geometries, and are able to distinguish between the various geometries from a current-time response curve. This potentially opens a unique way to characterize modified particles according to their geometry.

## 9.2 Model

The characterization of charge dissipation by electro-active redox sites was initiated by Andrieux and Savéant in 1980[18]. They characterized the diffusion coefficient for the propagation of electrons through a polymeric thin film using voltammetry. In another notable work, Amatore and co workers[20] showed the behaviour of non-Cottrellian diffusion of a charge hopping mechanism on a dendrimer surface via voltammetric measurements. This mechanism is also utilized for characterization of electro-grafting processes on electrodes[21].

The diffusion of charge involves electrons that 'hop' from site to site in thin film or on the surface of a solid. The main assumption of the model is that charge hopping is purely random. This can be valid only in a fully supported solution, where counter ions (in the case of electrons transfer these are cations) can travel in solution to locally screen the charge from other sites[18,21]. This is possible only if the diffusion coefficient of the counter ions is comparable to or higher than this of the electron hopping, allowing fast rearrangement of the ions to give electro-neutrality at each site. Additionally, the presence of a fully supported electrolyte allows the neglect of the variation of the potential along the particle surface-solution interface.

In order to achieve the above conditions, the distance between sites is assumed to be in the order of a few nanometres, within the electron tunnelling distance.

The numerical model for solving the charge hopping as a diffusion equation is developed in this chapter for four different particle geometries as illustrated in Figure 9.1. The first geometry is for surface diffusion on a 'cylinder on its base' where the cylinder's base is in contact with the electrode surface. The second case is for surface diffusion on a 'cylinder on its side' where the cylinder's side is laying on the electrode surface. The third model is the diffusion on a surface of spherical particle as modelled previously by Thompson et al.[17] and the last model is for diffusion on a surface of a cubical particle. In all cases it can be assumed that the coverage is considered dense in comparison to the size of the particle, and the current is significant. This allows the modelling of a continuous statistical diffusion flux, and solve the diffusion equation that is described by Fick's second law as:

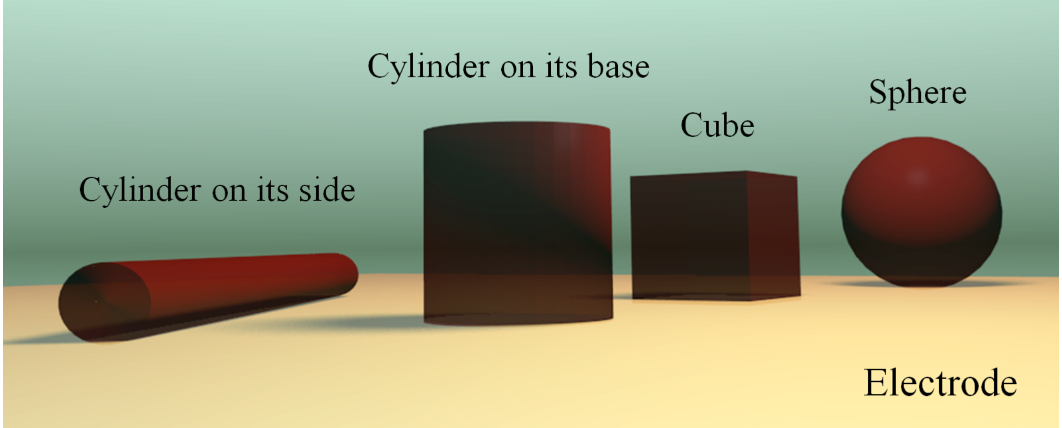

Figure 9.1: The geometries of the particles considered in this study and their orientation on the electrode.

$$\frac{\partial c}{\partial t} = D\nabla^2 c \tag{9.2}$$

where $c$ is the coverage ($mole/m^2$) and $D$ is the diffusion coefficient ($m^2/s$) of the electron transfer. For each space the appropriate Laplace operator is adapted as shown below.

The solutions for all cases are done using the finite difference method (FDM) and solving using the Thomas algorithm for 1D symmetry and utilizing the ADI method for 2D domains (for the cube case). It is necessary to point out in this stage that since the geometry spaces are all primitives, I am convinced that a 'self-developed' algorithm is more appropriate in this problem, where a careful care of the continuous boundary conditions should be taken. The straight forward implementation of the FDM allows us to create a continuous one space, rather than by using continous flux conditions. This is especially relevant with primitive geometries as in this study, where finite element modelling has no significant advantage, over using the finite difference method[22,23]. Convergence of the solutions for all cases were studied using a mass conservation check and with other electrochemical simulation convergence criteria[24].

## 9.3 Numerical model

### 9.3.1 'Cylinder on its base'

The diffusion equation for the case when the Laplace operator is given in cylindrical coordinates, is written as:

$$\frac{\partial c(r,z,t)}{\partial t} = D\left(\frac{\partial^2 c(r,z,t)}{\partial r^2} + \frac{\partial^2 c(r,z,t)}{\partial z^2} + \frac{1}{r}\frac{\partial c(r,z,t)}{\partial r}\right) \tag{9.3}$$

The symmetry allows us to divide the two dimensional (2D) surface domain into two sub one dimensional (1D) domains. One is for the cylinder side, where $r$ is a constant which reduces the problem to 1D along the z axis; from ($r_c$,0) to ($r_c$,$h_c$) as illustrated in Figure 9.2. Then, the top can be calculated with 1D radial coordinate, where the $z$ component is

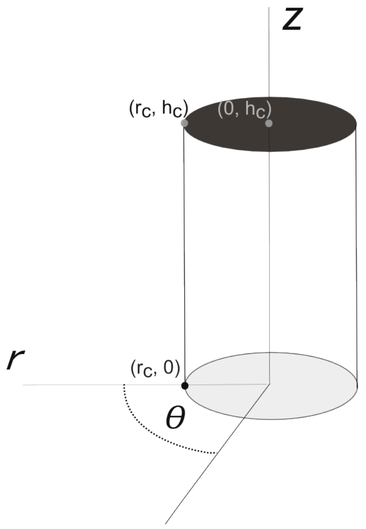

Figure 9.2: A scheme of the relevant points for a model of diffusion on a surface of a 'cylinder on its base'.

constant and $r$ varies from the point ($r_c$,$h_c$), the upper edge of the cylinder, to the point (0,$h_c$), the upper centre of the cylinder. The two domains are coupled via the continuity point at ($r_c$,$h_c$) to give the coverage profile as function of time.

### 9.3.2 Dimensionless form

It is convenient to convert the physical parameters to dimensionless units: The space can be normalised to $r_c$(m) which is the radius of the cylinder: $R = r(m)/r_cL(m)$, and $Z = z(m)/r_c(m)$. The coverage can be also given as a fraction from the maximum 1D coverage: $C = c(mol/cm^2)/c_{max}(mol/cm^2)$. A dimensionless time can be used via: $\tau = Dt/r_c^2$. The dimensionless diffusion coefficient then set to 1 due to dimensionless space and time. The diffusion equation in dimensionless cylindrical coordinates form is now simplified to:

$$\frac{\partial C}{\partial \tau} = \left( \frac{\partial^2 C}{\partial R^2} + \frac{\partial^2 C}{\partial Z^2} + \frac{1}{R}\frac{\partial C}{\partial R} \right) \tag{9.4}$$

and for the reduced 1D model is:

$$\frac{\partial C}{\partial \tau} = \frac{\partial^2 C}{\partial Z^2} \tag{9.5}$$

at the side of the cylinder, and:

$$\frac{\partial C}{\partial \tau} = \frac{\partial^2 C}{\partial R^2} + \frac{1}{R}\frac{\partial C}{\partial R} \tag{9.6}$$

at the top of the cylinder.

### 9.3.3 Boundary conditions and flux

The boundary conditions are as follows: at point ($r_c$,$h_c$) symmetry boundary conditions are used:

$$\left.\frac{\partial C}{\partial Z}\right|_{Z=0} = 0 \tag{9.7}$$

At the continuity point between the top domain and the side domain, the first term in the diffusion equation above is used as normal since its the same for both domains and add the contribution of the radial part only in the upper half space:

$$\frac{\partial C}{\partial \tau} = \left.\frac{\partial^2 C}{\partial R \partial Z}\right|_{(h_c,r_c=1)} + \left.\frac{1}{R}\frac{\partial C}{\partial R}\right|_{(h_c,R=r_c=1)} \tag{9.8}$$

For the boundary conditions at ($r_c$,0) chronoamperometry conditions are used by applying a high over-potential, so the coverage is set to 0 at all time, i.e all sites are reacted. The initial value for $C$ is set to 1 for all space.

The flux density in dimensional units is then given by:

$$j_d = -\frac{Dc_{max}}{r_c}\left.\frac{\Delta C}{\Delta Z}\right|_{Z=0} \tag{9.9}$$

The simulated current measured in chronoamperometry is calculated at each time by integrating the flux density over the whole cylinder edge at ($r_c$,0):

$$I = F\int_{0}^{2\pi} j_d \cdot r_c d\theta = 2\pi F D c_{max}\frac{C_{i=1} - C_{i=0}}{\Delta Z} \tag{9.10}$$

The grid setup and full discretization equations for the FDM and boundary conditions are supplied in the Appendix.

## 9.4 ‘Cylinder on its side’

For simplicity, in this case only long cylinders are considered, where the edges of the cylinder can be neglected. The cylindrical Laplacian operator in the diffusion equation which describes the cylinder on its side depends only on the angle $\phi$, since $r$ is a constant along the surface and a full symmetry is observed around the $z$ axes (see Figure 9.3). This results in the following 1D diffusion equation:

$$\frac{\partial c(\phi)}{\partial t} = D\frac{1}{r_c^2}\frac{\partial^2 c(\phi)}{\partial \phi^2} \tag{9.11}$$

where $r_c$ is the constant radius of the cylinder. The calculation is therefore applied in the range $\phi[0,\pi]$ as shown in figure 9.3.

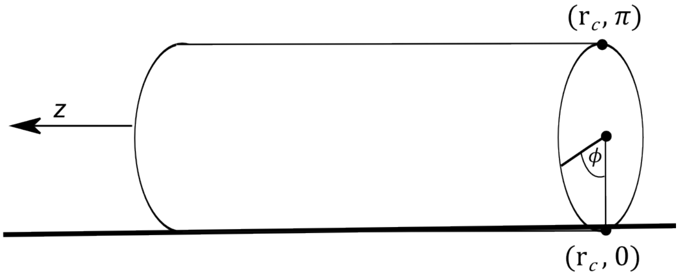

Figure 9.3: A scheme of the ’Cylinder on its side‘ and the relevant points for one-dimensional (1D) diffusion model.

### 9.4.1 Dimensionless form

As in the cylinder on its base case, the dimensionless coverage is: $C = c(mol/cm^2)/c_{max}(mol/cm^2)$, and the dimensionless time can be used via: $\tau = Dt/r_c^2$. Thus the diffusion equation in dimensionless form is written as:

$$\frac{\partial C(\phi)}{\partial \tau} = \frac{\partial^2 C(\phi)}{\partial \phi^2} \tag{9.12}$$

### 9.4.2 Boundary conditions and flux

At $\phi = \pi$ symmetry boundary conditions are used:

$$\left.\frac{\partial C}{\partial \phi}\right|_{\phi=0} = 0 \tag{9.13}$$

On the interface electrode-cylinder, at $\phi = 0$, high overpotential step is applied and thus the coverage is set to zero at all time ($C = 0$). The initial value of $C$ at all space is set to 1 ($\tau = 0$). The dimensional flux density is obtained via:

$$j_d = \frac{Dc_{max}}{r_c} \left.\frac{2 \cdot \Delta C}{\Delta \phi}\right|_{\phi=0} \tag{9.14}$$

and the current response is:

$$I = F \cdot l \cdot j_d \tag{9.15}$$

## 9.5 Numerical model: a sphere

The spherical Laplacian operator in the diffusion equation on the sphere surface or laying down cylinder only depends on the angle $\theta$, since $r$ is a constant and a full symmetry around the $\phi$ angle can be applied. This results in a the 1D diffusion equation:

$$\frac{\partial c(\theta)}{\partial t} = D\frac{1}{r_c^2}\left(\frac{\partial^2 c(\theta)}{\partial \theta^2} + \frac{\cos\theta}{\sin\theta}\frac{\partial c(\theta)}{\partial \theta}\right) \tag{9.16}$$

$r_c$ is the constant radius of the sphere. The calculation is therefore applied in the range

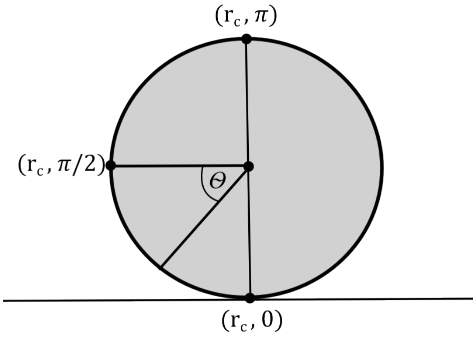

Figure 9.4: The surface of a sphere and the relevant points for the 1D diffusion model.

$\theta[0,\pi]$ as shown in figure 9.4. See appendix for the full discretization equations.

### 9.5.1 Dimensionless form

The same normalization can be used as in the case of the 'cylinder on its side'. The coverage can be also a fraction from the maximum 1D coverage: $C = c(mol/cm^2)/c_{max}(mol/cm^2)$. Dimensionless time can be used via: $\tau = Dt/R^2$. The diffusion equation in dimensionless form becomes:

$$\frac{\partial C(\theta)}{\partial \tau} = \frac{\partial^2 C(\theta)}{\partial \theta^2} + \frac{\cos\theta}{\sin\theta}\frac{\partial C(\theta)}{\partial \theta} \tag{9.17}$$

### 9.5.2 Boundary conditions and flux

At $\theta = \pi$ symmetry boundary conditions are used:

$$\left.\frac{\partial C}{\partial \theta}\right|_{\theta=0} = 0 \tag{9.18}$$

On the interface electrode-sphere at $\theta = 0$ high overpotential step is simulated and thus the coverage is set to zero at all time ($C = 0$). The initial value of $C$ at all space is set to 1 ($\tau = 0$).

In the case of the sphere, the overall dimensionless flux is the integration along $\phi$ with the infinitesimal radius of $\theta \to 0$:

$$J = 2\pi \frac{\Delta C}{\Delta \theta}\bigg|_{\theta \to 0} \quad \theta \to 0 \tag{9.19}$$

and in dimensional units:

$$J_d = -2\pi D c_{max} \frac{\Delta C}{\Delta \theta}\bigg|_{\theta \to 0} \quad \theta \to 0 \tag{9.20}$$

Thus the current response is found via:

$$I = F \cdot J_d \tag{9.21}$$

The current can be also found by charge conservation. Finding the change in the charge during each time step would give the dimension flux over the whole sphere:

$$J_d = 2\pi \int\limits_0^\pi \frac{dc}{dt} R^2 \sin\theta d\theta \tag{9.22}$$

In dimensionless form is converted to:

$$J/D c_{max} = 2\pi \int\limits_0^\pi \frac{dC}{d\tau} \sin\theta d\theta \tag{9.23}$$

In simulation, both values in equation 9.20 and in 9.23 should fully agree. Comparing these values allows an essential way to check the correctness of the model and also a good way to estimate the convergence. On the interface electrode-sphere at $\phi = 0$ the coverage is set to zero at all time ($C = 0$). The dimensional flux density is obtained via:

$$j_d = \frac{Dc_{max}}{r_c} \frac{2 \cdot \Delta C}{\Delta \phi}\bigg|_{\phi=0} \tag{9.24}$$

and the current response is:

$$I = F \cdot j_d \tag{9.25}$$

The grid setup and full discretization equations in the FDM are supplied in the Appendix.

## 9.6 Numerical model: a cube and a cuboid

The surface of a cube can be divided into two distinguishable domains, the sides and the top of the cube. The dissipation of charge along the sides of the cube can be described by a one-dimensional (1D) solution of the Fick's 2nd law:

$$\frac{\partial c(z,t)}{\partial t} = D \frac{\partial^2 c(z,t)}{\partial z^2} \tag{9.26}$$

For the top of the cube a 2D space must be considered:

$$\frac{\partial c(x,y,t)}{\partial t} = D(\frac{\partial^2 c(x,y,t)}{\partial x^2} + \frac{\partial^2 c(x,y,t)}{\partial y^2}) \tag{9.27}$$

In general, the diffusion equation is solved for 2D together with a 1D solution. To reduce computational costs the symmetry of the cube is utilised, and a quarter of the cube (as shown in Figure 9.5) can be simulated. In order to increase the accuracy and

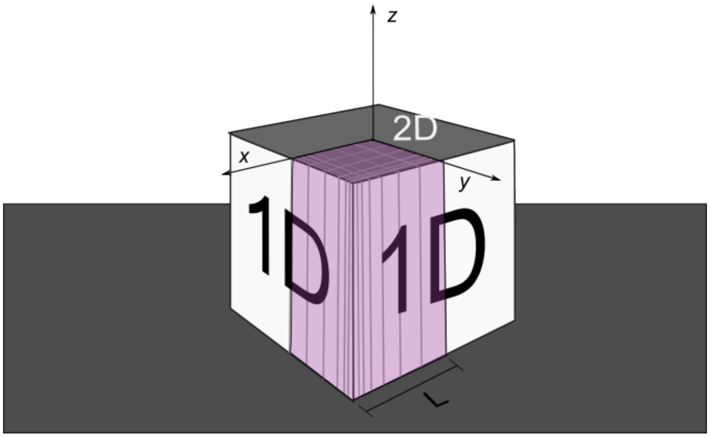

Figure 9.5: A scheme for the surface of the cube and the illustrated grids (along the grey lines) and dimensions for the finite difference calculations. The coloured region in pink is the actual calculated zone.

performance the solution of the 2D and 1D are coupled together to one set of discrete equations that solved through the ADI method and not to two separated solutions that are coupled at the side-top interface. The technique and the full discretization including all continuity points and boundary conditions definitions are provided in the Appendix.

### 9.6.1 Dimensionless form

The space is normalised to the length of half the edge of the cube $L(m)$. $X = x(m)/L(m)$, $Z = z(m)/L(m)$, and $Y = y(m)/L(m)$. The coverage can be also a fraction from the maximum 1D coverage: $C = c(mol/m^2)/c_{max}(mol/m^2)$.

Dimensionless time can be used via: $\tau = Dt/L^2$. The dimensionless diffusion coefficient can be now set to 1 due to dimensionless space and time. The diffusion equation in dimensionless cylindrical coordinates form is now:

For the 1D model on the side of the cube is

$$\frac{\partial C}{\partial \tau} = \frac{\partial^2 C}{\partial Z^2} \tag{9.28}$$

and for the 2D diffusion on the top of the cube:

$$\frac{\partial C}{\partial \tau} = \frac{\partial^2 C}{\partial X^2} + \frac{\partial^2 C}{\partial Y^2} \tag{9.29}$$

### 9.6.2 Boundary conditions and flux

The boundary condition for each 1D grid point is solved with a boundary condition of $C = 0$ at the interface electrode-cube for all time. The initial value of $C$ at all space is set to 1. At the top edge of the quarter cube symmetry boundary conditions are applied:

$$\left.\frac{\partial C}{\partial X}\right|_{Y=L} = 0, \quad and \quad \left.\frac{\partial C}{\partial Y}\right|_{X=L} = 0 \tag{9.30}$$

The continuous edges at the top-side of the cube are discussed in the appendix. The flux density in dimensional unit is then given by:

$$j_d = -\frac{Dc_{max}}{L} \left.\frac{\Delta C}{\Delta Z}\right|_{Z=0} \tag{9.31}$$

Integrating (summing) over all 1D grids.

$$J_d = Dc_{max} \int\limits_0^L \left.\frac{\Delta C}{\Delta Z}\right|_{Z=0} dY + Dc_{max} \int\limits_0^L \left.\frac{\Delta C}{\Delta Z}\right|_{Z=0} dX \tag{9.32}$$

Since the calculation is made for a quarter of a cube the current measured is calculated as:

$$I = 4 \cdot F \cdot J_d \tag{9.33}$$

### 9.6.3 Cuboid

Alteration of the cube simulation to a cuboid case is simply done by using various grid sizes. For example, the Y grid space can end at n (n time the size of $L$) and Z grid can and at m (m time the size of $L$). This will give a cuboid with the ratio: 1:n:m. The upper integration limit for calculating the flux at equation 9.32 should be then accordingly modified to n.

## 9.7 Results and Discussion

The results first discusses the current-time response from the various shapes of particles. Second, a comparison of the current responses is presented to explore the capability of using the method to distinguish between the various geometries in a current time response measurement.

### Surface diffusion on a cylinder

#### Cylinder on its base

Figure 9.6 provides the characteristic current-time response of a representative cylinder on its base with a ratio of l:r=2:1 (length:radius) in dimensionless flux and time. Charge injection arises from the substrate electrode at the circumference of the base.

The result shows that at short time the diffusion of charge is characterized with a Cottrell one-dimensional diffusion process, since the slope in the logarithmic curve (figure 9.6b) is measured to be -0.5, which follows the relation $log I \propto -log\sqrt{t}$ from the Cottrell equation (eq. 1). This observation is due to the domination of one-dimensional diffusion along the side of the cylinder with only a little effect from the top of the cylinder. At

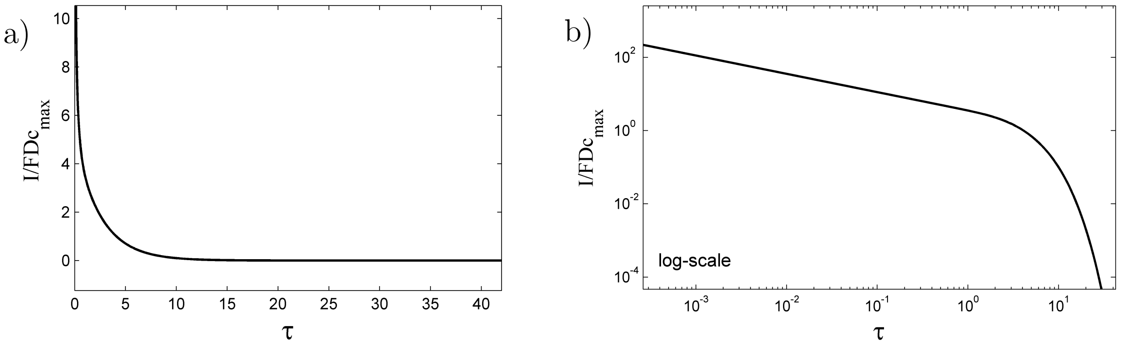

Figure 9.6: Cylinder on its base: Dimensionless current-time response (a) and logarithmic scale presentation (b), for the diffusion of charge process on a surface of a cylindrical particle with a ratio of l:r=2:1 between the radius of the base and the length of the side.

long times, the current drops quickly to zero, due to the dilution of all the electro-active locations on the surface of the cylindrical particle, at the side and at the top.

In order to provide more information about the top radial diffusion, figure 9.7a presents the dimensionless coverage density at time $\tau$=2 on the surface of the cylindrical particle. In Figure 9.7b only the coverage density on the top of the cylinder is shown. It can be seen from figure 9.7a that most of the coverage gradient evolves on the side due to the slow one-dimensional diffusion. The top radial diffusion shows fast relaxation, and therefore the concentration gradient evolution is very small, from 0.0135 at the edge of the top to 0.016 at the centre of the top as shown in figure 9.7b.

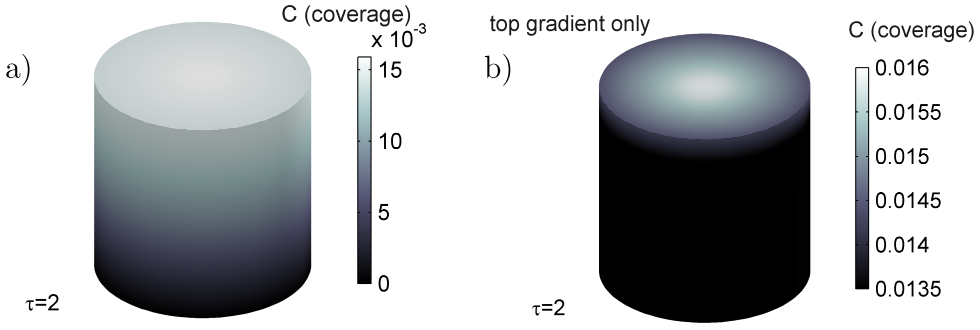

Figure 9.7: Dimensionless coverage map on the surface of a cylinder with a ratio l:r=2:1 at $\tau$=2 (a), and the coverage only at the top (b).

Further, a comparison of the current-time response for various top to side ratios is provided. In order to make a practical comparison, the dimensionless currents and time are adjusted to the same area for any ratio. Hence the fraction $X = h_c/r_c$ is defined, and the area of the cylinder can be expressed as: $(2X+1)\pi r_c^2$. By choosing $r_c$ to be $\frac{1}{\sqrt{2X+1}}$, the area is constrained to $\pi$. Therefore in the comparison between every top/side ratio, i.e. any fraction X adjusts $\tau$ to:

$$\tau_\pi = \tau/(2X+1) \tag{9.34}$$

The expression for the dimensionless total flux stays the same but the symbol have been changed to $J_\pi$ for clarity. Figure 9.8 shows the current-time response for various ratios of cylindrical particles with a constrained area of $\pi$. It is shown that by increasing the base radius the absolute current response is higher at short times, but the Cottrellian slope is preserved (the slope equals -0.5). Additionally, the steep drop of current is observed earlier for larger radius of bases due to the shorter length of the cylinder sides. This behaviour shows that various current-time response can be observed for the same area of

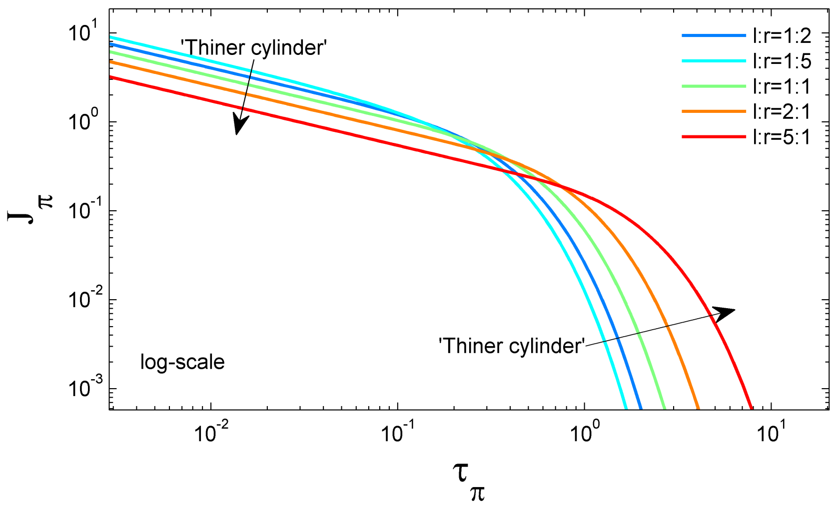

Figure 9.8: The dimensionless current-time response in logarithmic scale for various ratios of cylinder sizes, in the case of adjusted $\tau_\pi$ to a particle surface area of a $\pi$.

cylindrical particle for various ratios. Nevertheless, in order to have a valuable information of the current response in the case of cylindrical particles, it is also necessary to take into account the case of 'cylinder on its side' which is discussed next.

### Cylinder on its side

Figure 9.9 the characteristic current-time response of cylinder on its base for any ratio (bearing in mind that since the bases of the cylinder are neglected in this model, a significant deviation occurs in the case of a short cylinders, i.e. a ratio of 1:1 or smaller). The result shows the Cottrellian diffusion and the flux slope measured to be -0.5 in the logarithmic scale curve at 9.9b, due to the 1D diffusion along the $\phi$ angle of the cylinder. The domination of Cottrellian diffusion is also observed in the case of cylinder on its base.

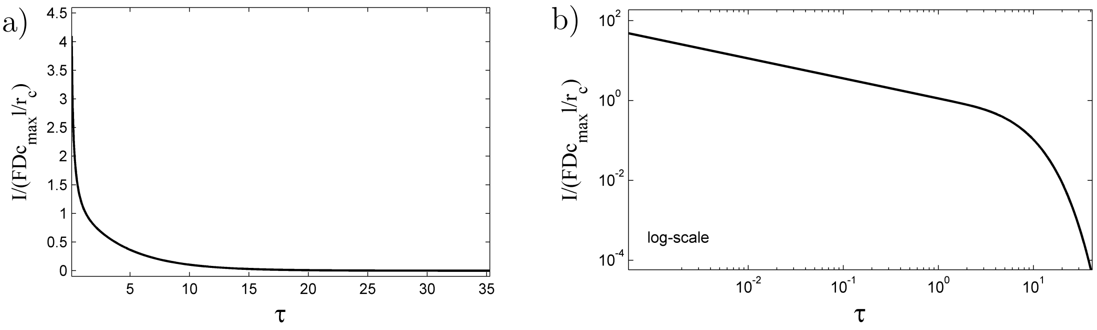

Figure 9.9: Cylinder on its side: Dimensionless current-time response (a) and in logarithmic scale (b), for the diffusion of charge process on a surface of a cylindrical particle for any ratio between the radius of the base and the length of the side.

In figure 9.10 the two cases are compared for a cylinder on its base and on its side. First figure 9.10a shows the behaviour of a long cylinder (ratio l:r=4:1)on base ('bamboo-like') and on its side ('tube-like'). The comparison shows the different response in the case of the same cylindrical particle lying on its base or on its side. The large current response at short times is due to the contact of the particle with the electrode along all the length of the cylinder in the case of the cylinder on its side. For a relatively short cylinder, it

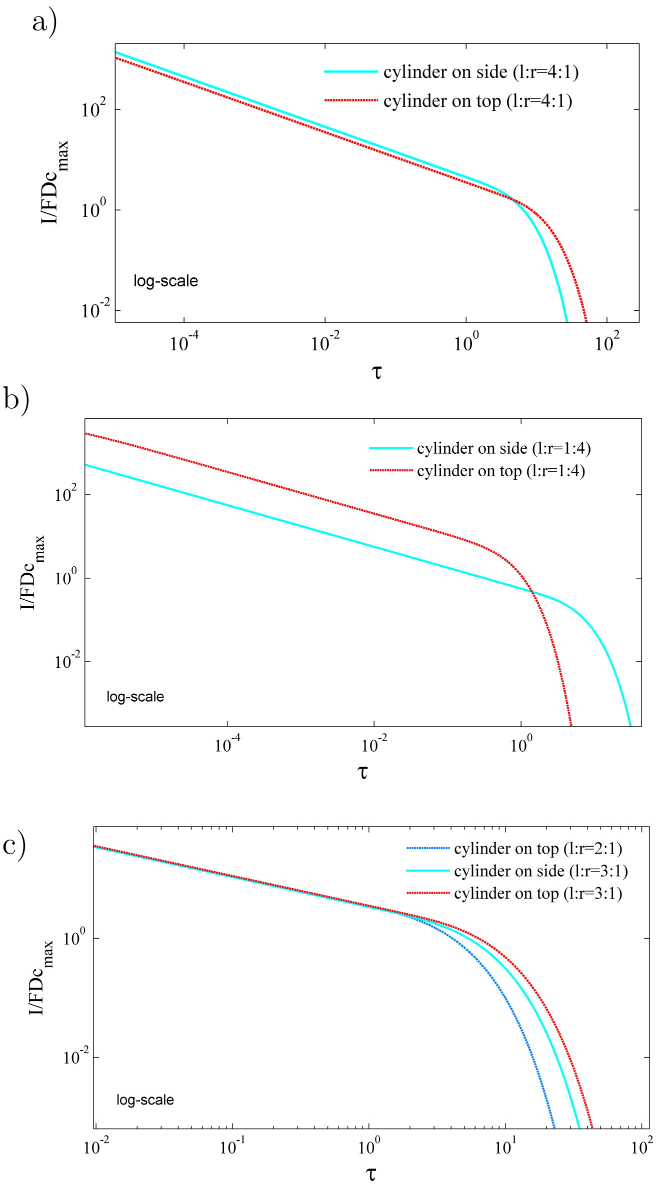

Figure 9.10: Comparison between cylindrical particle on its base and on its side, for a long cylinder with ratio l:r=4:1 (a), short cylinder with ratio l:r=1:4 (b), and for mixed ratios (c).

is easy to distinguish between the cases as shown in figure 9.10b. However, the deviation is due to the neglecting of the bases in the calculation and the result is therefore only valuable only for distinguishing between the cases but not for determining the diffusion coefficient or the coverage for this case of small ratios. Moreover, although it was shown in figures 9.10a-b that it is easy to distinguish between cylindrical particles on their base and on their side from the current-time response, in a mixed ratios this becomes more complex as shown in figure 9.10b. For example, the current response of a cylinder on a side with a ratio l:r=3:1, can have the same response of cylinder on its base between the ratio l:r=3:1 to 2:1 at short time and also at long time.

The results of the current-time response for different ratios of cylindrical particles can be used directly by fitting the modelled curves to experimental data in order to determine the coverage or the diffusion of charge along a surface. It can also be used for having a good indication about the average ratio of the cylinder in large number of particles from a simple chronoamperometry measurement.

## Surface diffusion on a sphere

After examining the cylindrical particle current response, figure 9.11 shows the behaviour of the spherical shape which fully agrees with the previous simulation by Thompson et al.[17]. We can see that neither the short time or the long time follows Cottrellian diffusion. At short times, a moderate decrease of the current is observed due to the expansion of the spherical space and therefore access to more active locations with time results in radial diffusion. In contrast, at long times when the upper sphere becomes more and more dominant there is a steep drop in the current due to the shrinking of the spherical surface.

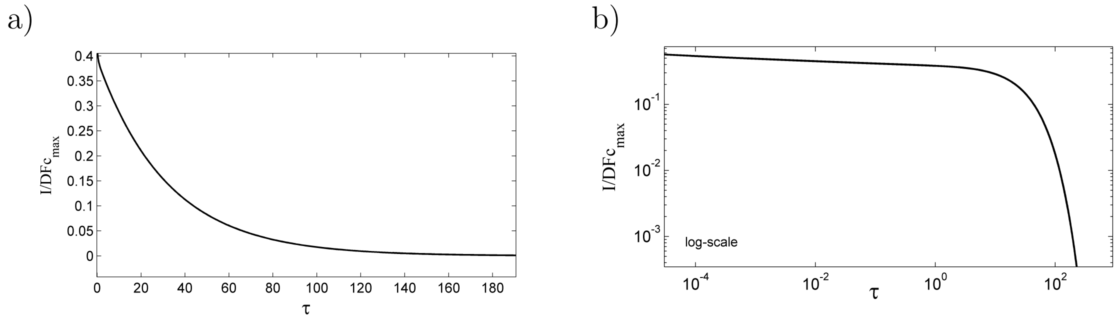

Figure 9.11: Sphere : Dimensionless current time response (a) and in logarithmic scale (b), for the diffusion of charge process on a surface of a spherical particle.

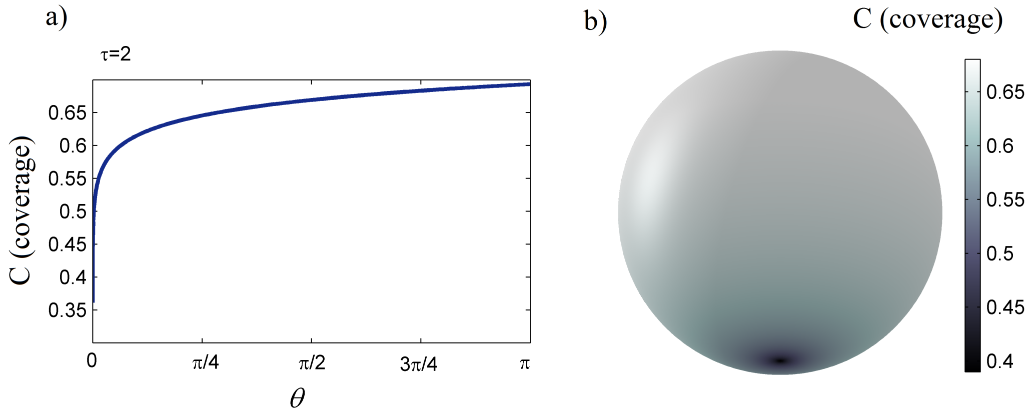

Figure 9.12: a) Dimensionless coverage profile along the surface of the spherical particle. b) A colour map of the coverage on the particle surface. The coverage is captured at time $\tau = 2$

This diffusion in spherical coordinates can also be shown by looking at the coverage profile along the sphere in figure 9.12. It shows that most of the coverage gradient evolves on the down side of the sphere, due to the radial expansion of the surface area from the injection point towards the top. The upper side of the sphere has a relatively uniform coverage implying that the relaxation of the concentration is fast. The fast relaxation is due to the fact that along the sphere towards the top, the amount of sites are decreased with a radial proportion, which results in a fast decrease of the available sites from charge diffusion. Later, the non-Cottrellian behaviour is utilised to distinguish between spherical particles and other particle shapes.

## Surface diffusion on a cube

The last particle shape in this study is a cube. Figure 9.13 shows the current time response in dimensionless units. The behaviour of the current-time response shows the same trend as in the cylinder case due to the characteristic Cottrellian diffusion on the sides of the cubic particle that dominates the short time behaviour. The coverage 2D map on the

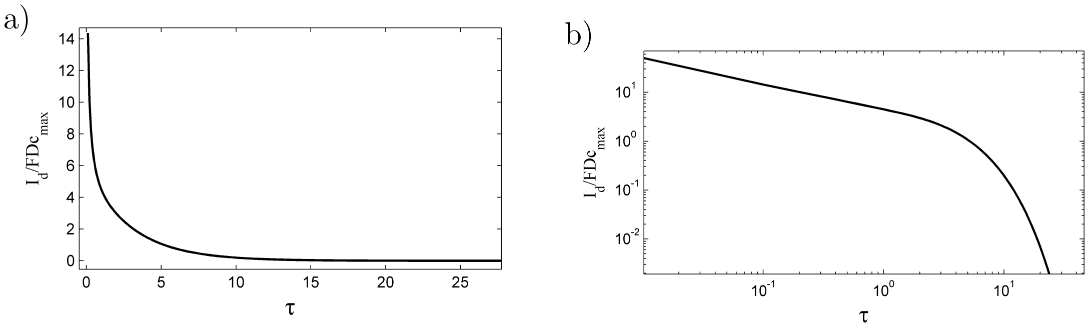

Figure 9.13: a) Current-time response of charge diffusion on a surface of a cubic particle. b) The current time-response in a logarithmic scale.

cubic particle is presented in figure 9.14a. The coverage map shows that the gradient is mostly evolved in the side of the cube where the Cottrellian diffusion is observed. By looking only at a smaller range of coverage (0.5-0.75) as provided in figure 9.14, we can see the 2D diffusion that dominates on the top and on the sides next to the top of the cube. It is also observed that the charge is not fully symmetric on the sides next to the top and at the top, the diffusion propagates towards the top-centre of the cube.

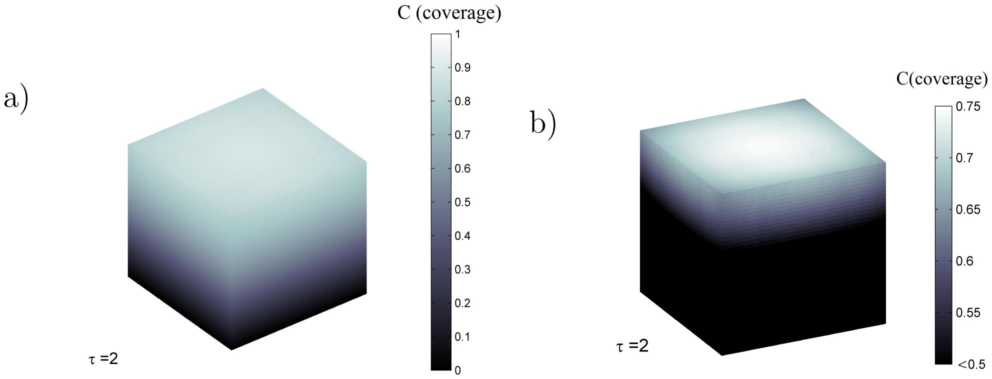

Figure 9.14: a) Coverage surface map on the whole surface of the cube. b) The coverage only on the top and next to the top of the cube. The coverage is captured at time $\tau = 2$.

### Cuboid particles

In case where the particles are not cubic but cuboid the time current-response is expected to change. The response for cuboid particles are simulated for two representative ratios and presented in figure 9.15.

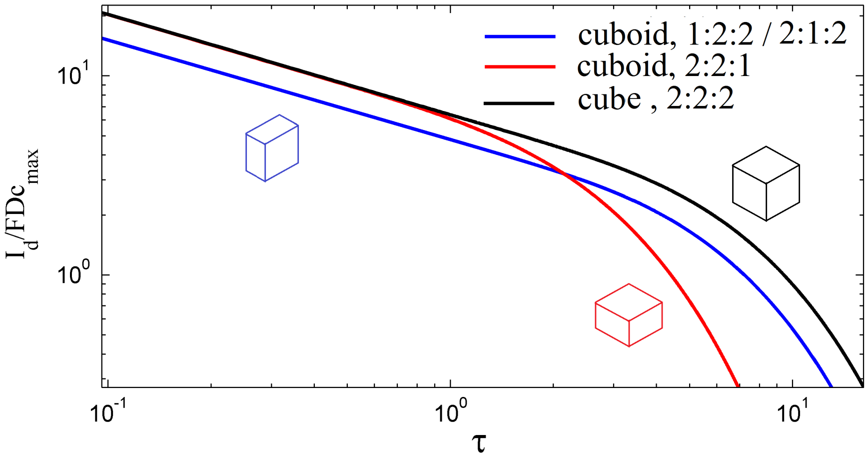

Figure 9.15: Current-time response of representative cuboid shapes: width:length:hight =2:2:2, 2:2:1, and 1:2:2.

When the cuboid has a short height, as shown in the ratio w:l:h(width:length:height) =2:2:1 the Cottrellian behaviour at the short times gets shorter than in a perfect cube. In the case where one of the base length is smaller, with a ratio of w:l:h=2:1:2 or w:l:h= 1:2:2, the length of the Cottrellian behaviour (where the logarithmic slope equals -0.5) would be the same as in the case of perfect cube with the same height, but the current density would be smaller and thus the curve would be offset. This behaviour is similar to that observed in the case of a cylinder on its base provided earlier. Measuring these changes of ratio in the current-time response from large number of particles can give an indication about the dominance of a specific aspect ratio, or the orientation on the electrode.

## Comparison of shapes

In order to compare the cases, the surface area is adjusted to $\pi$ for all cases. Simulations of a cube, sphere, and three types of cylinder shapes are discuseed in this study. For the three cylinder cases, one is a cylinder on its base with ratio of l:r=1:10, modelling a 'Flake-like' particle. The second is a cylinder on its side with the ratio l:r=10:1, modelling a ‘tube-like’ particle. The third cylinder is a regular l:r=1:2 cylinder on its base to be comparable in shape with the sphere and the cube. For the sphere, the area is $4\pi r^2$ so $r = 1/2$ is used to normalize it to the area of $\pi$. This means that $\tau$ is changed to $\tau_\pi = \tau/4$. The flux expression remains the same. In the case of a cube, the ground base is not considered in the area (assuming it is blocked or immediately reacts). Therefore $L = \sqrt{\pi/20}$, and $\tau_\pi = \pi\tau/20$ are chosen.

For the side down long cylinder, the area is giving $2\pi r_c l$ (omitting the bases), and $l = 1/(2r_c)$ to get an area of a $\pi$. The whole cylinder then depends on $r_c$ as follows:

$$J_\pi = \frac{1}{r_c^2}\int_0^\pi \frac{dC}{d\tau}d\phi \tag{9.35}$$

In all cases the symbol $J_\pi$ is used instead of $I_d/FDc_{max}$ for clarity) and $\tau = \tau_\pi$ remains the same. For the case of the top cylinder we treat it as earlier, $\tau_\pi = \tau/(2h_c/r_c + 1)$, and $J_\pi$ remains the same.

The current-time responses are presented in a log-plot at figure 9.16. The integration of the flux over time in all cases was checked to be close enough to $\pi$ (within 2%) to ensure mass conversion which indicates the convergence of the simulation and the correctness of the adjustments of $\tau_\pi$ and $J_\pi$ described above.

It is shown that the sphere can be distinguished from the other cases due to the non-Cottrellian diffusion. The characteristic slope of -0.5 in the log scale dominates all the other cases. It can be seen that it is also easy to distinguish between different ratios of cylinders, i.e. the case of the flake-like and tube-like have a different current response to the regular cylinder 1:2 or the cube, both at the short and long times. However, as we saw earlier the flake-like and the tube-like particles show similar responses due to the same area and exact inverse ratio. Further, the cubic particle shows a close behaviour

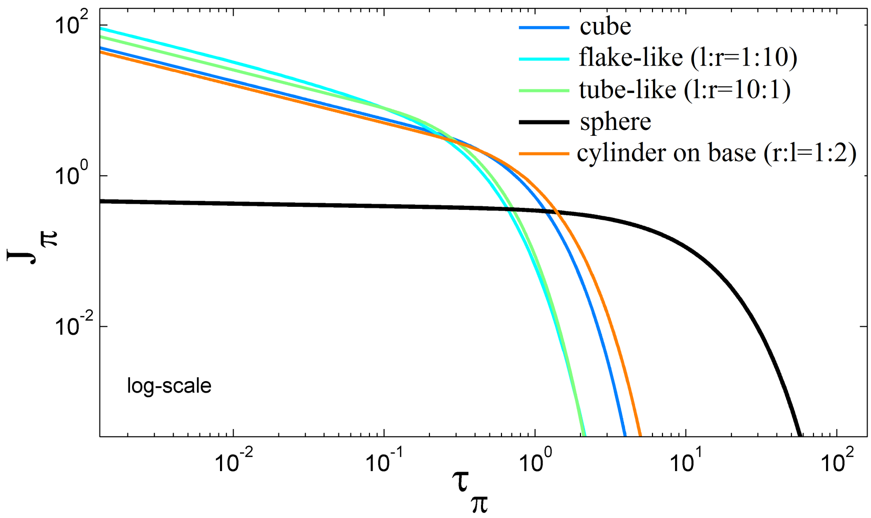

Figure 9.16: Comparison current-time response of various shapes: cube, flake-like(cylinder on its base, l:r=1:10), tube-like (cylinder on its side, l:r=10:1), sphere, and cylinder on its base(r:l=1:2).

to the regular size (r:l=1:2) cylinder, and therefore provides a clear difference from the spherical particle. However, the analysis is not likely to distinguish between a cube and a cylindrical shape. It can be concluded, that in order to determine coverage or the charge diffusion coefficient it is enough to simulate the simplified cylinder case.

Finally, a dimensional example of the charge diffusion on the surface of graphite particles is discussed. The examples has similar parameters as provided by the work of Thompson et al. for a spherical particle case[17], with a $5\mu m$ radius of particles with a coverage of $3 \cdot 10^{-5} mol/m^2$, and a charge transfer diffusion coefficient of $10^{-11} m^2/s$. The current-time response is provided in figure 9.17 for the case of a sphere, 'flake-like' and a cylinder with a ratio r:l=1:2. The result shows the ability to distinguish between the current responses of various modified particle shapes. The unique current-time response for each primitive shape can be utilized to determine the coverage on the surface of the particle or the diffusion coefficient of charge over a particular shape. Additionally, it gives

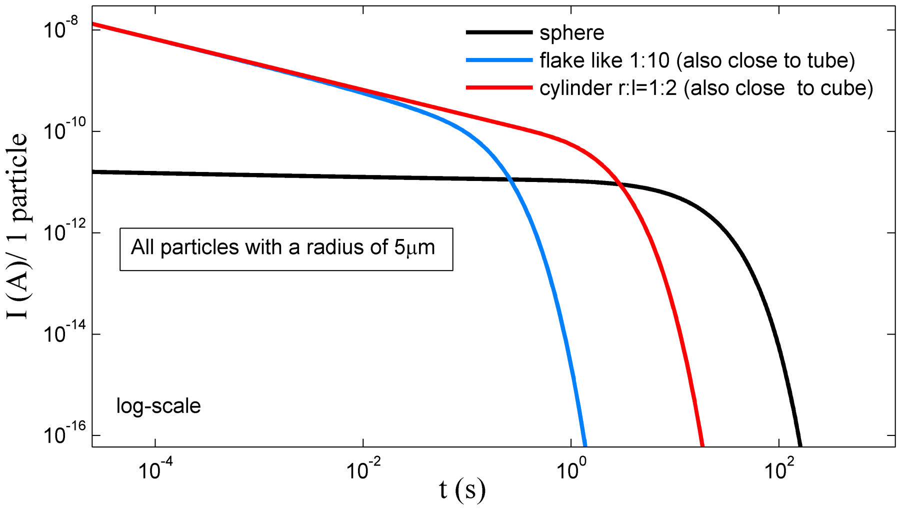

Figure 9.17: Comparison of the current-time response of various types of cylinders vs sphere. The coverage ($3 \cdot 10^{-5} mol/m^2$), the radius($5\mu m$), and the diffusion coefficient($10^{-11} m^2/s$) were chosen to be the same for all cases.

information about the shape of the particle in a cell or its orientation on the electrode.

## 9.8 Conclusions

The charge measurement through electro-active sites on a modified surface of insulating particles have been modelled using random diffusion for various shapes. This allowed to numerically simulate the current-time responses of an impact of particles with a shape of a sphere, a cube/cuboid, and a cylinder on an electrode. The characteristic current-time responses can be used to determine the coverage or the diffusion of charge coefficient of the modified insulating particles in the various shapes. It was shown that the current-time response has different profiles, which reflect the particle shape and the aspect ratio. This allows one to distinguish between the various shapes and can also provide information on their orientation on the electrode. It is clearly shown that spherical particles has a non-Cottrellian behaviour whilst cylinders, and cubes have a characteristic Cottrellian current that is easily distinguished from the sphere. The cube and a cylinder in an aspect ratio of radius:length=1:2, showed a similar behaviour. Nevertheless, various aspect ratios of cuboid or cylinders such as flake-like, tube or bamboo-like, change the current-response significantly and can be distinguished and characterized by comparing the current values at short and long time, giving information about the average sizes in a system and the orientation on the electrode.

## 9.9 Appendix

In this appendix the grids and discretization of the diffusion of charge equations are provided for the cases of cylinder on its base, cylinder on its side, a sphere, and a cube. The discretization of the equations are shown also with their coefficients that were used in the implicit - finite difference method and solved with the Thomas algorithm.

### 9.9.1 Discretization and grids: ‘cylinder on its base’

$i$ is defined to be an integer index along the $z$ expanding grid, which starts at 0 (the bottom of the cylinder, see figure 9.18) in coordinates (0,R) and ends at $l$ (on the top, see figure 9.18) in coordinates ($r_c$,H). For the top of the cylinder, another integer index is defined, $j$, which starts at zero (the centre) in coordinates ($r_c$,0) (the centre of the top), and increases up to the number $h$ in coordinates ($r_c$,H), which is also shared with the $i$ index.

On the side of the cylinder, the coverage in a grid $C_{l>i>0}$ (except of the boundaries), at time step $\tau_k$ is expressed as:

$$\frac{C_i - C_i^{k-1}}{\tau_k - \tau_{k-1}} = \frac{\frac{C_{i+1}-C_i}{\Delta Z_+} - \frac{C_i - C_{i-1}}{\Delta Z_-}}{\frac{1}{2}(\Delta Z_+ + \Delta Z_-)} \tag{9.36}$$

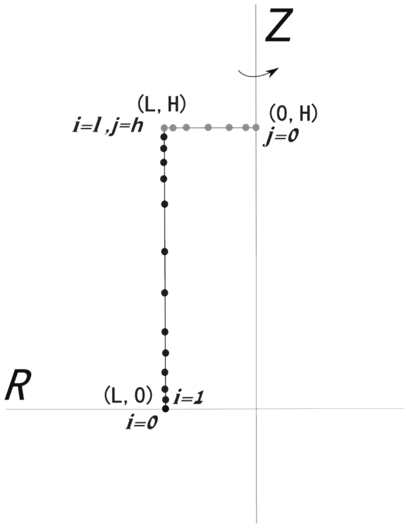

Figure 9.18: Two 1D representation of top and side of the cylinder with expanding grids.

and can be rearranged to

$$\delta_i = C_i^{k-1} = \alpha_i C_{i-1} + \beta_i C_i + \gamma_i C_{i+1} \tag{9.37}$$

where:

$$\alpha_i = -\frac{2(\tau_k - \tau_{k-1})}{\Delta Z_-^2 + \Delta Z_+ \Delta Z_-},\ \beta_i = \frac{2(\tau_k - \tau_{k-1})}{\Delta Z_-^2 + \Delta Z_+ \Delta Z_-} + \frac{2(\tau_k - \tau_{k-1})}{\Delta Z_+^2 + \Delta Z_+ \Delta Z_-} + 1,\ \gamma_i = -\frac{2(\tau_k - \tau_{k-1})}{\Delta Z_+^2 + \Delta Z_+ \Delta Z_-} \tag{9.38}$$

At the top of the cylinder, $C_{h>j>0}$ (except to the boundaries R=H and R=0):

$$\frac{C_j - C_j^{k-1}}{\tau_k - \tau_{k-1}} = \frac{\frac{C_{j+1} - C_j}{\Delta R_+} - \frac{C_j - C_{j-1}}{\Delta R_-}}{\frac{1}{2}(\Delta R_+ + \Delta R_-)} + \frac{1}{R}\frac{C_{j+1} - C_{j-1}}{\Delta R_+ + \Delta R_-} \tag{9.39}$$

and rearranging:

$$\delta_j = C_j^{k-1} = \alpha_j C_{j-1} + \beta_j C_j + \gamma_j C_{j+1} \tag{9.40}$$

where:

$$\alpha_j = -\frac{2(\tau_k - \tau_{k-1})}{\Delta R_-^2 + \Delta R_+ \Delta R_-} + \frac{1}{R}\frac{\tau_k - \tau_{k-1}}{\Delta R_+ + \Delta R_-}, \tag{9.41}$$

$$\beta_j = \frac{2(\tau_k - \tau_{k-1})}{\Delta R_-^2 + \Delta R_+ \Delta R_-} + \frac{2(\tau_k - \tau_{k-1})}{\Delta R_+^2 + \Delta R_+ \Delta R_-} + 1,$$

$$\gamma_j = -\frac{2(\tau_k - \tau_{k-1})}{\Delta R_+^2 + \Delta R_+ \Delta R_-} - \frac{1}{R}\frac{\tau_k - \tau_{k-1}}{\Delta R_+ + \Delta R_-}$$

We also need to express the missing equations for the boundaries points: ($r_c$,0),($r_c$,H),(H,0). At point $r_c$,0 i=0, the rate of charge transfer is assumed to be fast enough to fill up all active sites:

$$C_{i=0} = 1 \tag{9.42}$$

and thus

$$\alpha_0 = 0,\ \beta_0 = 1,\ \gamma_0 = 0,\ \delta_0 = 1 \tag{9.43}$$

at point ($r_c$,H), we add continuity by:

$$\frac{C_{h,l} - C_{h,l}^{k-1}}{\tau_k - \tau_{k-1}} = \frac{\frac{C_{h-1} - C_{h,l}}{\Delta R_h} - \frac{C_{h,l} - C_{l-1}}{\Delta Z_l}}{\frac{1}{2}(\Delta R_h + \Delta Z_l)} + \frac{1}{R_h}\frac{C_{h-1} - C_{h,l}}{\Delta R_h} \tag{9.44}$$

and rearrange to get:

$$\delta_{h,l} = C_{h,l}^{k-1} = \alpha_{h,l} C_{l-1} + \beta_{h,l} C_l + \gamma_{h,l} C_{h-1} \tag{9.45}$$

where

$$\alpha_{h,l} = -\frac{2(\tau_k - \tau_{k-1})}{\Delta Z_l^2 + \Delta R_h \Delta Z_l},\ \beta_{h,l} = \frac{2(\tau_k - \tau_{k-1})}{\Delta R_h^2 + \Delta R_h \Delta Z_l} + \frac{2(\tau_k - \tau_{k-1})}{\Delta Z_l^2 + \Delta R_h \Delta Z_l} + \frac{\tau_k - \tau_{k-1}}{R_h \Delta R_h} + 1, \tag{9.46}$$

$$\gamma_{h,l} = -\frac{2(\tau_k - \tau_{k-1})}{\Delta R_h^2 + \Delta R_h \Delta Z_l} - \frac{\tau_k - \tau_{k-1}}{R_h \Delta R_h} \tag{9.47}$$

The last boundary condition is at the coordinates (0,$r_c$) on the top-centre of the cylinder. Symmetry boundary condition can be used at that point:

$$C_{j=1} - C_{j=0} = 0 \tag{9.48}$$

and thus

$$\alpha_0 = 0,\ \beta_0 = 1,\ \gamma_0 = -1,\ \delta_0 = 0 \tag{9.49}$$

Now a set of $h + l + 1$ equations are obtained with $h + l + 1$ coverage variables that can be solved directly by the Thomas algorithm at each time step. This can be solved with the initial values of zero charge coverage in all space at $\tau = 0$. The time step is also an expanding grid, and starts with a sufficiently small difference of $\Delta\tau$ to meet the large concentration gradients at short times.

The flux of 'coverage' can then be calculated by the gradient at $i = 0$ :

$$J = \frac{C_{i=1} - C_{i=0}}{\Delta Z} \tag{9.50}$$

or in dimensional units:

$$J_d = -\frac{Dc_{max}}{r_c}\frac{C_{i=1} - C_{i=0}}{\Delta Z} \tag{9.51}$$

and the integration over the cylinder at R=$r_c$, simulates the current response via:

$$I = F\int_0^{2\pi} J_d \cdot r_c d\theta = 2\pi F D c_{max}\frac{C_{i=1} - C_{i=0}}{\Delta Z} \tag{9.52}$$

### 9.9.2 Discretization: 'cylinder on its side'

The discretization of the diffusion equation in the implicit method, at time step $\tau_k$ is expressed as:

$$\frac{C_j - C_j^{k-1}}{\tau_k - \tau_{k-1}} = \frac{\frac{C_{j+1}-C_j}{\Delta\phi_+} - \frac{C_j - C_{j-1}}{\Delta\phi_-}}{\frac{1}{2}(\Delta\phi_+ + \Delta\phi_-)} \tag{9.53}$$

and rearranging:

$$\delta_j = C_j^{k-1} = \alpha_j C_{j-1} + \beta_j C_j + \gamma_j C_{j+1} \tag{9.54}$$

where:

$$\alpha_i = -\frac{2(\tau_k - \tau_{k-1})}{\Delta\phi_-^2 + \Delta\phi_+\Delta\phi_-},\ \beta_i = \frac{2(\tau_k - \tau_{k-1})}{\Delta\phi_-^2 + \Delta\phi_+\Delta\phi_-} + \frac{2(\tau_k - \tau_{k-1})}{\Delta\phi_+^2 + \Delta\phi_+\Delta\phi_-} + 1,\ \gamma_i = -\frac{2(\tau_k - \tau_{k-1})}{\Delta\phi_+^2 + \Delta\phi_+\Delta\phi_-} \tag{9.55}$$

At point (R,0) when $i = 0$, we can assume that the rate of charge transfer is fast enough to fill up all the active sites:

$$C_{i=0} = 1 \tag{9.56}$$

and thus

$$\alpha_0 = 0,\ \beta_0 = 1,\ \gamma_0 = 0,\ \delta_0 = 1 \tag{9.57}$$

At coordinates ($R$,$\pi$) on the top-centre of the sphere. Symmetry boundary condition can be used:

$$C_{j=1} - C_{j=0} = 0 \tag{9.58}$$

and thus

$$\alpha_0 = 0,\ \beta_0 = 1,\ \gamma_0 = -1,\ \delta_0 = 0 \tag{9.59}$$

The set of equations can be solved directly by the Thomas algorithm at each time step. This can be solved with the initial values of zero charge coverage in all space at $\tau = 0$. The flux of 'coverage' can be calculated by the gradient at $i = 0$ :

$$j = 2\frac{C_{i=1} - C_{i=0}}{\Delta\phi} \tag{9.60}$$

The overall dimensional flux is obtained via:

$$J_d = 2\frac{l \cdot Dc_{max}}{r\Delta\phi}(C_{i=1} - C_{i=0}) \tag{9.61}$$

and the current response is:

$$I = FJ_d \tag{9.62}$$

In order to get an accurate result $\theta_1$ should be very small. The current can also be found by charge conservation. Finding the change in the charge during each time step would give the dimension flux over the whole sphere:

$$J_d = 2l\int_0^\pi \frac{dc}{dt}r d\phi \tag{9.63}$$

In dimensionless form it is converted to:

$$J/Dc_{max} = \frac{2l}{r}\int_0^\pi \frac{dC}{d\tau}d\phi \tag{9.64}$$

In simulation both values, in equation 9.61 and in 9.64 should fully agree. Comparing these values provides a good estimation of the simulation convergence.

### 9.9.3 Discretization: 'sphere'

The discretization of the diffusion equation in the implicit method, at time step $\tau_k$ is expressed as:

$$\frac{C_j - C_j^{k-1}}{\tau_k - \tau_{k-1}} = \frac{\frac{C_{j+1}-C_j}{\Delta\theta_+} - \frac{C_j - C_{j-1}}{\Delta\theta_-}}{\frac{1}{2}(\Delta\theta_+ + \Delta\theta_-)} + \frac{1}{\tan(\theta)}\frac{C_{j+1} - C_{j-1}}{\Delta\theta_+ + \Delta\theta_-} \tag{9.65}$$

and rearranging:

$$\delta_j = C_j^{k-1} = \alpha_j C_{j-1} + \beta_j C_j + \gamma_j C_{j+1} \tag{9.66}$$

where:

$$\alpha_j = -\frac{2(\tau_k - \tau_{k-1})}{\Delta\theta_-^2 + \Delta\theta_+\Delta\theta_-} + \frac{1}{\tan(\theta)}\frac{\tau_k - \tau_{k-1}}{\Delta\theta_+ + \Delta\theta_-}, \tag{9.67}$$

$$\beta_j = \frac{2(\tau_k - \tau_{k-1})}{\Delta\theta_-^2 + \Delta\theta_+\Delta\theta_-} + \frac{2(\tau_k - \tau_{k-1})}{\Delta\theta_+^2 + \Delta\theta_+\Delta\theta_-} + 1,$$

$$\gamma_j = -\frac{2(\tau_k - \tau_{k-1})}{\Delta\theta_+^2 + \Delta\theta_+\Delta\theta_-} - \frac{1}{\tan(\theta)}\frac{\tau_k - \tau_{k-1}}{\Delta\theta_+ + \Delta\theta_-}$$

Expressing the missing equations for the boundaries points, $(R, 0)$ and $(R, \pi)$ is needed. At point (R,0) when i=0, the rate of charge transfer is:

$$C_{i=0} = 1 \tag{9.68}$$

and thus

$$\alpha_0 = 0,\ \beta_0 = 1,\ \gamma_0 = 0,\ \delta_0 = 1 \tag{9.69}$$

At coordinates $(R,\pi)$ on the top-centre of the sphere. Symmetry boundary condition can be used:

$$C_{j=1} - C_{j=0} = 0 \tag{9.70}$$

and thus

$$\alpha_0 = 0,\ \beta_0 = 1,\ \gamma_0 = -1,\ \delta_0 = 0 \tag{9.71}$$

The set of equations can be solved directly by the Thomas algorithm at each time step. This can be solved with the initial values of zero charge coverage in all space at $\tau = 0$.

The flux of 'coverage' can be calculated by the gradient at $i = 0$ :

$$j = \frac{C_{i=1} - C_{i=0}}{\Delta\theta} \tag{9.72}$$

The overall dimensionless flux is the integration along $\phi$ with the infinitesimal radius of $\theta_{i=1}$:

$$J = 2\pi\frac{C_{i=1} - C_{i=0}}{\Delta\theta}\theta_{i=1} = 2\pi(\Delta C_{1-0}) \tag{9.73}$$

since,$\theta_1 = \Delta\theta_{1-0}$. In dimensional units:

$$J_d = -2\pi D c_{max}\Delta C_{1-0} \tag{9.74}$$

and the integration over the whole sphere, simulates the current response via:

$$I = FJ_d \tag{9.75}$$

In order to get an accurate result $\theta_1$ should be very small. The current can also be found by charge conservation. Finding the change in the charge during each time step would give the dimension flux over the whole sphere:

$$J_d = 2\pi\int_0^\pi \frac{dc}{dt}R^2\sin\theta d\theta \tag{9.76}$$

In dimensionless form is converted to:

$$J/Dc_{max} = 2\pi \int_{0}^{\pi} \frac{dC}{d\tau} \sin\theta d\theta \tag{9.77}$$

In simulation both values in equation 9.74 and in equation 9.77 should fully agree. Comparing this values allows good estimation of the convergence.

### 9.9.4 Discretization and grids: cube/cuboid

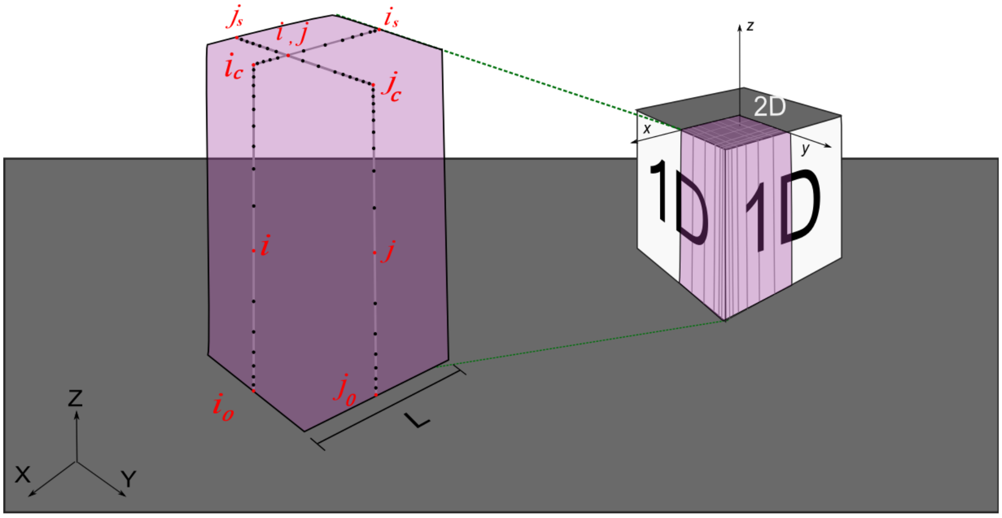

Figure 9.19: A scheme for the surface of the cube and the illustrated grids (along the grey lines) and dimensions for the finite difference calculations. The coloured region in pink is the actual calculated zone.

$i$ is defined to be an integer index along the $Z$ grid in the surface that is perpendicular to $X$, starts at 0 (the bottom of the cube) and at the ends of the side of the cube (see illustration above in figure 9.19) a point $i_c$ is defined for applying the flux continuity conditions. At the top of the cube the index increases further towards the symmetry boundary which is defined as $i_s$. The same is defined for the $Y$ axes: $j$.

On the top of the cube, the ADI method is used to solve numerically the 2D diffusion equation. Therefore, each time is divided into two half steps where at the first time step we sweep in the Y direction to solve all the X grids whilst using the known previous solution of the values in the Y grid. Therefore the discretization of the first step is defined as:

$$\frac{C_{i,j}^{k-\frac{1}{2}} - C_{i,j}^{k-1}}{\tau_{k-\frac{1}{2}} - \tau_{k-1}} = \frac{\frac{C_{i+1,j}^{k-\frac{1}{2}} - C_{i,j}^{k-\frac{1}{2}}}{\Delta X_+} - \frac{C_{i,j}^{k-\frac{1}{2}} - C_{i-1,j}^{k-\frac{1}{2}}}{\Delta X_-}}{\frac{1}{2}(\Delta X_+ + \Delta X_-)} + \frac{\frac{C_{i,j+1}^{k-1} - C_{i,j}^{k-1}}{\Delta Y_+} - \frac{C_{i,j}^{k-1} - C_{i,j-1}^{k-1}}{\Delta Y_-}}{\frac{1}{2}(\Delta Y_+ + \Delta Y_-)} \tag{9.78}$$

and rearranging:

$$\delta = \alpha^X C_{i-1,j}^{k-\frac{1}{2}} + \beta^X C_{i,j}^{k-\frac{1}{2}} + \gamma^X C_{i+1,j}^{k-\frac{1}{2}} = \alpha^Y C_{i,j-1}^{k-1} + \beta^Y C_{i,j}^{k-1} + \gamma^Y C_{i,j+1}^{k-1} \tag{9.79}$$

where the coefficients are:

$$\alpha^X = \frac{2}{\Delta X_+ + \Delta X_-}(\frac{1}{\Delta X_-}),\ \alpha^Y = \frac{2}{\Delta Y_+ + \Delta Y_-}(\frac{1}{\Delta Y_-}) \tag{9.80}$$

$$\beta^X = \frac{2}{\Delta X_+ + \Delta X_-}(-\frac{1}{\Delta X_-} - \frac{1}{\Delta X_+}) - \frac{2}{\Delta \tau},\ \beta^Y = \frac{2}{\Delta X_- + \Delta X_-}(-\frac{1}{\Delta X_-} - \frac{1}{\Delta X_+}) - \frac{2}{\Delta \tau}$$

$$\gamma^X = \frac{2}{\Delta X_+ + \Delta X_-}(\frac{1}{\Delta X_+}),\ \gamma^Y = \frac{2}{\Delta Y_+ + \Delta X_-}(\frac{1}{\Delta Y_+})$$

In the second step we sweep along the X direction to solve all the Y equation using the previous solved values of the X grid from the first step. Therefore the discretization of the 2D diffusion equation is defined as:

$$\frac{C_{i,j}^{k} - C_{i,j}^{k-\frac{1}{2}}}{\tau_k - \tau_{k-\frac{1}{2}}} = \frac{\frac{C_{i+1,j}^{k-\frac{1}{2}} - C_{i,j}^{k-\frac{1}{2}}}{\Delta X_+} - \frac{C_{i-1,j}^{k-\frac{1}{2}} - C_{i,j}^{k-\frac{1}{2}}}{\Delta X_-}}{\frac{1}{2}(\Delta X_+ + \Delta X_-)} + \frac{\frac{C_{i,j+1}^{k} - C_{i,j}^{k}}{\Delta Y_+} - \frac{C_{i,j}^{k} - C_{i,j-1}^{k}}{\Delta Y_-}}{\frac{1}{2}(\Delta Y_+ + \Delta Y_-)} \tag{9.81}$$

and rearranging:

$$\delta = \alpha^X C_{i-1,j}^{k-\frac{1}{2}} + \beta^X C_{i,j}^{k-\frac{1}{2}} + \gamma^X C_{i+1,j}^{k-\frac{1}{2}} = \alpha^Y C_{i,j-1}^{k} + \beta^Y C_{i,j}^{k} + \gamma^Y C_{i,j+1}^{k} \tag{9.82}$$

The coefficients are the same for both steps.

On the sides of the cube, the coverage in a grid $2 > Z > 0$ (except to the boundaries), at each half time step the discretization of the 1D equations are:

$$\frac{C_{i,j}^{k} - C_{i,j}^{k-\frac{1}{2}}}{\frac{1}{2}\Delta\tau_k} = \frac{\frac{C_{i+1,j} - C_{i,j}}{\Delta Z_+} - \frac{C_{i,j} - C_{i-1,j}}{\Delta Z_-}}{\frac{1}{2}(\Delta Z_+ + \Delta Z_-)} \tag{9.83}$$

and can be rearranged to

$$\delta_i = C_i^{k-\frac{1}{2}} = \alpha_i C_{i-1} + \beta_i C_i + \gamma_i C_{i+1} \tag{9.84}$$

where:

$$\alpha_i = -\frac{2(\frac{1}{2}\Delta\tau_k)}{\Delta Z_-^2 + \Delta Z_+ \Delta Z_-},\ \beta_i = \frac{2(\frac{1}{2}\Delta\tau_k)}{\Delta Z_-^2 + \Delta Z_+ \Delta Z_-} + \frac{2(\frac{1}{2}\Delta\tau_k)}{\Delta Z_+^2 + \Delta Z_+ \Delta Z_-} + 1,\ \gamma_i = -\frac{2(\frac{1}{2}\Delta\tau_k)}{\Delta Z_+^2 + \Delta Z_+ \Delta Z_-} \tag{9.85}$$

The same coefficients and equation are defined for the index, j, the side of the cube which is perpendicular to the Y axis:

$$\delta_j = C_j^{k-1} = \alpha_j C_{j-1} + \beta_j C_j + \gamma_j C_{j+1} \tag{9.86}$$

The equations for the boundaries $i_s/j_s$, $i_0/j_0$ and for the continuity flux points $i_c/j_c$ are as follows.

At points $i_c/j_c$, continuity is added by mixing the side 1D expression with the 2D expression. For $i_c$, the discretizaiton for the first half time step is:

$$\frac{C_{i,j}^{k-\frac{1}{2}} - C_{i,j}^{k-1}}{\tau_{k-\frac{1}{2}} - \tau_{k-1}} = \frac{\frac{C_{i+1,j}^{k-\frac{1}{2}} - C_{i,j}^{k-\frac{1}{2}}}{\Delta X_c} - \frac{C_{i,j}^{k-\frac{1}{2}} - C_{i-1,j}^{k-\frac{1}{2}}}{\Delta Z_c}}{\frac{1}{2}(\Delta X_c + \Delta Z_c)} + \frac{\frac{C_{i,j+1}^{k-1} - C_{i,j}^{k-1}}{\Delta Y_+} - \frac{C_{i,j}^{k-1} - C_{i,j-1}^{k-1}}{\Delta Y_-}}{\frac{1}{2}(\Delta Y_+ + \Delta Y_-)} \tag{9.87}$$

and for the second half time step:

$$\frac{C_{i,j}^{k-\frac{1}{2}} - C_{i,j}^{k-1}}{\tau_{k-\frac{1}{2}} - \tau_{k-1}} = \frac{\frac{C_{i+1,j}^{k-\frac{1}{2}} - C_{i,j}^{k-\frac{1}{2}}}{\Delta X_c} - \frac{C_{i,j}^{k-\frac{1}{2}} - C_{i-1,j}^{k-\frac{1}{2}}}{\Delta Z_c}}{\frac{1}{2}(\Delta X_c + \Delta Z_c)} + \frac{\frac{C_{i,j+1}^{k} - C_{i,j}^{k}}{\Delta Y_+} - \frac{C_{i,j}^{k} - C_{i,j-1}^{k}}{\Delta Y_-}}{\frac{1}{2}(\Delta Y_+ + \Delta Y_-)} \tag{9.88}$$

Therefore the coefficients stay unchanged where $X_-$ equals $Z_c$. A similar approach is applied for the case of $i, J_c$ and in the corner $i_c, j_c$ both $X_-$ equals to $Z_c$ that corresponds to the 1D grid of $i_c$ index and $Y_-$ equals to $Z_c$ and corresponds to the 1D grid of the $j_c$ index.

At $i_0$, and $j_0$ we can assume that the rate of charge transfer is fast enough to fill up all active sites:

$$C_{i=0} = 1 \tag{9.89}$$

and thus

$$\alpha_0 = 0,\ \beta_0 = 1,\ \gamma_0 = 0,\ \delta_0 = 1 \tag{9.90}$$

The boundary condition at the edges on the top of the cube with the index $i_s/j_s$, is set to symmetry for the respective direction:

$$C_{j/i=s} - C_{j/i=s+1} = 0 \tag{9.91}$$

For $i_s$, the discretization for the first half time steps is:

$$\alpha^X = 0 \tag{9.92}$$

$$\beta^X = -1$$

$$\gamma^X = 1$$

$$\delta^X = 0$$

and the second time step is as normal. For $j_s$, the discretization for the first half time steps is as normal. The second time step is:

$$\alpha^Y = 0 \tag{9.93}$$

$$\beta^Y = -1$$

$$\gamma^Y = 1$$

$$\delta^Y = 0$$

The sets of equations with 3 unknown concentrations at each equation in each grid can be solved using the coefficients and with the Thomas algorithm. The solution for each grid is used in the ADI mehtod for every half time step to get the solution of the whole domain. Initial values are set to zero charge coverage in all space at $\tau = 0$. The time step is also an expanding grid, starts with a sufficiently small difference of $\Delta\tau$ to meet the large concentration gradients in the short times.

The flux of 'coverage' can be calculated by the gradient at $i = 0$:

$$J = \frac{C_{i=1} - C_{i=0}}{\Delta Z} \tag{9.94}$$

and finally, integrating (summing) over all 1D grids provide the total flux from a cube.

$$J/4 = \int\limits_0^L \frac{C_{i=1} - C_{i=0}}{\Delta Z} dY + \int\limits_0^L \frac{C_{j=1} - C_{j=0}}{\Delta Z} dX \tag{9.95}$$

# References

[1] S. Eloul and R. G. Compton *The Journal of Physical Chemistry C*, vol. 119, no. 49, pp. 27540–27549, 2015.

[2] F. Cottrell *Z Phys Chem*, vol. 42, pp. 385–431, 1903.

[3] A. J. Bard and L. Faulkner, *Electrochemical Methods: Fundamentals and Applications.* Wiley New York, 2001.

[4] R. G. Compton and C. E. Banks, *Understanding Voltammetry.* London, UK: Imperial College Press, 2006.

[5] D. Shoup and A. Szabo *J. Electroanal. Chem.*, vol. 140, no. 2, pp. 237–245, 1982.

[6] L. C. R. Alfred and K. B. Oldham *J. Phys. Chem.*, vol. 100, no. 6, pp. 2170–2177, 1996.

[7] M. Levi, Z. Lu, and D. Aurbach *Solid State Ionics*, vol. 143, no. 34, pp. 309 – 318, 2001.

[8] K. Gmucová, J. Orlický, and J. Pavlásek *Collection of Czechoslovak Chemical Communications*, vol. 69, no. 2, pp. 419–425, 2004.

[9] X.-F. Zhou, W. Cheng, and R. G. Compton *Nanoscale*, vol. 6, pp. 6873–6878, 2014.

[10] W. Cheng, C. Batchelor-McAuley, and R. G. Compton *ChemElectroChem*, vol. 1, no. 4, pp. 714–717, 2014.

[11] S. Eloul, E. Kätelhön, C. Batchelor-McAuley, K. Tschulik, and R. G. Compton *J. Phys. Chem. C*, vol. 119, no. 25, pp. 14400–14410, 2015.

[12] E. J. E. Stuart, K. Tschulik, D. Omanović, J. T. Cullen, K. Jurkschat, A. Crossley, and R. G. Compton *Nanotechnology*, vol. 24, no. 44, p. 444002, 2013.

[13] W. Cheng and R. G. Compton *Angew. Chem., Int. Ed.*, vol. 53, no. 50, pp. 13928–13930, 2014.

[14] X. Xiao and A. J. Bard *J. Am. Chem. Soc.*, vol. 129, no. 31, pp. 9610–9612, 2007.

[15] A. J. Bard, H. Zhou, and S. J. Kwon *Isr. J. Chem.*, vol. 50, no. 3, pp. 267–276, 2010.

[16] B. M. Quinn, P. G. van 't Hof, and S. G. Lemay *J. Am. Chem. Soc.*, vol. 126, no. 27, pp. 8360–8361, 2004.

[17] M. Thompson, G. G. Wildgoose, and R. G. Compton *ChemPhysChem*, vol. 7, no. 6, pp. 1328–1336, 2006.

[18] C. P. Andrieux and J. M. Savéant *J. Electroanal. Chem.*, vol. 111, no. 23, pp. 377 – 381, 1980.

[19] Q. Lin and R. G. Compton *J. Phys. Chem. C*, vol. 119, no. 41, pp. 23463–23469, 2015.

[20] C. Amatore, Y. Bouret, E. Maisonhaute, J. I. Goldsmith, and H. D. Abruna *ChemPhysChem*, vol. 2, no. 2, pp. 130–134, 2001.

[21] C. Rinfray, G. Izzet, J. Pinson, S. Gam Derouich, J.-J. Ganem, C. Combellas, F. Kanoufi, and A. Proust *Chem. Eur. J*, vol. 19, no. 41, pp. 13838–13846, 2013.

[22] P. N. R.W. Lewis and K. N. Seetharamu., *Fundamentals of the Finite Element Method for Heat and Fluid Flow,*. John Wiley & Sons Ltd, Southern Gate, Chichester, West Sussex, 2004.

[23] M. N. O. Sadiku, *Numerical Techniques in Electromagnetics.* CRC Press, Boca Raton, Florida, 2001.

[24] E. Kätelhön and R. G. Compton *Analyst*, vol. 140, pp. 2592–2598, 2015.

# Chapter 10

# Conclusions

This thesis set out to develop new diffusion models for modern electrochemical methods, where the transport can be that of nanoparticles or larger, and the electrodes can be of miniature sizes. Using accurate and high performance simulation along with analytical models, diffusion to electrodes was investigated, with the following conclusions.

In the first area of the thesis, the stochastic arrivals/impacts of particles at the electrode were studied for the case of pure Brownian particles. The connection between Einstein's diffusion equation and the Fick's second law was utilised and simple expressions were established to predict the number of particles impacting on macro electrodes in the stochastic limits. The results along with random walk simulations provided a verification of a Poisson process, which enabled the calculation of the variance of the observations in an impact experiment. This work also introduced the estimation of the limit of detection, which was defined as the case of one impact assuming unity variance.

Following that, approximate analytical expressions for the practical cases of microdisc and microwire electrodes were developed. The expressions can be applied directly to 'nano-impact' experiments and provide the relation between the electrode geometry, its size, the concentration, and the number of observed impacts expected. We also provided expressions which can be used as an indication for the lower limit of detection in ultra-dilute solutions. The results for the number of hits/impacts and the lower limit of detection, revealed the advantage of using the wire over the use of microdisc electrodes in particular at ultra-low concentrations and in the femto-Molar region.

In the second area of the thesis, the inclusion of the loss of hydrodynamic mobility as the particle moves close to a surface was investigated. This hindering of diffusion is usually neglected in non-confined spaces. However, it was shown that for sufficiently small targets the transport is effectively confined by the diffusion layer. Subsequently, it was shown that the flux strongly depends on the size of the particle and the size of the target regardless of the cell size. Analytical and numerical studies enabled the development of equations that showed the flux dependency on the ratio between the size of the target and the size of the particle. The functions estimate the flux of particles in experimental studies such as the electrochemical 'impact' method. Additionally, calculations of the mean first passage time in sub micro sized targets, shows that the expected mean first passage time is drastically changed due to hindered diffusion. Hence it is particularly important for the understanding of diffusion processes such as biomolecules searching for sub-micrometre size targets. This includes synapse regulation of the exit rate, drag delivery applications and modelling travel of viruses towards a nuclear pore. The importance of the tunnelling distance was also realised in this work. This realisation opened a new way for further development of a unified model for the flux of particles towards an electrode, as function of the diffusion layer in comparison to the hindered diffusion layer, and the tunnelling layer.

The third area of the thesis investigated an adsorbing supporting surface effect on voltammetry and chronoamperometry. It was shown that if an irreversible adsorption occurs on the sheath used to insulate a microdisc electrode, then this can have a high impact on the measured current-time data. This was quantitatively related to a 'shielding effect'. The observed quasi-steady state currents were shown to be a function of the sheath to disc electrode radius ratio and the adsorption rate. The data which was reported can be directly used in experimental systems and can be identified in future ‘impact method’ experiments.

Later, the model was extended to explore a reversible adsorption on the insulating surface. It was shown that an adsorbing surface adjacent to the disc electrode can provide an enhancement of the voltammetry signal. This may be useful for analytical methods but the current enhancements are found to be limited due to the need for the both high surface coverage *and* fast desorption kinetics. It was also realised that desorption to adsorption rate constant ratio should be close to unity in order to achieve a maximum enhancement of the signal.

In the last area of the thesis, a simulation model was developed to explore the shape effects and the surface coverage of insulating particles modified with an electroactive surface layer immobilised on an electrode. The model described a diffusion of charge transfer between electro-active sites on a modified surface of insulating particles, assuming charge injection from an electrode supporting the particle. The simulation carried out to measure the effect of the current-time responses of particles with a shape of a sphere, a cube/cuboid, and a cylinder. The characteristic current-time responses can be used to determine the coverage or the diffusion of charge coefficient of the modified insulating particles of the various shapes. It was shown that the current-time response has different profiles, which reflects the particle shape and aspect ratio. The model allows one to distinguish between the various shapes in chronoamperometry experiments in which the particles impact an electrode held at a suitable potential.

Overall, the thesis demonstrated the importance of understanding and modelling diffusion towards electrodes in modern electrochemistry. Although the numerical and analytical models are inspired by diffusion to electrodes, the insights and conclusions have a relevant to a broader range of processes in physical chemistry such as adsorption processes and diffusion to targets.